THE METAL PHOTODISSOLUTION EFFECT IN As-S GLASSES

AND ITS APPLICATION IN IR GRATING FABRICATION

by

A. Zakery

A thesis presented for the degree of

Doctor of Philosophy

University of Edinburgh

Department of Electrical Engineering

May 1991

To my parents

CONTENTS

ACKNOWLEDGEMENTS

I would like to thank my supervisors Dr. P.J.S. Ewen and Professor A.E. Owen for their help and advice during the project, and would like to express my gratitude to Dr. C.W. Slinger of RSRE, Malvern for many useful discussions during the project. I would also like to thank Drs. P. Hill, J. Craven and S. Kearns of the Geology Department at Edinburgh University for their help with the Electron Microprobe and Ion probe analysis. I would like to express my gratitude to the technical staff of the Electrical Engineering and Physics Departments at Edinburgh University for their technical assistance. I am grateful to the U.K. Ministry of Defence for their sponsorship of this project and also to the Ministry of Higher Education in Iran for their co-operation in the financial arrangements. Finally, I am obliged to my family for their encouragement, understanding and support.

Abstract

This work investigates the feasibility of using the metal photodissolution effect peculiar to chalcogenide glasses as a means for producing grating structures for use at infrared wavelengths. The material properties and characteristics of the effect relevant to grating fabrication and performance have been examined, the study dealing exclusively with Ag photodissolution in As-S glasses. Different fabrication techniques have been investigated and the performance of the gratings produced has been compared with theoretical predictions.

A technique based on simultaneous reflectivity and transmissivity measurements has been developed and used to probe the kinetics of photodissolution, in particular its dependence on wavelength and intensity of illumination. A composition around $As_{30}S_{70}$ was found to be optimum for applications since it had maximum sensitivity and also exhibited negligible photodarkening. A model has also been proposed for photodissolution which explains the spectral dependence and the intensity dependence of the photodissolution rate and suggests that the actinic radiation is absorbed in the photodoped layer. Gratings were produced both holographically and by mask exposure and suitable etchants identified for removal of the undoped material and the residual Ag layer. A coupled-wave model has been developed which predicts that diffraction efficiencies of up to 90% can be achieved in the multiwave regime at 10.6 μm. Diffraction efficiencies of up to 20% have been measured for both the zero and ± 1 orders at 632.8 nm which are in good agreement with the results of the theoretical model. Optical constants of both the undoped and Ag-doped As-S films have been measured over the wavelength range 0.5-12 μm to enable the analysis of kinetics measurements and also the development of the theoretical model. The results of these measurements show that there is a significant change in the refractive index (by up to 0.5, depending on Ag content) and also in the optical gap of the As-S films upon incorporation of silver, although the absorption coefficient of the Ag-doped As-S films remains small in the IR. The results of a secondary ion mass spectroscopy analysis showed that the composition of the As-S films varies very little with depth while the silver concentration may vary by up to 20 % in the Ag-doped As-S films.

1. INTRODUCTION

1.1 Chalcogenide glasses

Chalcogenide glasses, that is, alloys of the chalcogen elements S, Se and Te with elements such as Ge, Si, As or P, are semiconductors with band gaps in the range 1-3 eV . The chalcogen elements are so called because they are chemical analogies of oxygen in the periodic table . Flexibility of their structure together with their high-lying lone-pair electron states make chalcogenide glasses susceptible to a wide variety of photoinduced changes. Their structure cannot be described by means of a continuous random network which is isotropic in three dimensions, as in the case of a-Si: for example, As_2S_3, As_2Se_3, GeS_2 and $GeSe_2$ are layer-like while pure S and Se are chain-like . For all these materials there is considerable flexibility of the structure as a result of the van der Waal's bonding between e.g. layers (Elliott 1986), so changes in the structure can be relatively easily accommodated.

1.2 Light-induced effects

A wide variety of light-induced effects have been observed in chalcogenide glasses. They are important because of their potential applications in, for example, optical mass memories, functional waveguides, and high resolution lithography. These light-induced effects generally do not occur in crystalline materials because their structure is rigid. They occur in chalcogenide glasses because of their structural flexibility and the fact that their band gap is smaller than or comparable with the energy of visible light. Amorphous chalcogenide semiconductors are thermodynamically in a non-equilibrium state and hence their physical and chemical properties can be changed by means of some source of energy e.g. heat treatment or light irradiation. These effects can also be induced by X-rays, γ-rays, electron beams and ion beams.

At least seven varieties of light-induced effect have been observed in chalcogenide glasses (Owen et al. 1985) and these are classified in Fig. 1-1. The light-induced effects which occur in chalcogenide glasses can generally be divided into two main classes, reversible and irreversible changes. Reversible changes (e.g. photodarkening), are those which can be removed by means of some form of heat treatment (normally at the glass transition temperature T_g), upon which the chalcogenide glass regains its initial physical and structural properties. The magnitude of the changes accompanying the reversible light-induced effects are small and these changes occur in melt-quenched glasses and well-annealed films. Irreversible changes (e.g. photopolymerization, photochemical effects, etc.) are those which are permanent and cannot be removed by any source of energy. The magnitude of these irreversible changes is large and they normally occur in poorly annealed or as-deposited films. Although light-induced effects in chalcogenides have been extensively studied, there is no complete understanding of the underlying processes. Extensive reviews of these light-induced effects in chalcogenide glasses and of the mechanisms involved (normally for reversible effects) are given by Tanaka (1982), Owen et al. (1985), Elliott (1986), Lyubin (1987) and Tanaka (1990).

1.3 Reversible effects

As mentioned above, this class of photoinduced effects occurs in well-annealed films and melt-quenched bulk glasses which have nearly the same structure. They are mainly classified according to whether they are of structural origin or whether they exhibit optical changes (e.g. photodarkening).

1.3-1 Photodarkening

Photodarkening was originally observed in As_2S_3 by DeNeufville et al. (1973/1974). Illumination with 2.4 eV light caused a red shift of the absorption edge and it was found that the photodarkened state could be recovered by annealing at the glass transition

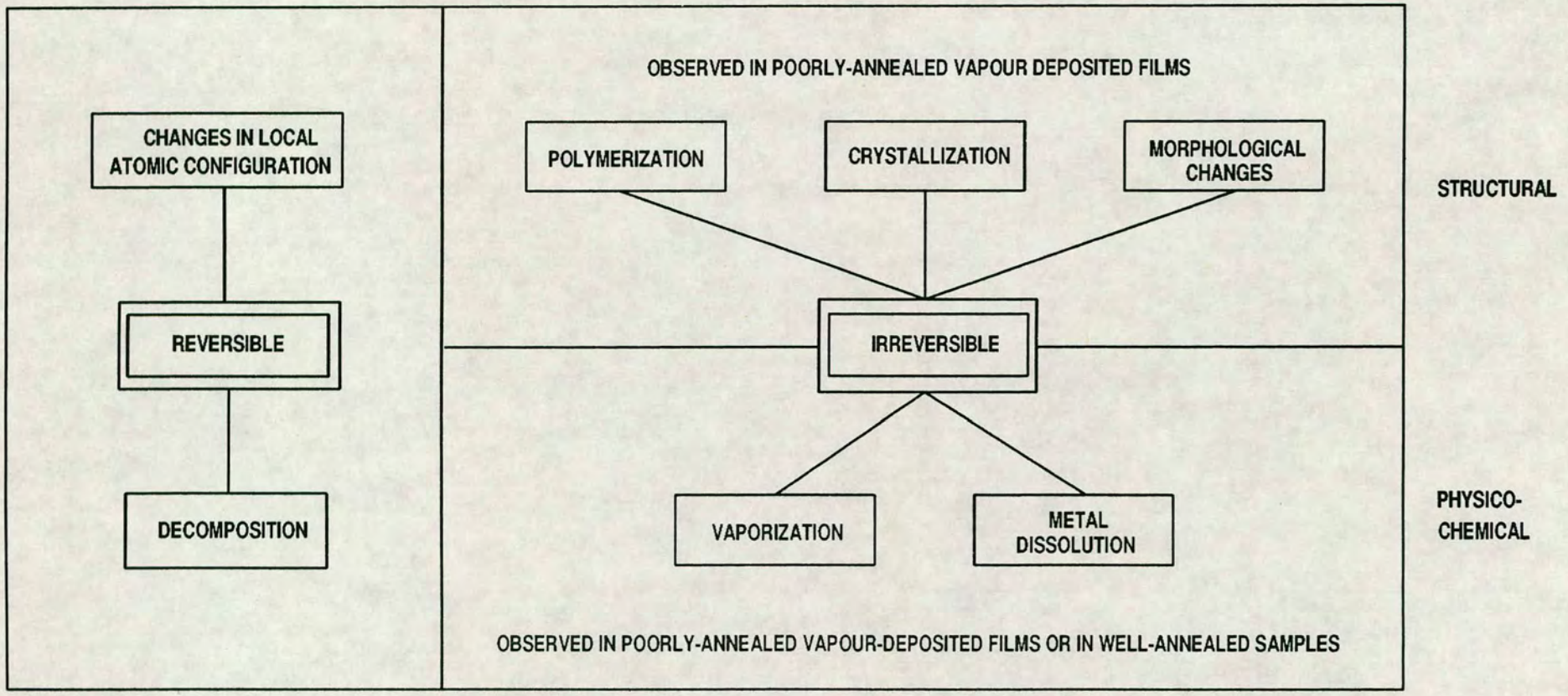

Fig. 1-1 Classification of photoinduced structural and physico-chemical phenomena in amorphous chalcogenide semiconductors. (From Owen et al. 1985).

temperature (T_g = 450 °K). Photodarkening is characterized by a nearly parallel shift of the absorption edge. The edge shift, ΔE, generally increases with decreasing temperature (Tanaka 1975). Chalcogenide glasses (both alloys and elements) all exhibit the effect to some degree. As-S(Se) films (Fritzsche et al. 1981), isolated chains of Se (Katayama et al. 1989) and P (Kawashima et al. 1987) exhibit the effect while As (Mytilineou et al. 1980) and crystalline chalcogenides (Tanaka 1982) do not show the red shift. It should be mentioned that photodarkening is only detectable in thin bulk samples (<10-20 μm) because photodarkening increases absorption at band gap illumination and hence reduces the effective penetration of the light. Lyubin (1987) has demonstrated that the photodarkening behaviour in films and bulk samples are somewhat different. In photodarkened films the initial optical properties (transmission) are totally restored by heating the sample at T_g, the glass transition temperature, while in bulk photodarkened samples exposed at 77 °K the total restoration of the initial optical properties was achieved by heating the sample to room temperature. The absence of darkening for X-ray or γ-quanta irradiation (Lyubin 1987) has been attributed to the fact that these kinds of irradiation do not excite the upper lone-pair electrons in the valence band in As-chalcogenides but rather the σ-electrons involved in interatomic bonds.

1.3-2 Photostructural changes

X-ray diffraction measurements have shown that reversible photostructural changes occur simultaneously with optical changes (Tanaka 1975). The diffracted X-ray intensity curve of evaporated As_2S_3 shows that the first diffuse peak is slightly shifted to higher angles and its intensity is lowered as a result of exposure. Similar behaviour has been reported in evaporated $As_4Se_5Ge_1$ (Tanaka et al. 1976). The other manifestation of the reversible photostructural change is observed in the photoinduced thickness increase of evaporated and melt-quenched As_2S_3 upon illumination (Tanaka 1980). A fractional change of $\Delta d/d \sim 0.40$ % has been obtained for evaporated films which is thickness independent while for melt-quenched glasses a nearly similar value of $\Delta d/d \sim 0.50$ % has

been obtained. These changes seem to increase with decreasing exposure temperatures, which is similar to the behaviour observed in photodarkening. Lyubin (1987) has observed that in bulk $As_{50}Se_{50}$ microhardness increases under γ-irradiation. The initial value of microhardness could be restored by annealing the sample at the glass transition temperature T_g.

1.3-3 Other reversible photoinduced effects

Illumination at low temperatures induces the reversible phenomenon of so called "photoinduced mid-gap absorption" extending from E_g to $E_g/2$, which disappears with annealing at around $T_g/2$ (Biegelsen and Street 1980). A possible mechanism for mid-gap absorption may be the creation of unpaired dangling bonds or valence alternation atoms (Elliott 1983).

"Photoinduced anisotropy" is another reversible optical phenomenon observed in chalcogenide films. As_2S_3 films illuminated with linearly-polarized light exhibit dichroism and birefringence (Kimura et al. 1985). The anisotropic states are determined by the polarization of the last illumination and can be removed by illuminating the sample with unpolarized or circularly polarized light. The magnitude of the anisotropies are roughly one tenth of the photodarkening and the related refractive index change (Kimura et al. 1985).

Photodecomposition is the light-induced dissociation of a compound into its constituents caused by illuminating the sample with light of photon energy greater than E_g (Tanaka 1981,1982). Photodecomposition is characterized by a red shift in the absorption edge, i.e photodarkening, and if the energy and intensity of illumination are not too high the photodecomposition is reversible at T_g. Photodecomposition in As chalcogenide glasses involves dissociation of the arsenic-chalcogen bond as a result of absorption of a photon of energy greater than E_g, followed by thermal diffusion of the As to form arsenic clusters, which are highly absorbing. In well-annealed films or bulk samples of a-As_2S_3 heteropolar As-S bonds are favoured, although a small percentage (about 1 %) of homopolar As-As and S-S bonds may be present (Ewen and Owen 1980). Owen et al. (1985) have stated

that it is possible that above-band-gap illumination alters the bond statistics from a distribution close to that for the chemically-ordered network model towards one characteristic of a random-network model, that is the randomness of the bond distribution is increased. Isolated As-As bonds are energetically unfavourable and when produced will soon return to the initial state. Large clusters, however are relatively more stable and hence can give rise to the photodarkening. Since at T_g the atoms are more mobile, annealing at this temperature causes dissociation of even large clusters and hence the effect is reversible.

1.4 Factors affecting reversible photoinduced changes

Several factors including temperature, composition, the wavelength of illumination and pressure seem to affect the magnitude of photoinduced effects. Tanaka (1983) has measured the change in ΔE (the edge shift) as a result of photoinduced changes for a variety of S- and Se-containing glasses as a function of temperature and his results show that the magnitude of these changes increases as temperature decreases and at T_g no photostructural effect can be induced at all. Elliott (1986) has explained the behaviour of photostructural effects at low temperatures. If the geminate recombination of the photoexcited electron hole pair is important, the probability of inducing a photostructural change would be largest at low temperatures, where the separation of photocarriers by thermal diffusion is minimized.

Another factor which influences the magnitude of the photoinduced effects is the composition of the chalcogenide glass. Generally S-containing glasses exhibit larger effects than Se-based materials which in turn show larger effects than Te-based chalcogenides. One likely explanation (Elliott 1986) for this observation is that the strength of inter-molecular bonding increases in the series S → Se → Te and as a result, the local flexibility of the structure will be progressively reduced. He states that these inter-molecular bonds are the most likely to be broken as a result of photon absorption because they are the weakest bonds and, in addition, the electron states associated with such bonds are the highest lying states in the valence band and hence the most likely to be excited.

The spectral dependence of the photoinduced effects in As_2S_3 has been determined by Tanaka et al. (1977). They have measured the edge shift (ΔE) at 293 °K as a function of photon energy for evaporated and melt-quenched As_2S_3 glass. Their results show that ΔE tends to a constant value for $h\nu > 2.4$ eV while it falls off steeply at low photon energies ($h\nu < 2.4$ eV). They state that the photodarkening is essentially induced by the interband optical absorption. This result clearly shows that the above-band-gap energy is most effective in inducing photodarkening.

Hydrostatic pressure is another factor which has some effect on the magnitude of the photostructural change in chalcogenide glasses. Tanaka (1986) has found that the photodarkening in Se disappears when it is subjected to high pressures. A similar result for As_2S_3 has been obtained by Pfeiffer et al. (1989). This disappearance of photodarkening has been attributed to the decrease in intermolecular space (Tanaka 1990).

1.5 Mechanisms of the reversible photoinduced effects

In order to understand the mechanisms of the photoinduced effects in chalcogenide glasses a knowledge of their electronic structure is required. Calculations of the electronic density of states (DoS) for materials such as Se, As_2Se_3 and $GeSe_2$ have revealed that the valence band can be separated into three contributions (Elliott 1986): deep-lying (non-bonding) S states, bonding p-σ states and lone pair p-π states. For the pure chalcogens Se and Te, the p-like bonding region of the DoS has two contributions, the upper part being associated with inter-molecular bonding due to charge density between chains, and the lower part with conventional intra-molecular p-σ bonds due to charge density between the atoms within chains. It is expected that the same situation applies to chalcogenide alloys. A variety of mechanisms have been suggested to explain the reversible photoinduced effects in chalcogenide glasses and the most important ones are discussed below.

Tanaka (1982) has concluded from the calculation of the density of local atomic displacements involved in photostructural changes ($10^{20} \sim 10^{21}$ cm^{-3}) that the origin of the photostructural change is not directly related to the native defects (i.e dangling bonds, which have a density of $\sim 10^{17}$ cm^{-3}) but to bulk-oriented features in a disordered network. He states that some extensive feature of the disorder such as fluctuations in bond angle is responsible for the origin of the photostructural effects in chalcogenide glasses. He has proposed a configurational model of bistable local bonding geometries in which the action of light is to cause minor bond re-arrangements involving chalcogen atoms. As a result, the potential energy of the system can relax between the minima of a double well potential.

Another model involving intra-molecular bond breaking has been suggested by Street (1977), in which an optically created exciton (electron-hole pair) can lower its energy by "self trapping" instead of a direct recombination. The self-trapped exciton model which involves the creation of a C_3^+ and C_1^- centre can explain the mechanism of photodarkening. The minimum energy of the self-trapped exciton lies outside the curve for the ground state. The action of light is to cause optical transitions between the ground and the self-trapped exciton states.

Elliott (1986) has given a unified model for reversible photostructural effects in chalcogenide glasses in terms of both inter-molecular and intra-molecular bond weakening mechanisms. He states that the particular microscopic mechanism that is dominant is determined by the composition of the material and in particular by the type of chalcogen present. He has proposed an inter-molecular bond breaking mechanism in which the weak, attractive (interlayer) interactions are particularly vulnerable to optical excitation. Two intra-molecular bond breaking mechanisms, namely the self-trapped exciton model (STE) and a random covalent network (RCN) transformation model in which two heteropolar bonds are transformed into two different homopolar bonds have also been suggested. In the case of As chalcogenide glasses, it is likely that inter-molecular bond-breaking processes are dominant.

Recently Tanaka (1990) has given a two-phase structural model. He assumes that amorphous chalcogenide semiconductors are composed of two phases; a more ordered phase (O) and a less ordered, or disordered phase (D). The average extent of the ordered region is ~ 20 A. He also postulates that photodarkening sites are located at boundaries between the two phases. The photoinduced changes which occur on an atomic scale convert the boundary regions from the O to the D phase, reducing the O-region fraction. This model can predict quantitatively the site density of the photodarkening and explains the decrease in the intensity of the first diffraction peak and the decrease in the elastic constants.

1.6 Irreversible photoinduced effects

As mentioned earlier the magnitudes of the irreversible photoinduced changes are usually large and these changes depend very much upon the preparation conditions. Changes of up to 0.7 in refractive index have been observed in As-S and As-Se films (Shvarts et al. 1987).

Photopolymerization is an irreversible photoinduced effect which occurs in some chalcogenide films. As-deposited thin films of certain chalcogenide compounds prepared by vacuum evaporation contain some of the molecular units which exist in the vapour. For example, in the case of As_2S_3, As_4S_4 molecules are present in the vapour and are also found in as-deposited a-As_2S_3 films. Illumination causes these molecular units to polymerize and combine with the amorphous As-S network. Photopolymerization is characterized by a densification and if the films are exposed to prolonged illumination the density and the structure of the thin film becomes identical with that of well-annealed films and melt-quenched glasses. Photopolymerization is also reported to occur (Porter et al. 1972) in the crystals of As_4S_4.

Photocontraction is another irreversible photoinduced effect which is accompanied by significant changes. Owen et al. (1985) proposed that the term 'photoinduced morphological changes' should be used to denote these effects, since the phenomenon has

its origin in changes in the macroscopic structure of the films, that is in their morphology. These changes have been observed mainly in thin films of Ge-Se compositions that during deposition grow in a columnar structure (Singh et al. 1979). When these films are illuminated, particularly with u.v. light, they contract in volume. The magnitude of these changes depends on the composition and particularly on the angle of incidence at which the vapour-deposited film is grown. Contractions in volume of up to 12% can occur. This effect is thought to be due to a collapse of the columnar morphology of the films.

Other irreversible effects include photocrystallization, which was first observed in a-Se (Dresner et al. 1968, DeNeufville 1974) and photovaporization. Kr-ion and dye lasers have been used to study photoinduced crystallization and re-amorphization in As-Te-Ge thin films. Re-amorphization requires that the temperature of the thin film be raised to the melting point of the crystals which can be achieved by a laser pulse. Photovaporization is a photooxidation reaction followed by thermal evaporation of the volatile oxidation products (Janai 1981) and has been studied mainly in As_2S_3 thin films.

1.6-1 Photodissolution

When a chalcogenide layer in contact with a metal layer is illuminated, metal ions dissolve into the glass and migrate through it in the direction of illumination, thereby altering the composition and structure of the glass and changing its physical properties, particularly its solubility and optical constants. The accepted explanation of the effect is that it is essentially a light-induced chemical reaction between the metal and the chalcogenide to form a new material which may be a single compound or a phase-separated mixture. This reaction product separates the metal and chalcogenide layers, so that for the reaction to proceed the new material must be both an ionic and electronic conductor, i.e it must allow the metal ions and electrons to diffuse through it to reach the product/chalcogenide interface, where they can continue to react with the chalcogenide. The effect has been observed in many chalcogenide systems and a variety of metals, metal compounds and alloys have been used as the metal-ion source (see Chapter 2).

Of the various irreversible photoinduced effects photodissolution is probably the most important as far as applications are concerned since it introduces the largest changes in the physical and chemical properties of the chalcogenide.

1.7 Applications

The wide variety of photoinduced phenomena exhibited by chalcogenide glasses enable them to be used as optical imaging media (Shimizu et al. 1975). A particularly important feature is the change in refractive index under the influence of light, which makes it possible to use chalcogenide glasses to record not only the amplitude but also the phase of illumination. The latter is particularly important in holographic optical data storage (Bordogna and Keneman 1977) and in the fabrication of various integrated-optics components and devices such as selective optical filters, mixers, couplers, modulators, etc. (Andriesh et al. 1986). Chalcogenide films have been suggested for optical mass memories (Watanabe et al. 1983) and Sb_2Se_3 and Sb_2Te_3 films have been extensively investigated since they have great promise for reversible video disc applications.

Chalcogenide glasses are also well known IR transmitting materials having pass bands (depending on composition) from the visible to beyond 15 μm (Savage 1985). Hence, by making use of the photoinduced phenomena that occur in these glasses, it should be possible to produce diffractive elements for use at IR wavelengths. These elements have a potentially large range of uses in this waveband. Examples include simple gratings, mirrors, lenses and beam combiners. These elements may have advantages over conventional IR refractive elements as regards weight, cost and ease of fabrication (Close 1975).

The high transparency of chalcogenide glasses in the IR together with the ability to draw long filaments open up extensive opportunities for the use of these materials as fiber waveguides for IR radiation (Andreish et al. 1986), typical losses being 35 dB/km at 2.44 μm for the stoichiometric composition As_2S_3 (Kanamori et al. 1984). Optical fibers made of chalcogenide glasses have a future in devices for matching both light sources to

radiation detectors and quartz fibers to thin-film waveguides, and also for the transfer and processing of optical data and the channelling of high-power infrared radiation (Andriesh et al. 1986).

Photosensitive chalcogenide systems also have potential as photoresists for submicron lithography in the fabrication of integrated circuits (Tai et al. 1982) and as some of the photoinduced effects can be stimulated by X-rays and electron beams, as well as by light, very high resolution can be achieved.

1.8 Aims and objectives

The metal photodissolution effect is probably the most useful of the various photoinduced phenomena as far as their applications are concerned because it produces the largest change in the physical and chemical properties of the chalcogenide, particularly the optical constants and etch resistance. In the present study the metal photodissolution effect has been employed to fabricate gratings in As-S chalcogenide glasses using Ag as the metal source. The objectives of the study being: first, to show that it is possible in principle to fabricate gratings suitable for IR operation ; secondly to determine how the effect might best be used to fabricate IR gratings ; thirdly, to investigate certain aspects of the metal photodissolution effect relevant to the fabrication of grating structures (e.g. the kinetics of the effect) ; and finally to evaluate the performance of the gratings produced.

A variety of techniques can be used to fabricate gratings using the metal photodissolution effect (e.g. mask exposure or the holographic technique) and different structures can be produced (i.e surface relief or bulk phase types). In order to optimize the use of the metal photodissolution effect in making these structures a knowledge of the kinetics of the effect is required, particularly its dependence on the wavelength and intensity of illumination. Sensitivity, however, depends on the composition of the chalcogenide and hence a compositional analysis of the photodissolution sensitivity in the As-S system is also required to find the optimum composition. For the analysis of the kinetics data a knowledge of the optical constants of the As-S glasses is required.

To investigate the response of the gratings produced it is possible to use a theoretical model and this can also be used to predict the required grating parameters for efficient operation in any particular waveband. This model also requires a knowledge of the optical constants of both the undoped and Ag-doped As-S glasses. In addition, the model requires a knowledge of how these optical constants vary with depth and hence some probe technique must be used to determine this information. Finally, measurements of diffraction efficiency of the fabricated gratings are necessary for comparison with those predicted by the model.

The work carried out in the present study is organised as follows. A review of the previous work on the photodissolution effect is presented in Chapter 2 while Chapter 3 describes the material preparation, sample fabrication and the compositional analysis of these chalcogenide glasses. Optical constant measurements of both the undoped and Ag-doped As-S thin films are presented in Chapter 4. Chapter 5 describes the kinetics of photodissolution of silver in amorphous As-S films. Both secondary ion mass spectroscopy (SIMS) and positron ion scattering have been employed to determine the silver distribution in As-S chalcogenide thin films after photodissolution and these results are presented in Chapter 6. Grating fabrication in As-S films using the metal photodissolution effect and the diffraction efficiency measurements of the fabricated gratings are discussed in Chapter 7. Finally, the conclusions reached in this study and suggestions for further work are presented in Chapter 8.

1.9 References

Andriesh, A.M., Ponomar, V.V., Smirnov, V.L., and Mironos, A.V., 1986, Sov. J. Quantum Electron., 16(6), p. 721.

Biegelsen, D.K., and Street, R.A., 1980, Phys. Rev. Lett., 44, p. 803.

Bordogna, J., and Keneman, S.A., 1977, " Holographic Recording Media, edited by

H.M. Smith", (Berlin : Springer-Verlag), p. 229.

Close, D.H., 1975, Opt. Eng., 14, p. 408.

DeNeufville, J.P., Moss, S.C., and Ovshinsky, S.R., 1973/1974, J. Non-Cryst. Solids, 13, p. 191.

DeNeufville, J.P., 1974, Amorphous and liquid semiconductors, edited by J. Stuke and W. Brenig (London : Taylor and Francis), p. 1351.

Dresner, J., and Stringfelow, G.B., 1968, J. Phys. Chem. Solids, 29, p. 303.

Elliott, S.R., 1983, "Physics of Amorphous Materials, (Longman, London).

Elliott, S.R., 1986, J. Non-Cryst. Solids, 81, p. 71.

Ewen, P.J.S., and Owen, A.E., 1980, J. Non-Cryst. Solids, 35-36, p. 1191.

Fritzsche, H., Smid, V., Ugur, H., and Gaczi, P.J., 1981, J. Phys. 42, C4-699.

Hamanaka, H., Tanaka, K., Tsuji, K., and Minomura, S., 1981, J. Phys., Paris, 42, p. 399.

Janai, M., 1981, J. Phys., Paris, 42, p. 1105.

Kanamori, J., Terunuma, Y., Takahashi, S., and Miyashita, T., 1984, J. Lightwave Technol. LT-2, p. 607.

Katayama, Y., Yao, M., Ajiro, Y., Inui, M., and Endo, H., 1989, J. Phys. Soc. Jpn., 58, p. 1811.

Kawashima, K., Sono, H.H., and Abe, Y., 1987, J. Non-Cryst. Solids, 95-96, p. 741.

Kimura, K., Murayama, K., and Ninomiya, T., 1985, J. Non-Cryst. Solids, 77-78, p. 1203.

Lyubin, V.M., 1987, J. Non-Cryst. Solids, 97-98, p. 47.

Mytilineou, E., Taylor, P.C., and Davis, E.A., 1980, Solid State Commun., 35, p. 497.

Owen, A.E., Firth, A.P., and Ewen, P.J.S., 1985, Phil. Mag., B, 52(3), P. 347.

Pfeiffer, G., and Peasler, M.A., 1989, J. Non-Cryst. Solids, 114, p. 130.

Porter, E.J., and Sheldrick, G.M., 1972, J. Chem. Soc. Dalton, p. 1347.

Savage, J.A., 1985, "IR Optical Materials and their Antireflection Coatings", (Adam Higler, Bristol), p. 79.

Shimizu, I., Kokado, H., and Inoue, E., 1975, Photogr. Sci. Engineering, 19, p. 136.

Shvarts, K.K., Teteris, J.A., Manika, J.P., Reinfelde, M.J., and Gebreder, V.I., 1987, J. Non-Cryst. Solids, 90, p. 509.

Singh, B., Rajagopolan, S., Bhat, P.K., Pandya D.K., and Chopra, K.L., 1979, Solid. St. Commun., 29, p. 167.

Street, R.A., 1977, Sol. St. Commun., 24, p. 363.

Tai, K.L., Ong, E., and Vadimsky, R.G., 1982, Proc. Electrochem. Soc., 82-89, p. 9.

Tanaka, Ka., 1975, Appl. Phys. Lett., 26, p. 243.

Tanaka, Ka., Iijimu, S., Aoki, K., and Minomura, S., 1976, : Proc. 6th Intern. Conf. Amorphous and liquid Semiconductors, Leningrad, ed. by B.T. Kolomiets, p. 442.

Tanaka, Ka., Hamanaka, H., and Iizima, S., 1977, : Proc. 7th Intern. Conf. Amorphous and liquid Semiconductors, Edinburgh, ed. by W.E. Spear, p. 787.

Tanaka, Ka., 1980, J. Non-Cryst. Solids, 35-36, p. 1023.

Tanaka, Ka., 1981, Fundamental Physics of Amorphous Semiconductors, edited by F. Yonezawa (Berlin : Springer-Verlag), p. 104.

Tanaka, Ka., 1982, Amorphous Semiconductor Technologies and Devices edited by Y. Hamakawa (Tokyo : Ohmsha), p. 227.

Tanaka, Ke., 1983, J. Non-Cryst. Solids, 59-60, p. 925.

Tanaka, Ke., 1986, Jpn. J. Appl. Phys., 25, p. 779.

Tanaka, Ke., 1990, Rev. of Solid State Sci., 4(2&3) p. 641.

von Gutfeld, R.J., and Chaudhari, P., 1972, J. Appl. Phys., 43, p. 4688.

Watanabe, K., Sato, N., and Miyaoka, S., 1983. J. Appl. Phys., 54, p. 1256.

Weiser, K., Gambino, R.J., and Reinhold, J.A., 1973, Appl. Phys. lett., 22, p. 48.

2. THE METAL PHOTODISSOLUTION EFFECT

2.1 Introduction

The photographic sensitivity of a thin amorphous chalcogenide film, such as As_2S_3, deposited on metallic silver was discovered by Kostyshin, Mikhailoskaya and Romanenko (1966). This process was termed "photodoping", "photodissolution" or "photoenhanced diffusion" of metal and has been proposed as the basis of several applications including resists for submicron lithography, using X-rays, e-beam, ion-beam or optical sources (Chang et al. 1978).

In the photodissolution process a thin layer of metal (e.g silver, zinc or copper) deposited above or underneath a chalcogenide glass film dissolves into the chalcogenide glass under light irradiation. Compounds such as Ag_2S and Ag_2Se can also be used as the metal source. The most widely studied amorphous chalcogenide systems are those based on As-S and Ge-Se compounds. The metal photodissolution effect has also been observed in other chalcogenide systems such as As-Se, Ge-S, As-S-Te and crystalline As_2S_3, although a much slower photodissolution rate was obtained in the latter case. Despite extensive investigations of this effect, there is as yet no complete physical model.

In the present study the terms "photodoping", "photodissolution" or "photoenhanced diffusion" have been used interchangeably, although it should be noted that the term "photodoping" is not strictly correct because normally doping refers to a very small amount of impurities being added to the semiconductor whereas in this case large amounts of metal (up to 30-40 atomic % in some cases) can be incorporated in the glass matrix.

2.2 Kinetics of photodissolution

2.2-1 Nature of the time dependence

Different time dependence behaviour for the photodissolution process has been reported by different investigators. Some reported that the propagation distance for the photodoped front depends on the square root of the irradiation time (Shimizu et al. 1974, Kostyshin et al. 1982). More quantitative results showed that the photodissolution process has three stages: an induction period where the photodissolution rate increases from zero, then a second stage with constant dissolution rate, and finally a third stage during which the photodissolution rate decreases slowly (Goldschmidt et al. 1976). This result is shown in Fig. 2-1. The length of the induction period has been found to be inversely proportional to the light intensity (Goldschmidt et al. 1976). Yaji et al. (1983) believe that during the induction period accumulation of radiation damage (e.g. due to photostructural changes) takes place whereas Buroff (1980) suggests that the induction period arises from the formation of a barrier layer between the silver and the chalcogenide during the evaporation procedure. The latter believes that the induction period can only be observed if there is a break in the vacuum during the evaporation of the layers, so that if both layers are evaporated consecutively in the same vacuum the induction period is absent. This result has also been confirmed by Chatani et al. (1977). Rennie (1986) believes that as photodissolution commences the metallic film becomes porous or island-like. As photodissolution begins at the boundaries of the metallic grains, the amount of silver available for the reaction is small and the amount of the reaction product is also small and hence the photodissolution rate is slow. As the photodissolution proceeds the number of pores between the crystallite grains increases, thereby increasing the amount of the reacting silver and the reaction product, which results in an increase of the dissolution rate. Elliott (1991) suggests that the induction period is associated with the period during which such dendrites located at metallic grain boundaries, form a continuous doped layer by a process of lateral diffusion.

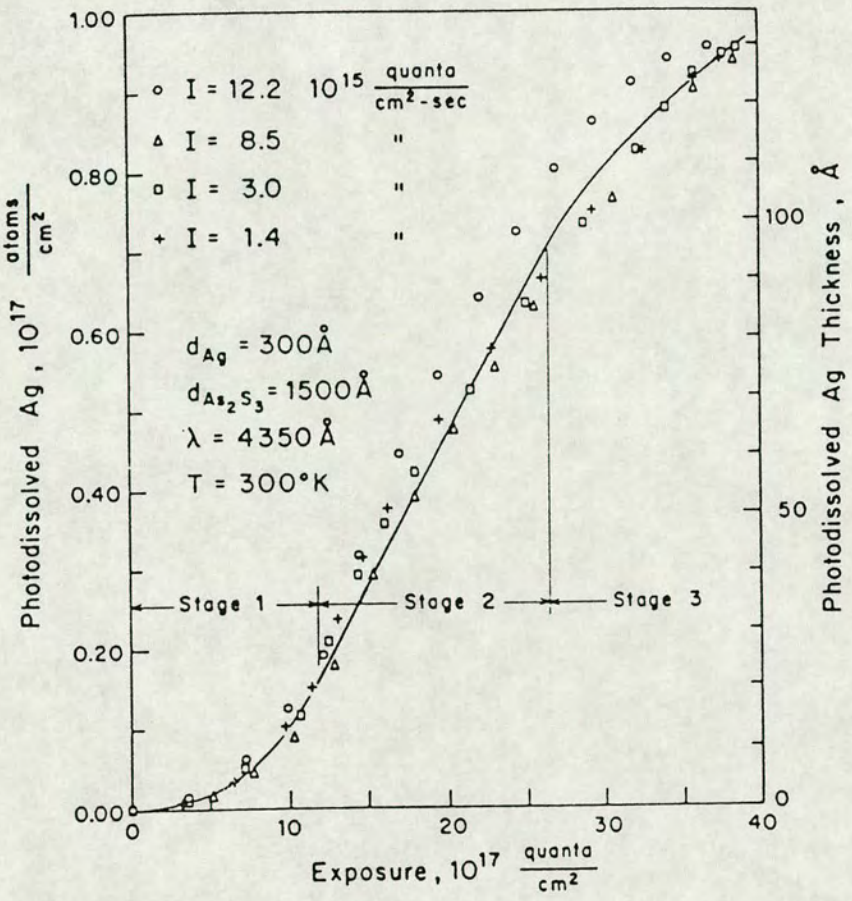

Fig. 2-1 The amount of Ag photodissolved into As_2S_3 as a function of exposure (exposure = intensity × time)[from Goldschmidt et al. 1976].

Ewen et al. (1988) have shown that the time dependence of the process may, in some cases, depend on the amount of silver available as the metal source (see Fig. 2-2). They found the photodissolution process had a square-root time dependence for thin layers of silver whereas when the thickness of the silver layer was comparable with the thickness of the chalcogenide layer, the photodissolution had a linear time dependence.

The final stage of photodissolution where the photodissolution rate slows down is believed to be connected with the exhaustion of one of the reactants (presumably silver) because most investigators believe that for the photodissolution to proceed a metallic layer is needed (Kokado et al. 1976, Kolwicz et al. 1980, Suptitz et al. 1984).

2.2-2 Spectral dependence

The spectral dependence of the photodissolution rate is very important since it reveals where the effective absorption of the actinic radiation is taking place. Shimizu et al. (1972) report that the spectral dependence of the photodissolution process roughly coincides with the absorption edge of the chalcogenide and moves toward longer wavelengths as the photodissolution proceeds [see Fig. 2-3(a)]. Kokado et al. (1976) have also reported that the shorter wavelength limit of sensitivity varies with the thickness of the chalcogenide layer [see Fig. 2-3(b)]. However, the photodissolution rate is very small at longer wavelengths. Kokado et al. (1976) and Ressel et al. (1987) have found similar results. These findings contradict those of Goldschmidt et al. (1976), Lis et al. (1983) and Mizuno et al. (1973) who found that at longer wavelengths the photodissolution rate is still high, although the absorption in the chalcogenide layer is quite small. The spectral dependence of Ag dissolution in As_2S_5 has been studied by Wagner et al. (1987) who found that the photodissolution rate is a maximum around 475 nm.

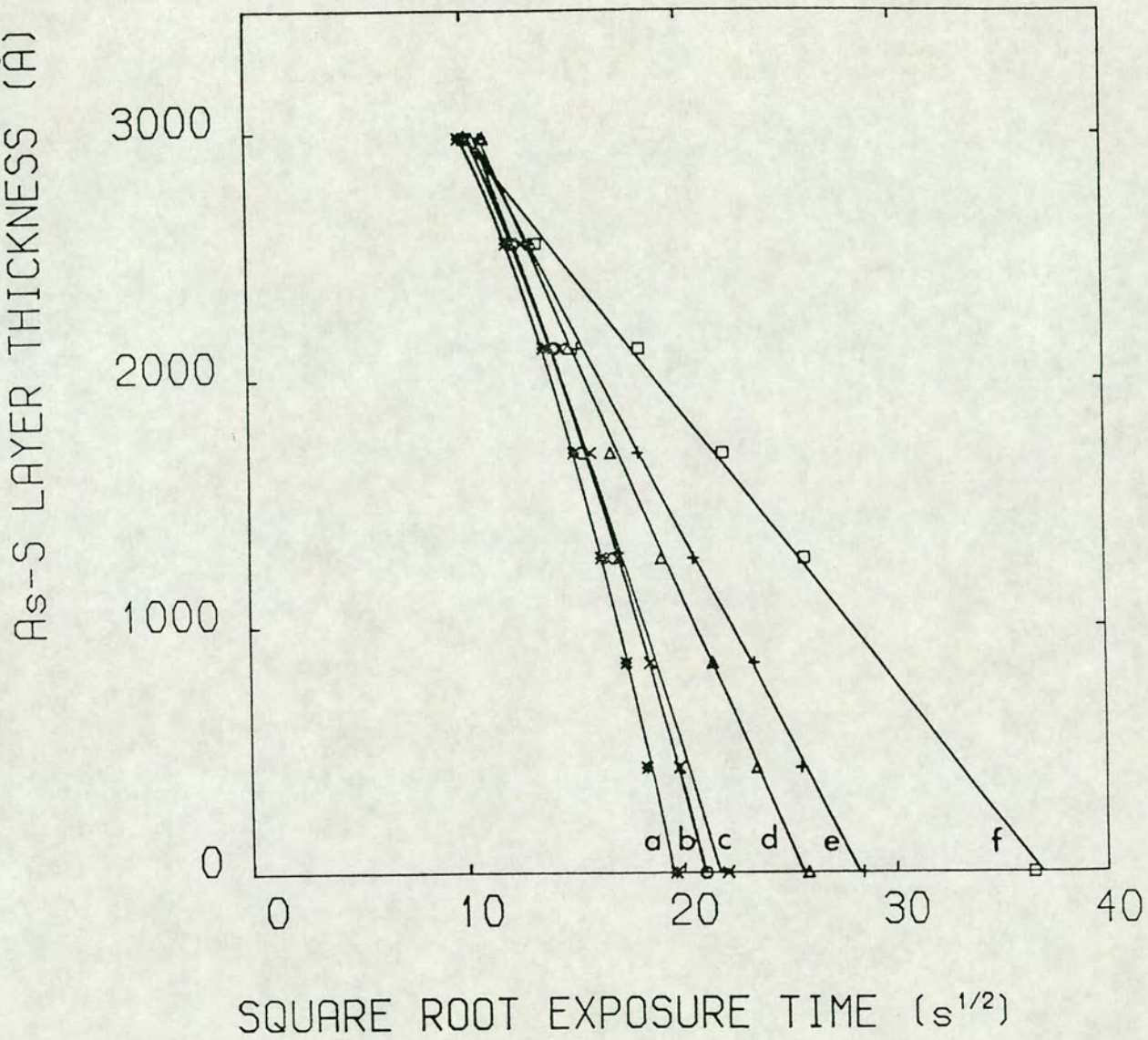

Fig 2-2 The variation of $As_{33}S_{67}$ layer thickness as a function of the square root of exposure time for the following thicknesses (in Angstroms) of the Ag layer: a,4150; b,2070; c,1400; d,1030; e,860; and f,630 [from Ewen et al. 1988].

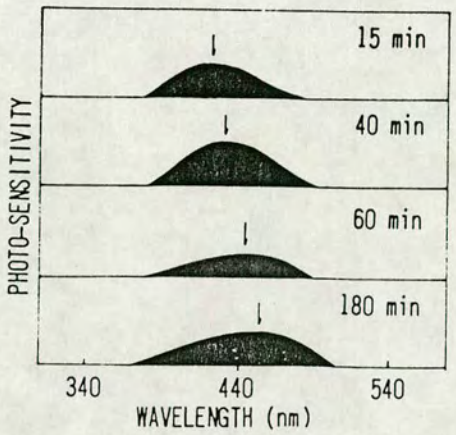

Fig. 2-3(a) The shift of the maximum sensitivity of photodissolution (marked by the arrows) in the Ag / a-As_2S_6 system with light exposure [from Kokado et al. 1976]. The sensitivity scales for the lower two figures are reduced.

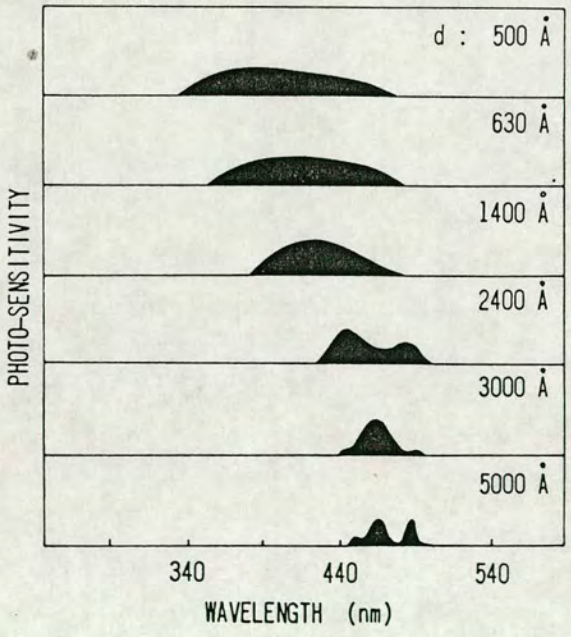

Fig. 2-3(b) Spectral photosensitivity of the Ag-As_2S_6 photodoping system, when illuminated through As_2S_6 layers of thickness d. Multiple peaks seen in thick layers are due to the interference effect and are not essential [from Kokado et al. 1976].

2.2-3 Intensity dependence

A linear dependence of the photodissolution rate on light intensity has been reported by many authors (Goldschmidt et al. 1976, Kokado et al. 1976, Leung et al. 1985). In some cases, however, (for instance in Ag / GeS_2) a sublinear dependence on intensity was observed (Oldale et al. 1988). Buroff et al. (1975) have found that the intensity dependence of the photodissolution rate in As_2S_3 was not linear but followed a power law as shown in Fig. 2-4. At low light levels the rate was found to vary with an exponent of 1.54 whereas at higher intensities the exponent was 0.9. However no mention of the intensity values is given.

2.2-4 Compositional dependence

Different results have been reported for the compositional dependence of the photodissolution rate in the As-S system. Kokado et al. (1976) have found that the photodissolution rate in As_2S_n films is a maximum for n=10 and this has been attributed to the role of S-S bonds. Kostyshin et al. (1970) also have obtained similar results. However, Ewen et al. (1988) and Wagner et al. (1990) have found that the photodissolution rate is a maximum around the composition $As_{33}S_{67}$ in the As-S system (see Fig. 2-5). This result has been attributed to the morphology of the reaction product. Glasses with compositions on both sides of $As_{33}S_{67}$ become more phase separated as a result of photodoping and the transport of electrons is likely to be slower through the reaction product for these compositions. In the Ge-Se system an increase of the photodissolution rate with increasing chalcogen content has been reported (Chen et al. 1980). Calas et al. (1990) have found similar results and in addition observed that the photodissolution rate was a maximum for the composition $GeSe_{4.4}$.

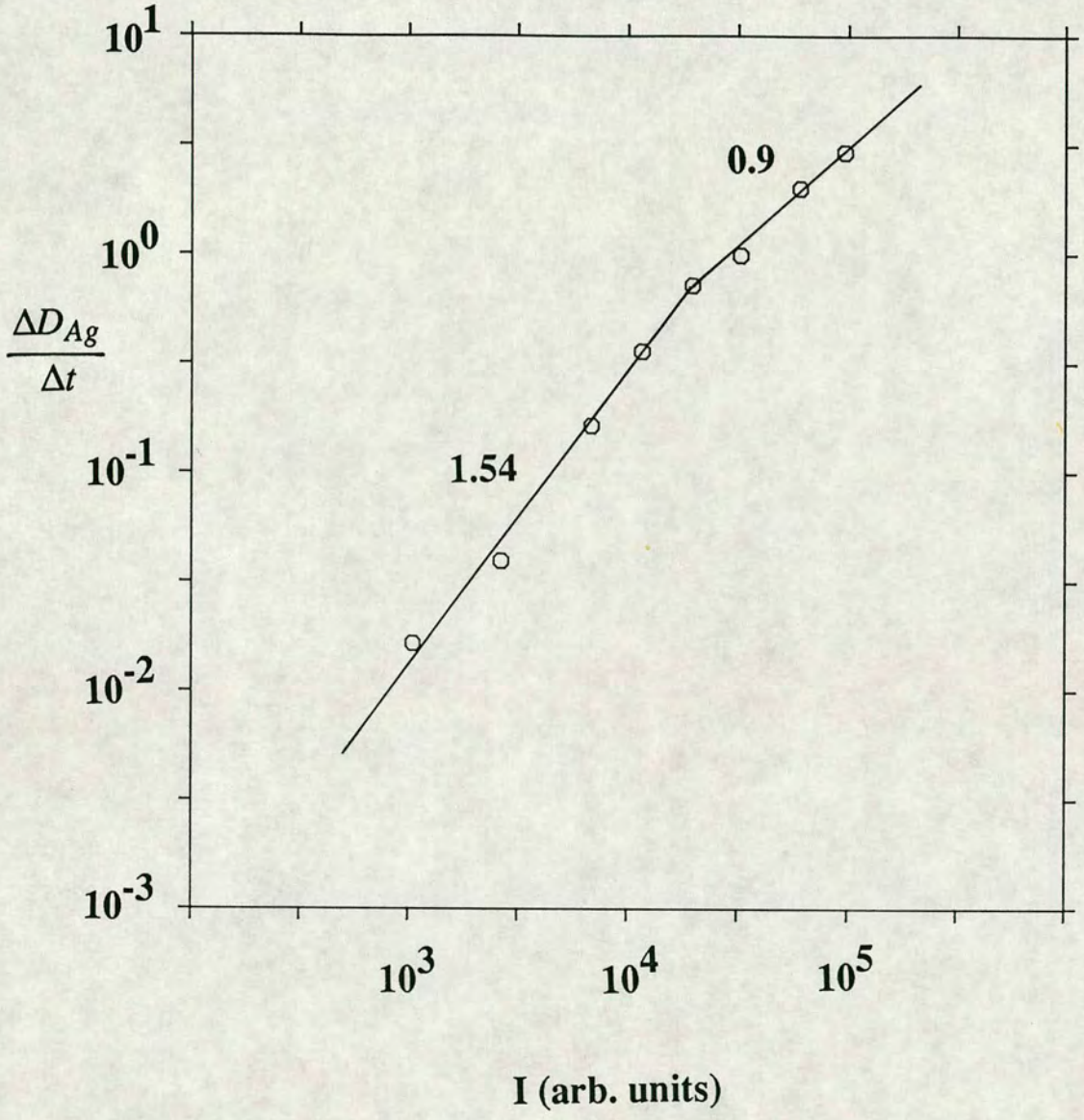

Fig. 2-4 Light-intensity dependence of the photodissolution rate (as monitored by the rate of change of silver thickness) for the system Ag / a-As_2S_3 [from Buroff et al. 1975].

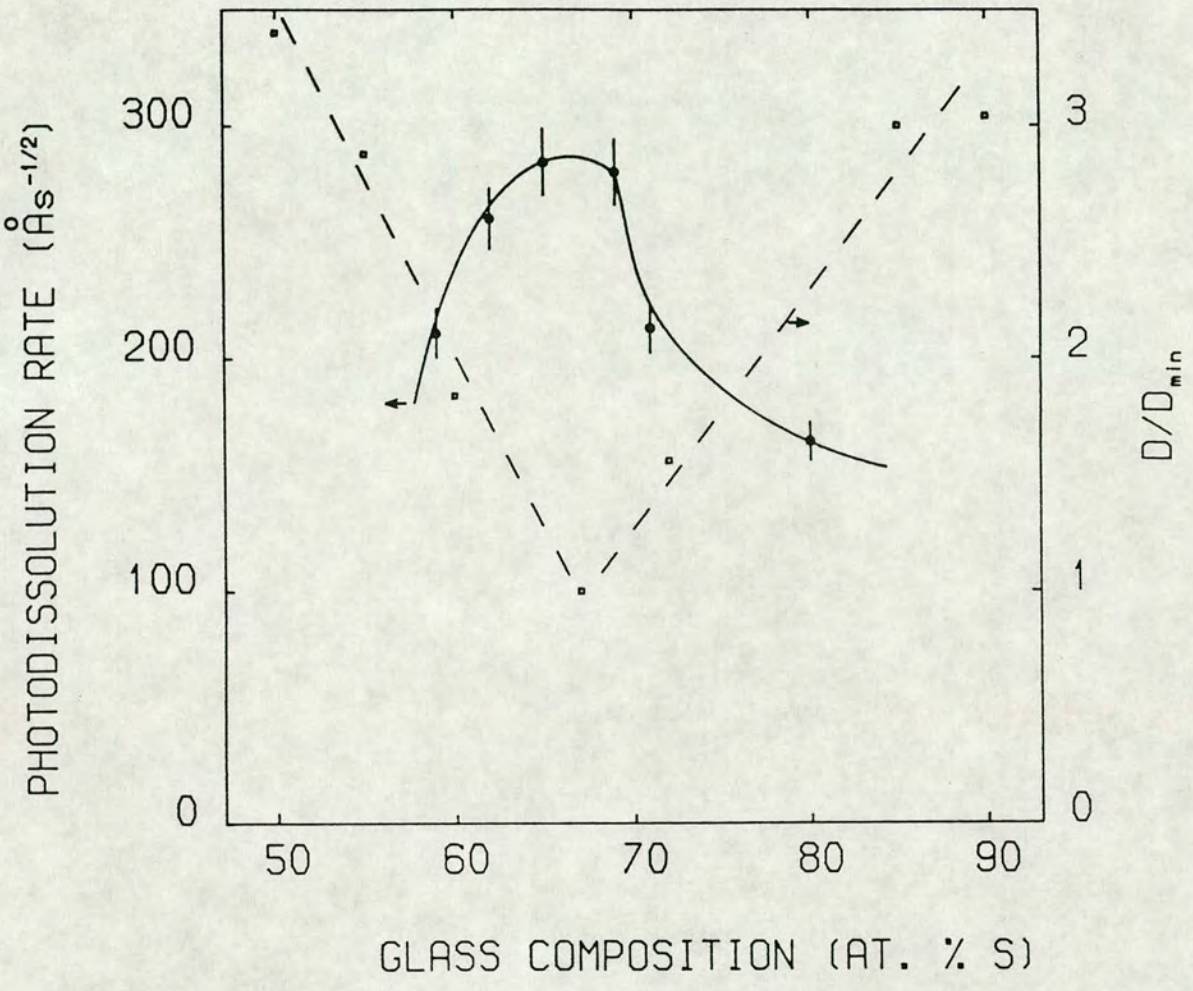

Fig. 2-5 Compositional dependence of the photodissolution rate in the system Ag / a-As_xS_{1-x} [from Ewen et al. 1987]. Also shown is the variation of the optical density, D, of a-As_xS_{1-x} films dipped in $AgNO_3$; D is a measure of the amount of Ag that can be taken up by the chalcogenide films.

2.3 Where is the actinic radiation absorbed?

Many investigators have tried to resolve where the actinic radiation is absorbed in the photodissolution process. Since the spectral dependence of the photodissolution rate resembles the absorptance profile of the chalcogenide glass (Goldschmidt et al. 1976), it is natural to assume that the basic optical excitation takes place in the glass, but the process is still effective for irradiation at photon energies below the optical band gap of the glass (Kokado et al. 1976, Shimizu et al. 1971). However, in that wavelength region the absorptance of the glass is too small to account for the observed photodissolution rate. So some investigators have concluded that at photon energies below the optical band gap the absorption of radiation occurs in the silver (Goldschmidt et al. 1976). However, Lis and Lavine (1983) stated that if photoemission of electrons from the silver was responsible for the reaction, a graph of the square root of the sensitivity versus the photon energy should be a straight line, which was not found to be the case. When the photon energy is increased above the optical band gap, the photodissolution rate increases by a factor of 10 if the illumination is incident from the chalcogenide side (Goldschmidt et al. 1976). In contrast, for illumination incident from the silver side the photodissolution rate changes only slightly over the same spectral range (Shimizu et al. 1974). These observations can be explained by the fact that the absorption coefficient of the chalcogenide glass changes by some five orders of magnitude over the above spectral range ($5200 < \lambda < 6300$ A).

Recent experiments on the lateral migration of silver atoms which occurs when photodissolution is carried out on a conducting substrate, indicated that the actinic radiation is absorbed in the photodoped layer, close to the interface between the doped and undoped regions (Owen et al. 1985). This suggestion has been confirmed by Rennie et al. (1987) and Kolobov et al. (1990).

2.4 Distribution of the photodissolved silver in the glassy matrix

Most reports agree that the dissolved silver has a step-like concentration profile (Shimizu et al. 1974, Yamamoto et al. 1976). This is supported by the constant etching rate of the photodissolved material (Yoshikawa et al. 1980). However, there is no agreement on the value of the silver concentration in the photodoped region. Kolwicz and Chang (1980) reported a value of 31 at. % for the silver concentration in As_2S_3, which does not change upon further exposure to light after the metallic silver has been completely dissolved. Similarly, the value given by Goldschmidt et al. (1977) for the silver concentration in As_2S_3 is 32 at. % . However, Kostyshin and Ushenin (1981) report 41 at. % Ag in As_2S_3 and Chatani et al. (1978) obtained a fixed and uniform concentration of photodissolved silver in As_2S_3 of 48 at. % . Rennie (1986) has used the Rutherford backscattering technique to find the concentration of silver in photodoped Ge-Se glasses, but has found that for $GeSe_2$, only the early stages of the reaction can be investigated. Later stages of the reaction could not be analysed due to the problem of overlapping of peaks for different elements present. He has found that the composition of the silver-doped region in a-$GeSe_2$ was $Ag_{0.28}Ge_{0.24}Se_{0.48}$ while Oldale (1989) determined the composition of silver-doped a-$Ge_{29}S_{71}$ to be $Ag_{0.23}Ge_{0.23}S_{0.54}$. Elliott (1991) suggests that the 1:1 correspondence between Ag and Ge concentrations in Ge-based chalcogenide is due to the formation of homopolar Ge-Ge bonds in the reaction product during the photodissolution process. He suggests that two Ag atoms can be incorporated for every homopolar Ge-Ge bond.

2.5 The structure of the reaction product

DeNeufville et al. (1973/1974) and Kokado et al. (1976) reported that no crystalline products were observed as a result of photodoping while Maruno et al. (1971) and Petrov et al. (1976) found that in As_2S_3-Ag_x glass with silver contents of several atomic % crystalline proustite (Ag_3AsS_3) and smithite ($AgAsS_2$) were formed upon annealing.

Ewen et al. (1983) used Raman spectroscopy to find the composition of the reaction product formed by photodoping As_2S_3 on an Ag_2S substrate and found that proustite was formed. One problem which is difficult to resolve is that although such large amounts of silver are incorporated into the chalcogenide glass, no new compound is detected by X-ray diffraction measurements in the photodissolution of silver to produce a concentration of up to 20 at. % (Janai 1982). Janai has suggested that the radial distribution function of the photodoped layer remains the same as that for a-As_2S_3 . Despite the fact that a new compound is formed, no new feature is observed because the bonding between the silver and the glass structure does not consume any of the As-S bonding electrons.

Regarding the structure of the photodoped material, it should be noted that the glass forming region in the As-S system extends approximately from As_5S_{95} to $As_{43}S_{57}$ (Flaschen et al. 1959). A raman scattering study (Firth et al. 1983) suggested that only for glass compositions in the approximate range of $As_{36}S_{64}$ to $As_{28}S_{72}$, is the resulting photodoped material homogeneous. Fig. 2-6 shows the glass forming region in the Ag-As-S system. For compositions outside this range the resulting photodoped material is phase-separated. Also, it has been shown that the amount of silver which can be taken up by an evaporated As-S film on dipping in $AgNO_3$ solution is at its lowest over this range of compositions reaching a minimum at $As_{33}S_{67}$ (Petrova et al. 1984).

Steel et al. (1989) have used EXAFS to investigate the structure of photodoped chalcogenides. Their analysis showed that in photodoped As_2S_3, silver atoms are only surrounded by chalcogen atoms. No silver-silver or silver-arsenic bonds were observed. The Ag interatomic distance was calculated to be 2.50 A. Oldale et al. (1988) also used EXAFS to analyse the structure of photodoped $GeSe_2$. They found that silver reacts with the chalcogen atoms: the Ag-Se bond length in photodoped films was found to be 2.63 A while in thermally doped films it was 2.62 A .

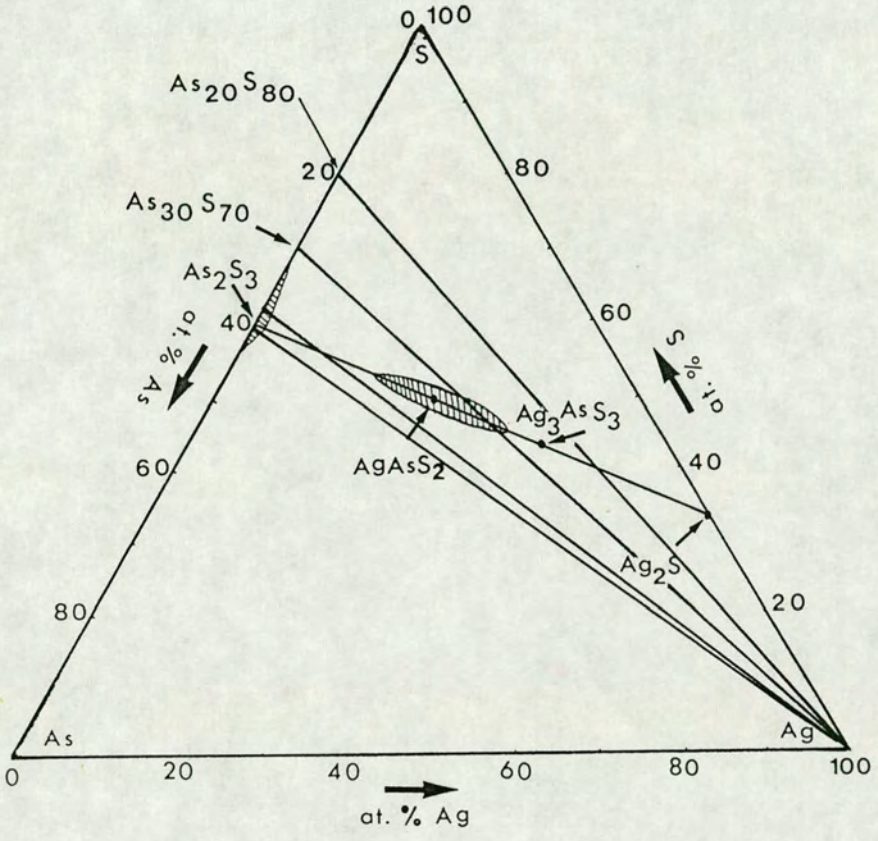

Fig. 2-6 Glass forming regions for the Ag-As-S system [from Firth et al. 1983].

2.6 Temperature dependence

The temperature dependence of photodissolution has been investigated by several authors. Inoue et al. (1974) and Kokado et al. (1976) have studied the effect of temperature on the photodissolution over a wide temperature range (−200 to +20 °C) and found a value of 0.033 eV for the activation energy of the process. The activation energies obtained by Kostyshin et al. (1972, 1984) in As_2S_3 vary from 0.01 to 0.4 eV using light with different wavelengths for photodoping. Rennie (1986) found an activation energy of 0.15 eV for the induction period and 0.21 eV for the dissolution rate in $GeSe_2$ and Oldale (1989) found an activation energy of 0.1 eV for Ag photodissolution in GeS_2. However, the values obtained for the activation energy of the dark thermal dissolution is higher. Buroff et al. (1977) have found an activation energy of 1 eV for the thermal diffusion of silver in As_2S_3 while Plocharski et al. (1987) also studied the Ag / As_2S_3 system and found a value of 0.18 eV for the activation energy of the photodissolution and a value of 1.5 eV for the dark thermal dissolution. This disparity has been ascribed by Elliott (1991) to the difference in activation energies for photoconductivity and dark electronic conductivity, respectively.

2.7 Effect of pressure and pre-treatment

The effect of hydrostatic pressure on the Ag photodissolution rate in $As_{25}S_{75}$ films has been studied by Tanaka (1990). He found that the photodissolution rate increased initially but subsequently decreased with increasing pressure, the photodissolution rate being inhibited at a pressure of 70 kbar. His explanation for this observation is that as the pressure increases, the interlayer spacing in the glass structure collapses, thereby inhibiting the intercalation of Ag^+ ions.

Yaji and Kurita (1983) have reported that annealing or pre-irradiating the chalcogenide layer before depositing the silver greatly affected the kinetics of photodissolution, in contrast to the results of Chatani et al. (1977). Annealing increased the

reaction rate by a factor of 4 while pre-illumination increased it by a factor of 10. In the Ge-Se system, however, a significant decrease of the photodissolution rate upon pre-treatment has been observed by many investigators (Kasai et al. 1976, Maruno et al. 1980). Since as-deposited Ge-based films have a columnar structure (Singh et al. 1979), the effect of pre-treatment (annealing or illumination) is to make the structure more dense (Spence et al. 1989), which results in the inhibition of the silver dissolution.

2.8 Photodoping using other metals

It has been reported (Kolobov et al. 1984, Mizushima et al. 1982) that group II metals (zinc and cadmium) can be photodissolved in As-S chalcogenides but in this case the illumination must be performed at elevated temperatures. However, Zn photodissolution was not observed in Ge-based chalcogenides (Bedel'baeva et al. 1987). The temperature dependence of the thermal and photoenhanced diffusion of Zn in As_2S_3 has been studied by Kolobov et al. (1985), who report activation energies of 2.4 and 0.9 eV for these processes respectively. Mizushima et al. (1982) have observed that at 150 °C, the dissolution rate of Zn becomes comparable with that of silver or even higher. A sublinear intensity dependence has been found for Zn photodissolution (the rate being proportional to I^{γ} , where γ = 0.25-0.30). The spectral dependence of Zn photodissolution is slightly different from that of Ag. The Zn photodissolution rate decreases by a factor of only 1.5 if the measurements are performed with a red wavelength (0.633 μm) as compared with a green wavelength (0.515 μm) (Kolobov et al. 1984, Lyubin et al. 1987). The dissolution rate of Zn increases with the arsenic content in the arsenic sulphide system (Bedel'baeva et al. 1987), the amount of dissolved Zn being approximately 55 at.% with the metal uniformly distributed throughout the doped layer (Kolobov et al. 1990).

Illumination of the As-chalcogenide / Cd combination results in a decrease of the metal dissolution rate (Kolobov et al. 1985). This effect is referred to as "negative photodissolution" and is supposed to be due to the formation of different reaction products

between Cd and the chalcogenide in the dark and on light illumination.

2.9 Optical properties of the reaction product

Photodoping with Ag results in changes in the optical properties of the chalcogenides and in particular their optical constants. The transmission through chalcogenide films has been observed to decrease upon introduction of silver into their structural network (Ishikawa et al. 1980). Shimizu et al. (1978) report a decrease of the Urbach energy while Kolomiets et al. (1974) claim that the Urbach energy increases on doping. Zakery et al. (1989) have extended the measurements of the optical constants in the Ag-As-S system to IR wavelengths. The optical gap was found to decrease on the introduction of Ag, though low absorption coefficients were still observed in the near-IR. Kolobov et al. (1985) have reported a decrease in the optical gap on the introduction of Zn into As_2S_3.

2.10 Electrical properties of photodoped chalcogenides

Shimizu et al. (1972) have found that as a result of photodoping, the conductivity of $As_{24}S_{70}Te_6$ films increases by several orders of magnitude. Kolobov et al. (1990) have found that the ionic component is approximately 20 times as large as the electronic one in Ag-doped GeS_2. The activation energies of the two components were approximately equal (0.2 eV). Danko et al. (1990) have found that in the Ag/As_2S_3 system the ionic component of the conductivity was about 10 times as large as the electronic one. The conductivity of chalcogenide glasses is increased significantly by the addition of even a few at.% of silver and this also results in the appearance of ionic conductivity. Since the ionic conductivity in Ag-containing glasses is usually much greater than the electronic conductivity, these materials may also be regarded as solid electrolytes.

2.11 Summary of existing models of photodissolution

Kokado et al. (1976) propose that a potential barrier exists at the interface between the metal (Ag) and the chalcogenide. When photons are absorbed at the interface, photocarriers (holes and electrons) are generated, the photoelectrons are repelled by the junction potential into the interior of the chalcogenide where they are trapped. The electron traps are associated with loosely bound chalcogen atoms. Photoholes are captured by silver atoms. These authors speculate that the coulomb force between these two ions is large enough for the Ag ion to be pulled into the chalcogenide. The equation they have derived for the growth rate of the photodoped region contains two terms, a linear term accounting for photoenhanced reactivity and a second term accounting for the Coulomb attraction between photogenerated ions which drives the photodissolution of the silver. This model, however, cannot explain why the number of dissolved Ag ions (atoms) is much higher than the number of defect centers (dangling bonds) present in the chalcogenide.

Malinowski and Buroff (1978) suggested that photodoping is a typical tarnishing-type reaction. They suggest that in the photodoping process, illumination produces mobile holes which is equivalent to excess S in the As_2S_3 film and if the photoexcitation is close enough to the Ag interface, then Ag-S bonds are formed. The illumination provides a supply of Ag ions which initially react at the Ag interface producing a layer of Ag_2S. Being both an electronic and ionic conductor, the Ag_2S allows the passage of both Ag ions and electrons and the Ag film will continue to react with the photogenerated holes (excess S atoms) in the chalcogenide until the Ag film is consumed. This model cannot explain the process at long wavelengths where the absorption in the glass is small.

A model by Lakshmikumar (1986) suggests that one can explain all the experimental observations for the photodissolution process by considering that there is a diffusion of silver which is enhanced by an electric field generated at the interface between the silver-rich and silver-deficient regions of the semiconductor. The field is the result of the optical excitation of carriers across the interface. When depositing silver on the chalcogenide layer, the silver reacts with S and a rapid formation of Ag_2S is expected, so

that at the beginning of the experiment one has a metallic silver layer, a layer of Ag_2S with high conductivity for silver ions and a layer of chalcogenide glass. Silver is only a source for Ag_2S formation. In this situation there is therefore a layer of doped silver-rich semiconductor with a lower band gap in close contact with an undoped chalcogenide layer with a higher band gap. Electrons from the smaller-gap material (doped region) will be transferred across the interface so as to form a depletion region in the larger-gap material (undoped region), so there is an electric field across the interface. He suggests that the effect of the illumination is to increase this electric field. Ag has a high diffusion coefficient in chalcogenides and this is enhanced by the electric field, so the silver diffuses into the exposed chalcogenide region. This model however, does not give any quantitative explanation of the spectral dependence or intensity dependence of the photodissolution effect.

Kluge (1987) has considered photodoping as an intercalation reaction. For an intercalation reaction to proceed a reversible transport of ions and electrons is necessary with the formation of bonds with the host matrix. The host must provide empty interatomic volumes and these sites are related to regions where van der Waal's bonding occurs. In addition, the material must possess both high electronic and ionic conductivity. Chalcogenides with no silver or small silver content are purely electronic conductors, an ionic component only appearing above a certain silver concentration. Within the doped region the silver ions are mobile while in the vicinity of the undoped chalcogenide the ion mobility decreases drastically, which accounts for the step like diffusion profile characteristic of photodoping. According to this model the actinic absorption of radiation takes place at the Schottky-barrier at the metal-chalcogenide interface in order to generate electrons and metal ions, and also within the bulk of the doped chalcogenide to supply free photoelectrons for maintaining charge neutrality during transport processes. During the transport processes cations migrate and are inserted into the amorphous network. The insertion is based on the capability of the chalcogens to form C_1^- centers and the appearance of $C_1^- M^+$ (M: Ag, Cu) ionic bond units within the amorphous chalcogenide ($C_2^0 + e^- + M^+ \rightarrow C_1^- M^+$). The observed sensitivity in the long wavelength region

can be explained by the model since the absorption coefficient of both the metal and the metal-doped chalcogenide is relatively high for wavelengths larger than that corresponding to the optical band gap of the undoped chalcogenide.

Elliott (1991) has put forward a unified mechanism for the phenomenon of photodissolution of metals (typically silver) in chalcogenide glasses. He has derived the parabolic-law kinetics in terms of a model wherein both ionic and electronic charge transport occur simultaneously. Under normal circumstances the rate will be controlled by the photoconductivity of the reaction product. His model can explain the linear dependence on light intensity, and the small activation energy of the photodissolution process, which are both determined by the photoconductivity. He proposes that the induction period is due to lateral diffusion in the chalcogenide between dendritic nuclei of the reaction product which originate from preferential reaction centres located at grain boundaries in the metal layer. This model predicts that the actinic light responsible for the photodissolution process is absorbed preferentially at the interface between the doped and undoped regions in the chalcogenide if the reaction product is a *p-type* electronic conductor. On the other hand if the reaction product is *n-type* then the effective absorption of radiation takes place at the metal/reaction-product interface. He concludes that to confirm his model quantitatively the reaction product must be much better characterized. Thus it is essential that the ionic conductivity, dark d.c electronic conductivity and photoconductivity, and their temperature dependence in the actual reaction product be measured independently. In addition, knowledge of the sign of the dominant electronic charge carrier is vital.

2.12 Applications of photodissolution

Although chalcogenide glasses such as As_2S_3 dissolve in alkaline solutions, the photodoped material is insoluble in these. This change in chemical solubility makes these materials suitable for use as a negative resist in lithography. Submicron features can be produced in these inorganic resists using conventional optical exposure sources and they are compatible with standard IC fabrication techniques such as spin-coating and plasma

etching. Dry etching is also possible since CF_4 and SF_6 plasmas can be used to etch the undoped chalcogenide. These inorganic resists have been extensively investigated (Tai et al. 1982, Mizushima et al. 1981). They are capable of very high resolution [400 nm in the UV (Tai et al. 1982) and 35 nm for electron-beam exposure (Bernstein et al. 1988)], and have a higher contrast than the organic resists currently in use. The high resolution capabilities of these resists are partly due to the phenomenon of edge sharpening observed by Tai et al. (1980), which is the lateral migration of silver from the non-illuminated region into the illuminated region.

X-rays in the wavelength range of 1-38 A have also been used (Buroff and Rush 1987) to produce high resolution gratings which have excellent edge quality. These authors were able to determine a maximum penetration depth of 0.15 μm for soft X-rays. This implies that As_2S_3 images may possibly serve as masks in X-ray photolithography. These authors also conclude that if appropriate powerful radiation sources are available, photoresists based on As_2S_3 may also be suitable for X-ray lithography.

Chen et al. (1986) have used an electron beam to develop 0.5 μm lines and spaces in $Ge_{0.1}Se_{0.9}$ inorganic resist. Good contrast and sharp edge definition provide a useful application in sub-half micrometer device fabrication. The sensitivity of the system is found experimentally to be comparable to that of a typical organic resist (PMMA). Bernstein et al. (1988) have used the metal photodissolution of Ag in $As_{30}S_{70}$ to produce lines as narrow as 35 nm on a 70 nm pitch using an electron beam. They have stated that these inorganic resists will likely be useful for the fabrication of nanometer structures due to their excellent resolution capabilities, although their sensitivity is lower than that for an organic resist such as Shipley SAL 601-ER7.

Photodoping was used by Zakery et al. (1988) to fabricate IR gratings because of the possibility of achieving high modulations in refractive index ($\Delta n > 0.5$) and high transmission in the IR. These authors have given a theoretical analysis of transmissive gratings of the type likely to be produced by the metal photodissolution effect in a typical As-S chalcogenide glass, namely $As_{30}S_{70}$. This was done to assess the potential for using these devices as diffractive elements for the 8-14 μm IR region. Predicted efficiencies in the

multiwave regime were over 90% for bulk diffractive devices while for surface relief gratings a maximum efficiency of at least 73% was predicted. The measured diffraction efficiency of such gratings fabricated by Kostyshin et al. (1986) exceeded 50% .

2.13 Summary

Although much contradictory data has been reported by the many different investigators who have studied photodissolution, there are a number of features which are generally accepted.

1- The photodissolution kinetics curve consists of three stages: an induction period, followed by a region of efficient dissolution where the photodissolution rate is constant, and a final stage during which the photodissolution rate decreases slowly.

2- The length of the induction period is determined by the sample preparation procedure.

3- Band gap illumination is the most efficient for producing photodissolution, although photodissolution still occurs at longer wavelengths.

4- The photodissolution rate dependence on light intensity is nearly linear.

5- The effective absorption of actinic radiation takes place at the doped-undoped interface.

6- Silver is uniformly distributed throughout the photodoped layer and has a step-like diffusion front.

7- Large amounts of silver (>30 at. %) can be incorporated in the chalcogenide.

8- In the reaction product silver forms bonds only with the chalcogen element.

9- The activation energy for photodissolution is in the range 0.1 to 0.4 eV while for thermal dissolution it is higher, ~ 1 eV.

10- Other metals such as Zn and Cd can also be dissolved in the chalcogenides.

11- Photodoping with metals results in significant changes in the properties of the chalcogenide, particularly its optical constants, conductivity and solubility.

12- Photodoping with metals has potential applications in photolithography as well as X-ray and e-beam lithography. Optical elements such as diffraction gratings and holograms have also been recorded in chalcogenide glasses using the metal photodissolution effect.

2.14 References

Bedel'baeva, G.E., Kolobov, A.V., and Lyubin, V.M., 1987, Zh. Nauchnoi & Prikl. Fotogr, & Kinematogr., 32, p. 208.

Bernstein, G.H., Liu, W.P., Khawaja, Y.N., Kozicki, M.N., and Ferry, D.K., 1988, J. Vac. Sci. Technol., B6 (6), p. 2298.

Buroff, A., and Baeva, R., 1975, Proc. VI Int. Conf. Am. Liquid Semiconductor, Leningrad ed. B.T. Kolomiets p. 437.

Buroff, A., Nebauer, E., Suptitz, P., and Willert, I., 1977, Phys. Stat. Sol., A(40) p. 195.

Buroff, A., 1980, PhD Thesis, Sofia.

Buroff, A., and Rush, A.D., 1987, J. Non-Cryst. Solids, 90, p. 585.

Calas, G., El-Ghrandi, R., and Galibert, G., 1990, J. de Phys., 51, p. 2449.

Chang, M.S., and Chen, J.T., 1978, Appl. Phys. Lett., 33, p. 892.

Chatani, K., Shimizu, I., Kokado, H., and Inoue, E., 1977, Jap. J. Appl. Phys., 16, p. 389.

Chatani, K., Shimizu, I., and Inoue, E., 1978, J. Soc. Photogr. Sci. Tech. Japn, 41, p. 21.

Chen, A.S., Addiego, G., Leung, W., and Neureuther, A.R., 1986, J. Vac. Sci.

Technol., B4(1), p. 398.

Chen, C.H., and Tai, K.L., 1980, Appl. Phys. Lett., 37, p. 1075.

Danko, V.A., Indutny, I.Z., and Minko, V.I., 1990, Proc. Int. Conf. "Non-Cryst. Semiconductor-90", Vzhgorod USSR, Pt. II, p. 234.

DeNeufville, J.P., Moss, S.C. and Ovshinsky, S.R., 1973/1974, J. Non-Cryst. Solids, 13, p. 191.

Elliott, S.R., 1991, J. Non-Cryst. Solids, in print.

Ewen, P.J.S., Taylor, W., Firth, A.P., and Owen, A.E., 1983, Phil. Mag., B48, L15.

Ewen, P.J.S., Zakery, A., Firth, A.P., and Owen, A.E., 1987, J. Non-Cryst. Solids, 97-98, p. 1127.

Ewen, P.J.S., Zakery, A., Firth, A.P., and Owen, A.E., 1988, Phil. Mag., B57, p. 1.

Firth, A.P., Ewen, P.J.S., and Owen, A.E., 1983, 'The structure of Non-Crystalline Materials, 1982', ed. P.H. Gaskell, J.M. Parker and E.A. Davis (London : Taylor and Francis), p. 286.

Flaschen, S., Pearson A., and Northover, W.J., 1959, Ceram. Soc., 42, p. 450.

Goldschmidt, D., and Rudman, P.S., 1976, J. Non-Cryst. Solids, 22, p. 229.

Goldschmidt, D, Bernstein, T., and Rudman, P.S., 1977, Phys. Stat. Sol., A41, p. 283.

Inoue, E., Kokado, H., and Shimizu, I., 1974, Oyo Butsuri, 43, p. 101.

Ishikawa, T., Kitao, M., Akao, H., and Yamada, S., 1980, Phys. Stat. Sol., A57, p. 373.

Janai, M., 1982, Proc. of the symposium on inorganic resist systems, Montreal, ed., D.A. Doane and A. Heller, (The Electrochemical Society, Inc.), p. 239.

Kasai, M., and Hajimoto, Y., 1976, J. Appl. Phys., 47, p. 3594.

Kluge, G., 1987, Phys. Stat. Sol., A101, p. 105.

Kokado, H., Shimizu, I., and Inoue, E., 1976, J. Non-Cryst. Solids, 20, p. 131.

Kolobov, A.V., and Lyubin, V.M., 1984, Sov. Phys. Solid State, 26(8), p. 1529.

Kolobov, A.V., and Lyubin, V.M., 1985, Sov. Tech. Phys. Lett., 11(3), p. 155.

Kolobov, A.V., Elliott, S.R., and Steel, A., 1990, Phys. Rev. B., 41, p. 9913.

Kolobov, A.V., Elliott, S.R., and Taguirdzhanov, M.A., 1990, Phil. Mag., B61, p. 857.

Kolomiets, B.T., Lebedev, E.P., and Rogachev, N.A., 1974, Sov. Phys. Semicond., 8(3), p. 348.

Kolwicz, K.D., and Chang, M.S., 1980, J. Electrochem. Soc., 127, p. 135.

Kostyshin, M.T., Mikhailovskaya, E.V., and Romanenco, P.F., 1966, Sov. Phys. Solid state, 8, p. 451.

Kostyshin, M.T., Romanenko, P.F., Shary, V.N., and Dembovsky, S.A., Vinogradova G.Z., 1970, Inorg. Mater., 6, p. 1073.

Kostyshin, M.T., and Romanenko, P.F., 1972, Ukr.Fiz.Zh., 17, p. 230.

Kostyshin, M.T., and Ushenin, Yu.V., 1981, Phys. Stat. Sol., (a)66, K47.

Kostyshin, M.T., Ushenin, Yu.V., 1982, Fiz and Tehk. Poluprovodn., 16, p. 19.

Kostyshin, M.T., Romanenko, P.F., and Stronsky, A.V., 1984, Ukr. Fiz. Zh 29, p. 510.

Kostyshin, M.T., Romanenko, P.F., Stronsky, A.V., Kolomiets, T.M., and Sopinsky, H.V., 1986, Ukr. Fiz. Zh., 31, p. 55.

Lakshmikumar, S.T., 1986, J. Non-Cryst. Solids, 88, p. 196.

Leung, W., Cheung, N.W., and Neureuther, A.R., 1985, Appl. Phys. Lett., 46, p. 543.

Lis, S.A., and Lavine, J.M., 1983, Appl. Phys. Lett., 42, p. 675.

Lyubin, V.M., and Kolobov, A.V., 1987, J. Non-Cryst. Solids, 90, p. 489.

Malinowski, J., and Buroff, A., 1978, Contemp. Phys., 19(2), p. 99.

Maruno, S., Yamada, T., Noda, M., and Kondo, Y., 1971, Jap. J. Appl. Phys., 10, p. 653.

Maruno, S., and Ban, S., 1980, Jap. J. Appl. Phys., 19, p. 97.

Mizuno, H., Tanaka, K., and Kikuchi, M., 1973, Sol. State Commun., 12, p. 999.

Mizushima, D., and Yoshikawa, A., 1982, in Amorphous Semiconductors:Technologies and Devices, ed. Y. Hamakawa(Tokyo-Amsterdam-New York-London)p. 227.

Oldale, J.M., Rennie, J.H.S., and Elliott, S.R., 1988, Thin Solid Films, 164, p. 467.

Oldale, J.M., 1989, PhD Thesis, University of Cambridge.

Owen, A.E., Firth, A.P., and Ewen, P.J.S., 1985, Phil. Mag., B52, p. 347.

Petrov, V.V., and Kryuchin, A.A., 1976, Sov. Phys. Dokl., 21(9), p. 525.

Petrova, S., Simidchieva, P., and Buroff, A., 1984, Proc. Int. Conf. "Amorphous Semiconductors-84" ed. E. Farhi-Vateva and A. Buroff (Sofia:Bulgarian Acad. Sci.), p. 256.

Plocharski, J., Przyluski, J., and Wycislik, H., 1987, J. Non-Cryst. Solids, 93, p. 303.

Rennie, J.H.S., 1986, PhD Thesis, University of Cambridge.

Rennie, J.H.S., and Elliott, S.R., 1987, J. Non-Cryst. Solids, 97-98, p. 1239.

Ressel, R., Kluge, G., and Suptitz, P., 1987, J. Non-Cryst. Solids, 97-98, p. 1247.

Shimizu,I., Sakuma, H., Kokado, H., and Inoue, E., 1971, Bull. Chem. Soc. Jap., 44, p. 1173.

Shimizu, I., Sakuma, H., Kokado, H., and Inoue, E., 1972, Photogr. Sci. Eng., 16, p. 291.

Shimizu, I., Inoue, E., Kokado, H., 1974, J. Jpn. Soc. Appl. Phys. Suppl., 43, p. 101.

Shimizu, I., Ikeda, T., and Inoue, E., 1978, Preprint Int. Congress Photogr. Sci., Rochester, New York, p. 235.

Singh, B., Rajagopalan, S., Bhat, P.K., Pandya, D.K., and Chopra, K.L., 1979 Sol. State Commun., 29, p. 167.

Spence, C.A., and Elliott, S.R., 1989, Phys. Rev., B39, p. 5452.

Steel, A.T., Greaves, G.N., Firth, A.P., and Owen, A.E., 1989, J. Non-Cryst. Solids, 107, p.155.

Suptitz, P., and Fischer, A., 1984, Phys. Stat. Sol., A82, p. 157.

Tanaka, Ke., 1990, Phys. Rev. Lett., 65, p. 871.

Tai, K.L., Vadimsky, R.G., Kemmerer, C.T., Wagner, J.S., Lamberti, V.E., and Timko, A.G., 1980, J. Vac. Sci. Technol., 17, p. 1169.

Tai, K.L., Ong, E., and Vadimsky, R.G., 1982, Proc. Electrochem. Soc., 82-9, p. 9.

Wagner, T., Frumar, M., and Benes, L., 1987, J. Non-Cryst. Solids, 90, (1987), p. 517.

Wagner, T., and Frumar, M., 1990, J. Non-Cryst. Solids, 116, p. 269.

Yaji, T., and Kurita, S., 1983, J. Appl. Phys., 54, p. 647.

Yamamoto, Y., Itoh, T., Hirose, Y., and Hirose, H., 1976, J. Appl. Phys. 47, p. 3603.

Yoshikawa, A., Ochi, O., and Mizushima, Y., 1980, Appl. Phys. Lett., 36, p. 107.

Zakery, A., Slinger, C.W., Ewen, P.J.S., Firth, A.P., and Owen, A.E., 1988, J. Phys.:D, 31, S78.

Zakery, A., Zekak, A., Ewen, P.J.S., Slinger, C.W., and Owen, A.E., 1989, J. Non-Cryst. Solids, 114, p. 109.

3. EXPERIMENTAL PROCEDURE

3.1 Introduction

As-S films can be produced using a variety of techniques (e.g. thermal evaporation, sputtering, spin coating, plasma deposition or hot pressing) and films with thicknesses of up to 100 μm can be prepared. The As-S films used in the present study were all prepared by vacuum evaporation, as were the Ag films used as the source of metal ions. Because of the differences in evaporation rates for the various As-S vapour species it is necessary to find out whether there is a difference between the compositions of the As-S glasses used as evaporation sources and the corresponding evaporated As-S films. A compositional analysis of Ag-doped As-S films is also required to determine the Ag concentration in these films. Electron Microprobe X-ray analysis (EM) was employed in the present study to find the compositions of the undoped As-S films and glasses and also those of the Ag-doped As-S films.

The optical constants of As-S films were obtained using both transmissivity and reflectivity measurements while a SIMS analysis was used to obtain the variation of composition with depth in the undoped As-S films and also the Ag distribution in the silver-doped As-S films. As far as grating fabrication is concerned, both mask exposure and holographic techniques were used to produce gratings in As-S films using the metal photodissolution effect. Some of the experimental techniques described below are discussed in more detail in the relevant chapters.

3.2 Preparation of As-S glasses

Bulk As-S glasses were prepared by melting the elements arsenic and sulphur in a $1cm^2$ bore quartz tube. In order to prepare a desired composition of glass, the required amounts of sulphur and arsenic were weighed out and then placed into the tube, the arsenic

being handled under a nitrogen atmosphere in order to avoid air-oxidation of its surface. The glass tube was then evacuated to a pressure of less than 10^{-4} torr, sealed and placed in a rocking furnace. Because of the high vapour pressure of arsenic and the consequent risk of explosion, the tube was first placed partially inside the furnace and heated to 500 °C gradually, where it was held for two hours to allow an initial reaction between arsenic and sulphur. At the end of this period the tube was checked for any damage and then placed completely inside the furnace, the temperature of which was then raised to 800 °C. The tube was left rocking in the furnace at 800 °C overnight and then removed the following morning and allowed to cool in air. In some cases, when preparing glasses with compositions less arsenic rich than As_2S_3, a known amount of bulk As_2S_3 was originally placed in the quartz tube and then the required amount of sulphur was added, the mixture then undergoing the same procedure as above. This reduced the likelihood of oxygen contamination, since As_2S_3 is less easily oxidised than pure arsenic, and also minimized the risk of explosion since As_2S_3 has a lower vapour pressure. A batch of optical grade As_2S_3 ("Servofrax") of high purity (5N) was also purchased from a commercial source (Servo Corporation of America) and this material was normally used for the fabrication of the gratings. A mass survey analysis using SIMS with an O^- probe beam was performed to identify any differences between the Servofrax As_2S_3 glass and the material prepared in this work. As is seen from Figs. 3-1 and 3-2, which show the results of this analysis, these two materials are fairly similar to each other, except that there are some extra light elements present in the material prepared in this work while in Servofrax glass the presence of some extra, heavy elements (impurities) are observed.

3.3 Preparation of thin films

3.3-1 Substrate preparation

In order to ensure film thickness uniformity and to increase the adhesion of the films to the substrates, they were cleaned before film deposition. The cleaning procedure used

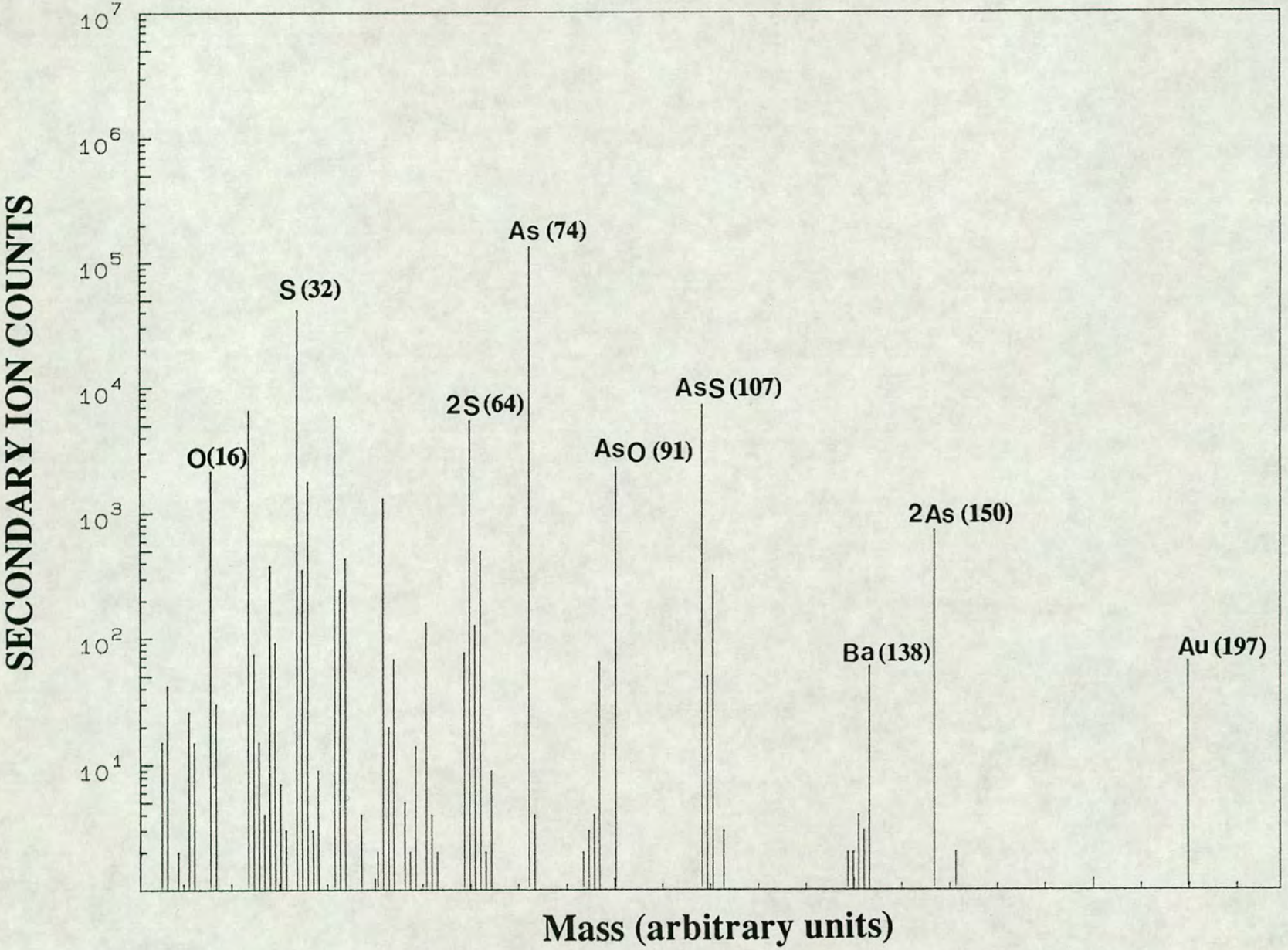

Fig. 3-1 Secondary ion count versus mass in a mass survey analysis using SIMS with an O^- ion beam for an $As_{40}S_{60}$ glass prepared in the present study.

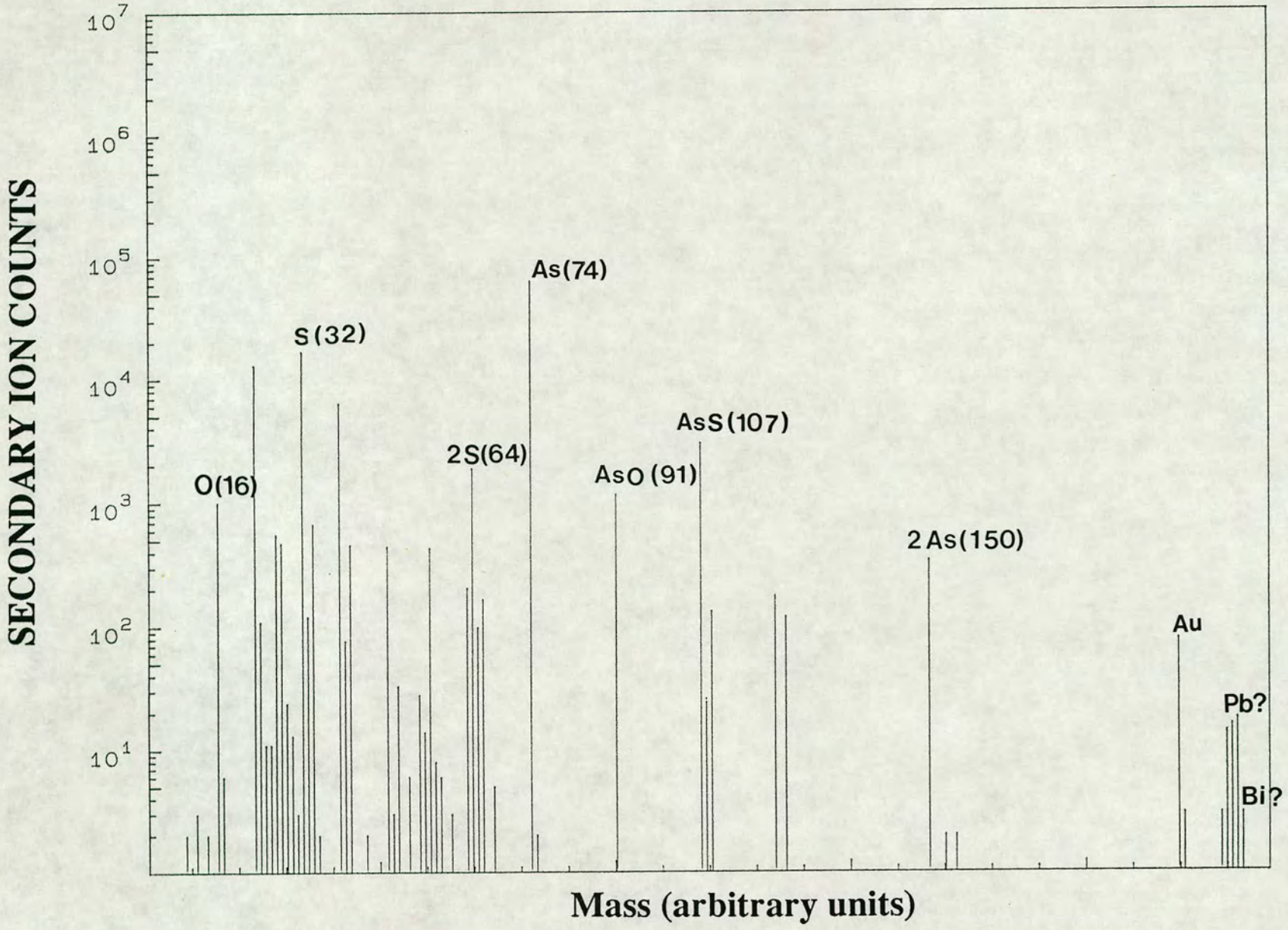

Fig. 3-2 Secondary ion count versus mass in a mass survey analysis using SIMS with an O^- ion beam for an $As_{40}S_{60}$ optical grade "Servofrax" glass.

was that the substrates were initially rinsed in a solution of T-pol detergent and hot water and then, after rinsing in distilled water, they were immersed in a solution of Decon-90 (a surface-active cleaning agent) and placed in an ultrasonic bath for a period of 30 minutes. Finally the substrates were rinsed in deionized water, dried with compressed nitrogen and placed in a desiccator for storage. NaCl flats (used for some IR measurements) were normally dry polished using alumina powder (a fine grain powder). In some experiments silicon wafers were used as substrates and these were normally cleaned using a silicon dioxide etch to remove the thin oxide layer formed on these wafers when they are exposed to atmospheric conditions.

3.3-2 Deposition of thin films by vacuum evaporation

Thin films of silver up to 2 μm in thickness and of As-S chalcogenides up to 8 μm were prepared by vacuum evaporation. For silver films thicker than 5000 A multiple evaporations were performed. Chalcogenide layers thicker than 2 μm were deposited using the material feeder of a flash evaporation system (Balzers BEF 103), which was used to refill the chalcogenide source. The evaporation sources for As-S films were fragments of glasses of the desired composition while Ag wire (99.998% pure) was used as the source for Ag films. A schematic diagram of the deposition system is shown in Fig. 3-3. It consisted essentially of a vacuum chamber and associated pumping system. Inside the vacuum chamber, there was a 1 cm diameter molybdenum or tungsten boat for evaporating silver, and a quartz glass boat inside a helical tungsten filament for evaporating the As-S chalcogenides. The boats were resistively heated. A step-down transformer controlled by a variac was used to produce the high currents needed to heat the boats. For all of the film evaporations the chamber was evacuated to a pressure of $< 10^{-1}$ torr by a rotary pump and then a diffusion pump was used to achieve a pressure of $< 1\times10^{-5}$ torr. For evaporating silver the boat was heated until the silver melted and the current was then increased to evaporate off the silver.

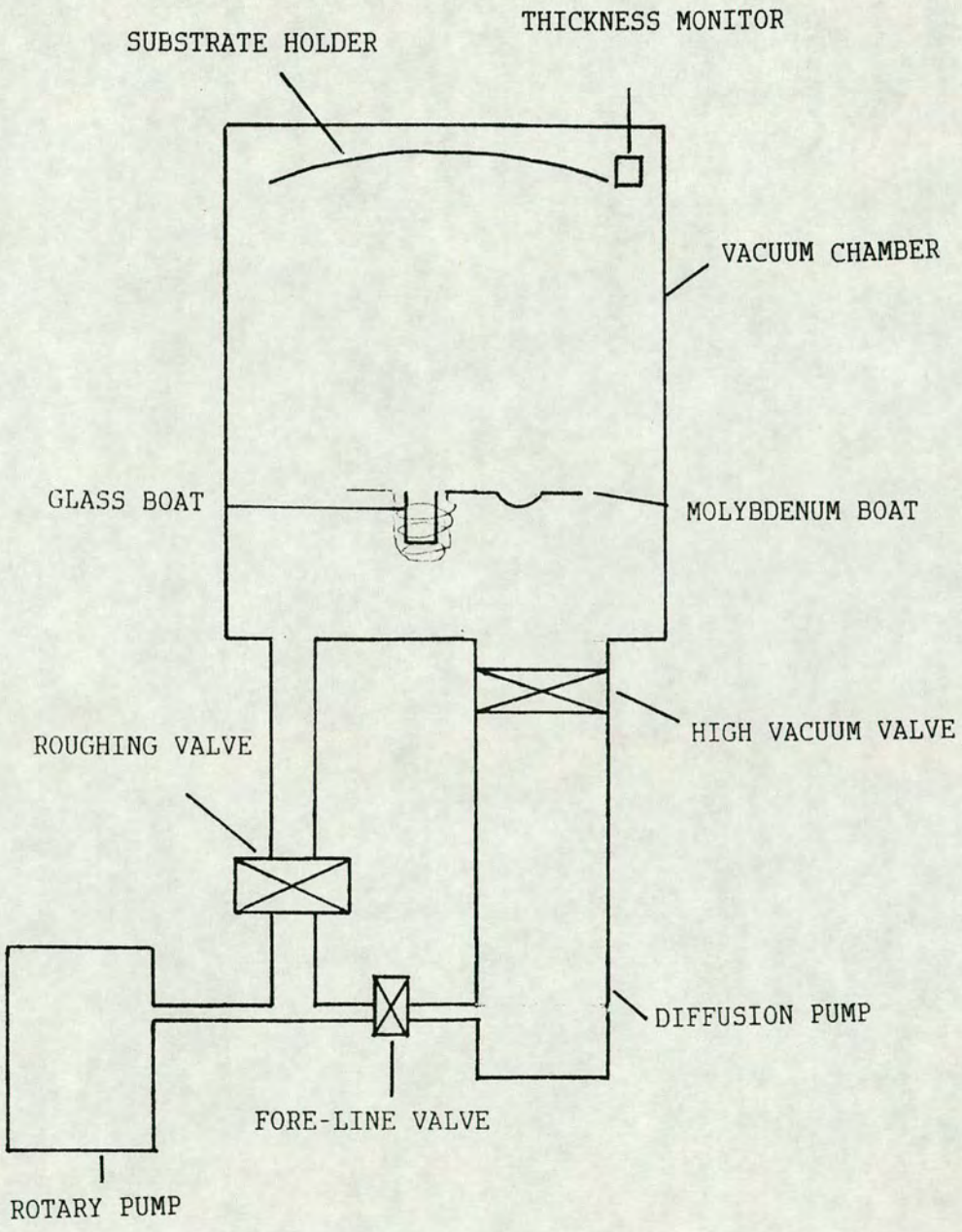

Fig. 3-3 Schematic diagram of the evaporating system.

It had been reported that silver films prepared by a slow evaporation rate of ~5 A/sec tend to be islanded (Sennett and Scott 1950). In view of this a deposition rate of ~60 A/sec was maintained for the silver evaporations. For chalcogenides it has been reported that a low evaporation rate of about 5 A/sec produces a film stoichiometry which is close to that of the source material (Goldschmidt and Rudman 1976). Consequently, when evaporating the chalcogenide layer the current was gradually increased until the material started to evaporate and then kept fixed to produce a deposition rate of ~6 A/sec. In order to maintain a uniform deposition rate for each composition, a thermocouple was attached to the chalcogenide boat to detect the melting point of different As-S compositions (and hence the start of the deposition process) and then the current was kept fixed.

3.3-3 Film thickness measurements

During deposition film thickness was continuously measured using a film thickness monitor, based on a 6 MHz Quartz crystal oscillator with Au electrodes, so that films of any desired thickness could be fabricated. As a check on thickness a mechanical stylus instrument (Talysurf) and occasionally a Dek Tak II surface profilometer were also used. As a film of a given material is deposited on the crystal, its resonant frequency changes to a lower value : it changes from its initial value F_q to a lower value F_c for a given film thickness L_f . An equation which relates the film thickness to the frequency change is given by Lu and Lewis (1972) :

$$L_f = \left(\frac{1}{c\rho}\right)\left(\frac{F}{F_q F_c}\right) \qquad (1)$$

Where ρ is the film density, $F = F_q - F_c$ and c is a constant (dependent on material composition). The oscillator output was fed to a frequency counter which could detect a change in frequency down to 1 Hz . In the absence of data for the densities of As-S films an empirical formula for the densities of As-S glasses given by Tanaka and Minami (1965) was used :

$$\log(93.3 - W_{As}) = -0.3815d \qquad (2)$$

Where W_{As} is the weight percentage of As in the compound and d is the density of the bulk glass. The actual thicknesses (determined by, for example, the Dek Tak II instrument) were smaller than those obtained using the crystal monitor. For Ag and the arsenic rich compositions the agreement was within ± 5 % while for the sulphur rich compositions the actual thicknesses were smaller than those measured by the crystal monitor by up to 30 % in the case of, for example, $As_{15}S_{85}$. This could be partly due to the position of the measuring crystal, which was not exactly at the same distance from the boats as the sample, and also due to inexact values used for the densities of the As-S compounds and the fact that the deposited material was different from the quartz crystal. Hence a correction factor was obtained for each As-S composition and the actual thicknesses of the samples were adjusted using this.

3.4 Compositional analysis

A CAMECA Camebax microbeam instrument was used for the EM compositional analysis of both the undoped and Ag-doped As-S films.

3.4-1 Compositional analysis of undoped As-S films

The samples used for compositional analysis were prepared by evaporating onto a cleaned glass substrate a layer of the desired As-S composition, the As-S evaporation sources being powdered melt quenched glasses of the appropriate composition. The film compositions of the undoped As-S compounds (and also those of the bulk glasses used as evaporation sources) were determined by the Electron Microprobe Analysis technique. In order to find the thickness required to get a reasonable signal, a set of samples was prepared in which a layer of Al was first deposited on the glass slide prior to As-S film deposition. For these samples, if the film was not thick enough, electrons could penetrate

through the film completely and a large Al signal would appear. By examining such samples with different As-S thicknesses, the minimum thickness required for As-S films was found to be about 1.25 μm. Al_2O_3 was used as the aluminum standard while FeS_2 and As_2S_3 were used as sulphur and arsenic standards respectively. The films were carbon coated prior to the analysis in order to avoid charging effects. An accelerating voltage of 10 kV with a beam current of 10 nA were found suitable for these measurements and the $As_{L\alpha}$, $S_{K\alpha}$ and $Al_{K\alpha}$ lines were used for the analysis.

Nine different glass compositions were used in this study. For each composition ten measurements were made and the mean value of the measurements was taken as the composition of the As-S glass or film. These measurements were correct to within $\pm$ 1 at. % . Fig. 3-4 shows the measured As-S film composition versus the source composition. For compositions richer in As than $As_{30}S_{70}$ there is good agreement between the film and source compositions. For sulphur rich compositions however, the films seem to be more As rich than the source. Tanaka (1979) reports a value of $\pm$ 2 at.% difference between the film and source compositions. In sulphur rich glasses, excess sulphur exists probably in chain-like form but in the range where the sulphur content is greater than that in the range $As_{17}S_{83}$ - $As_{20}S_{80}$, both chain-like and ring-type forms coexist. The bond strengths of the three bonds As-As, As-S and S-S are 43.4, 52.8 and 55.0 kcal $mole^{-1}$ respectively. Hence for sulphur rich compositions some of the sulphur is not evaporated at the same rate as the other units during film deposition. Also, evidence of some sulphur being left behind during evaporation was observed during the cleaning procedure of the As-S boat with NaOH since a white precipitate (Na_2SO_4?) was formed. Yamaguchi (1985) has used the same argument (i.e the relative strength of different bonds) to explain the increase in average band gap of sulphur rich compositions in the As-S system.

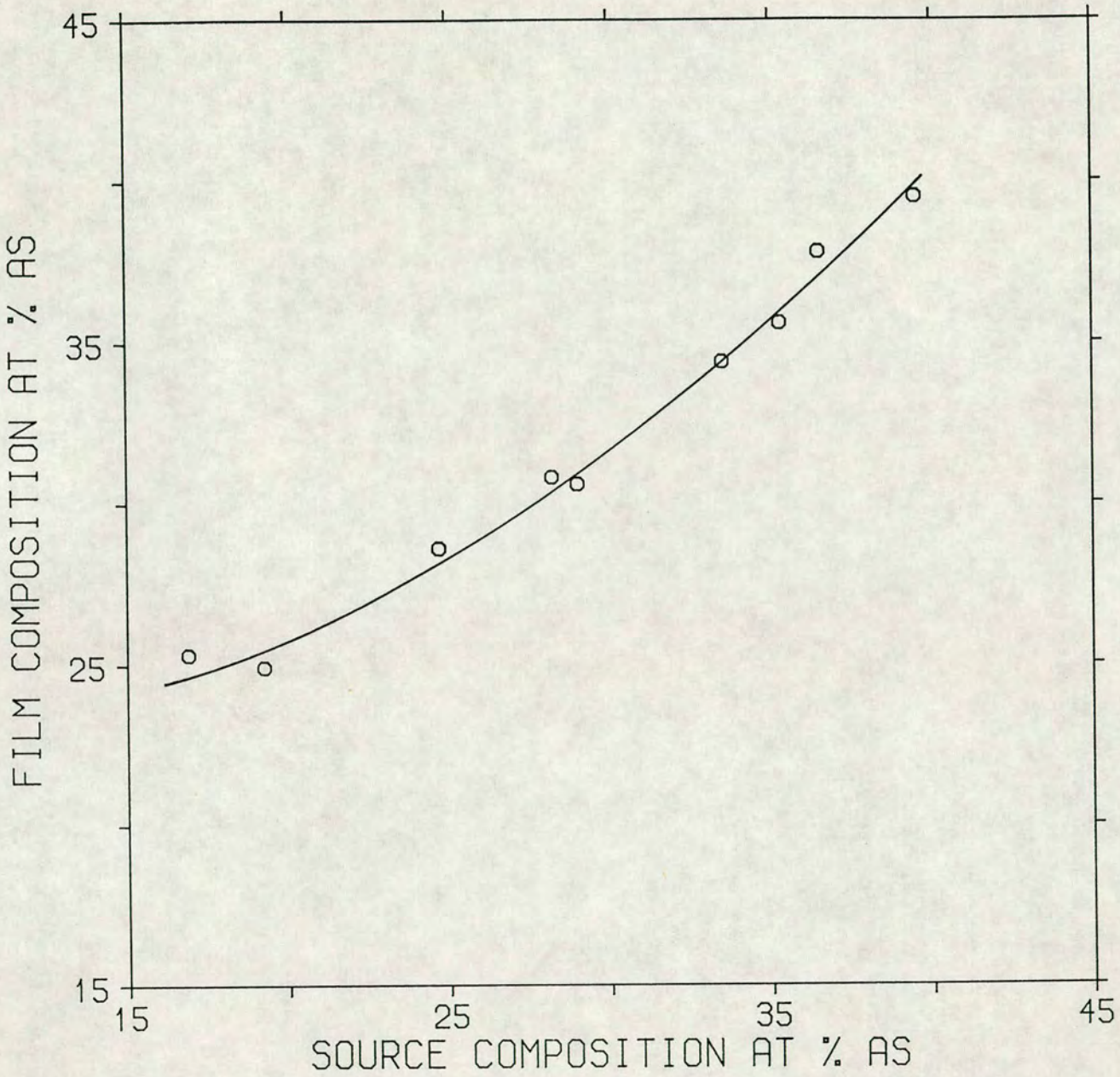

Fig. 3-4 The variation of film composition as a function of the As-S source composition as determined from an Electron Microprobe analysis. The full line is a guide for the eye.

3.4-2 Compositional analysis of the silver-doped As-S films

Two different compositions of glass were used in this study and care was taken to ensure that the silver had penetrated all the way through the chalcogenide layer. Photodoping of the samples was achieved using a 200 W mercury lamp. The first sample examined consisted of a 1.3 μm $As_{33}S_{67}$/ 0.27 μm Ag combination. The electron microprobe analysis was performed at 20 kV and at a beam current of 10 nA. The raster area on the sample was ~ 10 μm and a 15 s count time was used in this analysis. The SEM image of the surface of this sample after photodoping is presented in Fig. 3-5 and shows bright regions on a darker background. The bright regions correspond to the compounds with higher mass number (Ag-containing phase). This figure indicates a phase-separated structure. The bright phases are typically 1-2 μm in diameter and cover approximately 5% of the surface. For compositional analysis, normally fifteen measurements were made on each region and results indicate that the composition of both the bright and darker regions are the same, namely $Ag_{25.9\pm2.65}As_{24.63\pm0.8}S_{49.4\pm1.2}$, which corresponds to the composition of the crystalline compound smithite ($AgAsS_2$). (The ± limits here are from the extreme values rather than the standard deviation). Fig. 3-6 shows a group of these bright phases at higher magnification and reveals their regular shape, indicating that they are crystalline. The presence of these crystals is possibly not due to the photodoping process itself but is instead a consequence of the long exposure time used for photodoping of the sample in these experiments (typically from 18-42 hrs), since photoinduced crystallization has been observed in some chalcogenides. An alternative, though less likely, explanation of the presence of these crystalline phases is that they are arsenic oxide crystals (As_2O_3), although it was not possible to confirm this by EM analysis since there was no detector for oxygen. This would be possible if the electron beam were deflected so that the composition obtained for the bright phases is actually due to the darker background. It should be noted that such crystallites have not been observed in previous SEM studies of photodoping in the Ag/As-S system under normal exposure conditions (Hajto et al. 1987).

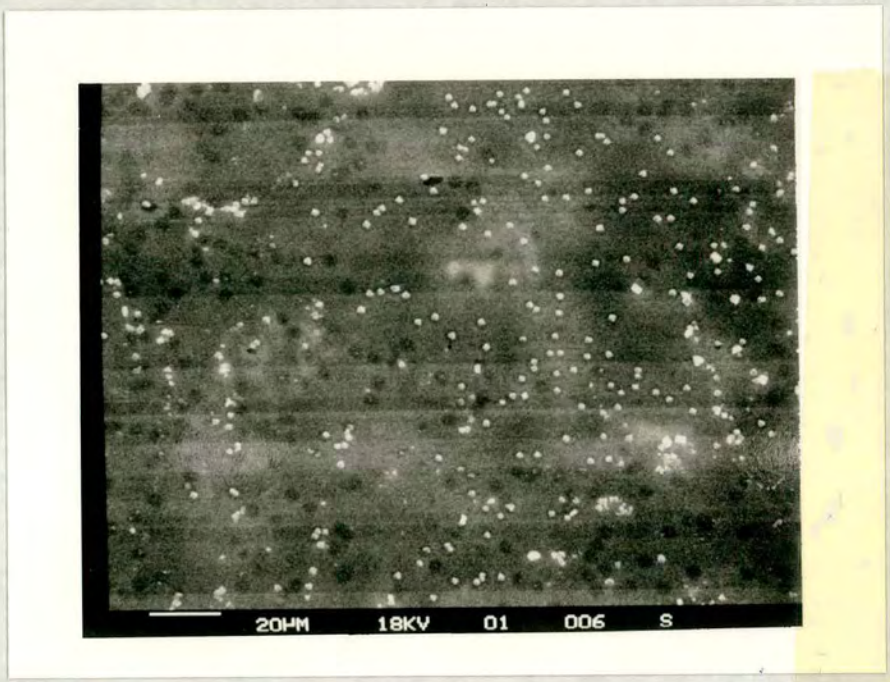

Fig. 3-5 SEM image of the surface of an $As_{33}S_{67}$ / Ag combination after photodoping.

Fig. 3-6 As Fig. 3-5 but at higher magnification. The regular shape of the bright regions is apparent.

The second sample was a 1.4 μm $As_{40}S_{60}$ / 0.46 μm Ag combination. Fig. 3-7 shows an SEM image of its surface, which is clearly different from that of the $As_{33}S_{67}$ sample. For the $As_{40}S_{60}$ sample the bright regions are more numerous and have congregated in some places to form extensive (~ 20 μm diameter) clusters. Fig. 3-8 is a higher magnification SEM image of one of these cluster regions and again shows clearly the crystalline nature of this phase. The EM analysis gives the composition of the darker background areas as $Ag_{24.77\pm1.8}As_{31.2\pm\ 1}S_{44.69\pm1.6}$ (~ $Ag_{1.59}As_2S_{2.86}$), and indicates that the brighter regions are more Ag rich than this, having Ag contents between 45 and 52 atomic % . These films are therefore less homogeneous than those produced by photodoping $As_{33}S_{67}$ in that the extent of the crystallization is larger and there is also a difference in composition between the bright and dark areas. The third sample was a 1.49 μm $As_{40}S_{60}$ / 0.21 μm Ag combination. This sample, with a smaller Ag/As-S thickness ratio, was examined in order to see the effect of Ag concentration. Fig. 3-9 is an SEM image of the surface and shows that for $As_{40}S_{60}$ the bright crystalline regions are present even for lower Ag concentrations. Phase separation has been observed (Tsutsumi et al. 1982) in melt-quenched $As_{40}S_{60}$ glass containing Ag, the Ag content and size of the Ag-rich regions varying with the amount of Ag in the melt. These results are similar to what is observed in the photodoped samples, although the Ag content of the background region is considerably smaller in the bulk glass case. From Fig. 3-9 it is clear that reducing the Ag content does not significantly affect the extent of microcrystal formation in $As_{40}S_{60}$, in which phase separation must occur anyway. In $As_{33}S_{67}$, which is the preferred composition for imaging applications because of its greater sensitivity, reducing the Ag content may affect the extent of phase separation and a sample with a lower Ag content will have to be examined in a future study.

3.5 Transmissivity and reflectivity measurements

For the measurement of the optical constants of different As-S compositions in the visible and the near IR a Perkin Elmer Lambda 9 spectrophotometer was used. This

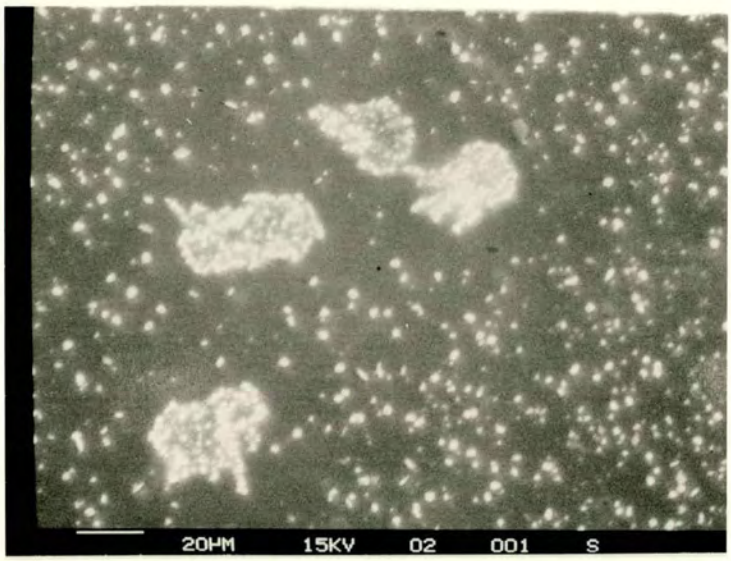

Fig. 3-7 SEM image of the surface of an $As_{40}S_{60}$ / Ag combination after photodoping.

Fig. 3-8 As Fig. 3-7 but at higher magnification, showing detail of one of the cluster regions.

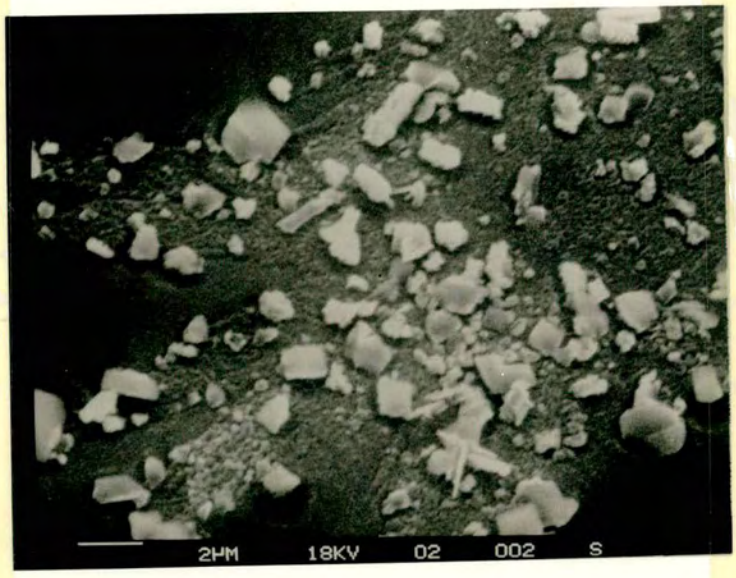

Fig. 3-9 SEM image of the surface of an $As_{40}S_{60}$ / Ag combination after photodoping. The Ag content in the photodoped film is less than for the film of Figs. 3-7 and 3-8, but phase separation is still apparent.

spectrophotometer operates in the range 185-3200 nm and has a default slit width of 1 nm. The spectrophotometer could correct for background irradiation so that the absolute value of transmissivity for the film and substrate combination could be obtained. Evaporated As-S films of about 1 μm thickness were prepared and both transmissivity and reflectivity measurements were made. Transmissivity curves were used to obtain the optical constants of the As-S films while reflectivity curves were analyzed as a check on the transmissivity measurements. The optical constants of these As-S films in the IR were obtained using a Perkin Elmer 1420 Ratio Recording IR spectrophotometer which operates in the range 2.5-16 μm. Both transmissivity and reflectivity measurements were made on these As-S films. As before, transmissivity curves were used to obtain the optical constants of the As-S films while reflectivity curves were analyzed as a check on the transmissivity results. For these IR measurements films of at least ~ 2 μm were required for the analysis.

3.6 SIMS measurements

A CAMECA ims-4f instrument, which can operate as either an ion microprobe or an ion microscope, was used for the SIMS measurements. Two primary ion sources are available, a gas source (for O_2^+, O^- or Ar^+ ions) and a Cs^+ microbeam source. The samples are inserted into a high vacuum chamber (~ 10^{-9} torr) and must be perfectly flat, although they can be any shape provided they fit within a 1 inch round area and are less than 10 mm thick. In SIMS analysis, the surface of the sample is bombarded with a finely-focussed beam of primary ions. The collision cascade generated by the impacting ions results in the ejection and ionization of atoms from the surface of the sample. These secondary ions are passed into a mass spectrometer for analysis. The ion microprobe can quantitatively analyze nearly all elements in the periodic table, from hydrogen to uranium. The number of secondary ions created is in part dependent on the choice of bombarding species. The ion yield of electropositive elements, e.g. Ca, Mg, Al, is increased by bombarding with an oxygen beam. In contrast, the number of electronegative elements, e.g. O, C, S, is increased by bombarding with caesium. A low primary beam current yields a

low sputter rate and permits analysis of surface layers; on the other hand high beam currents can be employed to obtain a high sputter rate and enable in-depth analysis. Detection limits between ppb and ppm levels exist for many elements.

3.7 Positron ion scattering

The development of mono-energetic positron beams in recent years has enabled studies of surface properties, in particular studies of atomic scale disorder at the surface and in the near-surface region. These measurements are based on a strong positron surface interaction, and on the capability of positron localization at open-volume lattice defects (Brandt et al. 1983). The depth distribution of vacancy-type defects has been measured (Vehanen et al. 1985), which is based on monitoring the energy-dependent fraction of positrons diffusing back to the surface. Deeper areas of the sample can be probed by measuring properties of the annihilation radiation inside the sample, following mono-energetic positron injection. This data is obtained by measuring the shape of the 511 keV annihilation line versus incident positron energy E. When positrons are implanted into a solid they thermalize after $\leq$ 10 psec and eventually annihilate with an electron, producing predominantly two annihilation γ rays. The experiments are normally performed with a variable energy positron beam in ultra-high vacuum ($\sim 10^{-10}$ torr). Using a 50 mCi $^{58}Co\ \beta^+$ source and a backscattering W(110) moderator, a slow positron beam intensity of 7×10^5 positrons per second corresponding to a moderation efficiency of $\epsilon = 0.25\%$ was obtained (Vehanen et al. 1986). An energy sensitive γ-ray detector (Ge detector) which measures the energy broadening of the 511 keV annihilation line is placed in the proximity of the sample. At each incident positron energy $\sim 10^6$ counts is collected into the 511 keV annihilation line. Such a spectrum is characterized by a single parameter S, the lineshape parameter, defined as the area of a fixed region in the center of the spectrum divided by the total area of the spectrum. Typical values are $\sim$ 1 keV for the central region and $\sim$ 10 keV for the total spectrum (Lynn et al. 1986). A review of the interaction of positron beams with surfaces, thin films and interfaces is given by Schultz and

Lynn (1988).

3.8 Mask exposure system

To produce some of the grating structures a Karl Suss MJB-3 mask alignment and exposure system was used which employs a 200 W UV mercury lamp as the illumination source. The system is equipped with a microscope for alignment purposes. The mask holder and the mask are held down by vacuum and the emulsion side of the mask is brought into contact with the substrate. During transport, the substrate is also held down by the vacuum. The contact pressure between the mask and the substrate is variable. For alignment purposes the mask and the substrate can be separated by ~20 μm . By looking through the microscope and adjusting the substrate in relation to the mask by means of micrometer screws alignment can be achieved. After bringing the mask and substrate into contact the system is set in its exposure mode during which compressed air presses the substrate against the mask and the electromagnetic shutter in the lamphouse opens. After exposure the system automatically returns to its original position, the contact lever is then set in the separation position and it is possible to withdraw the transport slide and exposed wafer.

3.9 Summary

Bulk As-S glasses have been prepared by a melt quenching technique and vacuum thermal evaporation has been employed to fabricate film samples. For Ag films, multiple evaporations have been used to prepare films with thicknesses of up to 2 μm, while As-S films with thicknesses of up to 8 μm have been prepared using the material feeder of a flash evaporation system. Compositional analysis of both As-S glasses and films and also Ag-doped As-S films has been performed using Electron Microprobe analysis. In Ag-doped $As_{33}S_{67}$ the composition determined using this technique is nearly the same as the smithite ($AgAsS_2$) composition. Some phase separation has been observed in this material although it is more likely to be due to the exposure conditions than to the actual

photodoping process. In the case of Ag-doped $As_{40}S_{60}$ a composition $\sim Ag_{1.59}As_2S_{2.86}$ which is richer in Ag than smithite has been determined. The extent of phase separation in the Ag-doped $As_{40}S_{60}$ film is higher than that in Ag-doped $As_{33}S_{67}$ which indicates that the latter composition is more suitable for applications such as grating fabrication. The presence of bright crystalline phases has been attributed to photocrystallization of the silver compound or possibly the formation of As_2O_3 crystals during illumination of the samples.

3.10 References

Brandt, W., and Dupasquier, A., 1983, editors, Positron Solid State Physics, North-Holland.

Goldschmidt, D., and Rudman, P.S., 1976, J. Non-Cryst. Solids, 22, p. 229.

Hajto, E., and Zentai, G., 1987, J. Non-Cryst Solids, 90, p. 581.

Lu, C., and Lewis, O.J., 1972, J. Appl. Phys., 43, p. 4385.

Lynn, K.G., Chen, D.M., Nielsen, Bent, and Pareja, R., 1986, Phys. Rev., B, 34(3), p. 1449.

Ohta, M., Tsutsumi, M., Izumi, F., and Ueno, S., 1982, J. Mat. Sci., 17, p. 2431.

Schultz, P.J., and Lynn, K.J., 1988, Rev. Mod. Phys., 60(3), p. 701.

Sennett, R.S., and Scott, G.D., 1950, J. Opt. Soc. America, 40, p. 201.

Tanaka, K., and Ohtsuka, Y., 1979, Thin Solid Films, 57, p. 59.

Tanaka, M., and Minami, T., 1965, Japn. J. Appl. Phys., 4, p. 939.

Vehanen, A., Makinen, J., Hautojarvi, P., Huomo, H., Lahtinen, J., Nieminen, R.M., and Valkealahti, S., 1985, Phys. Rev., B Rapid Commun., 32, p. 7561.

Yamaguchi, M., 1985, Phil. Mag., B, (51)6, p. 651.

4. OPTICAL CONSTANT MEASUREMENTS

4.1 Introduction

Chalcogenide glasses are well known IR transmitting materials, having pass bands (depending on composition) from the visible to beyond 15 μm (Savage 1985). By making use of the photoinduced phenomena that occur in these glasses, it should be possible therefore to produce diffractive elements for use at IR wavelengths. A particularly important feature is the change in the refractive index that occurs under the influence of light, which makes it possible to use chalcogenide glasses to record not only the amplitude but also the phase of the incident light. The latter is particularly important in holographic optical data storage and in the fabrication of various components and devices, such as selective optical filters, mixers, couplers, modulators, etc (Andriesh et al. 1986). The metal photodissolution effect is probably the most useful of the photoinduced effects that occur in chalcogenide glasses because it produces the largest change in the chemical and physical properties of these glasses, particularly the optical constants. For the analysis and modelling of the performance of the fabricated devices a knowledge of their optical constants is essential. Although measurements have been made of the absorption coefficient (Young 1971, Kosek et al. 1970) and refractive index (Cimpl et al. 1987, Young 1971, Tanaka 1979) of several As-S glasses, the optical properties of materials in the As-S-Ag system have not been investigated extensively and what little information exists is mainly concerned with the crystals in this system (Hulme et al. 1967, Wehmeier et al. 1968, Andreichin et al. 1966, Golovach et al. 1975 and Shauren et al. 1986). In this chapter the metal photodissolution effect is used to investigate the changes in the optical constants that occur in As-S thin films on the introduction of silver. Calculation of the refractive index is based on both transmissivity and reflectivity measurements on these films in the visible and IR part of the spectrum.

For the calculation of the absorption coefficient in the visible and near IR a model based on a method outlined by Goldschmidt (1984) is used. Photodoping of films was achieved by illumination with a 200 W mercury lamp. Transmittance and reflectance measurements of the films in the visible and near IR were performed using a Perkin Elmer Lambda 9 spectrophotometer, and a Perkin Elmer 1420 ratio recording IR spectrophotometer was used to measure the transmittance and reflectance of the films in the IR.

4.2 Refractive index measurements

4.2-1 Refractive index measurements of the undoped as-deposited As-S thin films as a function of composition in the visible.

Films of different As-S compositions were prepared by vacuum evaporation of the desired composition onto cleaned Corning 7059 glass substrates. The Corning glass substrates were used because they had an approximately constant refractive index in the visible and near IR part of the spectrum (Fig. 4-1) . The measurement of the transmittance and reflectance was carried out immediately after film deposition or on films kept in a desiccator for at most a few days. For calculation of the refractive index of the As-S films, the transmittance spectra of the samples were used and the results were checked with reflectance data. A typical transmissivity spectrum for these films is shown in Fig. 4-2. Calculation of the refractive index was performed using the interference fringes of the transmittance spectra using a model proposed by Swanepoel (1983). The practical situation for a thin film on a transparent substrate is shown in Fig. 4-3. The film has a thickness d and complex refractive index $n^* = n - iK$ where n is the refractive index and K is the extinction coefficient, which is related to the absorption coefficient α by : $K = \alpha\lambda/4\pi$. The transparent substrate has a thickness several orders of magnitude larger than d, a refractive index s and an absorption coefficient $\alpha_s = 0$. The index of the surrounding air is $n_0 = 1$. As is shown in Fig. 4-2, the spectrum can roughly be divided into four regions. In the

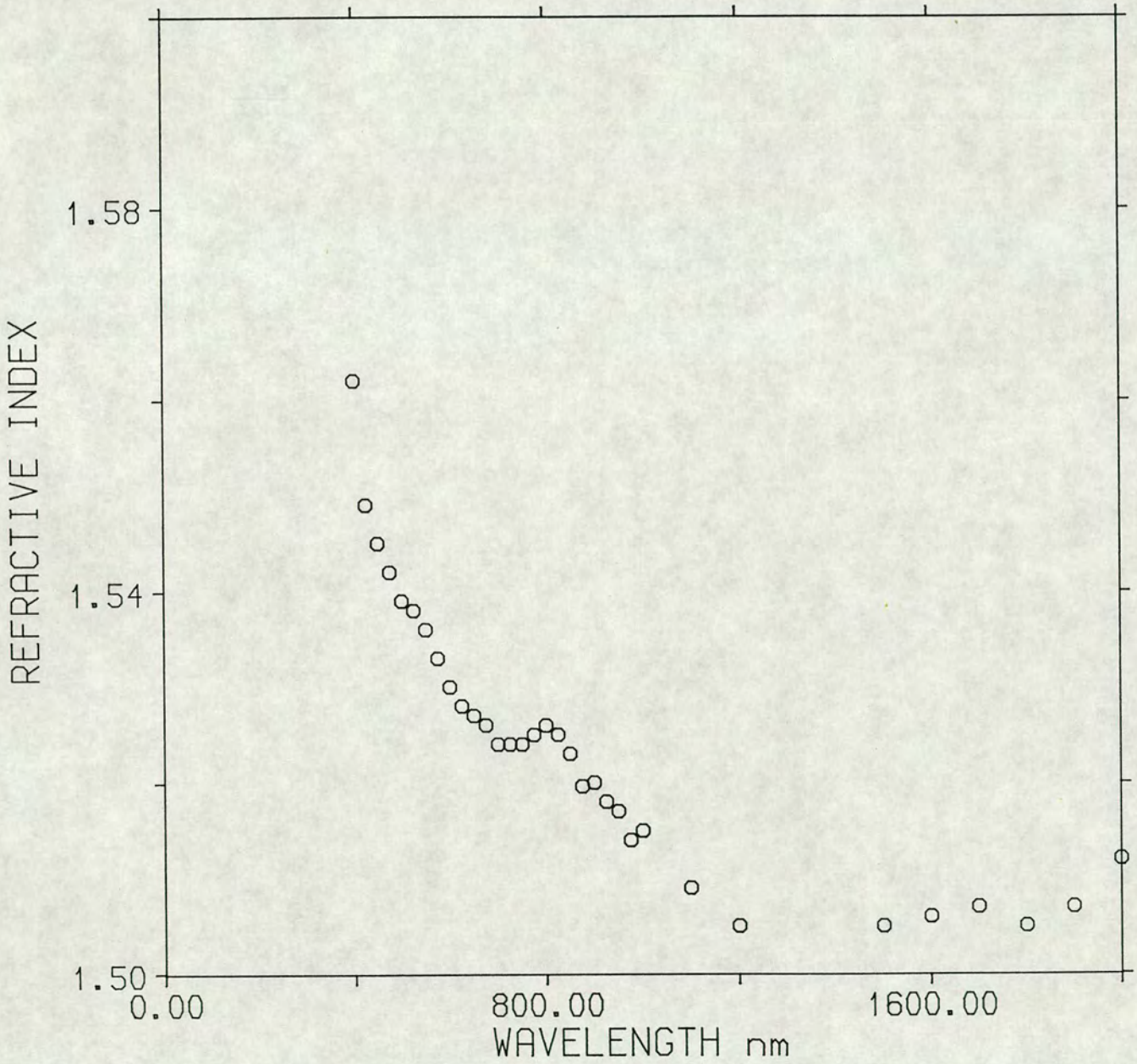

Fig. 4-1 Refractive index versus wavelength for a 7059 corning glass substrate.

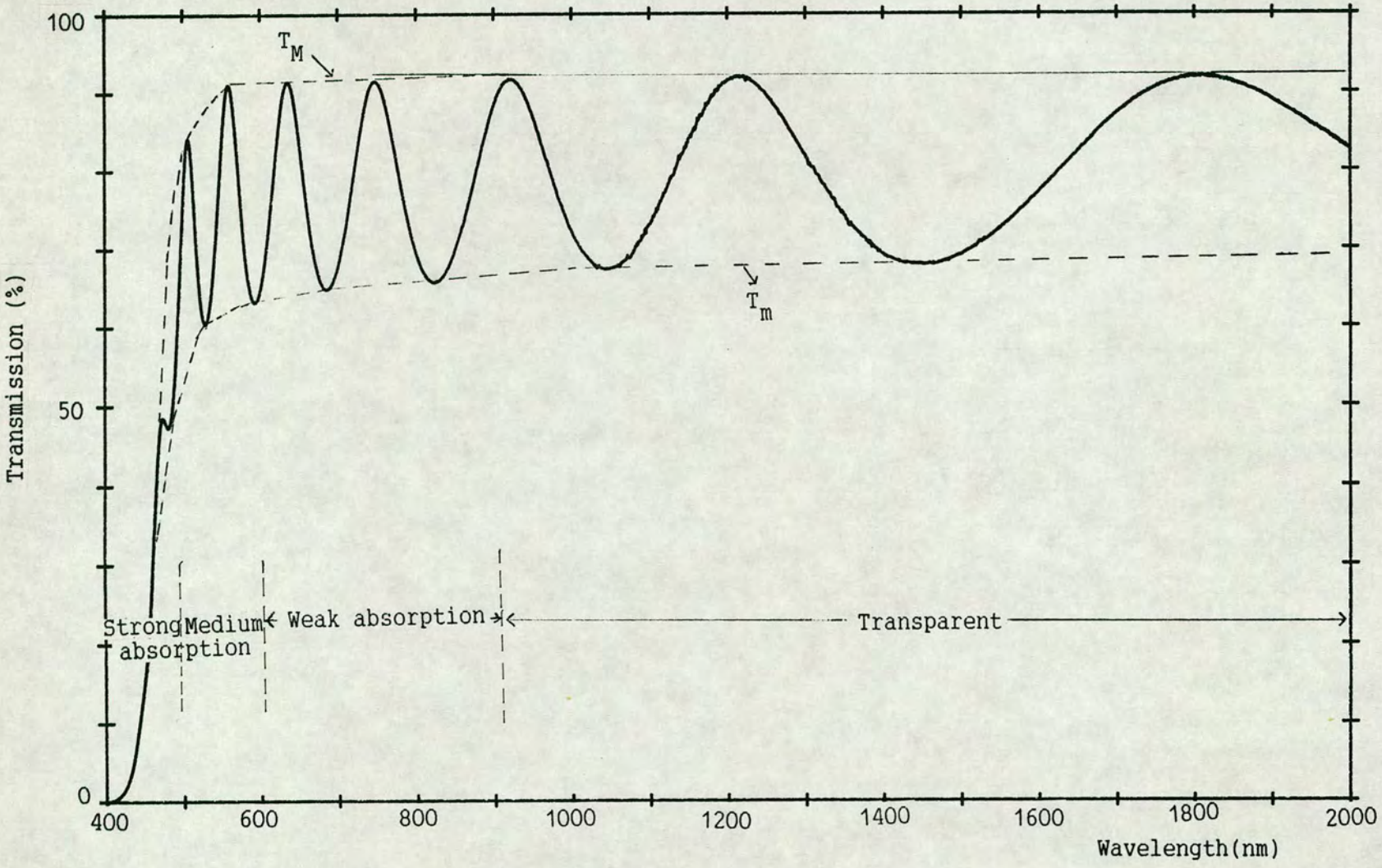

Fig. 4-2 Transmissivity versus wavelength of a film of composition $As_{33}S_{67}$ and of thickness 832 nm.

region of weak absorption α is small but starts to reduce the transmission. In the region of medium absorption α is large and transmission decreases, and in the region of strong absorption the transmission decreases drastically. If the thickness d is uniform, an interference effect is observed and can be used to calculate the optical constants of the film. The transmittance in the transparent region corresponds to the transmissivity of the substrate. The transmissivity of the substrate is given by :

$$T_s = \frac{(1-R)^2}{(1-R^2)} \tag{1}$$

where R is given by :

$$R = \frac{(s-1)}{(s+1)}$$

s being the refractive index of the substrate. Hence:

$$s = \frac{1}{T_s} + [\frac{1}{T_s^2} - 1]^{1/2} \tag{2}$$

Knowing that the value of transmissivity in the transparent region was 92 %, a value of s = 1.51 was obtained for the refractive index of the substrate. The extremes T_M and T_m of the interference fringes are considered as continuous functions of λ as indicated by the envelopes in Fig. 4-2. T_M corresponds to a maximum in intensity and T_m to a minimum in intensity. It should be noted that the transmission values should be read on the curves of T_M and T_m at each wavelength and not on the actual spectrum. In the transparent region the film refractive index is given by :

$$n = [M + (M^2 - s^2)^{1/2}]^{1/2} \tag{3}$$

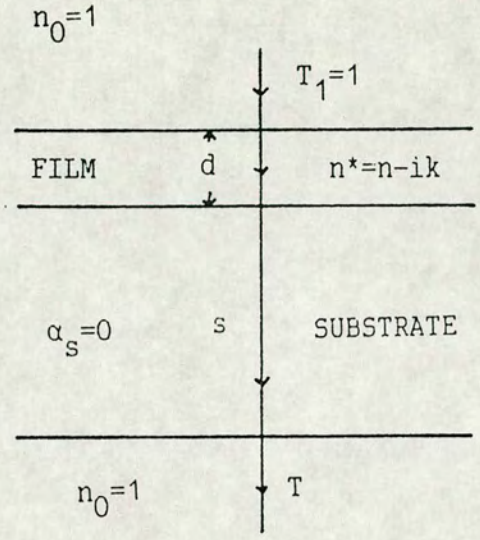

Fig. 4-3 System of an absorbing thin film on a thick finite transparent substrate.

where:

$$M = \frac{2s}{T_m} - \frac{s^2+1}{2}$$

In the region of weak and medium absorption, the film refractive index is given by :

$$n = [N + (N^2 - s^2)^{1/2}]^{1/2} \qquad (4)$$

where:

$$N = 2s \frac{T_M - T_m}{T_M T_m} + \frac{s^2+1}{2}$$

In order to find the value of n at shorter wavelengths in the region of strong absorption, where no interference fringes exist, the single oscillator dispersion equation was used

$$n = [1 + \frac{A\lambda^2}{\lambda^2 - \lambda_c^2}]^{1/2} \qquad (5)$$

The positions of the maxima and minima of the fringes were also used to find the refractive index of the films from the relation :

$$2nd = m\lambda \qquad (6)$$

where m was the order of interference, n the refractive index, λ the wavelength and d was the film thickness. Film thicknesses were directly measured by a mechanical stylus. This was achieved by fabricating a sharp step on the films during the film deposition. Normally six measurements were made and the mean value of the measurements was taken as d.

The results obtained in the present study for undoped, as-deposited As-S films are shown in Fig. 4-4, which plots the refractive index at a red wavelength (632.8 nm) versus film composition. The error bar shows the uncertainty involved in the measurements. An expression for the relative error, $\Delta n/n$, in the refractive index was obtained by re-writing Eqn. 6 in the form shown in Eqn. 7 and then differentiating this to obtain Eqn. 8

$$n = m\lambda/2d \tag{7}$$

$$\Delta n/n = \Delta m/m + \Delta\lambda/\lambda + \Delta d/d \tag{8}$$

As is seen from Eqn. 8, there are two contributions to the uncertainty in the refractive index since the order of the interference was constant, being an integer for maxima and half integer for minima. Also $\Delta\lambda/\lambda$ is negligible since λ could be read relatively accurately from the spectrometer, $\Delta\lambda$ being 1 nm. So the contribution to the uncertainty in the refractive index is mainly due to the uncertainty, Δd, in the film thickness: Δd was typically 200 A. For a film of thickness 1 μm, this corresponded to 200/10000 or 2%. For comparison, data obtained by Tanaka (1979) which was measured by a prism coupling technique, is also shown and is in reasonable agreement with the present results. The values of the refractive indices agree with the results of Tanaka (1979) to within 2 % for $As_{40}S_{60}$. The difference in the two results is probably due to differences in film composition (see section 3-4). Recently, this technique has been used for the measurement of the optical constants of arsenic triselenide films (Hammam et al. 1986), and has proved to be easy and accurate. The results of the refractive index measurements for undoped As-S films were used for the analysis of the reflectivity measurements (see section 5-2). It should be mentioned that the analysis of the uncertainty only considers some measurable sources of error in the measurements. Other factors such as pinholes, surface or bulk scattering due to dust particles or surface roughness, the presence of an oxide layer, etc. cannot be accounted for.

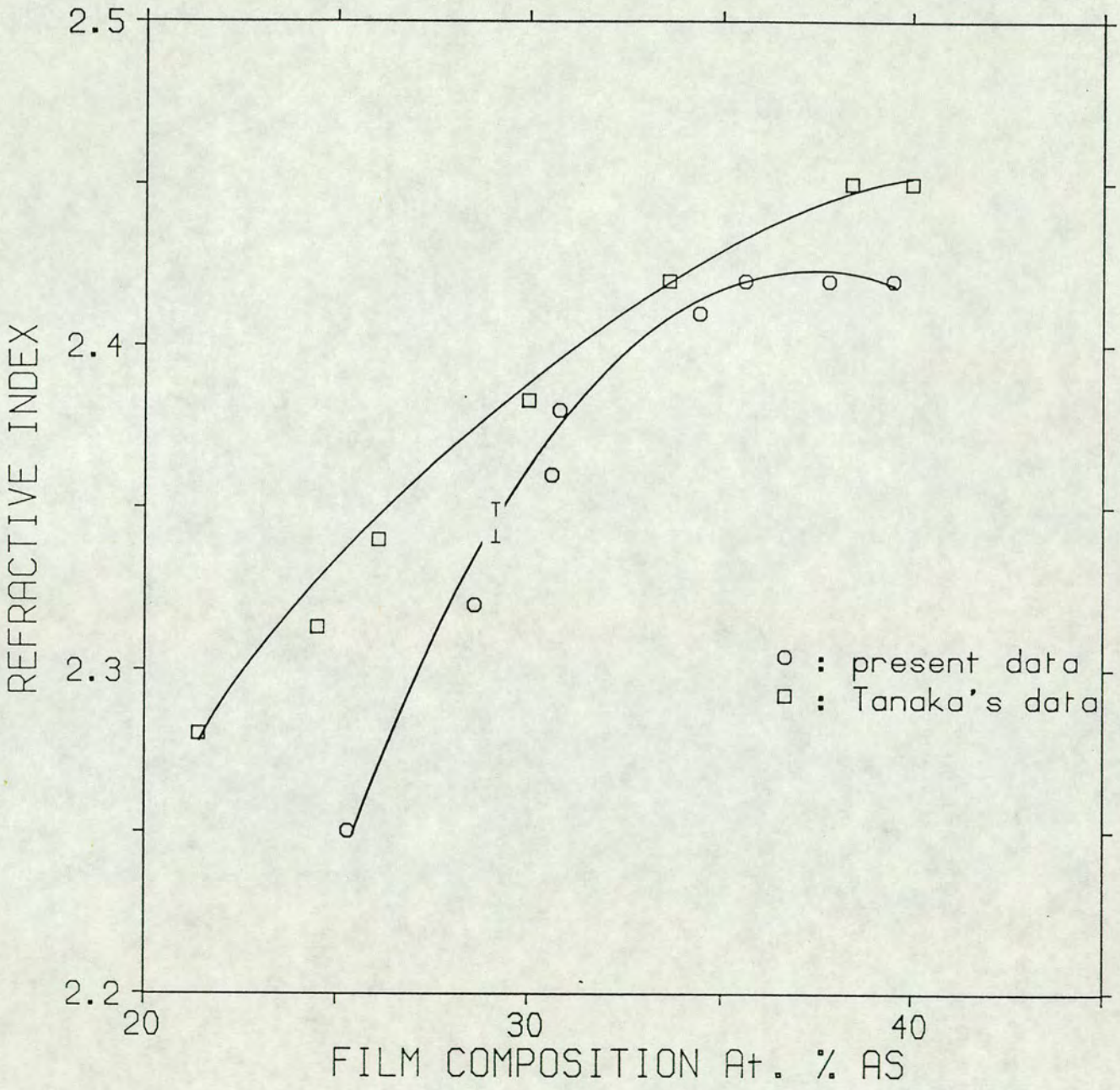

Fig. 4-4 The variation of refractive index as a function of the composition of the as-deposited As-S film at 632.8 nm. The full lines are guides for the eye. The data obtained by Tanaka (1979) is also shown for comparison.

The values of m and d can also be determined by a simple graphical method. Suppose the order number (integer or half integer) of the first extreme is m_1 . Eqn. 6 can now be written for the extremes of the spectrum as :

$$2nd = (m_1 + l/2)\lambda \tag{9}$$

where: l = 0,1,2,3, ...

Hence:

$$l/2 = 2d(n/\lambda) - m_1 \tag{10}$$

This is in the form of a straight line. If $l/2$ is plotted versus n/λ, a straight line will be obtained with slope 2d and intersect on the y axis $-m_1$. Fig. 4-5 shows a typical result for an undoped $As_{40}S_{60}$ film.

Eqn. 5 can also be approximated, using a binomial expansion, by the form shown in Eqn. 11, which was used for each composition. The experimental values of refractive index were fitted to this equation using a least squares fit :

$$n = c + \frac{a}{\lambda^2} \tag{11}$$

4.2-2 Refractive index measurements of the silver photodoped As-S thin films as a function of silver concentration in the visible

Samples were prepared by evaporating onto Corning 7059 glass substrates first a layer of Ag and then a layer of $As_{30}S_{70}$ glass, there being no break in the vacuum between evaporations. The composition $As_{30}S_{70}$ was chosen for these measurements because earlier studies have shown that it is around the optimum composition with regard to resolution and

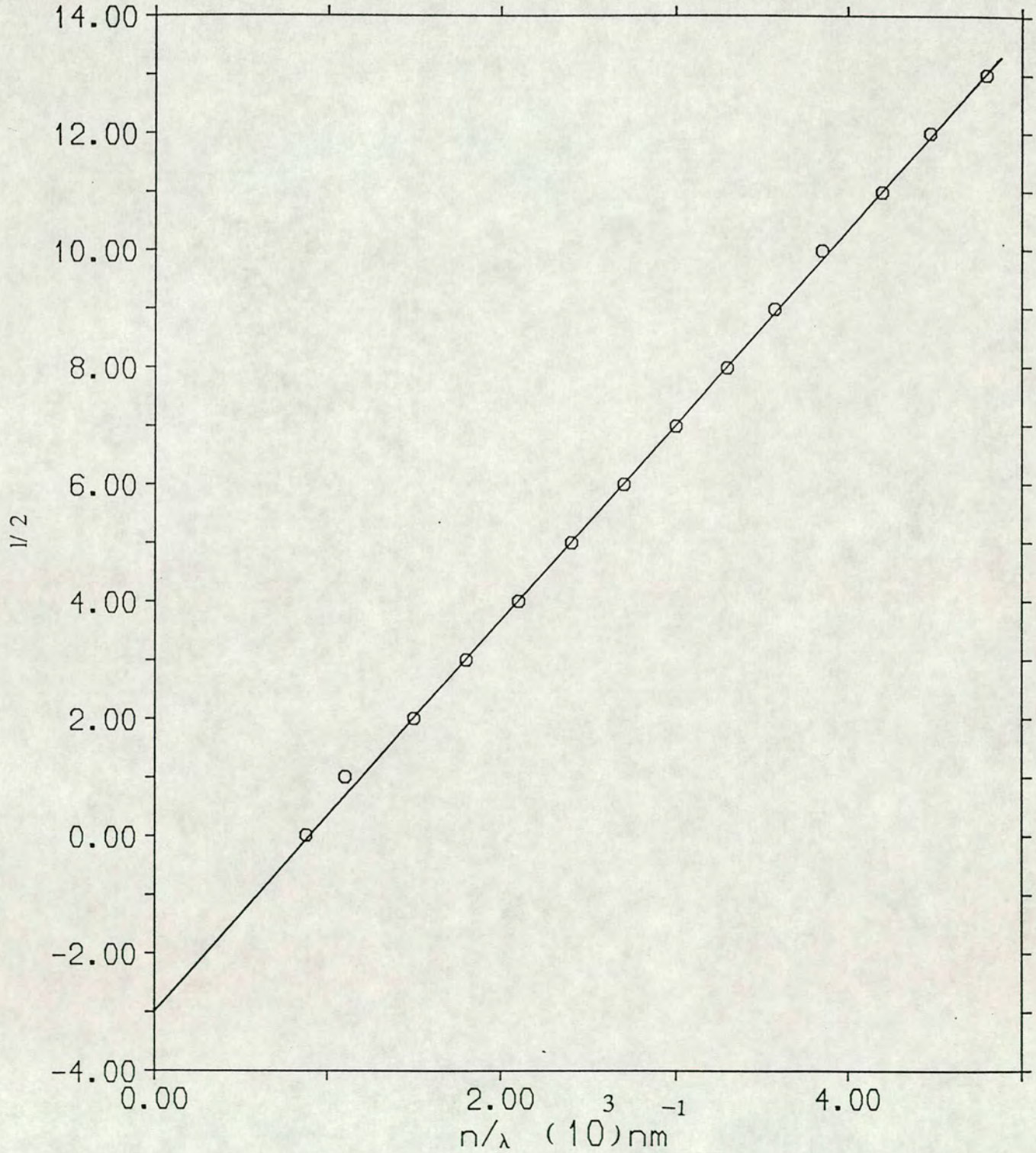

Fig. 4-5 The variation of l/2 versus n/λ (10^3) of a film of composition $As_{40}S_{60}$ and of thickness 1.71 μm. The thickness obtained from the slope of this line was 1.67 μm.

sensitivity and because it exhibits negligible photodarkening (see section 5-7). The $As_{30}S_{70}$ film thickness was approximately 5000 A for all samples but the thickness of the underlying Ag layer was different for each sample varying from 500 to 1500 A ; by varying the thickness of the Ag layer in this way it was possible to control the amount of Ag that photodissolved into the $As_{30}S_{70}$ film and hence the Ag concentration in the final photodoped material. The maximum possible Ag concentration is around 33 at. % for $As_{40}S_{60}$ (Janai 1981) but may vary with As-S composition.

Photodissolution was achieved by illuminating samples with a 200 W mercury lamp. To confirm that silver reached the top surface of the As-S layer, the etching properties of the final photodoped layer were checked. If silver had not reached the top surface of the As-S layer, the unreacted As-S layer could be removed by using the As-S etchant (described in section 7-4). The thickness of the exposed sample was, however, the same before and after etching, as checked by a mechanical stylus instrument. The transmission of the samples was measured as a function of wavelength and the refractive index was calculated from the interference fringes. Fig. 4-6 shows the resulting values of refractive index obtained over the wavelength range 500-2000 nm for undoped $As_{30}S_{70}$ and four photodoped samples containing various amounts of Ag. The curves are similar in shape but are displaced to higher values of n as the Ag content is increased. Single oscillator fits were obtained for each of the curves and extrapolation of these to longer wavelengths showed that for the most heavily doped sample $\Delta n > 0.5$ at 10.6 μm. Fig. 4-7 shows values of refractive index versus initial Ag layer thickness at three wavelengths (632.8 nm, 1.4 μm, and 10.6 μm). Measured values for the refractive index at 1.4 μm are included since future optical communication systems will probably operate around 1.3-1.6 μm to take advantage of the low loss and dispersion characteristics of optical fibers (Stewart et al. 1981). The data for 10.6 μm was obtained by extrapolating the single oscillator fits to the curves of Fig. 4-6.

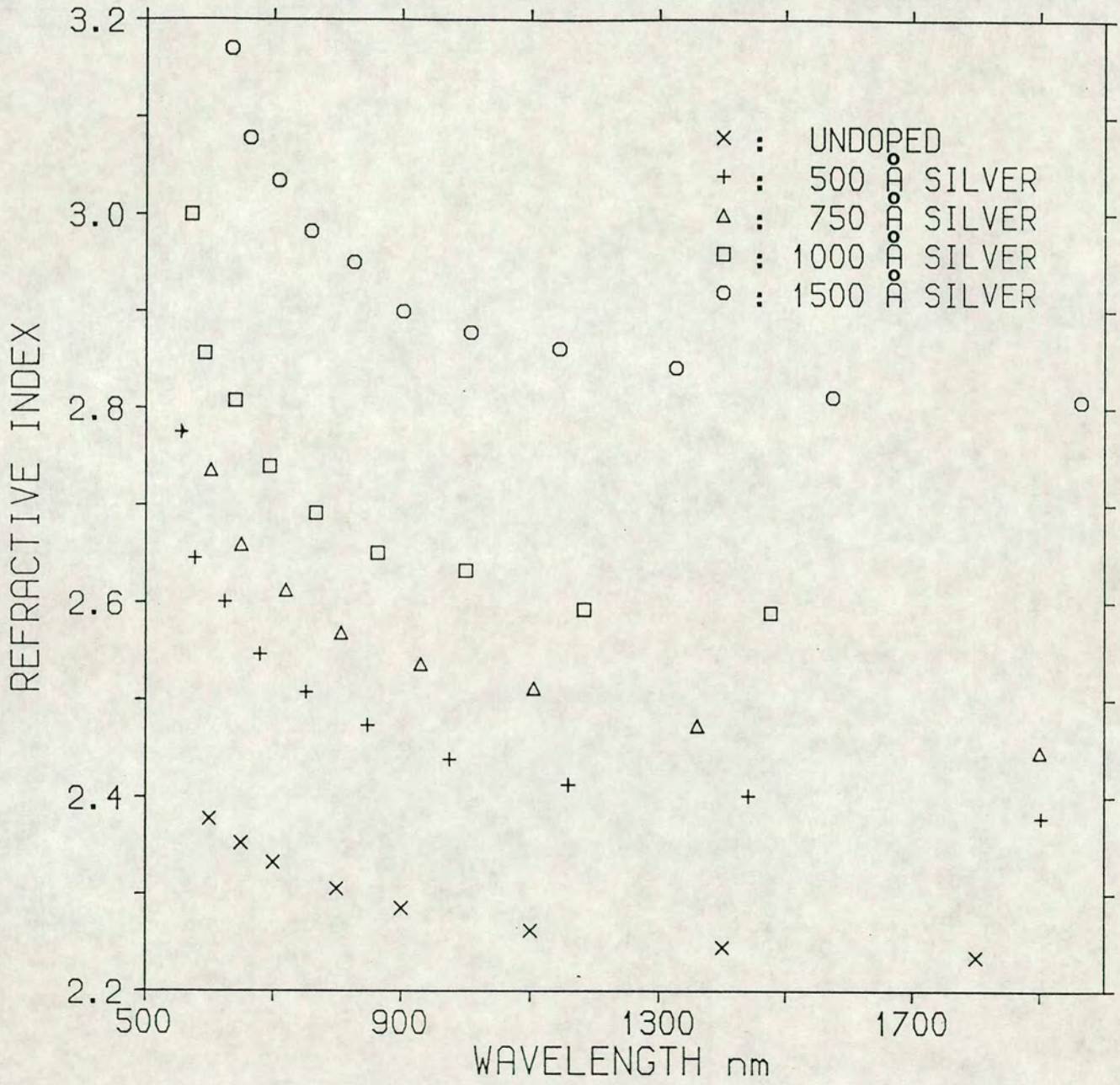

Fig. 4-6 Refractive index versus wavelength for 0.5 μm thick $As_{30}S_{70}$ films photodoped with various amounts of Ag. The thicknesses of the initial Ag layers are indicated in the figure.

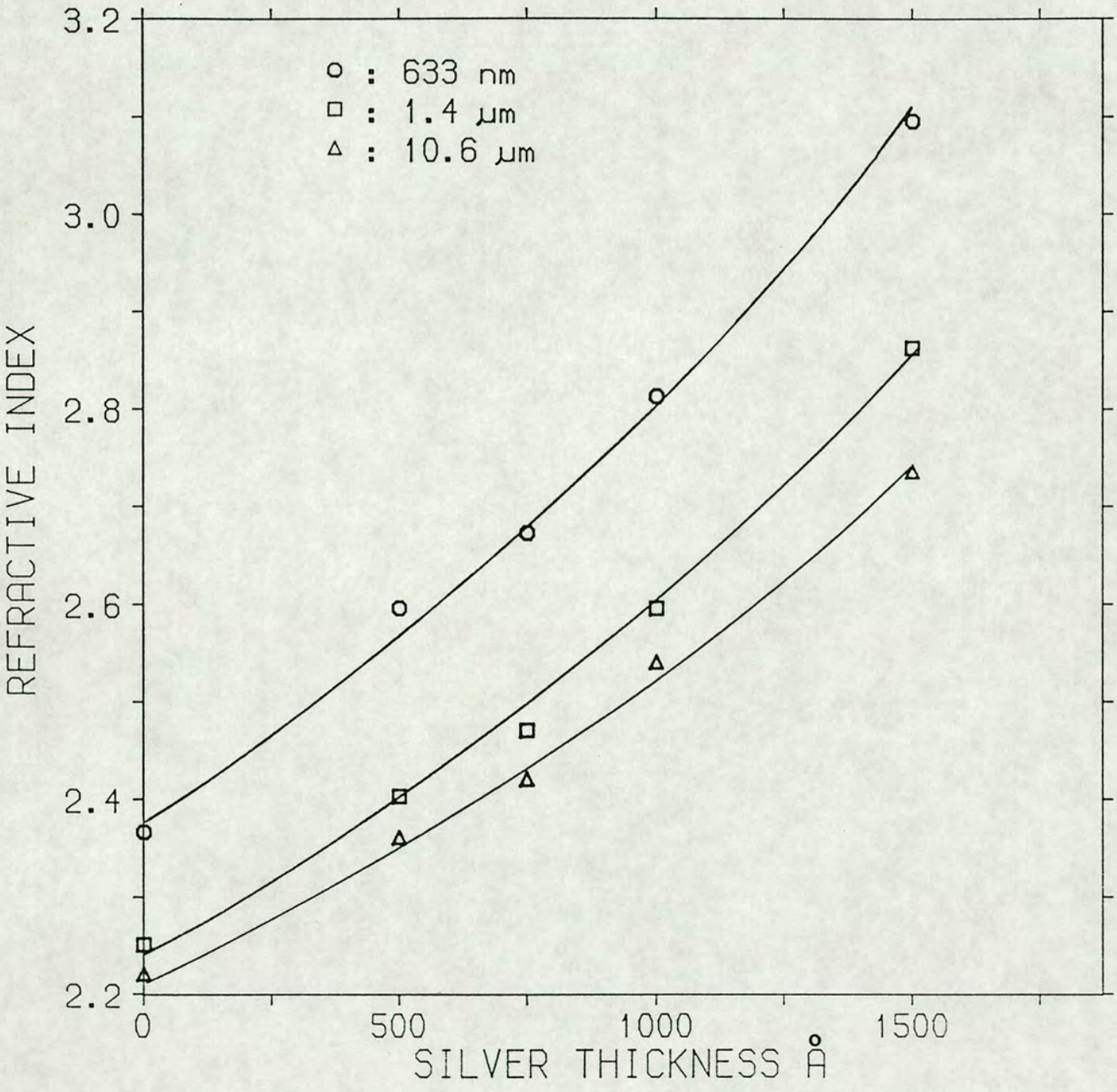

Fig. 4-7 Refractive index versus initial Ag layer thickness for photodoped $As_{30}S_{70}$ films at three wavelengths : 632.8 nm, 1.4 μm and 10.6 μm.(The data for 10.6 μm was obtained by extrapolating the single oscilator fits to the curves of Fig. 4-6).

4.2-3 Refractive index measurements of undoped $As_{40}S_{60}$ and photodoped $As_{40}S_{60}$ in the infrared

For the measurements of refractive index of undoped $As_{40}S_{60}$ in the IR a layer of $As_{40}S_{60}$ was deposited on a NaCl flat or on a float glass flat. The NaCl flat was used because of its good transmission in the near and far IR . Float glass flats on the other hand have good reflection properties in the near and far IR and hence were used for reflection measurements. The refractive index n was calculated using the interference fringes in the transmission and reflection spectra of the sample. For the measurement of refractive index of a photodoped $As_{40}S_{60}$ film in the IR, first a layer of $As_{40}S_{60}$ was deposited on a NaCl flat. A layer of Ag was then deposited on top. Because of the hygroscopic properties of NaCl flats, they were kept in a desiccator and the transmission measurements on the sample were carried out immediately after film deposition. The green line of an argon ion laser was used to photodope silver into the $As_{40}S_{60}$ film.

Fig. 4-8 shows the transmission spectra of both the undoped and photodoped $As_{40}S_{60}$ from the visible to the IR. Here $T_\alpha = \sqrt{T_M T_m}$ is plotted versus wavelength. The calculated values of refractive index are shown in Fig. 4-9 . The error bar shows the uncertainty in refractive index measurements. For these IR measurements, the contribution from $\Delta\lambda/\lambda$ needs to be taken into account since $\Delta\lambda/\lambda$ or correspondingly $\Delta k/k$ where k is the wave number is typically 10/1000 or 1 % .

4.3 Absorption coefficient measurements in the visible

4.3-1 Theoretical results for transmission through a film

The absorption coefficient, α, of the films was calculated from their transmission spectra. As mentioned in the introduction, these calculations were based on a method outlined by Goldschmidt. In this method the reflection losses at the film-air and film-substrate interfaces were taken into account. For the analysis, the refractive indices of the film and substrate were required and the values obtained in the previous sections were

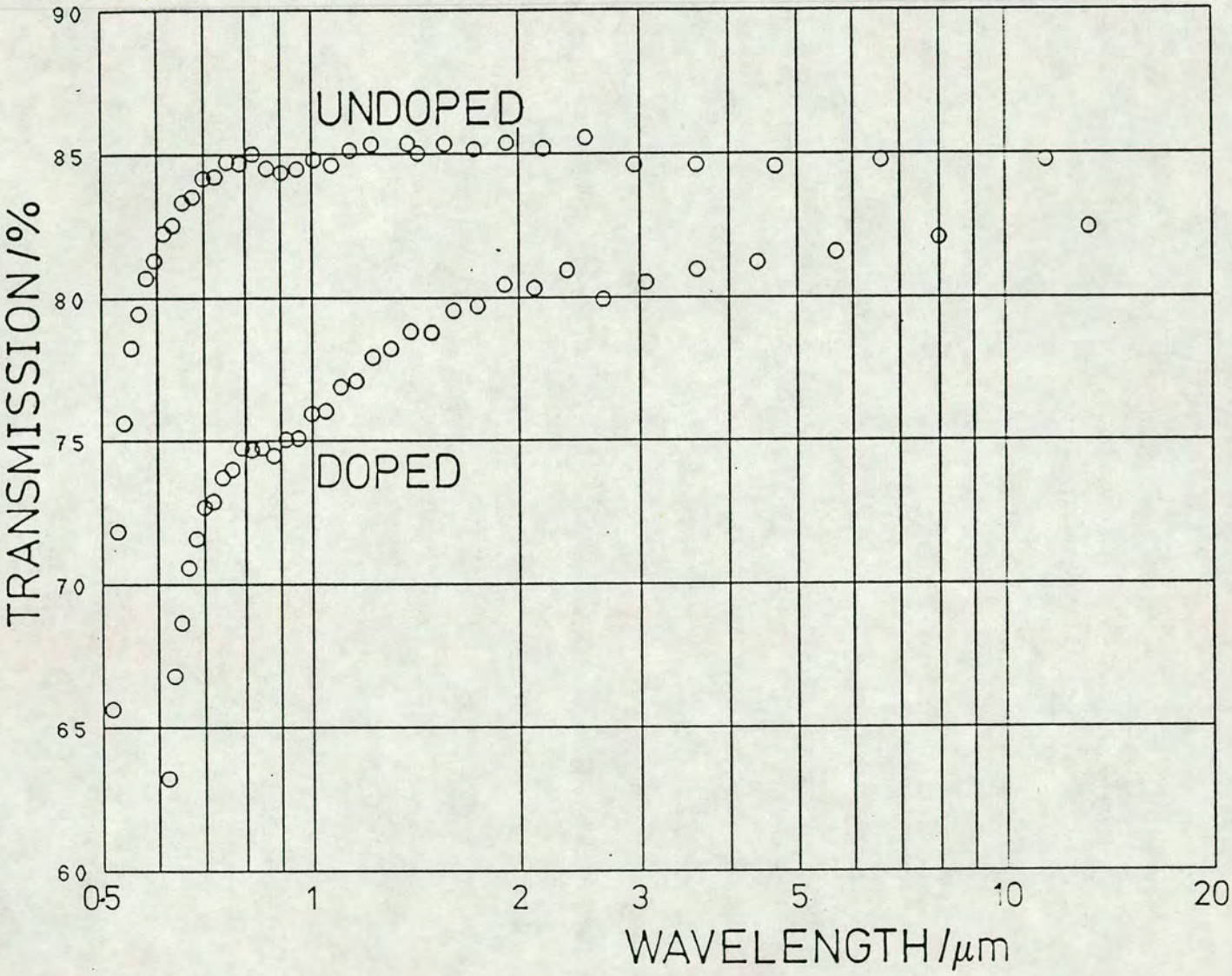

Fig. 4-8 Transmission (T_α) versus wavelength for an undoped and Ag photodoped $As_{40}S_{60}$ film. The thickness of the photodoped and undoped films were approximately the same, being 1.77 and 1.7 μm respectively; for the photodoped sample, the initial thicknesses of the Ag and $As_{40}S_{60}$ film were 0.17 and 1.6 μm respectively.

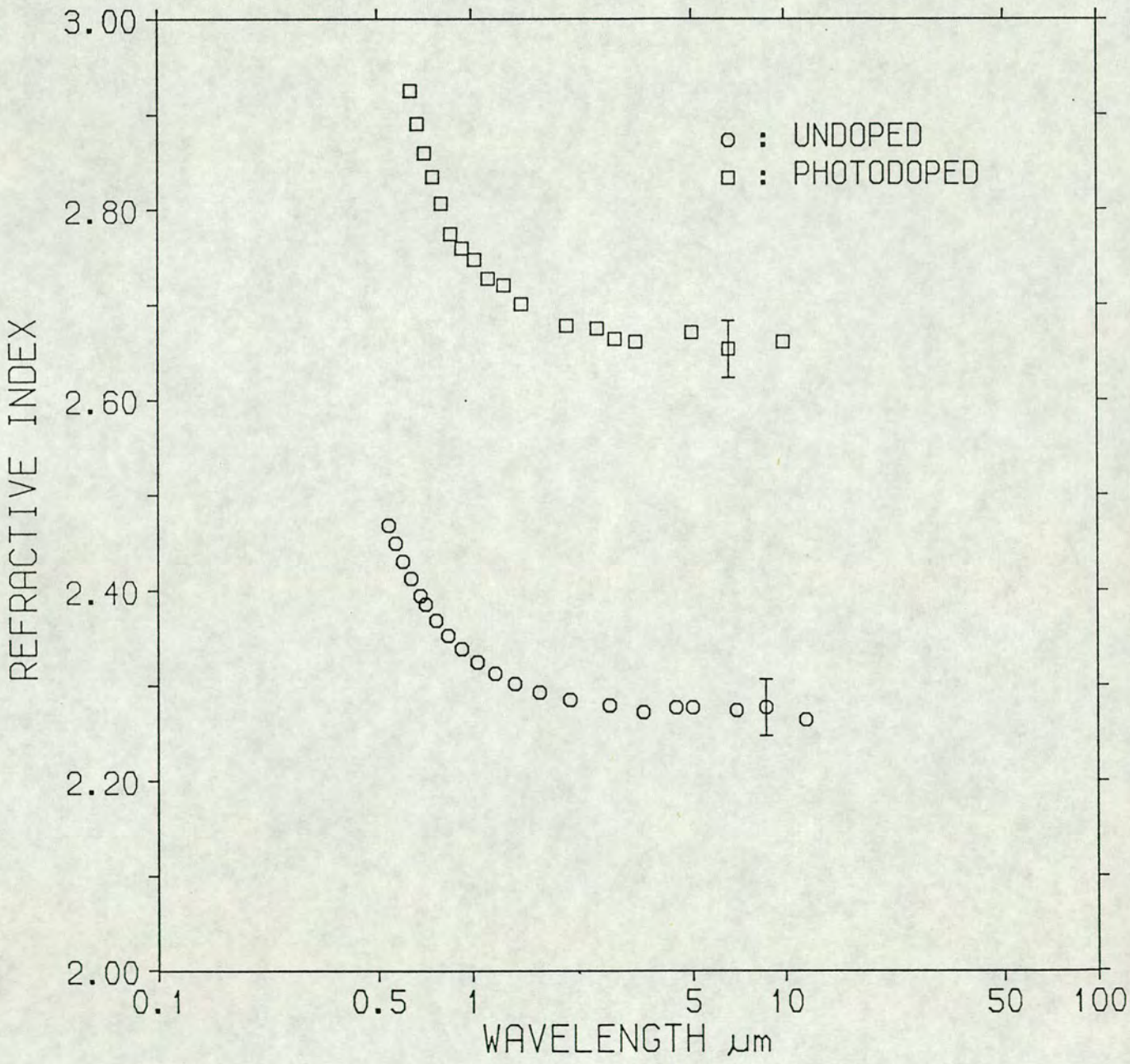

Fig. 4-9 Refractive index versus wavelength for undoped and Ag photodoped $As_{40}S_{60}$. As for Fig. 4-8 the initial Ag and $As_{40}S_{60}$ film thicknesses being 0.17 and 1.6 μm respectively.

used for this purpose. An undoped $As_{30}S_{70}$ film and four $As_{30}S_{70}$ films photodoped with different silver concentrations were used in these calculations. This method considers a plane-parallel absorbing thin layer (medium 1) deposited onto a thick transparent substrate (medium 2), medium 0 being air. The first step is to determine the air-to-substrate transmission and reflection coefficients by using coherent ray tracing and assuming a semi-infinite substrate. Then the finite thickness of the substrate is treated by summing over the incoherent rays, which are transmitted from the film into the substrate, where they are multiply reflected. One obtains the intensity transmission (T_{AS}) and reflection (R_{AS}, R_{SA}) coefficients :

$$T_{AS} = \frac{(1+\frac{K^2}{n^2})(1-R_{01})(1-R_{12})exp(-\alpha d)}{1-2(R_{01}R_{12}exp(-\alpha d)cos(2kd))+R_{01}R_{12}exp(-2\alpha d)} \qquad (12)$$

$$R_{AS} = \frac{R_{01}-2(R_{01}R_{12})^{1/2}exp(-\alpha d)cos(2kd)+R_{12}exp(-2\alpha d)}{1-2(R_{01}R_{12})^{1/2}exp(-\alpha d)cos(2kd)+R_{01}R_{12}exp(-2\alpha d)} \qquad (13)$$

$$R_{SA} = \frac{R_{12}-2(R_{12}R_{01})^{1/2}exp(-\alpha d)cos(2kd)+R_{01}exp(-2\alpha d)}{1-2(R_{12}R_{01})^{1/2}exp(-\alpha d)cos(2kd)+R_{12}R_{01}exp(-2\alpha d)} \qquad (14)$$

where:

$$R_{ij} = (\frac{n_i - n_j}{n_i + n_j})^2$$

and $i, j = 0,1,2$.

Here the first subscript denotes the medium from which the beam is coming and the second denotes the medium to which it is transmitted or reflected. (A stands for air and S for substrate); α is the absorption coefficient, $K = \alpha\lambda/4\pi$ is the extinction coefficient, n is the refractive index, d is the thickness, λ is the vacuum wavelength and $k = 2\pi n/\lambda$ is the wave number. The equations are similar to those given by Stratton (1941) and by Hall and

Ferguson (1955). The minus in front of the oscillating term reflects the assumption that $n_{film} > n_{substrate} > n_{air}$.

In the second step, which is treated incoherently, the approach by Connell and Lewis (1973) was used to sum over the multiple incoherent reflections in the substrate. Using their results and substituting from Eqns. 12-14 one obtains :

$$T = \frac{T_{AS}(1-R_{20})}{1-R_{20}R_{SA}}$$

or :

$$T = \frac{(1+\frac{K^2}{n^2})(1-R_{01})(1-R_{12})(1-R_{20})exp(-\alpha d)}{(1-R_{12}R_{20})-2(R_{01}R_{12})^{1/2}(1-R_{20})exp(-\alpha d)cos(2kd)+R_{01}(R_{12}-R_{20})exp(-2\alpha d)} \quad (15)$$

4.3-2 Determination of the absorption edge

There exist a few points on the transmission curve that deserve particular attention because of the relative ease with which they can be used to determine α. The first two points are at the maximum and the minimum of the interference fringes as obtained by letting $cos(2kd) = \pm 1$ in Eqn. (15). Thus:

$$T_{max,min} = \frac{(1-R_{01})(1-R_{12})(1-R_{20})exp(-\alpha d)}{(1-R_{12}R_{20}) \mp 2(R_{01}R_{12})^{1/2}(1-R_{20})exp(-\alpha d)+R_{01}(R_{12}-R_{20})exp(-2\alpha d)} \quad (16)$$

The $-$ and $+$ in the denominator yield T_{max} and T_{min} respectively. The wavelengths corresponding to T_{max} and T_{min} and the value of the transmission are determined quite accurately from the transmission curve, and thus a dense array of data points is obtained for the absorption spectrum. It should be mentioned that the sensitivity of α to errors in the transmission is much higher for T_{min} than for T_{max} because of the different sign in the denominator of Eqn. 16 ; T_{max} reflects roughly the sum of the

intensities of the interfering beams, whereas T_{min} reflects their difference. Hence the values of T_{max} were used to calculate the absorption coefficient of the films. The results of the absorption coefficient measurements are shown in Fig. 4-10 . Although the increase in the absorption due to photodoping with silver is significant in the visible region, in the near-IR and far-IR part of the spectrum the absorption coefficient is small and remains so. Detailed measurements of absorption coefficient in the IR requires thick samples, since the absorption coefficient of As_{40} S_{60} is so small in the IR that only a significant change in thickness can show an appreciable change in the transmittance. Young (1970) quotes a value of < 1 cm^{-1} in the wavelength range from 2-10 μm.

4.4 Optical gap measurements

Band theory for crystalline semiconductors suggests that the absorption coefficient α for indirect transitions can be written as :

$$\alpha = const.M^2 \frac{(h\nu - E_g)^2}{h\nu} \qquad (17)$$

where M is the matrix element of the electrical transition. With the assumption of parabolic bands the absorption in many amorphous semiconductors is observed to obey this relation above the exponential edge (Mott and Davis 1979). If M is constant, plotting $(\alpha h\nu)^{1/2}$ versus $h\nu$ should result in a straight line. The optical gap is obtained from the intersection of this line with the energy axis. Fig. 4-11 shows plots of $(\alpha h\nu)^{1/2}$ versus $h\nu$ for the data of Fig. 4-10.

The change in the optical gap of the $As_{30}S_{70}$ film with incorporation of silver into the film is shown in the inset in Fig. 4-11. Also, in the inset the corresponding results for the composition $As_{40}S_{60}$ obtained by Shimizu (1978) is shown. The gap changes from a value of 2.5 eV for undoped $As_{30}S_{70}$ to a value of 1.9 eV for the most heavily Ag doped $As_{30}S_{70}$ and appears to approach a saturation value for high concentrations of Ag. This is

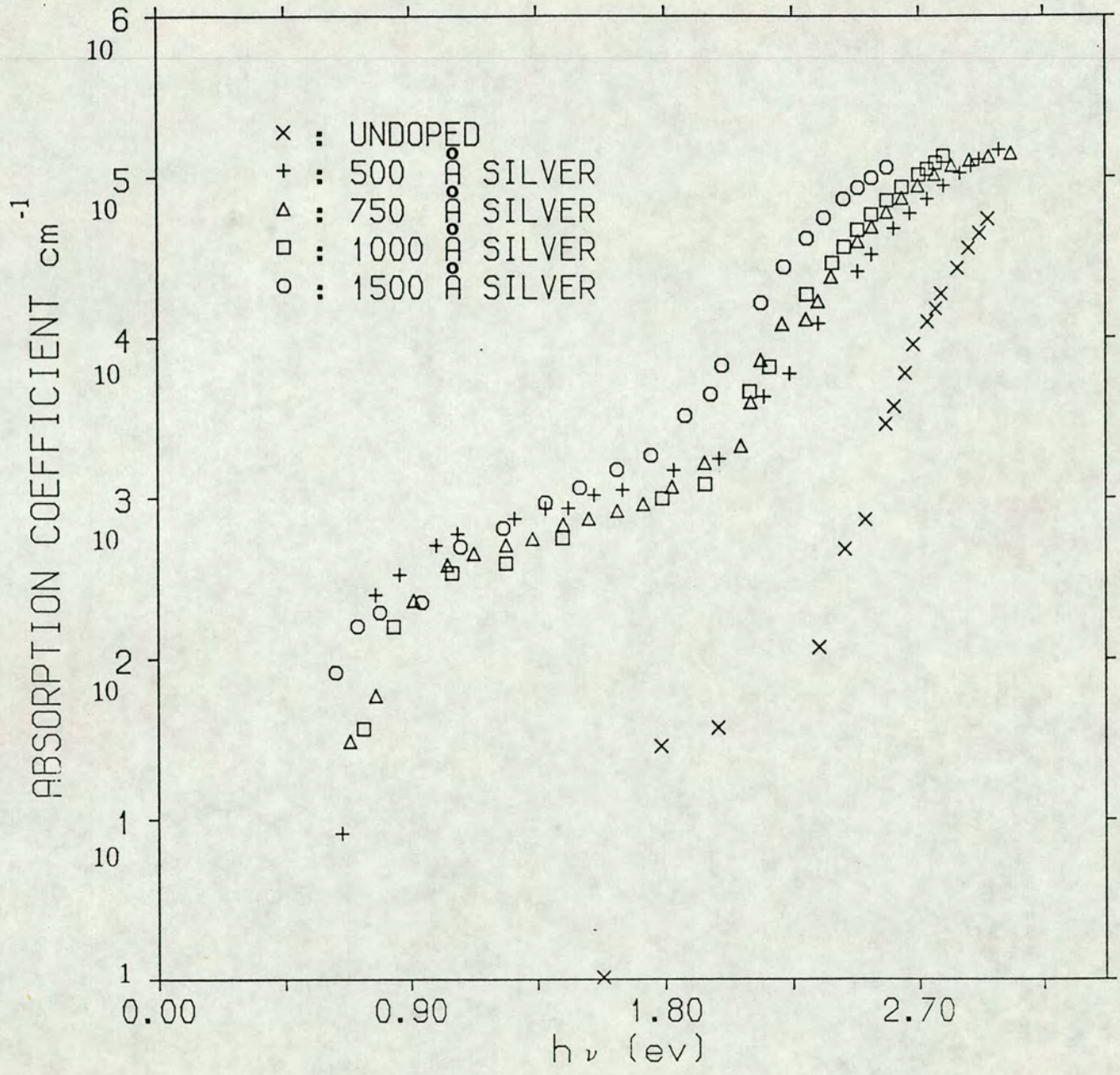

Fig. 4-10 Absorption coefficient versus photon energy for $As_{30}S_{70}$ films photodoped with various amounts of Ag. The thicknesses of the initial Ag layers are indicated in the figure.

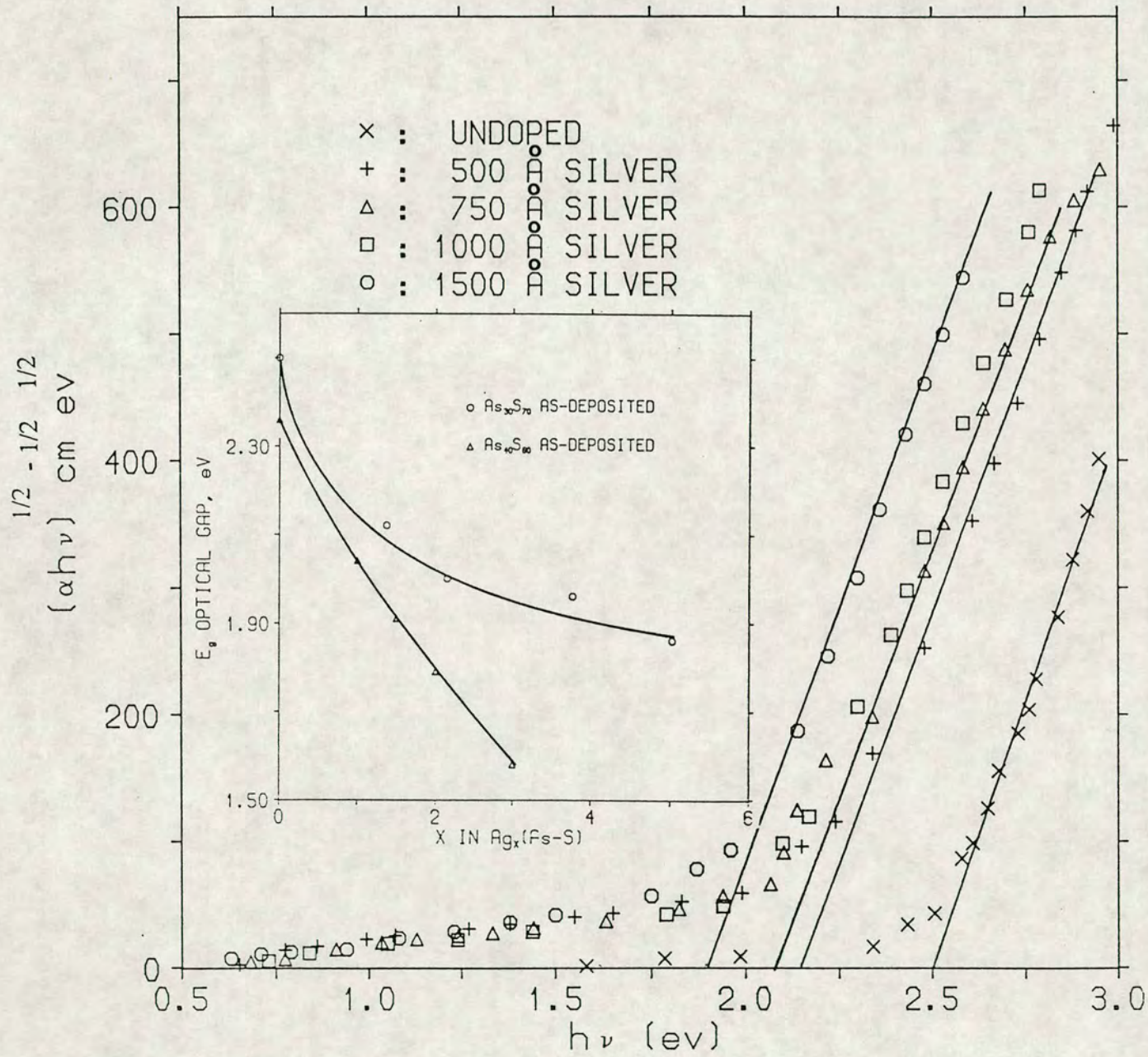

Fig. 4-11 $(\alpha h\nu)^{1/2}$ versus photon energy for $As_{30}S_{70}$ films photodoped with various amounts of Ag. The optical gap, E_g, obtained by extrapolation of the linear parts of these curves is plotted as a function of Ag concentration in the inset.

probably indicative of a difference in the structure of photodoped $As_{30}S_{70}$ and $As_{40}S_{60}$. The decrease in the optical gap E_g with the incorporation of Ag arises from the smaller binding energy of Ag-S bonds compared with that of As-S bonds. Photodoped silver behaves as a structure modifier in these chalcogenide glasses. The optical gap for the undoped $As_{30}S_{70}$ film (2.5 eV) is in reasonable agreement with that for the bulk glass (2.4 eV) (Mott and Davis 1971). The optical gaps for the crystals proustite (Ag_3AsS_3) and smithite ($AgAsS_2$) are approximately 2 and 2.1 eV respectively (Shauren et al. 1986 and Golovach et al. 1975). These values are similar to the values which were obtained for the optical gap of the silver rich photodoped $As_{30}S_{70}$ films in this work.

4.5 Summary

Photodoping with silver affects all the physical and chemical properties of the As-S chalcogenide films, particularly their electronic and optical properties. It is possible to control the properties of the photodoped layer simply by varying the amount of metal available for dissolution. Both the refractive index and optical gap vary in a smooth fashion with Ag content. Modulations in refractive index as high as 0.5 or more can be achieved over the whole wavelength range from the visible up to the far-IR. Also, changes of > 0.6 eV in the optical gap can be achieved. Although the introduction of Ag increases the absorption coefficient in the visible region, in the near IR and far IR part of the spectrum, α remains small. Chalcogenide glasses are one of the few low loss materials for the fabrication of transmissive devices in the near- and far-IR.

Arsenic sulphide glasses may also have applications in the interconnection of optical devices in integrated optics because of the low loss property of arsenic sulphide films and their ease of preparation. They are also low temperature materials with a melting point of ($\sim$ 300 °C), so avoiding thermal damage to the underlying waveguide during film deposition.

4.6 References

Andreichin, R.E., Getov, G.K., and Simidchieva, P.A., 1966, Sov. Phys., Solid State, 8, p. 1546.

Andriesh, A.M., Ponomar, V.V., Smirnov, V.L., and Mironos, A.V., 1986, Sov. J. Quantum Electron., 16(6), p. 721.

Cimpl, Z., and Kosek, F., 1987, J. Non Crystalline Solids, 90, p. 577.

Connell, G.A.N., and Lewis, A., 1973, Phys. Status Solidi, B 60, p. 291.

Goldschmidt, D., 1984, J. Opt. Soc. Am., A, 1(3), p. 275.

Golovach, I.I., Slivka, V.Y., Dovgoshei, N.I., Syrbu, N.N., Bogdanova, A.V., and Golovei, M.I., 1975, Sov. Phys. Semicond., 9, p. 834.

Hall jr., J.F., and Ferguson, W.F.C., 1955, J. Opt. Soc. Am., 45, p. 714.

Hammam, M., Abdel Harith, M., and Osman, W.H., 1986, Solid State Comm., 5(59), p. 271.

Hulme, K.F., Jones, O., Davies, P.H., and Hobden, M.V., 1967, Appl. Phys. Lett., 10, p. 133.

Janai, M., 1981, Phys. Rev. Lett., 47, p. 726.

Kosek, F., and Tauc, 1970, J., Czech. J. Phys., B20, p. 94.

Mott, N.F., and Davis, E.A., 1971, "Electronic Processes in Non-Crystalline Materials", 1st edition (Oxford: Clarendon), pp. 334-335.

Mott, N.F., and Davis, E.A., 1979, "Electronic Processes in Non-Crystalline Materials", 2nd edition (Oxford: Clarendon), p. 289.

Savage, J.A., 1985, "IR Optical Materials and their Antireflection Coatings" (Adam Higler, Bristol), p. 79.

Shauren, J., and Taylor, K.N.R., 1986, Sov. Phys. Solid State, 28, p. 1459.

Shimizu, I., Ikeda, T., and Inoue, E., 1978, preprint Int. Congress Photogr. Sci., Rochester, New York, p. 235.

Stewart, G., Hutchins, R.H., and Laybourn, P.J.R., 1981, J. Phys. D : Appl. Phys., 14, p. 323.

Stratton, J.A., 1941, "Electromagnetic Theory", (McGraw- Hill, New York), p. 513.

Swanepoel, R., 1983, J. Phys. E : Sci. Instrum., 16, p. 214.

Tanaka, Ke., and Ohtsuka, Y., 1979, Thin Solid Films, 57, p. 59

Wehmeier, F.H., Laudise, R.A., and Shiever, J.W., 1968, Mat. Res. Bull., 3, p. 767.

Young, P.A., 1971, J. Phys. C, 4, p. 93.

5. KINETICS MEASUREMENTS

5.1 Introduction

The metal photodissolution effect is one of the most important of the various photoinduced phenomena that occur in chalcogenide glasses. It is currently of interest because of its potential applications in holography (Bordogna and Keneman 1977) and VLSI lithography (Tai, Ong and Vadimsky 1982). A knowledge of the kinetics of the effect is required not only for understanding the basic mechanism but also for exploiting its technological applications.

In order to produce a usable image in the glass film, it is necessary to know how the process depends on time and also how this dependence is influenced by the wavelength and intensity of the exposing light. Various techniques have been used to study the kinetics of photodissolution, including X-ray diffraction (Rennie and Elliot 1985, Wagner,Frumar and Benes 1987), optical transmission (Matsuda and Kikuchi 1973, Kawaguchi, Maruno and Masui 1987) and electrical resistance measurements (Goldschmidt and Rudman 1976, Yaji and Kurita 1983, Konan, Galibert and Calas 1988, Plocharski, Przyluski and Teodorczyk 1987).

In the present study a technique involving simultaneous transmissivity and reflectivity measurements has been used to examine how the photodissolution kinetics are affected by the composition of the chalcogenide glass, and the wavelength and intensity of illumination. The photodissolution of Ag into As-S films is one of the most widely investigated examples of the effect, the majority of these studies being concerned with the stoichiometric composition As_2S_3. It has been suggested (Ewen, Zakery, Firth and Owen 1988) however, that As_2S_3 may not be the optimum composition as far as technological applications are concerned, so there is a need to investigate other compositions in this system.

At least seven distinct photoinduced effects, including photodissolution, have been reported in chalcogenide glasses (Owen, Firth and Ewen 1985). Since it is possible that some of these other effects may occur simultaneously with, and influence, photodissolution during exposure, they have also been investigated.

5.2 Experimental arrangement

A schematic diagram of the experimental set up which is used to perform the reflectivity and transmissivity measurements is shown in Fig. 5-1. Monochromatic illumination from an Ar ion laser is focussed onto the sample via a mirror and a series of attenuating filters. A prism filter was used to remove the plasma lines from the laser beam and so avoid their effect on the photodissolution process.

By using a glass slide as shown in the figure both reflectivity and transmissivity measurements can be made simultaneously. The reflected beam is directed onto an eye-response silicon photodiode and the current output from this was fed to an I-V convertor which had a linear response as shown in Fig. 5-2. The voltage output of the I-V convertor was then fed to the input of a Keithley Electrometer. For the transmissivity measurements, the transmitted light intensity was measured using a second I-V convertor and electrometer combination.

It was observed during the preliminary measurements that the exact position of peaks and valleys on the plotted reflectivity curve could not be easily detected by eye, so it was decided to automate the measurements using a BBC microcomputer-controlled system. The Analog-to-Digital (A-D) conversion facilities of the BBC microcomputer enabled the data to be collected via continuous time measurement software. One of the requirements of A-D conversion was that the input voltage signal to the microcomputer should have been between 0 and 1.8 V and this was achieved using the electrometer, which adjusted the output voltage of the I-V convertor to be between these limits. Software for controlling a

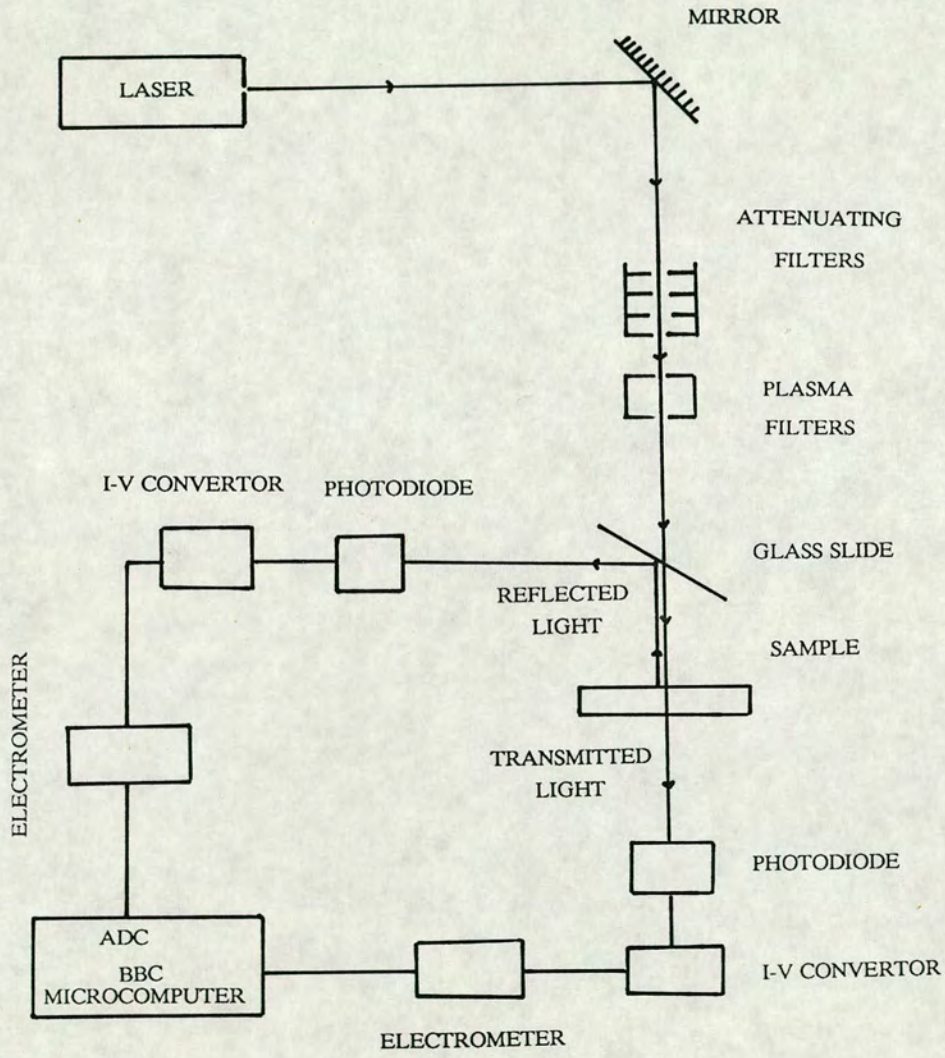

Fig. 5-1 Schematic diagram of reflectivity and transmissivity measurements.

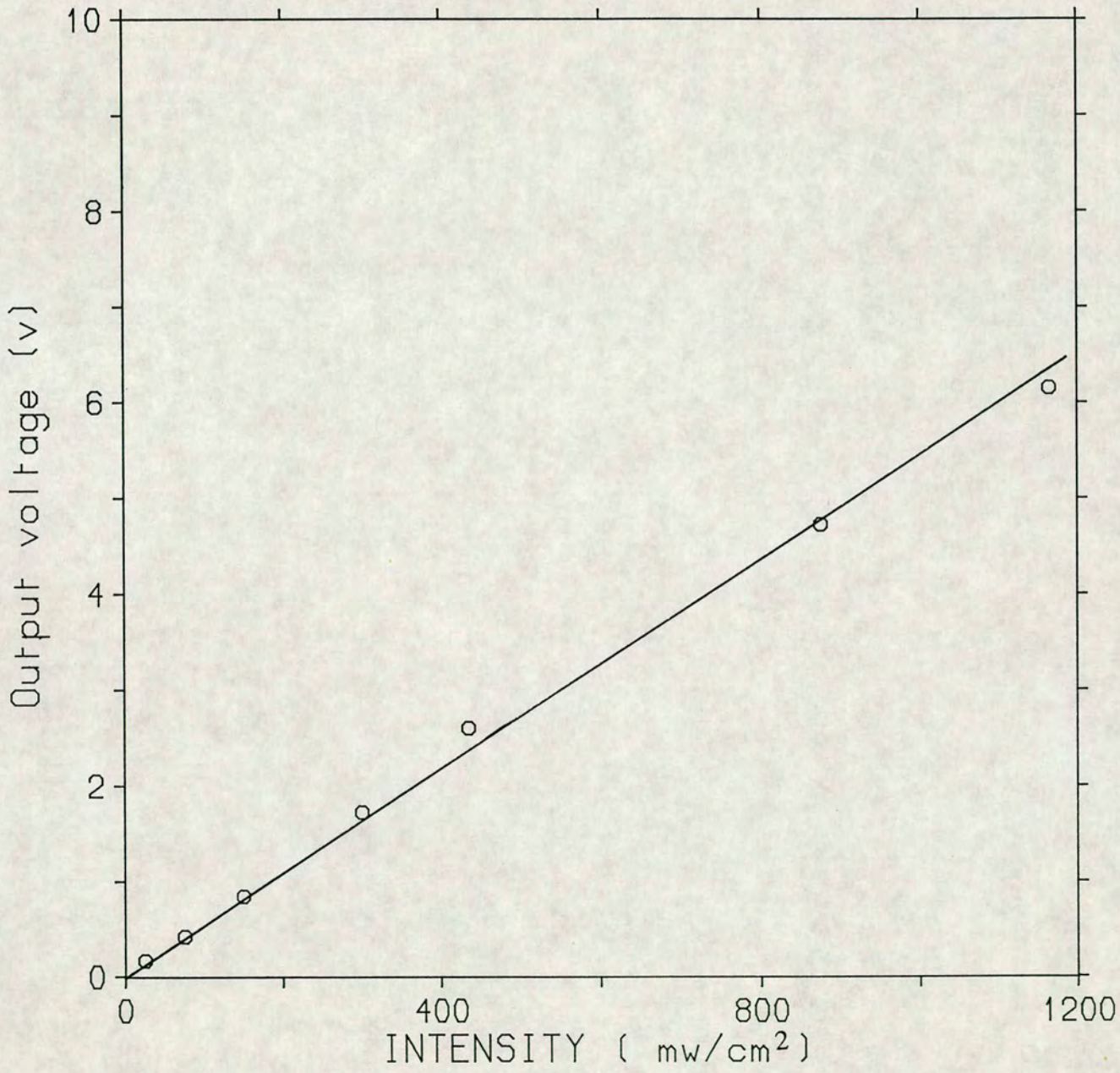

Fig. 5-2 I-V convertor response versus the illumination intensity at 514.5 nm. The full line is a guide for the eye.

continuous time measurement was provided by Dr. C. Adie (EUCS) and modified according to the special needs of these particular experiments.

The technique used to measure the photodissolution rate is based on the fact that the reflectivity of a thin, weakly absorbing film varies periodically with its thickness due to interference between light reflected from the top and bottom surfaces of the film. Fig. 5-3 shows a schematic cross-section through a sample during the photodissolution process. If there is a well defined interface between the doped and undoped regions of the film and the doped region is highly absorbing, then as the photodoped layer expands towards the top surface of the film, reflectivity changes will be observed due to the decreasing thickness of the undoped layer. Typical plots of reflectivity as a function of exposure time during this process are shown in Fig. 5-4 . As photodissolution starts, the reflectivity of the composite layers goes through a series of maxima and minima. The reflectivity is initially that of the As-S film above a silver layer. For calibration purposes, a thick, freshly deposited aluminium film was used instead of silver because the optical properties of aluminium are relatively constant with time whereas a silver film oxidises fairly quickly in atmospheric conditions. The time between successive maxima or minima in the reflectivity curve corresponds to the time required for the thickness of the undoped layer to decrease by $\lambda/2n$, where λ is the wavelength of the light and n the refractive index of the As-S film. At the end of the photodissolution process, the undoped layer thickness is zero provided the initial Ag film is sufficiently thick (Kolwicz and Chang 1980) so the maxima and minima occur when the As-S layer thickness is an integer multiple of $\lambda/4n$, this integer being 1 for the last minimum, 2 for the last maximum, and so on. By noting the times corresponding to the maxima and minima it is thus possible to determine how the thickness of the photodoped layer varies with time.

As mentioned above reflectivity measurements probe the changes in the thickness of the As-S layer during photodissolution. Transmissivity measurements on the other hand mainly probe changes that occur in the thickness of the silver layer during the photodissolution process. A typical transmissivity curve is also shown in Fig. 5-4a . The

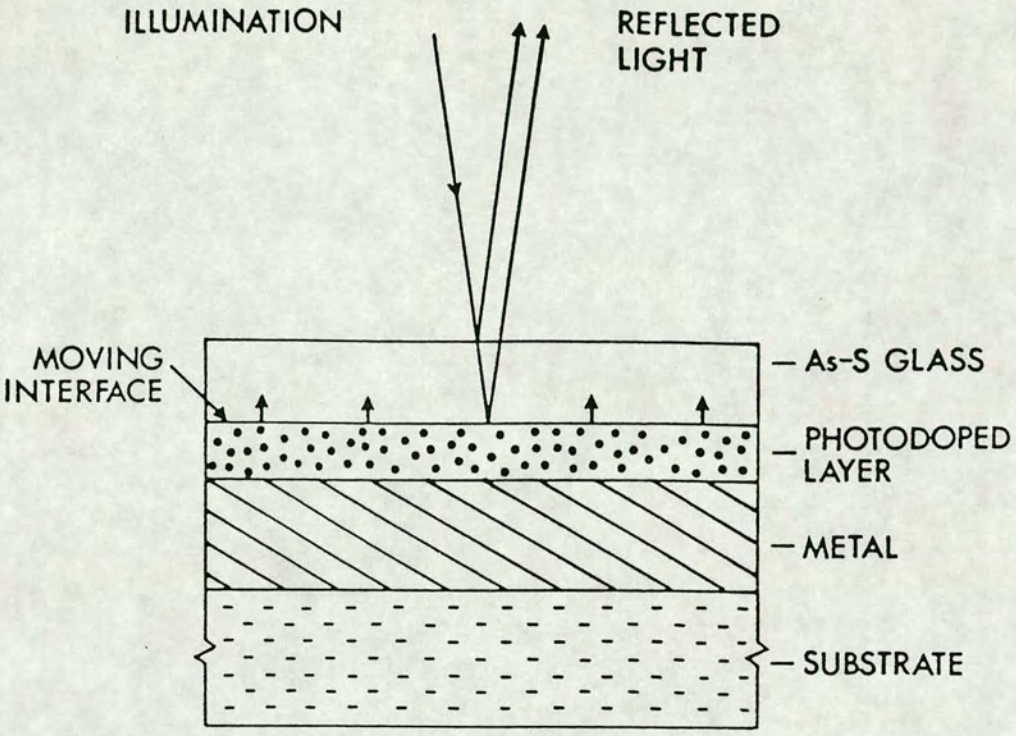

Fig. 5-3 A schematic cross-section through a sample during the photodissolution process.

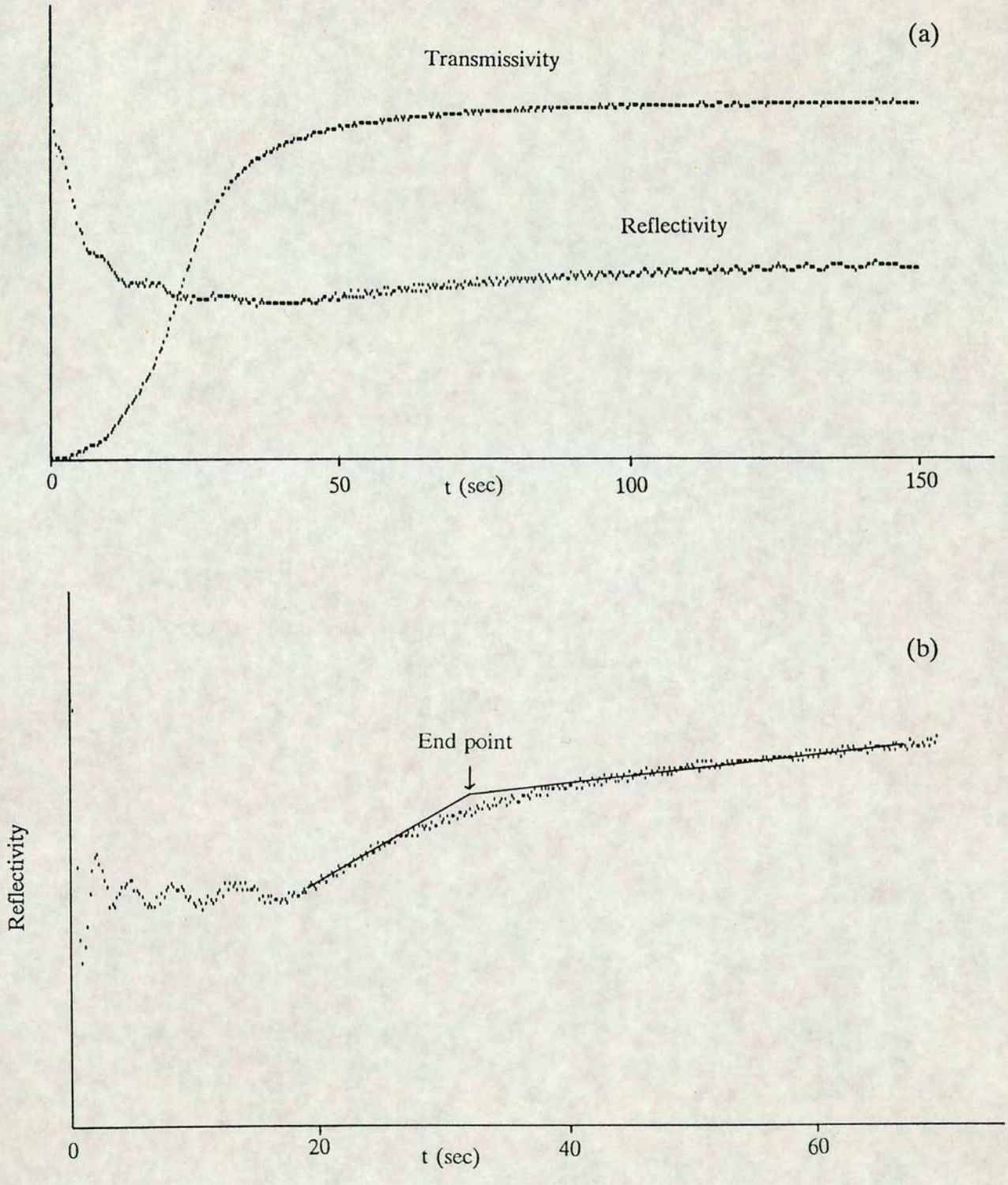

Fig. 5-4 a: A typical reflectivity and transmissivity versus time at 514.5 nm in a composition $As_{35}S_{65}$. Illumination intensity was 200 mW/cm^2.

b: A typical reflectivity versus time at 488 nm in a composition $As_{35}S_{65}$. Illumination intensity was 200 mW/cm^2.

transmissivity of the composite layers goes through three stages: initially the transmissivity is very small because a thick absorbing silver layer is present but as the silver layer thickness decreases the transmissivity increases; the second stage in the transmissivity curve is almost linear and can be used to determine the photodissolution rate; in the third stage the transmissivity increases very slowly towards saturation.

5.3 Time dependence of the photodissolution process

In order to use the metal photodissolution effect for technological applications, it is necessary to have a knowledge of how the photodoped front propagates with time. This information can enable one to assess the suitability of the process for various possible applications as regards time and hence the cost of device fabrication. These measurements will also provide information on the basic mechanism of the metal photodissolution effect. In the present experiments, samples were prepared by evaporating onto a cleaned glass substrate first a layer of Ag and then a layer of the desired As-S composition, there being no break in the vacuum between evaporations. Reflectivity data was analysed to determine the variation of As-S layer thickness with time. Figs. 5-5 and 5-6 show typical plots of the photodissolution time dependence, the data being plotted versus both the square root of time (Fig. 5-5) and time (Fig. 5-6). In both cases, the photodissolution has an essentially linear response at the beginning and then goes to saturation at longer times. This is characteristic of a photochemical solid state reaction, which has an S-shaped kinetics curve. The photodissolution rate will be small initially (possibly due to an induction period), it then becomes constant and finally it goes to saturation at longer times. The reason that we do not observe the beginning of the reaction is possibly due to the high intensities used in the present measurements, since the induction period depends inversely on the illumination intensity (Goldschmidt and Rudman 1976). By finding the $t=0$ intercept of the plot in Fig.5-5 a value of $\sim$ 5400 A is obtained for the initial As-S film thickness, which is larger than the measured value (4000 A). This implies that photodissolution must have had a slower rate at the beginning, although it is difficult to detect it directly from the reflectivity

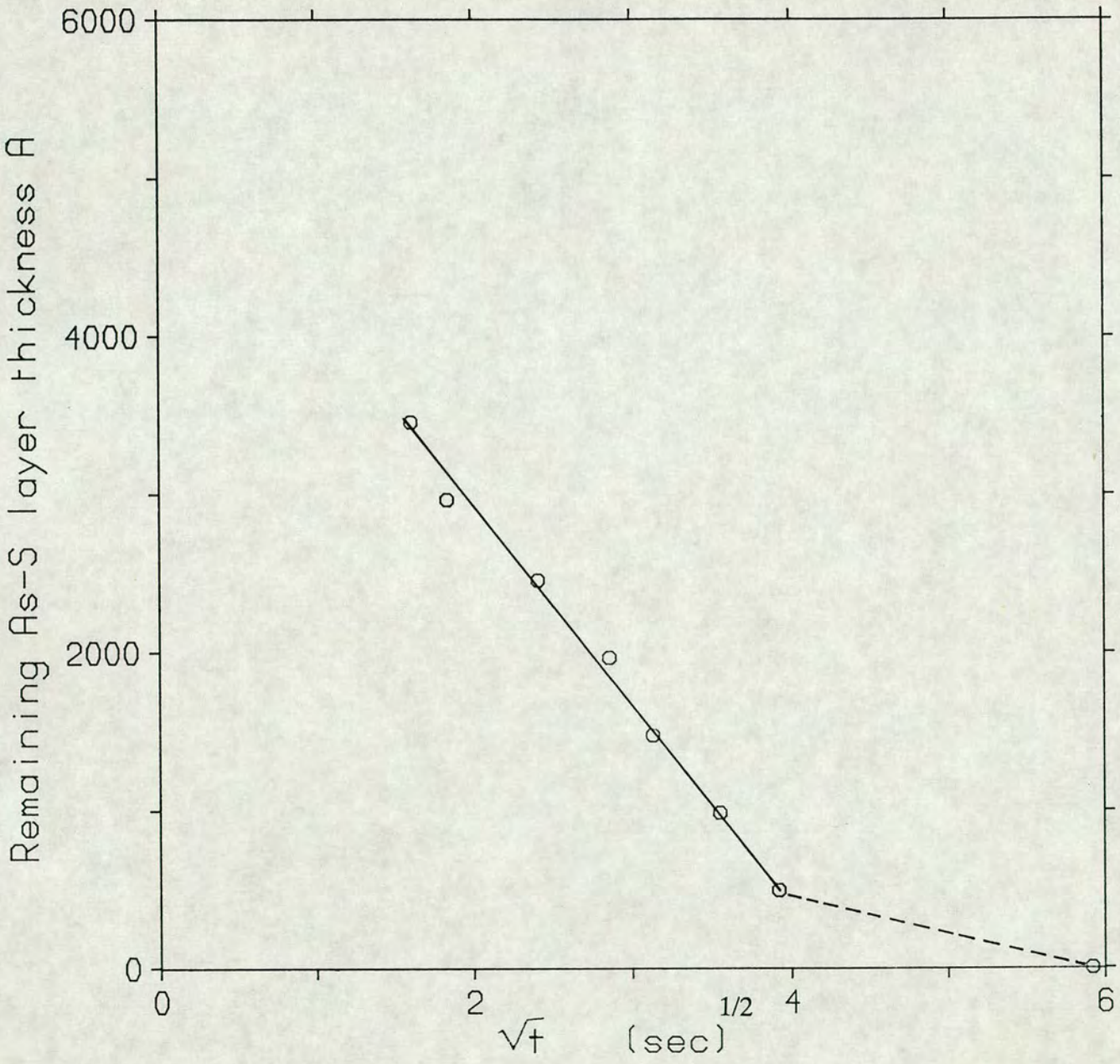

Fig. 5-5 $As_{33}S_{67}$ layer thickness versus the square root of exposure time. The full and dashed lines are guides for the eye. The full line was used to determine the photodissolution rate.

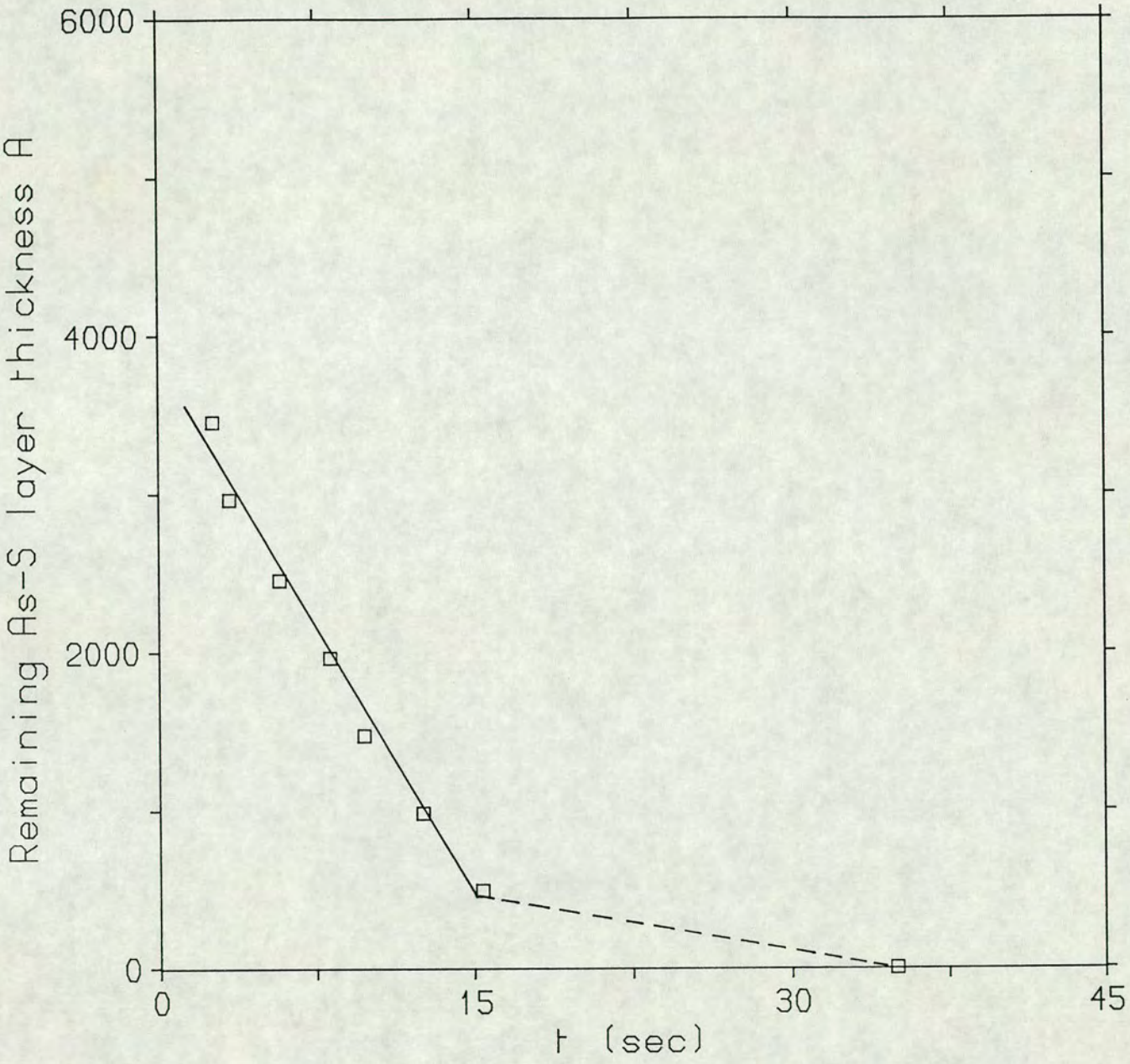

Fig. 5-6 $As_{33}S_{67}$ layer thickness versus exposure time. The lines are guides for the eye. The full line was used to determine the photodissolution rate.

measurements. A linear regression procedure was used to find the slope of the linear part of both of these curves and it was generally found that the linear fit for the square-root-time curve had a better correlation coefficient than that for the data plotted as a function of time, which indicates a diffusion-controlled process. Perhaps one of the limitations of the reflectivity monitoring technique is that the number of the collected data points for each sample is small and for a complete analysis more data points are required. (Note that the total number of points depends on the initial As-S film thickness, thicker films providing more data points). The slope of either of these lines can be used to determine the photodissolution rate.

In a previous study (Zakery 1986) it was found that the photodissolution rate depends on the amount of metal available for dissolution: photodissolution had a linear dependence on time when a thick silver layer was used while for thin silver layers a square-root-time dependence was observed. However, thin chalcogenide films (up to 0.5 μm) were used in that study. To observe the photodissolution kinetics in thicker chalcogenide layers, a set up using a phase-sensitive detection system and a W-halogen lamp was used. Two samples with identical chalcogenide layer thicknesses (0.8 μm) were used but two different silver layer thicknesses (2210 and 4660 A) were employed. The data obtained from these reflectivity measurements is shown in Fig. 5-7. Here, the remaining As-S layer thickness is plotted versus exposure time. It is interesting to see that at the beginning of the process both samples have a similar time dependence while at longer exposure times they exhibit a different time dependence. For the sample with the thicker silver film, the photodissolution rate decreases only slightly while for the sample with the thinner silver film the photodissolution rate decreases significantly. It is also interesting to note that the change in the photodissolution regime occurs when about 3000 A of the As-S layer remains. This probably corresponds to the point at which the Ag is exhausted, since a thickness, d, of silver will photodope a thickness $\sim$ 3d of As-S glass (see below). This shows that when the silver layer is exhausted photodissolution still continues but with a slower rate, possibly due to the fact that the source of dissolving metal ions is no longer the pure metal but rather metal ions in the already photodoped layer. This result is in good agreement with the

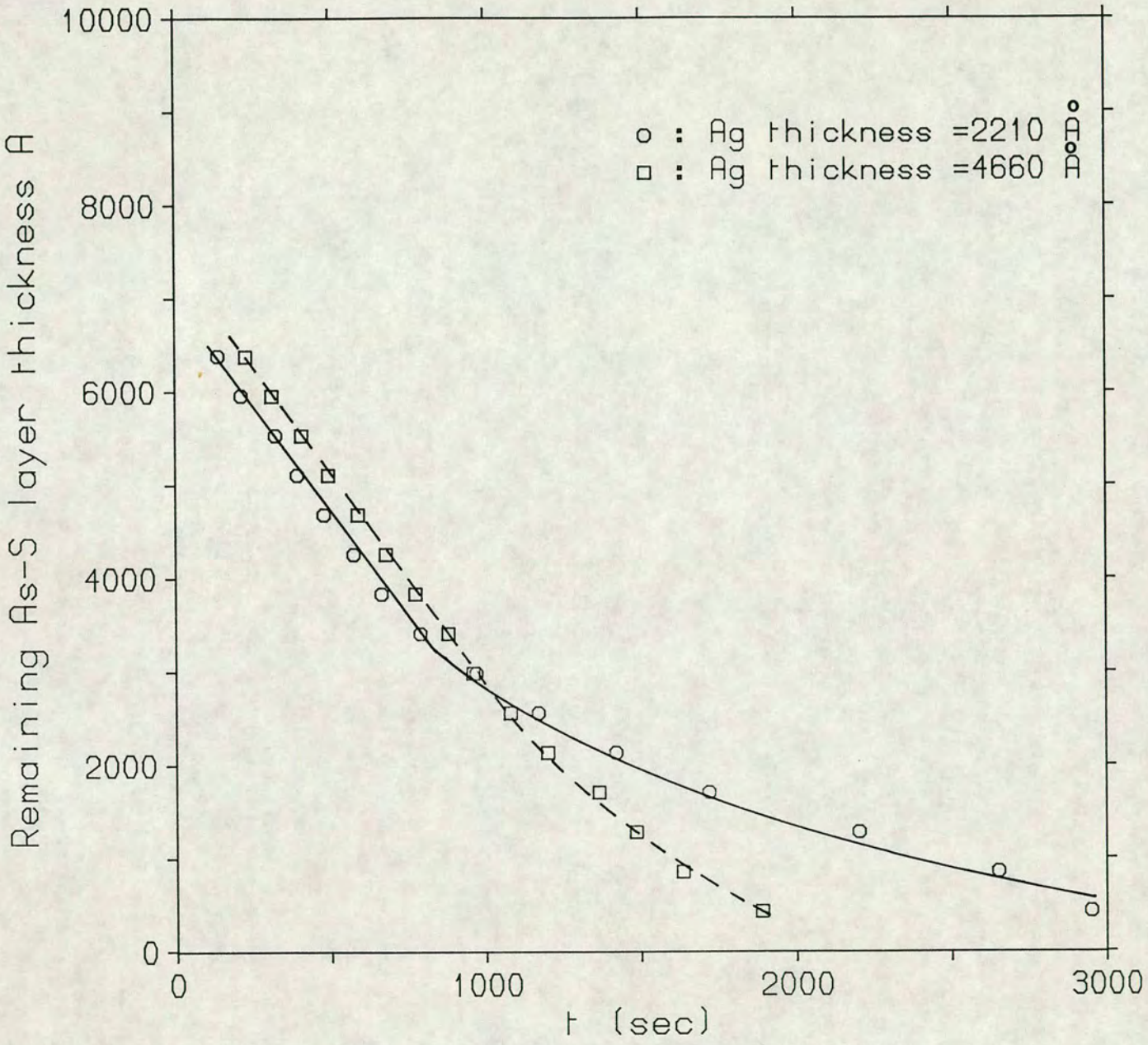

Fig. 5-7 $As_{28}S_{72}$ layer thickness versus exposure time for two different Ag thicknesses. The initial Ag layer thicknesses are indicated in the figure. The full and dashed lines are guides for the eye.

findings of an earlier study (although for a slightly different As-S composition): it was shown that in $As_{30}S_{70}$ a thickness ratio of 1/3 for the silver and As-S layers is sufficient for complete exhaustion of the metal layer (Firth, Ewen and Owen 1985). Fig. 5-8 shows a plot of the data for the 2210 A Ag film sample after the onset of the new regime, versus the square root of time. Since a good linear fit is obtained for this plot it can be concluded that the photodissolution time-dependence strongly depends on the amount of the metal source available for dissolution.

5.4 Variation of photodissolution rate as a function of composition

As before, the samples for these experiments were prepared by evaporating onto a cleaned glass substrate first a layer of Ag and then a layer of the desired As-S composition, there being no break in the vacuum between evaporations. Nine different compositions in the range $As_{15}S_{85}$ to $As_{40}S_{60}$ were used in these measurements. As the photodissolution rate was found to be sensitive to the relative thicknesses of the As-S and Ag layers, these were kept constant from sample to sample at 4000 A and 1500 A respectively, the thicknesses being determined with a Gold-Crystal monitor and checked using a mechanical stylus or occasionally a Dek-Tak 2 instrument. Simultaneous reflectivity and transmissivity measurements were used to monitor the photodissolution kinetics in this case. The reflectivity data was analysed to determine As-S thickness as a function of time. It was found that in most cases plots of thickness versus the square root of time could be satisfactorily fitted by a straight line and the gradient of this line was taken as the rate of the process. Provided care was taken to ensure sample-to-sample uniformity, these rates were reproducible to $\pm$ 5 % . Fig. 5-9 shows the variation of the photodissolution rate as a function of As-S film composition at two different laser wavelengths (488 and 514.5 nm) for an illumination intensity of $\sim$ 100 mW/cm^2. Although there is significant scatter in the points, there are some similarities between the two sets of data, so a common guide based on the average of the data has been drawn through the points. The photodissolution rate is approximately twice as fast for blue light as compared to green light. As is seen, the

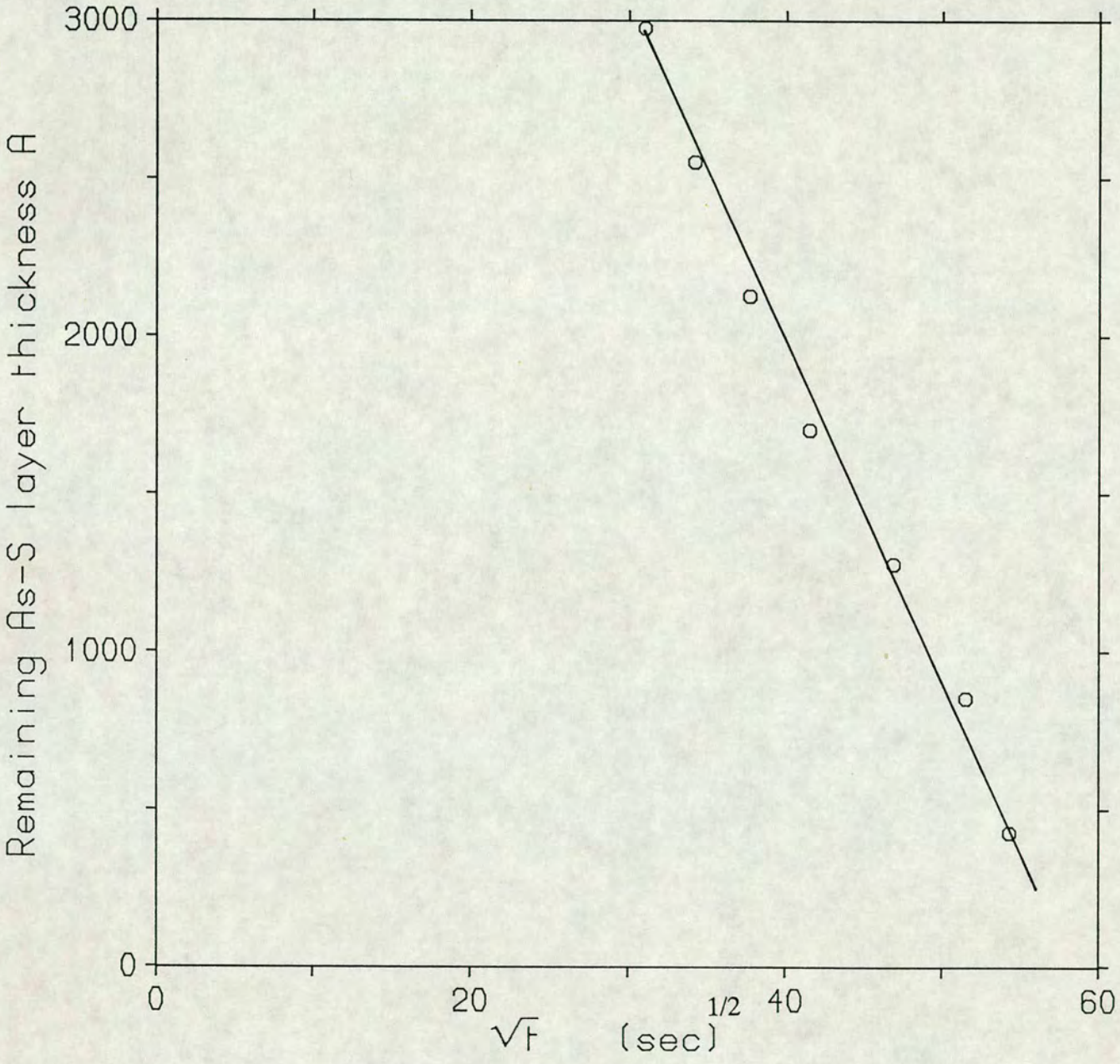

Fig. 5-8 $As_{28}S_{72}$ layer thickness versus the square root of time for the new photodissolution regime. The full line is a guide for the eye.

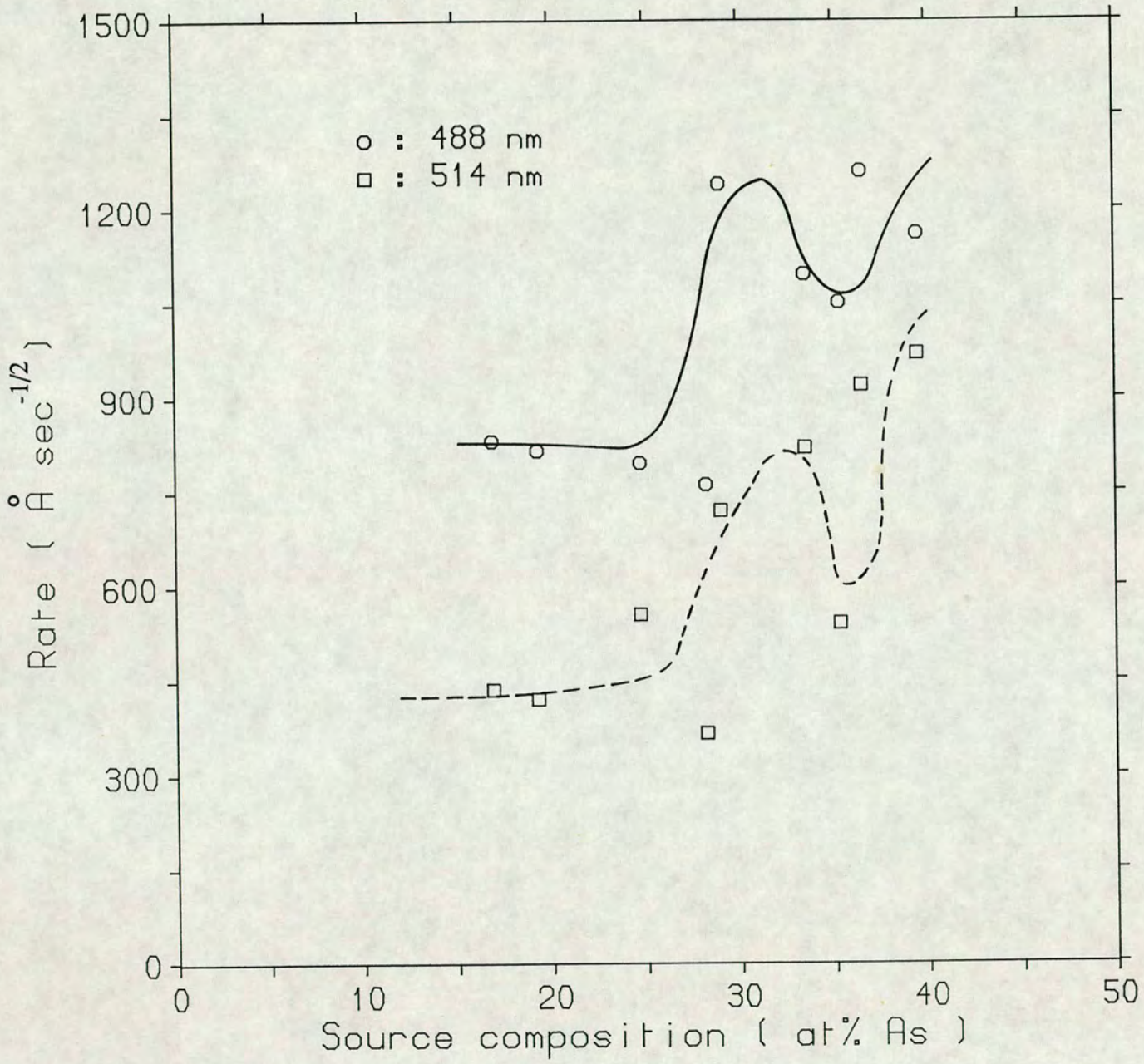

Fig. 5-9 Compositional dependence of the photodissolution rate at 100 mW/cm^2. The full and dashed lines are guides for the eye and explained more fully in the text.

photodissolution rate has a pronounced local maximum around the composition $As_{30}S_{70}$. The variation of the photodissolution rate can be explained as follows. It has been shown in an earlier study (Firth, Ewen and Owen 1983) that As-S compositions in the range $As_{28}S_{72}$ to $As_{36}S_{64}$ yield a homogeneous material on photodoping with Ag, whereas compositions on either side of this range yield a phase-separated mixture. It is therefore possible that the sharp increase in the photodissolution rate around the composition $As_{30}S_{70}$ is connected with this change in morphology, because the basic process involves the transport of electrons as well as silver ions, and the passage of electrons through the phase-separated material is likely to be slower than through a homogeneous As-S-Ag glass due to the presence of phase boundaries and additional defects in the phase-separated material.

The overall increase in the photodissolution rate with increasing As concentration can be explained by the fact that the absorption coefficient of the photodoped layer increases monotonically with increasing As concentration in the Ag-As-S system. Light absorption within the photodoped region is important in order to promote ionic transport (see section 5.9) and hence to increase the photodissolution rate. Also, other photoinduced effects become more pronounced with increasing As content in the As-S system (see section 5.7) and it is possible that for compositions that are more As-rich, an additional increase in absorption occurs during the photodissolution process.

Increasing the illumination intensity to 750 mW/cm^2 results in almost the same behaviour as is shown in Fig. 5-10. The guides are drawn, as before, based on the average of the data. The compositional dependence of Ag photodissolution in the As-S system for a white light (W-halogen) source has been investigated previously (Zakery 1986). In that study, the peak in the photodissolution rate occurred around the composition $As_{33}S_{67}$ and was also attributed to the change in the morphology of the Ag-As-S reaction product. The difference between the compositional dependence of the photodissolution rate using a white source and that for a monochromatic source can be explained as follows. In the case of a white source, the photodissolution rate measured corresponds to the peak in the spectral sensitivity for a given composition while for a monochromatic source the detected

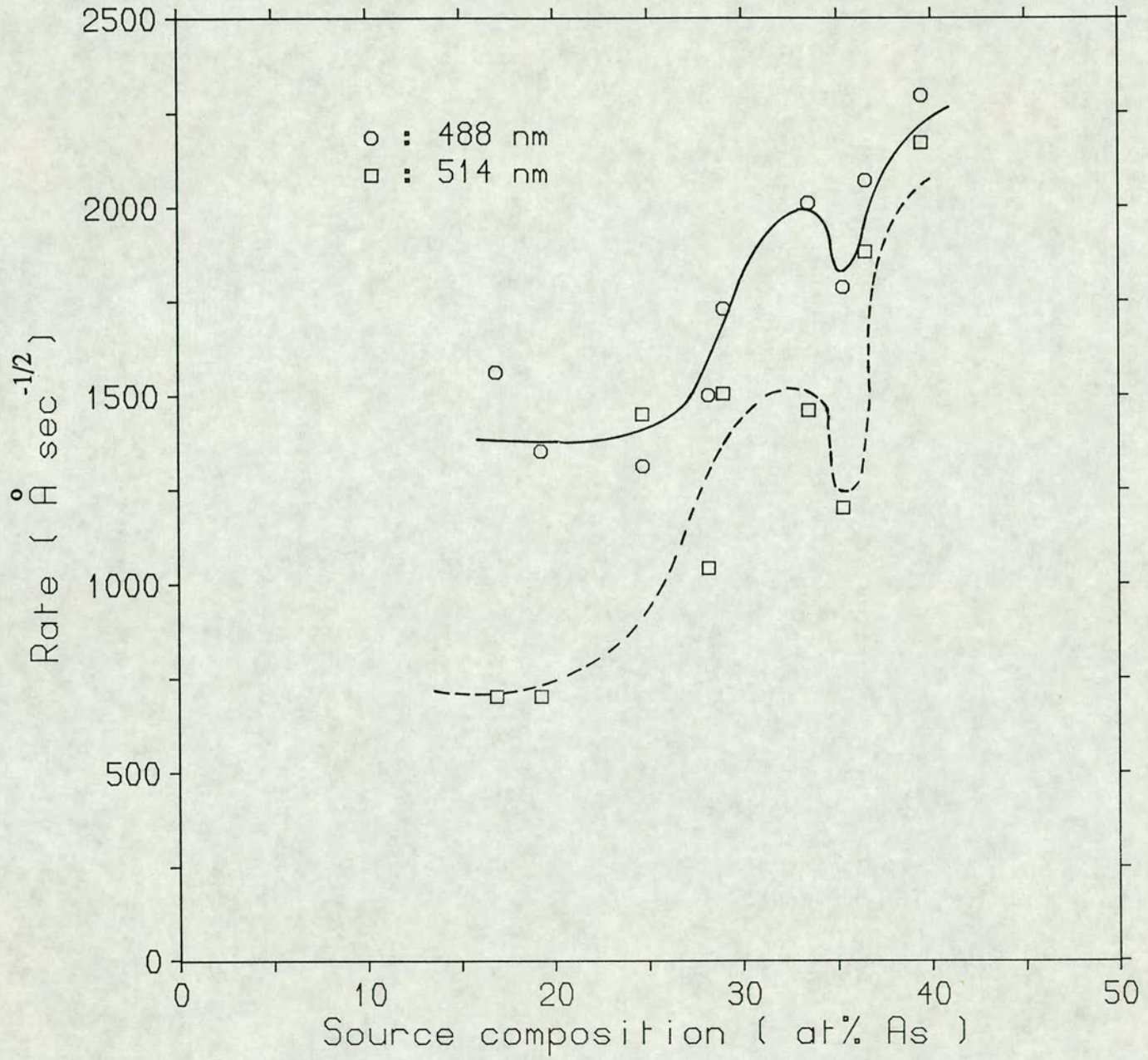

Fig. 5-10 Compositional dependence of the photodissolution rate at 750 mW/cm^2. The full and dashed lines are guides for the eye and explained more fully in the text.

photodissolution rate corresponds to a single wavelength on the spectral sensitivity curve which in general will not be at its maximum. Another factor which might influence the dependence of photodissolution rate on composition is the compositional variation of the height of the potential barrier associated with the interface between the metal and the doped chalcogenide since this forms a metal-semiconductor contact at which, during photodoping, the electron/silver-ion pairs are generated. The variation in barrier height versus composition in the Ge-Se system has been reported by Resel et al. (1987). The barrier height reflects the band gap of the chalcogenide and it is known that this decreases with increasing As concentration in the As-S system (Yamaguchi 1985). It is likely that for a fixed concentration of Ag, the band gap of the photodoped layer also decreases with increasing As concentration in the Ag-As-S system.

5.5 Spectral dependence of photodissolution rate

A knowledge of the spectral dependence of the photodissolution rate is also important as far as applications are concerned, for example in the fabrication of holographic optical elements. The sample characteristics were similar in these experiments to those described in section 5.4. The blue (488 nm) and green (514.5 nm) lines of an argon ion laser and the red line (647 nm) of a krypton ion laser were used for these measurements. Fig. 5-11 shows the spectral dependence of the photodissolution rate for 3 different As-S compositions. The data obtained using a W-halogen lamp (assuming a peak wavelength of 600 nm) is also shown in the figure. These results clearly show that photodissolution is very sensitive to above-band-gap illumination ($<$ 500 nm). For below-band-gap illumination, metal photodissolution still occurs but the rate is much slower than when above-band-gap illumination is used, the rate being almost two orders of magnitude smaller for the case of below-band-gap illumination. This result agrees well with the results of other workers (Goldschmidt et al. 1986, Wagner et al. 1987) who, using different techniques, have found that the silver dissolution rate is a maximum around 475 nm for these thinner films. Light absorption is necessary within the doped region to promote ionic transport by the

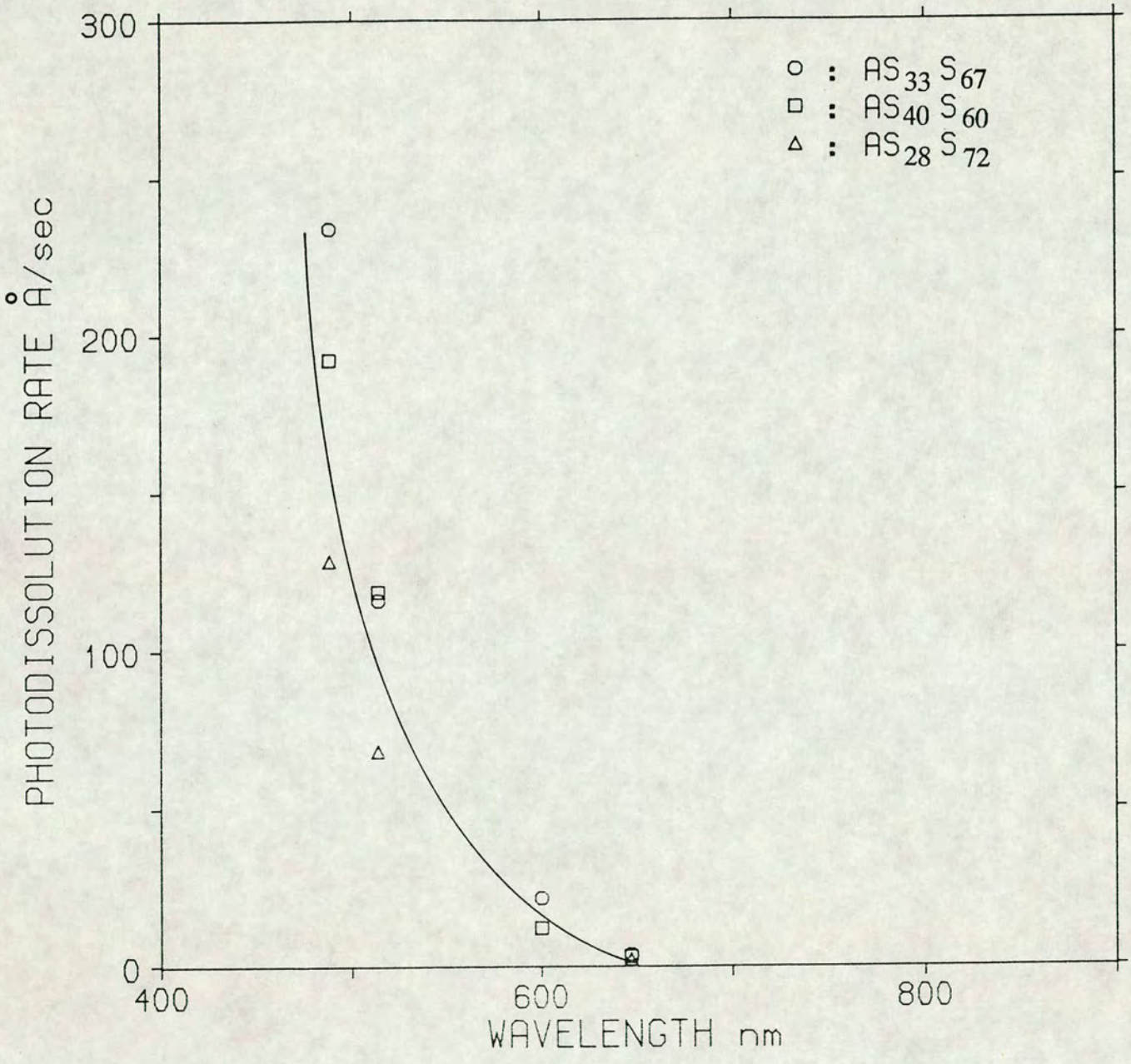

Fig. 5-11 Spectral dependence of the photodissolution rate for three different As-S compositions at 100 mW/cm^2. The full line is a guide for the eye.

generation of free photocarriers and also in the vicinity of the interface between the metal and the doped chalcogenide in order to generate electrons and metal ions (see section 5.9). Both silver and silver-doped arsenic sulphide possess a relatively high absorption coefficient for wavelengths larger than that corresponding to the optical band gap of the undoped chalcogenide. However, the absorption in the silver-doped arsenic sulphide decreases monotonically with increasing wavelength. This might explain partly why at longer wavelengths the spectral sensitivity drops sharply.

The spectral dependence of the photodissolution effect can be explained as follows. If photogenerated carriers are important for photodissolution to proceed, one can express (Mott and Davis 1979) the rate of generation of carriers G as :

$$G = \eta\left[\frac{I_0(1-R)(1-exp(-\alpha d))}{d}\right] \qquad (1)$$

Where the quantity in square brackets is the number of photons absorbed per second in a sample of thickness d in the direction of the incident radiation. I_0 is the incident flux density, α the absorption coefficient and R the reflectivity. The quantum efficiency for photogeneration is denoted by η. Let us now calculate the contribution due to absorption in the photodoped layer. For a 0.5 μm thick photodoped $As_{30}S_{70}$ film the values for absorption coefficient at red and blue wavelengths are 4×10^3 cm^{-1} and 10^5 cm^{-1} respectively (see section 4.3). If the photodissolution rate, r, is proportional to the number of photogenerated carriers, one obtains :

$$\frac{r_{red}}{r_{blue}} = \frac{1}{5}\left[\frac{\eta_{red}}{\eta_{blue}}\right] \qquad (2)$$

The ratio 1/5 is much smaller than the observed experimental values. One can speculate therefore, that another factor, namely the quantum efficiency of the photogeneration, is also an important quantity to be considered. The most striking features of photogeneration

in amorphous chalcogenides are the strong dependencies of the quantum efficiency on photon energy, temperature and the applied electric field (Enck and Pfister 1976). The strong dependence on photon energy continues for energies substantially greater than the absorption edge. In the absence of any data for the spectral dependence of the quantum efficiency of photogeneration in the photodoped As-S glasses we can estimate approximate values from the quantum efficiency of some other chalcogenide glasses. Fig. 5-12 shows the spectral dependence of quantum efficiency for a-Se and a-As_2Se_3. The results for a-Se were obtained by Hartke et al. (1965) while those for a-As_2Se_3 were obtained by Main and Owen (1973) by a direct normalization of the photoconductivity in terms of photocurrent per absorbed photon. If the quantum efficiency of photogeneration has roughly the same dependency on photon energy in the Ag-doped As-S material, then the resulting factor of 10 decrease in η at red wavelengths compared to blue can explain the spectral dependence of the photodissolution rate obtained in this study. At short wavelengths absorption in the undoped chalcogenide is high, which results in attenuation of the illuminating photon flux. Since the absorption coefficient of the undoped glass decreases monotonically with wavelength, the absorption of actinic radiation in the undoped layer is also partly responsible for the shape of the spectral dependence curve.

5.6 Intensity dependence of the photodissolution rate

Information on the dependence of the photodissolution rate on illumination intensity is necessary in order to establish the maximum and minimum level of exposure required to obtain a usable image, that is to avoid under- or over-exposure. The results of these measurements are shown in Fig. 5-13. As is seen, the photodissolution rate increases with intensity of illumination but goes to saturation at high intensities. The saturation in the rate may yield information on the maximum amount of silver ions which can be incorporated in different As-S compositions. This data can be fitted to different power laws in the low and high intensity regimes, as shown by Buroff et al. (1975), who used a white light source and obtained similar results. If the photodissolution rate is expressed as $r=I^a$, where I is the

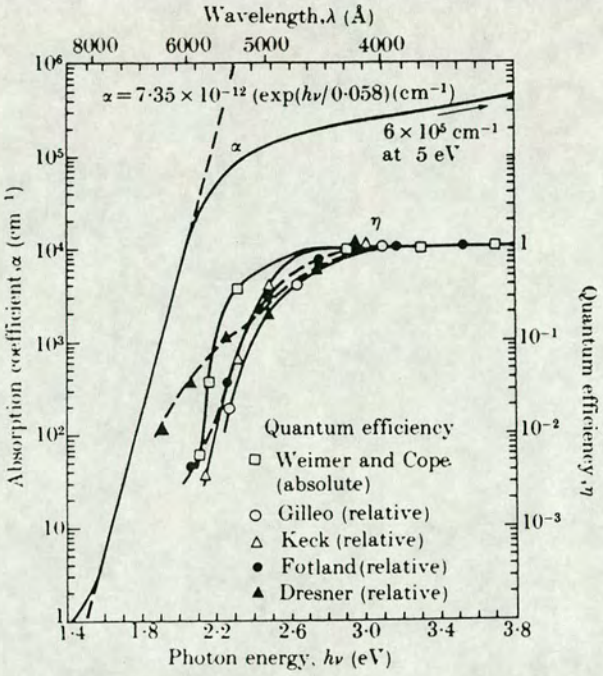

a Optical absorption edge and quantum efficiency in amorphous selenium at room temperature. (From Hartke and Regensburger 1965.)

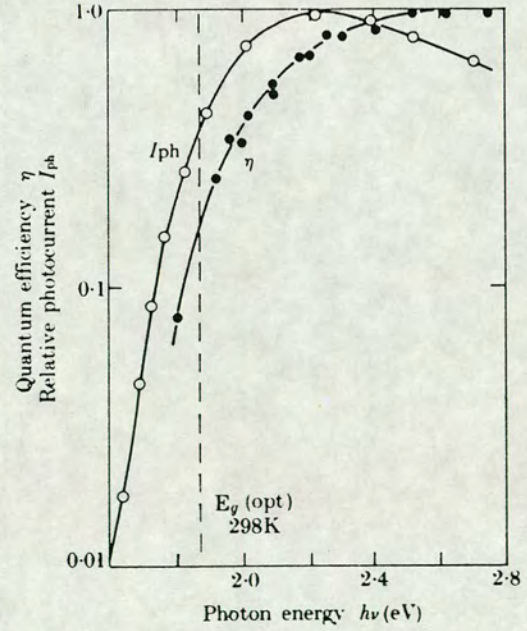

b Spectral dependence of normalized photocurrent and quantum efficiency for As_2Se_2 at room temperature. (From Main and Owen 1973.)

Fig. 5-12 Spectral dependence of quantum efficiency at room temperature. a: a-Se , b: a-As_2Se_3.

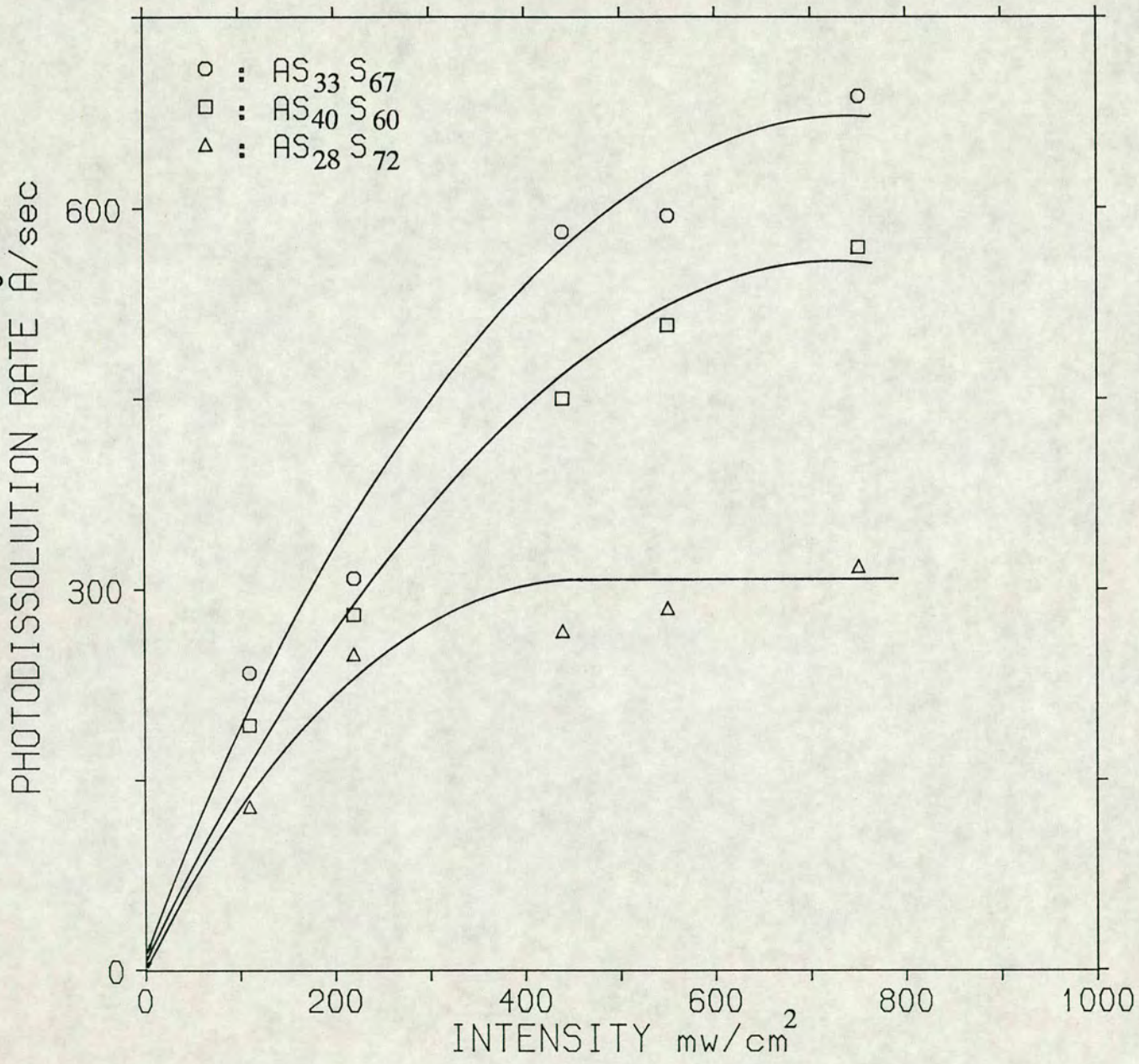

Fig. 5-13 Intensity dependence of the photodissolution rate for three different As-S compositions at 488 nm. Full lines are guides for the eye.

illumination intensity, one obtains the exponent a as:

$$a = \frac{\ln r}{\ln I} \tag{3}$$

Fig. 5-14 shows the plots of a versus the illumination intensity for the present data. Different power laws apply to different compositions possibly due to different ionic, electronic and structural properties of the photodoped layer. In general, however, it can be concluded that the photodissolution process has a superlinear dependence on intensity at low levels and a sublinear dependence on intensity at higher levels. The sublinear dependence on light intensity can be explained by the behaviour of the photoconductivity of the photodoped layer versus temperature (see section 5.9).

The quantum efficiency of photodissolution (that is, the number of dissolved silver atoms per incident photon) can be determined from the relation :

$$r = \epsilon I \tag{4}$$

where r here is the rate at which Ag ions dissolve into the As-S film, ϵ the quantum efficiency and I the illumination intensity. Note that ϵ is possibly intensity and wavelength dependent. For $As_{33}S_{67}$ and 220 mW/cm^2 of blue (488 nm) illumination, a value of 308 A/sec is obtained for the photodissolution rate in the above measurements. Since the rate at which the Ag layer is consumed is about 3 times smaller than the rate of change in the As-S layer thickness, a value of 103 A/sec is obtained for the rate of change of Ag layer thickness. By considering that 220 mW/cm^2 corresponds to 5.37×10^{17} photons/cm^2 sec and that there are 5.85×10^{22} silver atoms per cm^3, a value of $\epsilon=0.11$ is obtained for the quantum efficiency of photodissolution in $As_{33}S_{67}$. It is interesting to compare this value with that for a photographic emulsion in which, through chemical amplification in the development process, one can obtain $\epsilon = 10^6$. The photodissolution efficiency is almost 7 orders of magnitude smaller than the efficiency for a photographic emulsion.

As is seen in Fig. 5-13 the photodissolution rate goes to saturation around an intensity of 200 mW/cm^2 for the composition $As_{28}S_{72}$, whereas for the compositions $As_{33}S_{67}$ and $As_{40}S_{60}$ the saturation in the rate occurs at higher intensities. This might imply that a

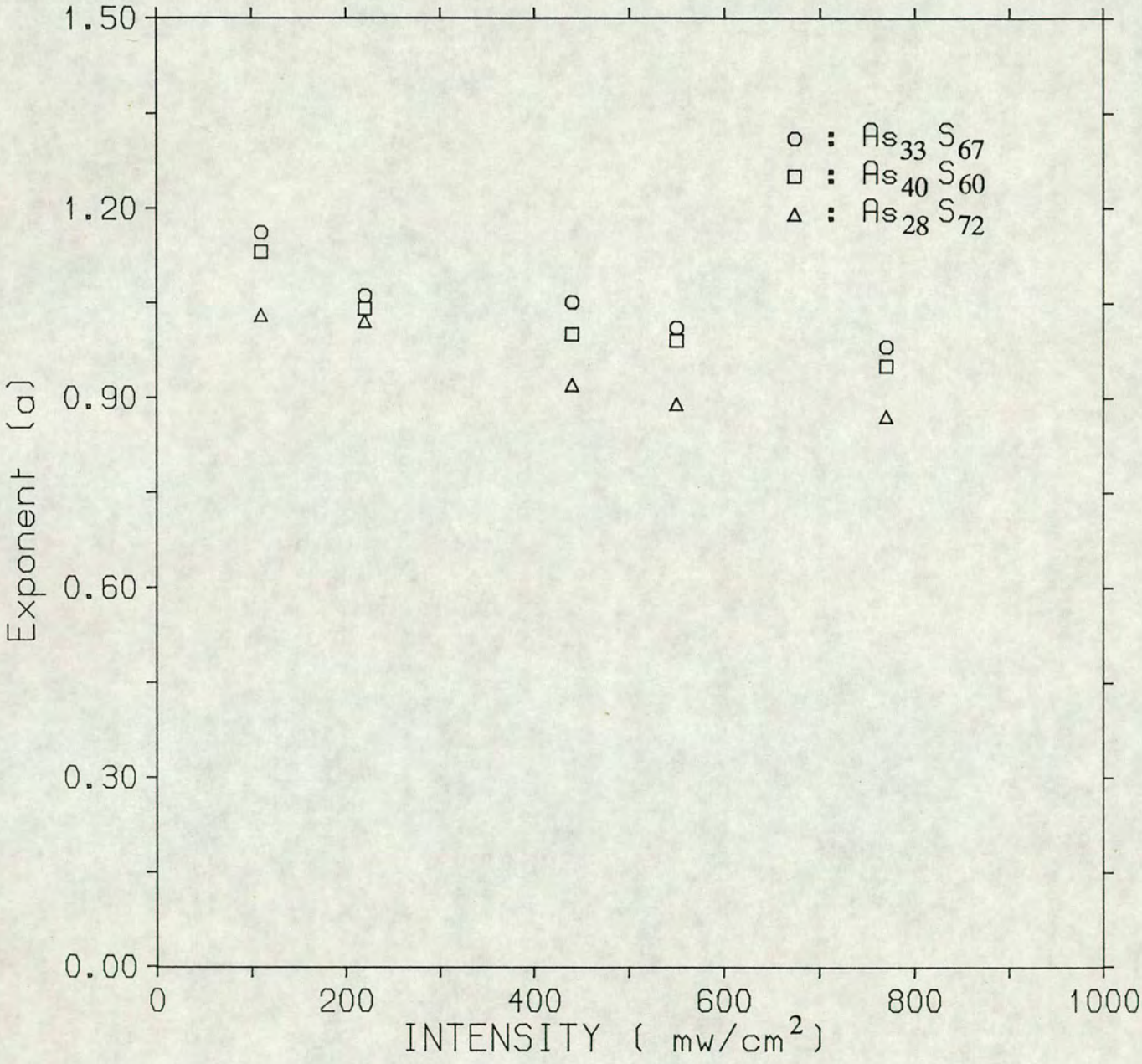

Fig. 5-14 The variation of the exponent *a* versus the illumination intensity for three different As-S compositions at 488 nm.

smaller concentration of silver can be incorporated into the composition $As_{28}S_{72}$ in comparis on with $As_{33}S_{67}$ and $As_{40}S_{60}$.

5.7 Other photoinduced effects

Other photoinduced effects, such as irreversible photodarkening, are likely to accompany the metal photodissolution effect. In order to be able to control the photodissolution effect for practical applications a knowledge of these other photoinduced effects is required, although under certain conditions these effects can be negligible and hence may not affect the photodissolution process. In these measurements nine different compositions of glasses in the As-S system were used. The technique used to monitor these effects was based on simultaneous transmissivity and reflectivity measurements. Films of these different compositions were prepared with thicknesses up to 1 μm and the measurements were made using the arrangement shown in Fig. 5-1. A typical transmissivity and reflectivity versus time plot is shown in Fig. 5-15. As is shown in this figure the transmittance of the as-deposited film decreases and goes to saturation after a few minutes. This time is normally comparable to the time required to photodope films of such thickness. Fig. 5-16 shows the variation of the percentage decrease in transmittance for different film compositions. The decrease in the transmittance is obtained by subtracting the saturated value of the transmittance from its original value. The interesting feature is that clearly for the As-S system the extent of photodarkening increases with increasing As concentration. The photodarkening becomes negligible around the composition $As_{30}S_{70}$. It is possible to explain this if photodarkening involves the formation of As-As bonds since the As-As separation increases as the S content increases due to the formation of As-S-S-As links. The other observation of note is that the spread in the data is higher for higher As concentrations.

By knowing the values of reflectance and transmittance at each instant of time, it is possible to work out the change in absorption coefficient or correspondingly the change in the extinction coefficient and also the change in the film refractive index due to

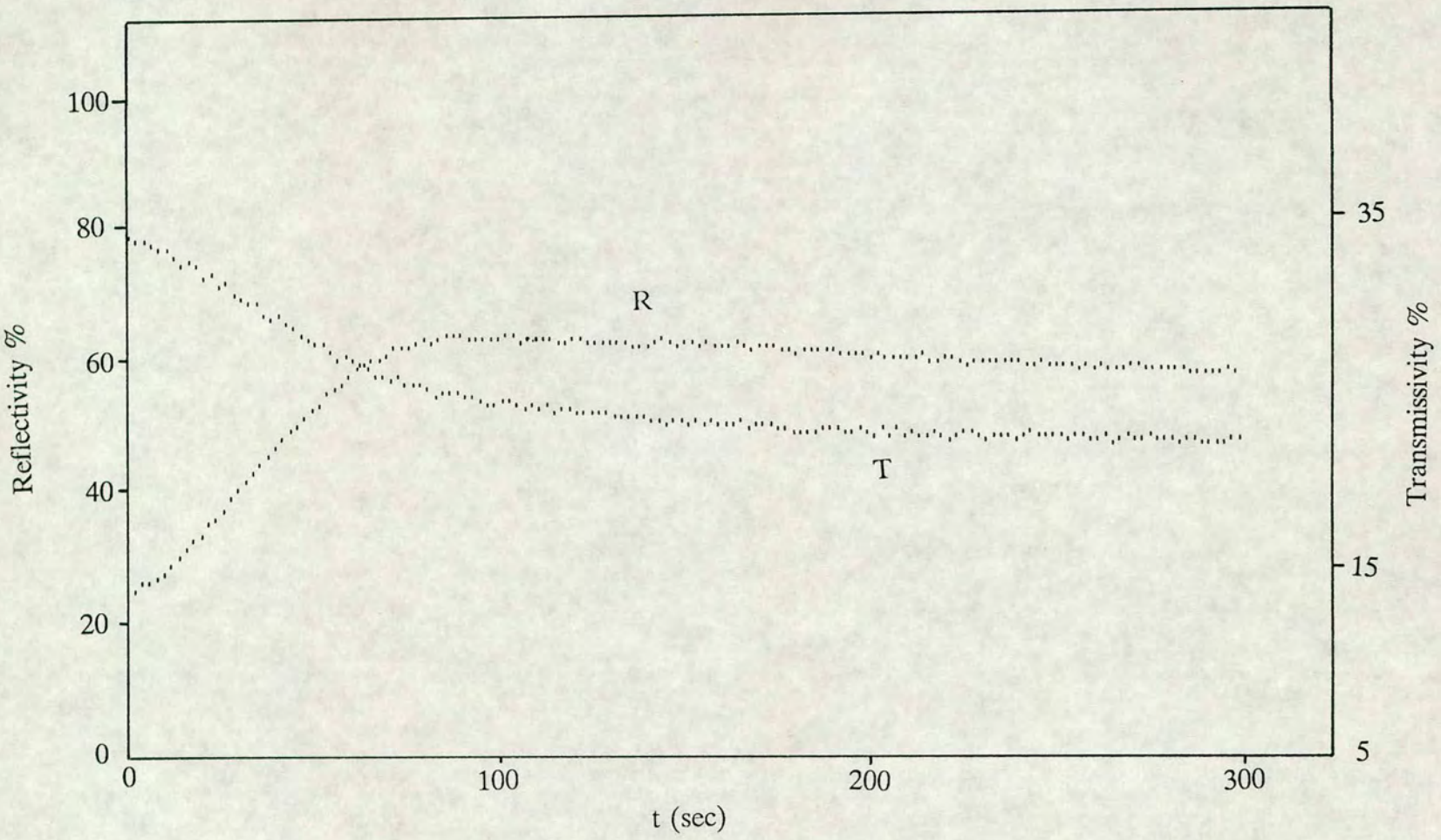

Fig. 5-15 A typical plot of reflectivity and transmissivity versus exposure time in a composition $As_{40}S_{60}$ at 514.5 nm. Illumination intensity was 100 mW/cm^2.

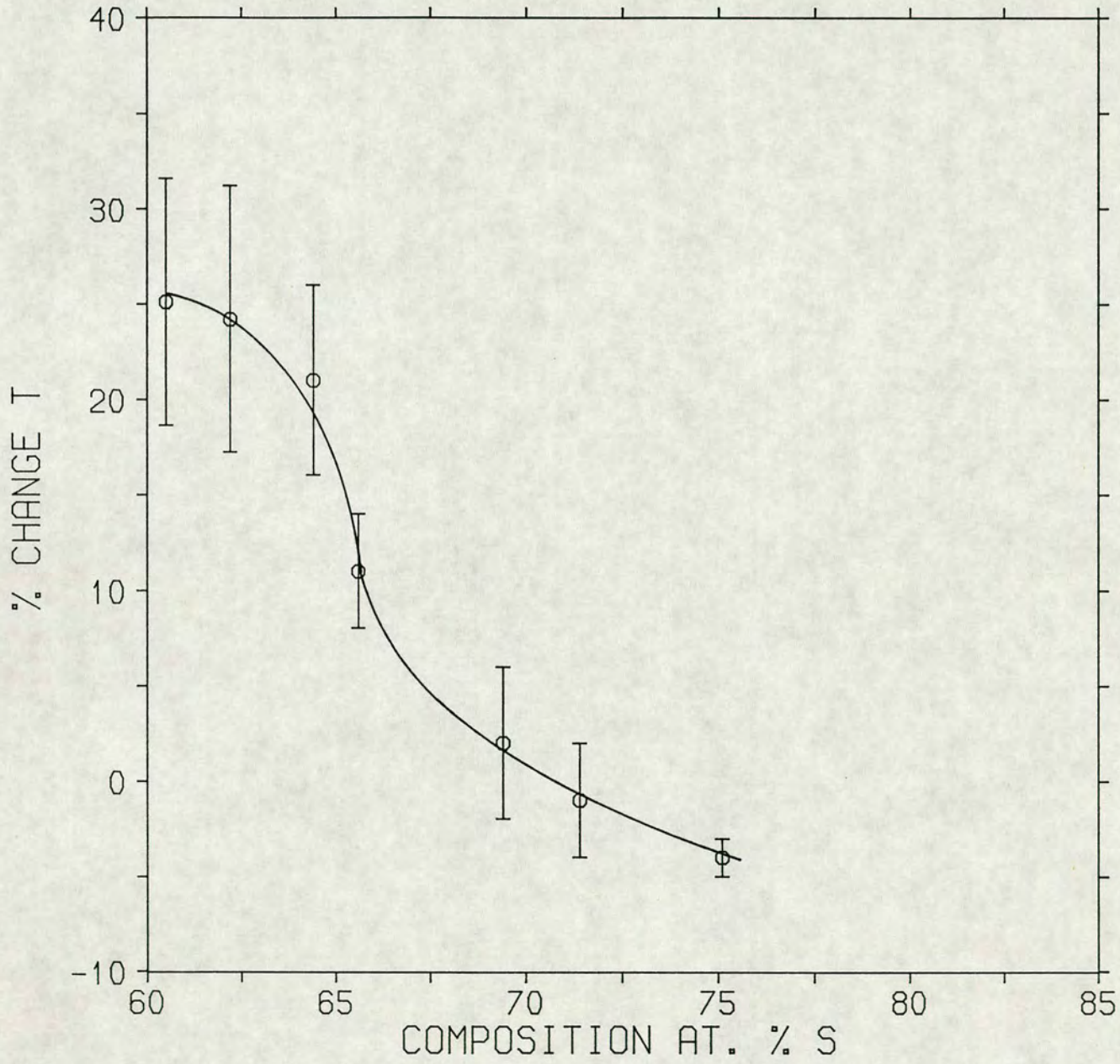

Fig. 5-16 Variation of the percentage change in transmittance versus As-S composition at 514.5 nm. Illumination intensity was 200 mW/cm^2. The full line is a guide for the eye. The error-bar shows the spread in data from sample to sample.

illumination. The relation

$$R+T+A=1$$

should hold at each wavelength, where R is the reflectance, T is the transmittance and A is the percentage of light being absorbed in the film. One can write :

$$R+(1-R)exp(-\alpha d)+A=1 \qquad (5)$$

Thus :

$$A=(1-R)(1-exp(-\alpha d)) \qquad (6)$$

By calculating A from the experimental values one can obtain the absorption coefficient. For example at the onset of illumination with 514.5 nm light, for a film of composition $As_{40}S_{60}$, the experimental values for R and T are 0.14 and 0.794 respectively. Hence the value of absorption is 0.066. This gives a value for $\alpha \sim 800$ cm^{-1} which is in good agreement with the result for the bulk glass. The values of R and T for the final illumination stage are 0.28 and 0.52 respectively. Hence the change in absorption is 0.134 or 13.4 %. The value obtained from the Eqn. (6) for α is 2712 cm^{-1}. Hence a change of $\Delta\alpha = 1912$ cm^{-1} is obtained due to illuminating the sample with 180 mW/cm^2 of green laser light. Knowing the values of α and $\Delta\alpha$ one can obtain the values for the extinction coefficient, k, at the onset and at the end of illumination. Equations for the reflectance and transmittance of a single absorbing film on a transparent substrate are given by Heavens (1955). By calculating the values of extinction coefficient using Eqn. (6), one can find the refractive index, n_0 , and the change in the refractive index, Δn, of the film due to illumination.

Table 5-1 lists, for four As-S compositions, the refractive index, the absorption coefficient and the change in these quantities as a result of illumination. Ohmachi et al. (1972) have measured the changes in the refractive index of different chalcogenide thin films as a result of exposure to the blue (488 nm) line of an argon ion laser. They calculated the change in the refractive index, Δn, from measurements of the

Composition As-S	Thickness (nm)	n_0	Δn	α_0 cm^{-1}	$\Delta\alpha$ cm^{-1}	ΔK
$As_{40}S_{60}$	1000	2.53	0.11	800	1912	0.0029
$As_{35}S_{65}$	1100	2.53	0.095	551.7	307.7	0.0012
$As_{33}S_{67}$	1000	2.50	0.1	525	247.3	0.0012
$As_{28}S_{72}$	1000	No detectable change in either transmittance or reflectance was observed.				

Table 5-1 Compositional dependence of the photoinduced effects in the As-S system.

diffraction efficiency of gratings that they produced in these thin chalcogenide films. The intensity of the first diffracted order, I_1, is given by Phariseau (1956) as :

$$\frac{I_1}{I_0} = \left(\frac{\pi \Delta n l}{2\lambda_0}\right)^2$$

where I_0 is the light intensity transmitted through the film without the grating, λ_0 is the wavelength of the illumination, Δn is the induced refractive index change, and l is the film thickness. Their results are in good agreement with the findings of this study, for example, they obtain $\Delta n = 0.056$ for $As_{40}S_{60}$. These results clearly show that these effects must accompany any of the other light-induced phenomena that occur in chalcogenide glasses, including metal photodissolution. Hence for a complete analysis of the metal photodissolution effect it is essential to consider these light-induced changes in the refractive index and absorption coefficient of the chalcogenide film. The time scale over which these light-induced changes occur seems to be comparable with the times involved in the photodissolution process. In passing, it should be noted that the observation of refractive index changes as large as 0.1 in these measurements make As-S thin films promising media for optical recording.

Illuminating the samples with red light (647 nm) did not induce any changes in either the transmittance or reflectance of the samples. This suggests that only above-band-gap illumination can produce these photoinduced effects, which is in agreement with previous observations.

5.8 Analysis of transmissivity data

Although transmissivity measurements provide more data points for the kinetics analysis, the analysis itself is more complicated than for the reflectivity data because it must take into account the fact that all 3 layers (undoped, photodoped and silver) are absorbing during photodissolution. Hence for a complete analysis, a solution for the case of a system of 3 absorbing layers on a transparent substrate is required. Other authors

(Kawaguchi et al. 1987) have tried to interpret their data using a simplified mathematical analysis. Their approach considers an ultra thin doped layer formed during the evaporation process and enables the data to be analysed analytically.

However, some valid approximations can be made which allow this multilayer system to be solved easily. Although both undoped and photodoped layers are strongly absorbing at blue or green wavelengths, they are weakly absorbing in the red. This approximation can simplify the analysis substantially. As mentioned earlier, transmissivity measurements probe the silver layer thickness during photodissolution. Fig. 5-17 shows a typical transmissivity plot during the photodissolution process. One can define the photodissolution rate as: $D \equiv dL/dt$, where L is the metal layer thickness and t is the exposure time. From the previous results on intensity dependence, D will be approximately proportional to the intensity of light reaching the silver layer after passing through both the undoped and photodoped layers. One can write for the transmitted light intensity, I_t :

$$I_t = I_0 exp(-\alpha L)$$

Hence :

$$\frac{dI_t}{dt} = \frac{d}{dt}(I_0 exp(-\alpha L))$$

or :

$$\frac{dI_t}{dt} = I_0(dL/dt)(d/dL)(exp(-\alpha L))$$

From the above relation one can work out :

$$\frac{dL}{dt} = (\frac{1}{\alpha I_t})(\frac{dI_t}{dt})$$

So the photodissolution rate D is :

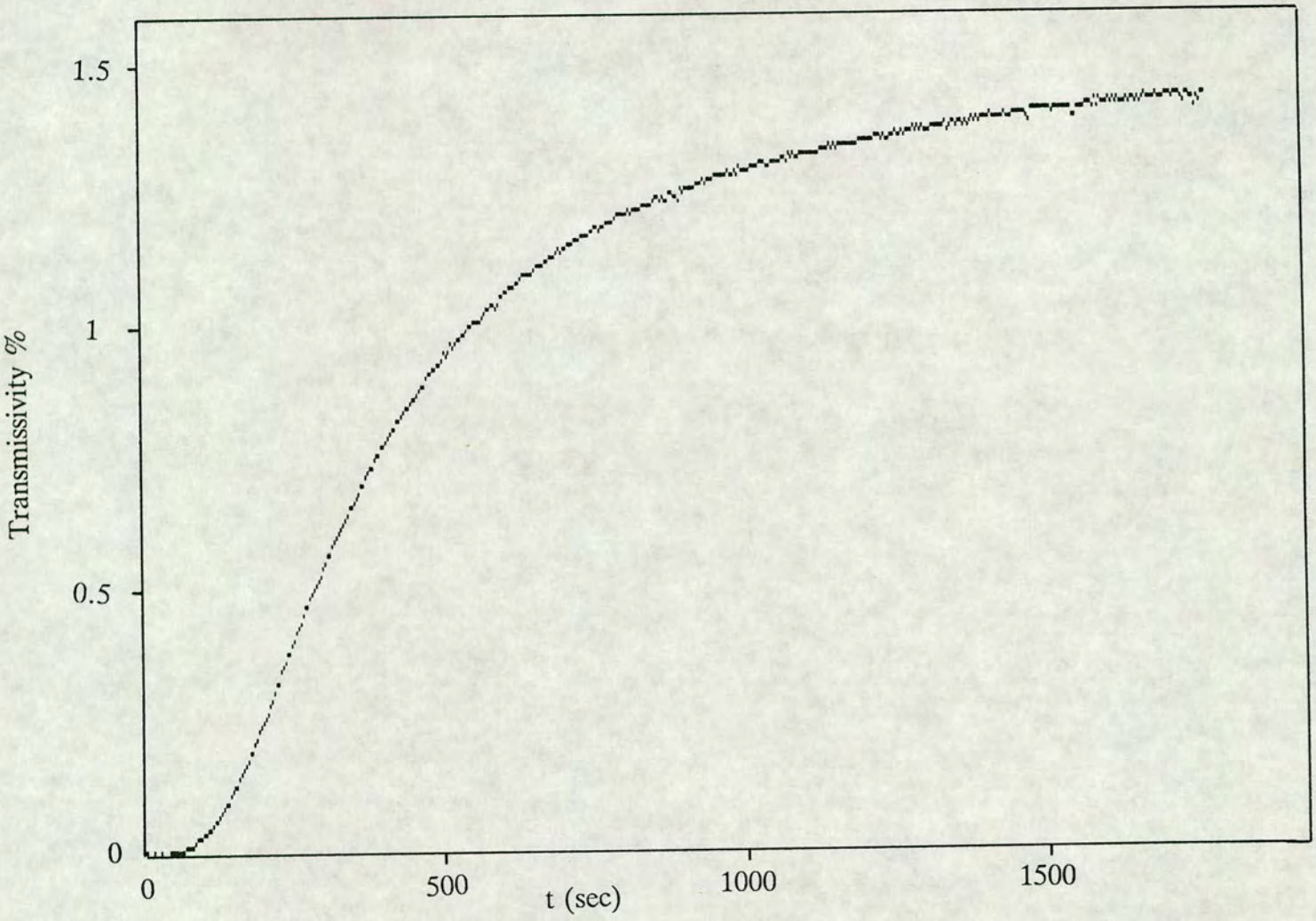

Fig. 5-17 A typical transmissivity versus exposure time in a composition $As_{33}S_{67}$, for 300 mW/cm^2 of 647 nm illumination.

$$D = \left(\frac{1}{\alpha I_t}\right)\left(\frac{dI_t}{dt}\right) \tag{7}$$

From Eqn. (7), one can obtain :

$$L = \frac{-1}{\alpha}\ln\left(\frac{I_t}{I_0}\right) \tag{8}$$

Fig. 5-18 shows a typical plot, obtained using Eqn. (8), of silver thickness versus time during the photodissolution of silver in a composition $As_{33}S_{67}$. As is seen from this figure, the S shape behaviour of the photodissolution process is partly observed, although it is difficult to calculate L at the beginning of the process since a thick silver layer is present which reduces I_t to zero. To find the photodissolution rate from Eqn. (7) it is necessary to differentiate the transmissivity versus time curve. For this purpose a Gregory-Newton algorithm (central difference notation) given by Milne-Thomson (1951) was used. Normally 5 points were chosen and the first derivative was calculated at the central point. Eqn. (9) was used to calculate the first derivative.

$$\omega f'(x) = \mu\delta u_0 - \frac{1}{6}\mu\delta^3 u_0 + \frac{\omega^5}{30} f^5(\zeta) \tag{9}$$

where ω is an increment of variable x and f' is the first derivative. u_0 is the value of function f(x) at the central point a, u_1 is the value of f(x) at $(a+\omega)$, u_{-1} = f(a-ω), u_2 = f(a+2ω), ...,etc. δ is the central difference operator with $\mu\delta u_0 = \frac{1}{2}(\delta u_{-1/2} + \delta u_{1/2})$ where $\delta u_{-1/2} = u_0 - u_{-1}$ and $\delta u_{1/2} = u_1 - u_0$. $\delta^2 f$ is defined as: $\delta^2 f = \delta[\delta f]$ and $\mu\,\delta^3 u_0 = \frac{1}{2}(\delta^3 u_{-1/2} + \delta^3 u_{1/2})$ where :

$$\delta^3 u_{-1/2} = \delta^2 u_0 - \delta^2 u_{-1} \text{ and}$$

$$\delta^3 u_{1/2} = \delta^2 u_1 - \delta^2 u_0$$

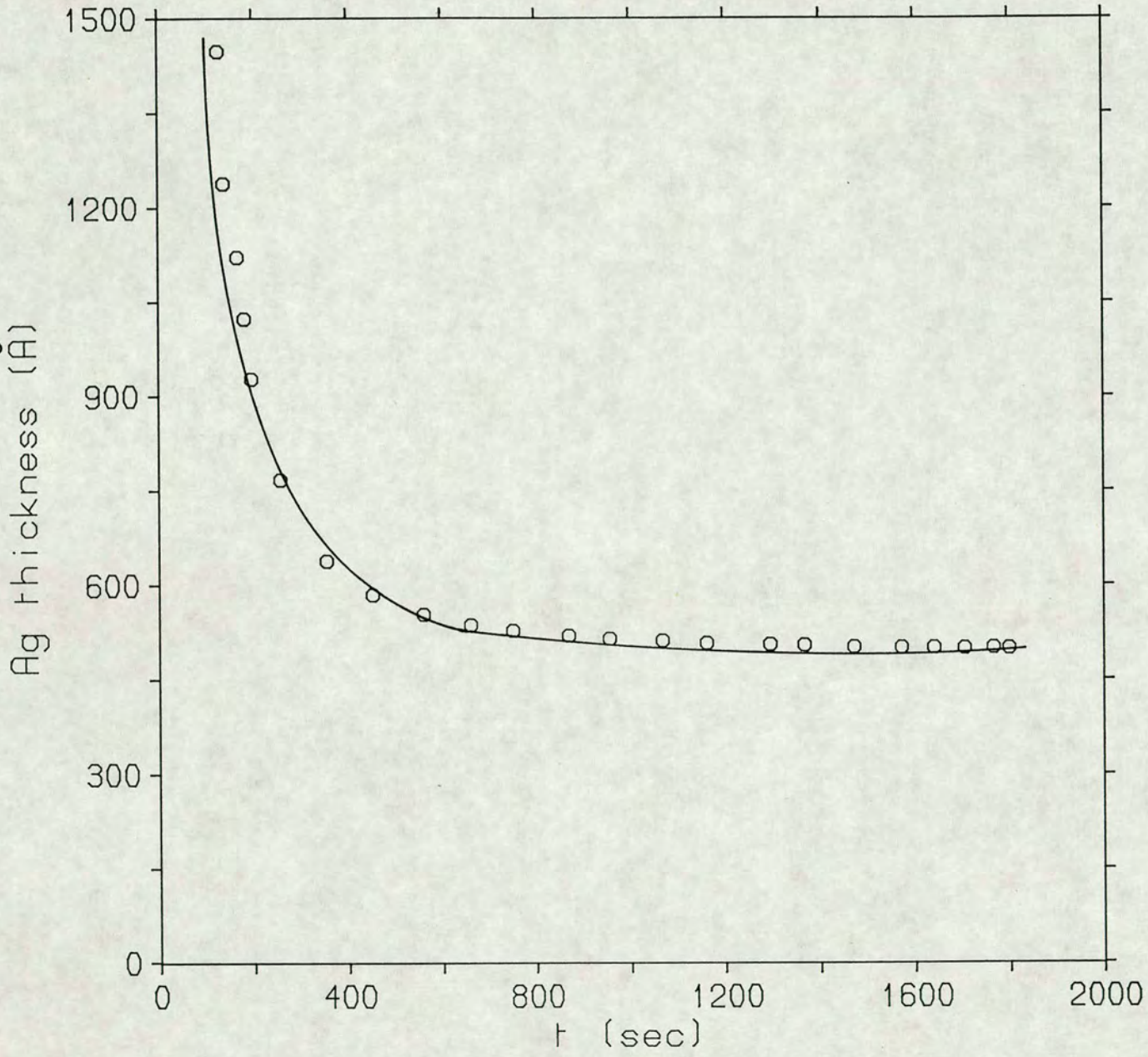

Fig. 5-18 Ag layer thickness versus exposure time in a composition $As_{33}S_{67}$, for 300 mW/cm^2 of 647 nm illumination. The full line is a guide for the eye.

The accuracy of this algorithm depends on the choice of ω and the remainder $\frac{\omega^5}{30} f^5(\zeta)$ where ζ lies between -2ω and 2ω . Only the first two terms were considered for the analysis of transmissivity data.

Fig. 5-19 shows the variation of photodissolution rate versus illumination time calculated using the above equation. The photodissolution rate decreases sharply at the beginning and then becomes constant at longer illumination times. It seems that only the deceleratory part of the photodissolution process can be analysed using the range of Ag layer thicknesses (1000-1500 A) employed in the present study. For a complete analysis using the above technique thin silver films < 500 A are required, because below this thickness the silver film becomes transparent. To determine a quantitative value for the photodissolution rate from Eqn. (7) one requires the value of α, the absorption coefficient of silver at red wavelengths. Johnson and Christy (1972) give a value of $\alpha = 8.572 \times 10^5$ cm^{-1}, which in turn gives a value of the photodissolution rate between 0.05-3 A/sec for the composition $As_{33}S_{67}$, as shown in Fig. 5-15. This is about two orders of magnitude smaller than the rates obtained with blue or green illumination.

5.9 A possible model for photodissolution

The model presented here is based on consideration of photodoping as an intercalation of an amorphous solid, as originally proposed by Kluge (1987). This model essentially regards photodoping as a radiation-enhanced solid state reaction. Brown et al. (1980) state that every solid state reaction consists of three distinct regimes : an induction period, an acceleratory time region and a deceleratory time region. During the acceleratory time region, the rate of the process is limited by the chemical reaction (due to electronic and ionic transfer processes at interfaces). The deceleratory time region occurs either because of exhaustion of one reactant or because of rate limitation by the physical transport processes responsible for transferring the reactants through the product layer. The square-root dependence of the position of the doping front on the doping time is an

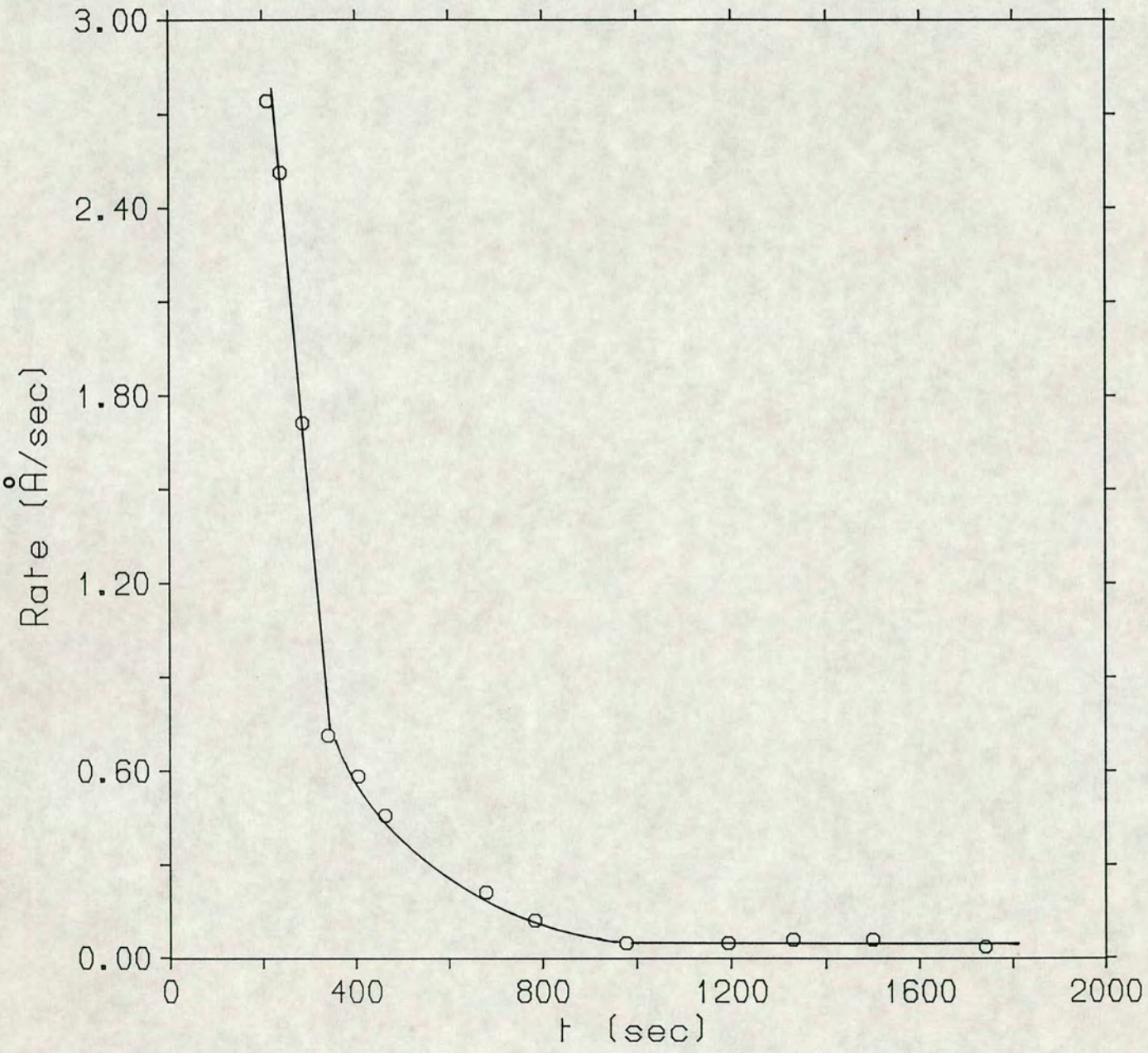

Fig. 5-19 The photodissolution rate versus exposure time in a composition $As_{33}S_{67}$, for 300 mW/cm^2 of 647 nm illumination. This was derived from the data of Fig. 5-18 using Eqn. 9. The full line is a guide for the eye.

indication of rate limitation by diffusion through the reaction product (Schmalzried 1981) and corresponds to the deceleratory time region. In the case of photodissolution, the solid state reaction can be considered as an intercalation reaction of an amorphous matrix. Intercalation reactions are volume reactions in which an ion (M^+) and an equivalent electron transfer from outside into a host matrix (Z) and lead to a reversible insertion of the ions (guests) into the host according to the equation:

$$xe^- + xM^+ + \blacksquare Z \rightarrow Mx^+ Zx^- \qquad (10)$$

The host matrix has to provide empty interatomic volumes shown by ■ in Eqn. (10) for accommodation of the guest ions. These sites are related to regions where van der Waal's bonding occurs. The intercalation product is characterized by a strongly increased ionicity as expressed in Eqn. (10) and, therefore, by a drastic change in chemical reactivity compared with the original host reactivity. The host matrix must fulfil two additional conditions for intercalation to occur. Firstly it should have a high ionic conductivity in order for the guest ions to be transported to the empty spaces, and secondly, a high electronic conductivity to ensure charge neutrality during ion transport and to produce negatively charged host atoms. The key features of the model are discussed in sections 5.9-1 - 5.9-7 below.

5.9-1 Ionic transport

The ionic conductivity of glasses is well known (Tuller et al. 1985). For amorphous silver-containing chalcogenides a high ionic conductivity was found (Kitao et al. 1986). Also the formation of Ag_2S, which is a good ionic conductor, is expected on illuminating the combination Ag : As_2S_3, due to an interface reaction between the silver and sulphur (Malinowski et al. 1978). Plocharski et al. (1987) give a value of $6\times10^{-5}\ \Omega^{-1}\ cm^{-1}$ at 35°C for the ionic component of the conductivity of As_2S_3 photodoped with silver.

5.9-2 Electronic transport

If charge neutrality is not maintained, internal electrostatic fields will restrict the movement of ions and hinder intercalation, and hence also the photodoping. Charge neutrality can only be ensured by mobile electronic charge carriers. For an amorphous material these can be either delocalized or localized carriers at thermodynamic equilibrium, or non- equilibrium carriers due to, for example, photoexcitation. The photoexcitation of additional free charge carriers strongly increases their concentration and, therefore, triggers the ionic transport. Because of the short lifetimes ($\mu\tau$ product) of the photocarriers the photodoped regions remain restricted to the vicinity of the light absorbing volume elements and lateral diffusion out of the illuminated region remains negligible. Both free electrons and holes may contribute to charge neutralization during photodoping, but for an intercalation reaction charge neutralization is accomplished by electrons.

5.9-3 The generation of electrons and ions

For an intercalation reaction to proceed a continuous supply of electrons and ions from outside is required. These two species are generated at the metal / metal-doped chalcogenide interface, which can be represented as a metal-semiconductor contact (Schottky barrier) having a band structure as given in Fig. 5-20 . The barrier height depends on the type of metal and possibly the preparation conditions of the chalcogenide. The barrier has to ensure separation of electron-hole pairs generated by light at that interface. At first a photogenerated electron-hole pair is created due to light absorption within the intercalation product and then the separation of electrons and holes by the interface space charge potential is achieved. In addition to the photodoped layer light absorption within the metal layer (for example Ag) can cause the internal photoemission of hot electrons within the metal layer (Lis and Lavine 1983) and hence generate another supply of electron/silver ion pairs to promote electronic and ionic processes.

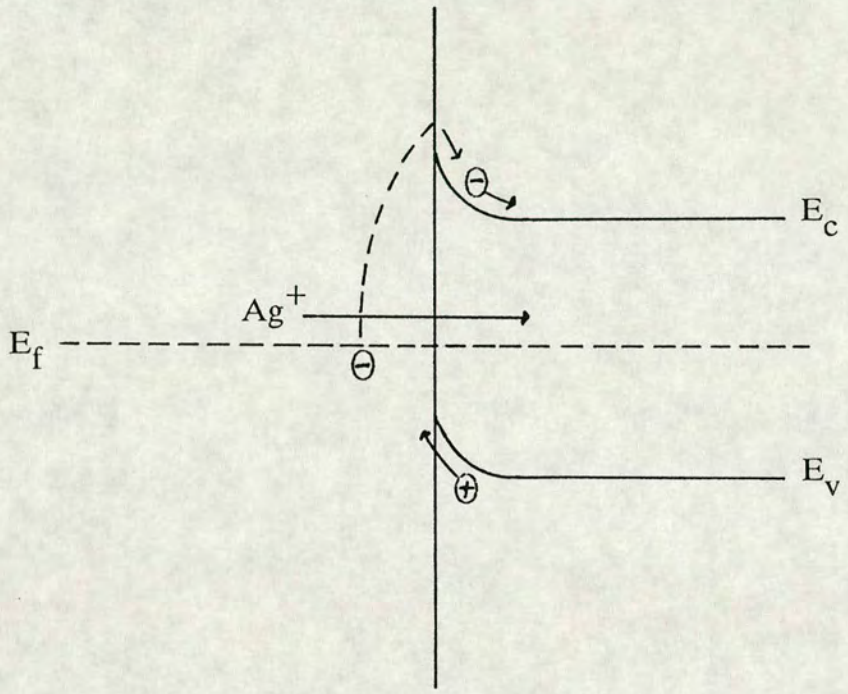

Fig. 5-20 Schematic diagram of the electron/ion generation at the metal/ metal-doped chalcogenide interface.

5.9-4 Spectral sensitivity

The spectral sensitivity of photodoping reflects where the actinic absorption of radiation is taking place. According to the above model, light absorption within the doped region (the amorphous intercalation product) is necessary to promote the ionic transport by the generation of free photocarriers and is also required in the vicinity of the interface between the metal and the doped chalcogenide to generate electrons and metal ions. The spectral dependence of the quantum efficiency of photogeneration in the reaction product can partly explain the spectral sensitivity of photodissolution (see section 5.5). The quantum efficiency of photogeneration changes by an order of magnitude over the wavelength range from blue to red.

5.9-5 Time dependence

The model considers photodoping as a photochemical solid state reaction which has an S-shaped kinetics curve. This is generally confirmed in the present work. The photodissolution rate has a linear time dependence at the beginning of the process while it goes to saturation at longer times. The results obtained in this work (see Fig. 5-7) clearly indicate that for a Ag-rich source the process is reaction limited (i.e photodissolution has a linear time dependence) while when the Ag source is exhausted a square-root-time dependence is observed for the photodissolution process, i.e the process is diffusion limited due to diffusion of the mobile reactants through the reaction product. This is in agreement with the prediction of the model. The induction period is not observed in the present study, possibly due to the high intensities and sample preparation method used in this work.

5.9-6 Compositional dependence

The model requires absorption of light within the reaction product to generate electron-hole pairs. The overall increase in the photodissolution rate in Fig. 5-9 can be

explained by the model. The absorption coefficient of As-S glasses increases monotonically with increase in As content. Also, for a fixed concentration of Ag, it is expected that the absorption coefficient of the reaction product increases with the increase in As content in the Ag-As-S system. Another factor which has to be taken into account is the compositional dependence of the ionic and electronic conductivities of the reaction product in the As-S system. Edmond (1968) has plotted the resistivity of various chalcogenide glasses versus their optical gap. His results indicate that the resistivity of chalcogenide glasses increases linearly with their band gap. In the As-S system the band gap decreases with increasing As-content, hence, from Edmond's observations, it is likely that their electronic conductivity will also increases with increasing As-content. Hence for a fixed concentration of Ag, it is expected that the conductivity of the reaction product (and therefore the photodissolution rate) increases with increasing As-content in the Ag-As-S system. The pronounced local maximum around the composition $As_{30}S_{70}$ in the As-S system is attributed to the change in morphology of the photodoped layer around this composition. The passage of electrons through a homogeneous As-S-Ag glass is likely to be faster than through a phase-separated material due to the presence of phase boundaries and additional defects in the phase-separated material.

5.9-7 Intensity dependence

As mentioned in section 5.6, different power law dependences on intensity have been obtained for the photodissolution rate in the present work with the exponent varying between 0.9 and 1.2 . Both electronic and ionic transport are involved in the photodissolution process. In the case of photoenhanced diffusion, the dark electronic conductivity is replaced by photoconductivity. In general, the photoconductivity of chalcogenide glasses is larger than the dark electronic conductivity by many orders of magnitude. The photoconductivity of the reaction product (photodoped layer) is the only factor which is affected by the light intensity. The typical temperature dependence of the photoconductivity of an amorphous semiconductor (Mott and Davis 1979) is shown in

Fig. 5-21. Three regimes can be considered. In regime I photoconductivity is smaller than dark conductivity $\sigma_{PH} < \sigma_d$; in regime II photoconductivity is characterized by bimolecular recombination, with $\sigma_{PH} \propto I^{1/2}$ where I is the illumination intensity. In regime III the recombination processes are monomolecular with $\sigma_{PH} \propto I$. In regimes II and III the activation energy for σ_{PH} is much less than that of dark conductivity. The small values of activation energies found for the photodissolution process (ΔE = 0.04 - 0.2 eV at room temperature) (Plocharski et al. 1987, Rennie 1986, Kokado et al. 1976) can be ascribed to the behaviour of the photoconductivity in regime III. The sublinear dependence of the photodissolution on light intensity can be ascribed to a crossover in the behaviour of photoconductivity from regime III to regime II (Elliot 1991).

5.10 Summary

Simultaneous reflectivity and transmissivity measurements have been employed to monitor the photodissolution kinetics of Ag in As-S films. The main points of the kinetics measurements are listed in 1-9 below.

1- Propagation of the photodoped front seems to be strongly dependent on the amount of Ag available for dissolution. For a thick silver layer, the data can be fitted to both time and square-root-time plots while for a thin silver layer the diffusive behaviour of the process is observed. The S shape typical of a photochemical solid state reaction is observed for the kinetics curves.

2- The variation in the photodissolution rate as a function of composition is attributed partly to the change in morphology of the photodoped material and partly to changes in the properties of the materials with increasing As content, e.g. changes in absorption or conductivity in the photodoped reaction product.

3- It is suggested that absorption alone in the photodoped layer cannot account for the

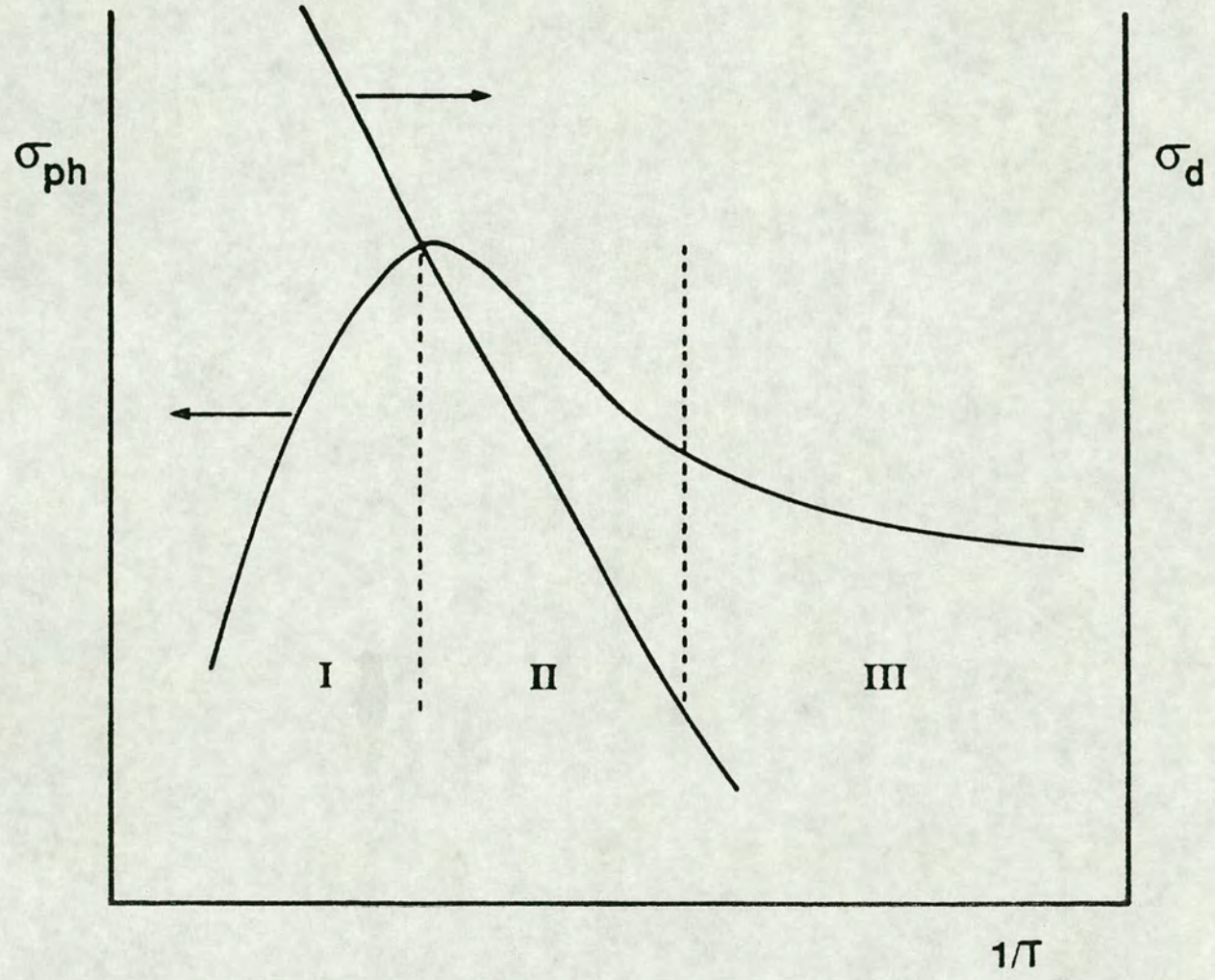

Fig. 5-21 Schematic illustration of the temperature dependence of the photoconductivity in an amorphous semiconductor showing three distinct regimes, I, II and III (see text for details). The temperature dependence of the dark conductivity is also shown for comparison. (From Elliott 1991).

observed spectral dependence of the photodissolution rate.

4- The photodissolution rate at blue wavelengths is higher than at green and red by a factor of ~ 2 and ~ 100 respectively.

5- The intensity dependence of the photodissolution rate has been fitted by a power law: the rate has a superlinear dependence on intensity at low levels but a sublinear dependence on intensity at high intensity levels. For each 10 incident photons approximately 1 silver ion is observed to be dissolved into the As-S film.

6- Other photoinduced effects such as irreversible photodarkening accompany the metal photodissolution process. An increase of up to 0.1 in refractive index as a result of illuminating the As-S film with green light makes these materials promising optical recording media. The extent of photodarkening increases with increasing As content.

7- A technique has been developed to analyse the transmissivity data at red wavelengths. The variation in the Ag layer thickness versus time can be obtained using this technique and the photodissolution rate can be determined by differentiating the transmissivity versus time curve using a Newton-Gregory algorithm.

8- A model is proposed for photodissolution based on the consideration of photodoping as an intercalation reaction of an amorphous solid. This model can explain the spectral dependence and the intensity dependence of the photodissolution rate and suggests that the actinic radiation is absorbed in the photodoped layer.

9- For creating grating structures a composition around $As_{30}S_{70}$ is optimum because it exhibits negligible photodarkening. The blue or green line of an argon ion laser with an intensity around 200-300 mW/cm^2 optimises the time of the fabrication process and hence the cost.

5.11 References

Bordogna, J., and Keneman, S.A., 1977, "Holographic Recording Media, edited by H. M. Smith (Berlin : Springer- Verlag), p. 229

Brown et al. 1980, in comprehensive chemical kinetics, Vol. 22 : Reactions in the solid state, Elsevier publ. co., Amsterdam/ Oxford/ New york, p. 80.

Buroff, A., and Baeva, R., 1975, Proc. VI Int. Conf. Am. Semiconductors, Leningrad.

Edmond, J.T., 1968, J. Non-Crystalline Solids, 1, p. 39.

Elliot, S.R., 1991, J. Non-Cryst. Solids, To be published.

Enck, S.W., and Pfister, G., 1976, in "Photoconductivity and related phenomena", edited by J. Mort and D.M. Pai, Elsevier scientific publishing company Amesterdam.

Ewen, P.J.S., Zakery, A., Firth, A.P., and Owen, A.E., 1988, Phil. Mag., B, 57(1), p. 1.

Firth, A.P., Ewen, P.J.S., and Owen, A.E., 1985, J. Non-Crystalline Solids, 77-78, p. 1153.

Firth, A.P., Ewen,P.J.S., and Owen, A.E., 1983, The structure of Non-Crystalline Materials, Edited by P.H. Gaskell, J.M. Parker and E.A. Davis (London:Taylor and Francis), p. 286.

Goldschmidt, D., and Rudman, P.S., 1976, J. Non-Cryst. Solids, 22, p. 229.

Hartke, J.L., and Regensburger, P.J., 1965, Phys. Rev., A, 139, p. 970.

Heavens, O.S., 1955, "Optical properties of thin solid films", (London:Butterworth scientific publications).

Ingram, M.D., 1985, J. Non-Crystalline Solids, 73, p. 247.

Johnson, P.B., and Christy, R.W., 1972, Phys. Rev., B,6(12), p. 4370.

Kawaguchi, T., Maruno, S., and Masui, K., 1987, J. Non-Crystalline solids, 95-96, p. 777.

Kitao, M., Ishikawa, T., and Yamada, S., 1986, J. Non-Crystalline Solids 79, p. 205.

Kluge, G., 1987, Phys. Stat. Sol., (a)101, p. 105.

Kokado, H., Shimizu, I., and Inoue, E., 1976, J. Non-Crystalline Solids, 21, p. 225.

Kolwicz, M.D., Chang, M.S., 1980, J. Electrochem. Soc., 127, p. 135.

Konan, K., Galibert, G., and Calas, 1988, J., Phys. Stat. Sol., (a)107, p. 273.

Lis, S.A., and Lavine, J.M., 1983, Appl. Phys. lett., 42(8), p. 675.

Malinowski, J., and Buroff, A., 1978, Contemp. Phys., 19, p. 99.

Main, C., and Owen, A.E., 1973, in "Electronic and Structural properties of Amorphous semiconductors", eds, P.G. LeComber and J. Mort, Academic press, p. 527.

Matsuda, A., and Kikuchi, M., 1973, Jap. J. appl. Phys., 42, suppl., p. 239.

Milne-Thomson, L.M., 1951, "The Calculus of Finite Differences", Macmillan.

Mott, N.F., and Davis, E.A., 1979, "Electronic Processes in Non-Crystalline Materials", Clarendon press, Oxford.

Ohmachi, Y., and Igo, T., 1987, Appl. Phys. Lett., 20(12), p. 506.

Owen, A.E., Firth, A.P., and Ewen, P.J.S., Phil. Mag., B, 52(3), p. 347.

Phariseau, P., 1956, Proc. Indian Acad. Sci., A44, p. 165.

Plocharski, J., Przyluski, J., and Teodorczyk, M., 1987, J. Non-Crystalline Solids, 93, p. 303.

Rennie, J.H.S., and Elliot, S.R., 1985, J. Non-Crystalline solids, 77-78, p. 1161.

Rennie, J.H.S., 1986, PhD Thesis, University of Cambridge.

Resel, R., Kluge, G., and Suptitz, P., 1987, J. Non-Crystalline solids 97-98, p. 1247.

Schmalzried, R., 1981, Solid State Reactions, Verlag Chemie Weinheim/Deerfield Beach(Florida)/Basel, p. 104.

Tai, K.L., Ong, E., and Vadimsky, R.G., 1982, Proc. Electrochem. Soc., 82-89, p. 9.

Tuller, H.L.P., and Barsoum, M.W., 1985, J. Non-Crystal. Solids, 73, p. 331.

Wagner, T., Frumar, M., and Benes, L., 1987, J. Non-Crystalline Solids, 90, pp. 517-520.

Yaji, T., and Kurita, S., 1983, J. Appl. Phys., 54(2), p. 647.

Yamaguchi, M., 1985, Phil. Mag., B,51(6), p. 651.

Zakery, A., 1986, 'An optical reflectivity study of silver photodissolution in amorphous As-S films', M.Sc. thesis, University of Dundee.

6. DISTRIBUTION OF SILVER AFTER PHOTODISSOLUTION

6.1 Introduction

In order to model the grating performance accurately it is necessary to know whether there is any variation of composition (and hence optical constants) with depth through the photodoped layer. Various techniques can be used to find the Ag profile and the composition variation of the photodoped As-S layer with depth. Of these, secondary ion mass spectroscopy (SIMS) is possibly the most powerful and has been used to monitor the Ag profile for photodissolution in Ge-Se glasses (Polasko, Tsai, Cagan and Pease 1986). Positron ion scattering is another, potentially useful, technique for monitoring the interfaces between different layers during photodissolution.

6.2 SIMS analysis

In SIMS a beam of ions is directed onto the sample and sputters from it atoms or groups of atoms. The spectrum of the different species in the sample can be mass analysed quantitatively. Cs^+ and O^- ion beams were used in this study. To avoid charging effects when analysing an As-S composition, a thin gold layer was deposited on the sample prior to the analysis. In the case of Cs^+, a 10 keV and 1 nA beam was used in these measurements. The raster area on the sample was 100 μm^2 while the beam diameter was $\sim$3 μm. The energy window used in this work was $\pm$10 eV . Although Cs^+ ions give a higher sputtering rate and a higher yield (and hence a higher sensitivity) than the O^- beam, an electron flood gun is needed for charge neutralization. On the other hand, for the O^- beam the charging effect is minimum. Hence for the analysis, a 10 keV and 5-10 nA O^- beam was used. In this case the raster area on the sample was $\sim 200 \mu m^2$ while the beam diameter was $\sim$20 μm.

Fig. 6-1 shows ion counts (on a linear scale) versus time for an undoped $As_{30}S_{70}$ film of thickness 0.5 μm undergoing sputtering from an O^- beam (the numerical labels 30, 16, and 75 denote the Si, O, and As signals respectively). The initial spike is due to the gold over-layer . As is seen, the As signal falls off gradually (by ~ 8%). This could be due to beam instability rather than a variation in the film composition because the same extent of variation was also obtained for an Al test film.

Fig. 6-2 shows the results for an $As_{30}S_{70}$ film fully photodoped with Ag (the initial film thicknesses being 0.5 and 0.13 μm for the $As_{30}S_{70}$ and Ag respectively). The Ag (109) signal rather than the Ag (107) signal was monitored because sulphur has 2 isotopes, S (32) and S (34), which means that As (75) can form As-S (107) and As-S (109) units which might interfere with Ag (107) or Ag (109). However, the abundance of S (32) is much higher than S (34) so that the Ag (109) signal is less affected. The Ag (109) signal drops by ~ 20 % with film depth and some of this decrease may well be due to variation of the Ag concentration with depth in the photodoped layer. This result indicates that the optical constants of these films may also vary slightly with depth. This variation in Ag distribution, however, is much less than for a typical Fickian diffusion profile as observed in $GeSe_2$ (Wagner and Barr 1982) using the Rutherford backscattering (RBS) technique.

An attempt was also made to determine the profile of the interface between the doped and undoped material by using an incompletely photodoped sample prepared by terminating the illumination before the Ag had reached the top surface of the film. However, during these experiments it became clear that the ion beam could affect the measurements. This is not surprising because an electron beam or an ion beam can be used as the radiation source for metal photodissolution in chalcogenide glasses (Chang et al. 1978). Since the Ag distribution may be sensitive to the ion beam, some caution is required in interpreting these SIMS results.

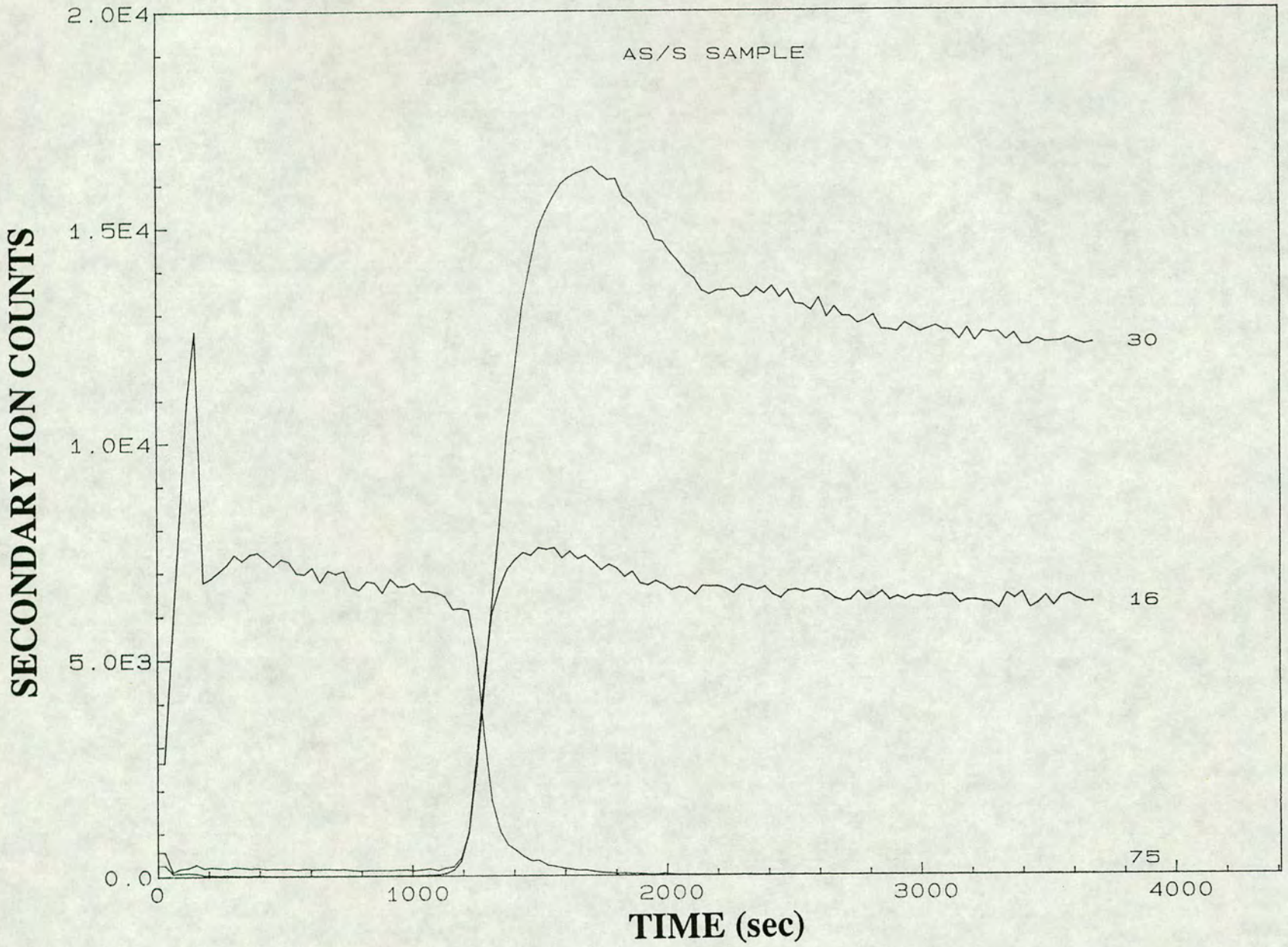

Fig. 6-1 Secondary ion count versus time for an undoped $As_{30}S_{70}$ film undergoing etching with an O^- beam. Note that the ion count (which is proportional to element concentration) is on a linear scale.

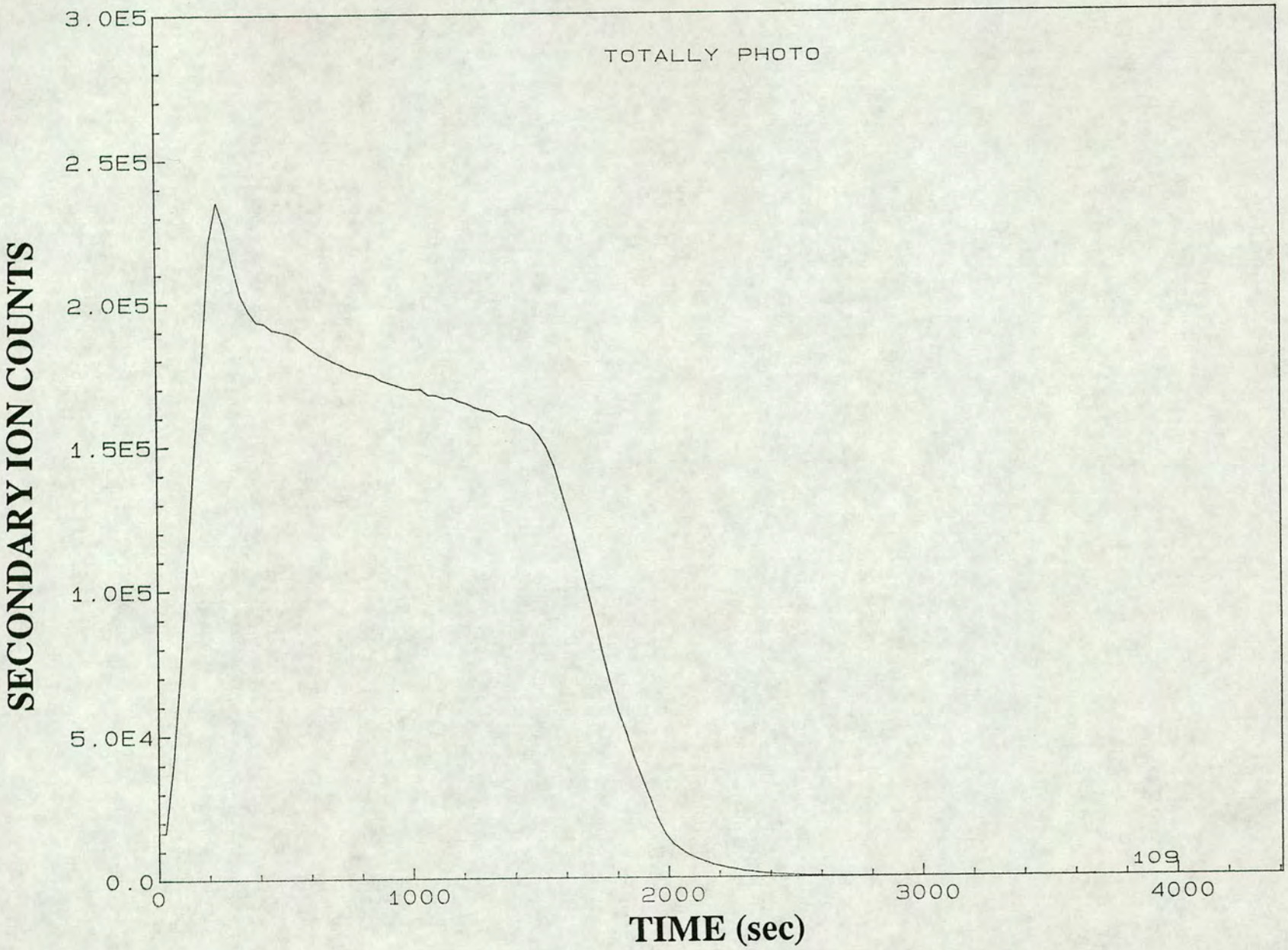

Fig. 6-2 Secondary ion count versus time for an $As_{30}S_{70}$ film completely photodoped with Ag and undergoing etching with an O^- beam. Note that the ion count (which is proportional to element concentration) is on a linear scale.

6.3 Positron ion scattering

In this non-destructive technique the measurements are performed with a variable energy (0-25 keV) positron beam (β^+) in ultra-high vacuum (10^{-10} torr) (Lathinen, Vehanen, Makinen, Huttunen, Rytsola, Hautojarvi and Bentzon 1986). When a positron annihilates with an electron, the 511 keV γ rays produced are Doppler-broadened due to the finite momentum of the annihilation. An energy sensitive γ ray detector which measures the energy broadening of the 511 keV annihilation line is used in these measurements and interface positions can be determined to within 100 A (Vehanen, Saarinen, Hautojarvi and Huomo 1987).

The ideal size of the sample for these measurements was 35 mm square. Two samples were used in these measurements. In both samples first a thin layer of chalcogenide glass ($As_{40}S_{60}$) was deposited onto a clean microscope slide and then a thin layer of Ag was deposited on top. The original thicknesses of the $As_{40}S_{60}$ and Ag were 12000 and 5000 A respectively. Both of these samples were exposed through the substrate with a 200 W mercury lamp. Sample 1 was exposed for 5 hrs and sample 2 for 9 hrs. The previously determined exposure characteristics of photodissolution using this light source showed that the photodoped layer in sample 1 was ~ 3000 A thick and ~ 6000 A in sample 2. In both of these samples the unreacted Ag on the surface was etched away using an etchant of $Fe(NO_3)_3$ in methanol. The parameter measured in these experiments is the lineshape parameter S which is defined as the area of a fixed region in the center of the spectrum divided by the total area of the spectrum.

Fig. 6-3 shows the variation of S versus energy for both of the samples. If there are different characteristic S values in the photodoped and undoped regions, then we should see the transition between the two in the energy regions indicated on the plots (i.e at about 7.6 keV for sample 1, and 11.7 keV for sample 2) and should therefore be able to identify the position of the doped/undoped interface. However, the only transition observed in both samples is that at the $As_{40}S_{60}$ /microscope-slide interface (marked at 12000 A on the plots). It might be that the change in S we are looking for is small compared with

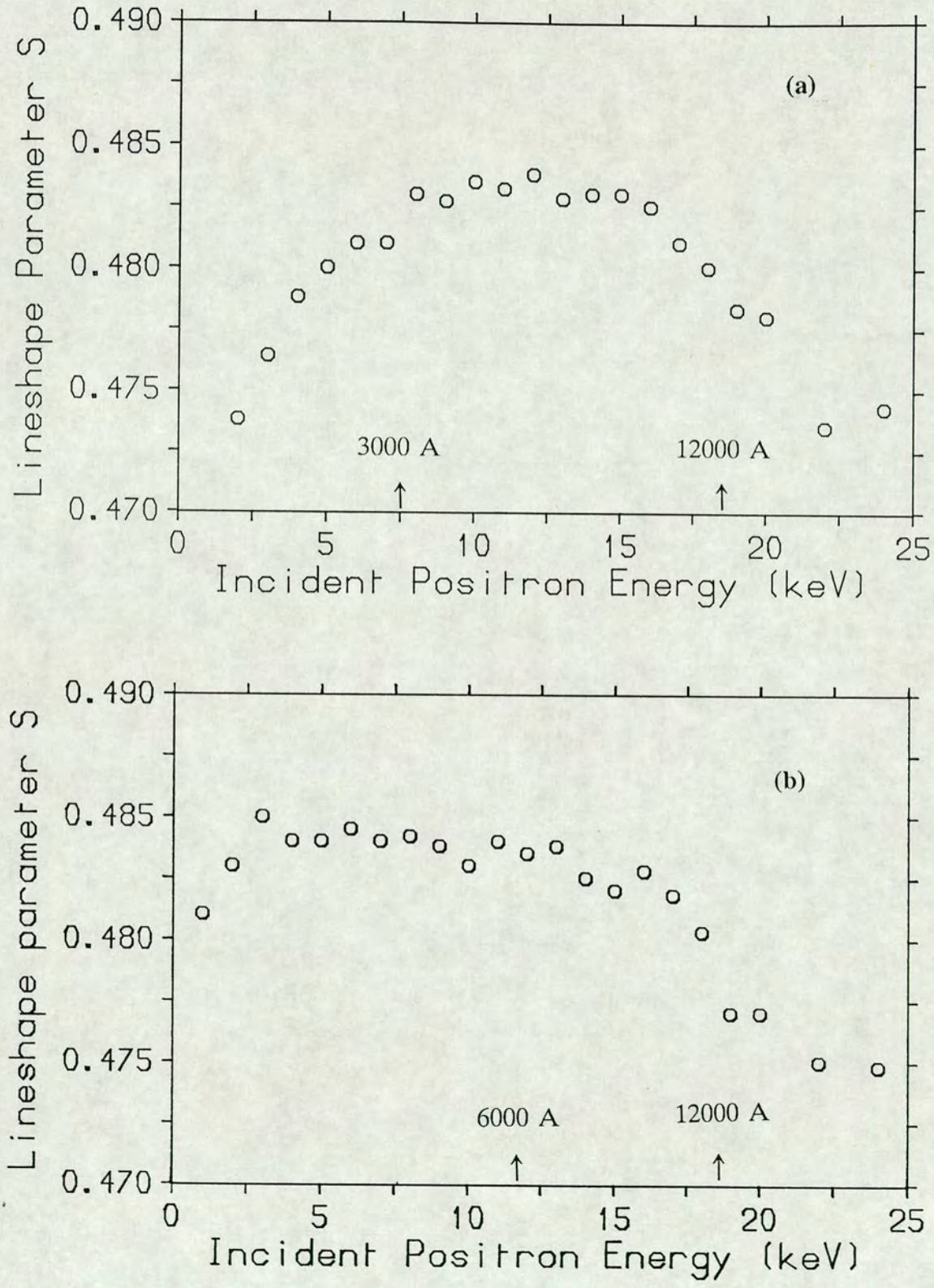

Fig. 6-3 Lineshape parameter S versus incident positron energy in $As_{40}S_{60}$ films partially doped with Ag. (a): Ag photodoped in $As_{40}S_{60}$ to 3000 A (sample 1); (b): Ag photodoped in $As_{40}S_{60}$ to 6000 A (sample 2). In both of these films the initial $As_{40}S_{60}$ thickness was 12000 A.

experimental uncertainties.

The most puzzling feature of the plots is the big difference at low implantation energies. The fall-off in S in sample 1 is similar to behaviour that is seen in semiconductor samples, usually associated with positron diffusion to the surface, although it is not clear why the positron diffusion length should be apparently so different between the two samples. It might be that the surface S values for the two samples are very different. An attempt was made to measure the S values of the undoped and completely photodoped $As_{40}S_{60}$ separately, but again very similar S values were obtained for these materials.

6.4 Summary

Secondary ion mass spectroscopy has been used to determine the interface profile and the variation in composition with depth in As-S films and As-S films photodoped with Ag. The composition of the As-S film seems to be constant throughout but the Ag concentration in the photodoped layer possibly decreases by ~ 10-20% with depth through the photodoped film. Positron ion scattering could not yield any conclusive results for the doped/undoped interface in the case of $As_{40}S_{60}$ photodoped with Ag.

6.5 Acknowledgements

I am grateful to Dr. Paul Coleman of the School of Mathematics and Physics at East Anglia University for his help in performing and analysing the results of the positron ion scattering measurements.

6.6 References

Chang, M.S., and Chen, J.T., 1978, Appl. Phys. Lett., 33, p. 892.

Lahtinen, J., Vehanen, A., Huomo, H., Makinen, J., Huttunen, P., Rytsola, K., Hautojarvi, P., and Bentzon, M.D., 1986, Nucl. Inst. Meth., B17, p. 73.

Polasko, K.J., Tsai, C.C., Cagan, M.R., Pease, R.F.W., 1986, J. Vac. Sci. Technol., B4, p. 418.

Vehanen, A., Saarinen, K., Hautojarvi, P., and Huomo, H., 1987, Phys. Rev., B35 p. 4606.

Wagner, A., Barr, D., 1982, in Proc. Symp. Inorganic Resists systems, D.A. Doane and A. Heller (eds) Proc. Electrochem. Soc. Vol. 82-9, p. 281.

7. GRATING FABRICATION AND DIFFRACTION EFFICIENCY MEASUREMENTS

7.1 Introduction

The concept of optical elements using diffraction is quite an old one, for example, Fresnel's zone plate dates from about 1830. The realization of ruled, planar, diffraction gratings and of ruled, concave, diffraction gratings gave rise to the first significant applications of diffractive optical elements. Their applications in, for example, monochromators, laser tuning devices, shapers, as well as gratings, in suitable recording media using holographic techniques.

The recording materials available can be divided into two main classes: latent image forming and dynamic (non-latent image forming). Latent image media require some form of processing after the recording exposure has been made in order to form the grating as some variation in material properties. Thus two step hologram formation is required: exposure and development. Dynamic media, on the other hand, produce the holographic gratings whilst being exposed to the recording beams. The recording media available are described below in sections 7.2-1 to 7.2-6.

7.2 Recording media

7.2-1 Photorefractive crystals

These materials include lithium niobate, barium titanate and bismuth silicon oxide (Burke et al. 1978). They are dynamic media and operate through a combination of photosensitivity and the electro-optic effect. Their sensitivity is relatively low (typically 10^{-3} to 1 J cm^{-2} for 1% efficiency) and crystal thicknesses used are usually from 10 μm to 1 cm. Resolution is nominally > 1500 lines/mm .

7.2-2 Photochromics

In these materials electromagnetic radiation can stimulate a change in colour (and/or refractive index) in one or both directions and photochromics are thus dynamic, reversible, materials. It is this reversibility which makes them potentially very useful. However they have low sensitivity (3×10^{-3} to 1 J cm^{-2}) and low efficiency could limit their use, although they have good resolution (> 2000 lines/mm) and typical thicknesses of 0.1 to 2 mm.

7.2-3 Photopolymers

These materials produce volume phase gratings by photoninduced polymerization. They have applications in holographic interferometry and information storage (Bartolini et al. 1976) and can be produced over a very wide range of thicknesses (up to 8 mm), which compensates somewhat for the rather low modulation achievable (0.2 to 0.5 %). Sensitivity can vary widely (10^{-3} to 10^{2} J cm^{-2}) and their resolution is in the 3000 - 5000 lines/mm range.

7.2-4 Dichromated gelatin

Dichromated gelatin is a latent material. Exposure requirements are reasonable (3×10^{-3} to 4×10^{-1} J cm^{-2} at 441-514 nm) and film thicknesses can be varied from 1-25 μm . The modulation available is high (~ 0.08) as is the resolution (> 5000 lines/mm), and high optical quality volume phase gratings approaching 100 % efficiency can be made.

7.2-5 Silver halide emulsions

This is the traditional holographic recording medium and is still used extensively. Its early utilization arose naturally from its use in photography. The main disadvantages are relatively high scatter and low resolution. To meet very high resolution requirements of ~6000 lines/mm, holographic emulsions (for example, Agfa Gevaert 8E56) have been

developed with very fine grain structures (Smith 1977). The sensitivity of silver halide emulsions used in holography (typically from 10^{-6} to 10^{-3} J cm^{-2}) is much higher than for most other available materials. It is this relatively high sensitivity, together with the wide commercial availability, good reproducibility and high potential efficiency –close to 80 %– (Slinger et al. 1985) which has made silver halide emulsions so attractive to holographers. The reason for the high sensitivity of this material is the great amplification that occurs during the development process. Silver halides are normally more sensitive to the blue/u.v. end of the spectrum. These materials need development as well as fixing, and yield, after fixing, an amplitude or absorption hologram. Such holograms are of low efficiency, the maximum possible for a planar, amplitude, transmission grating being only 6.25 % . The amplitude grating can, however, be converted into a phase grating by a bleaching step in which the metallic silver is converted into a transparent silver salt. Because of the difference in refractive index between the silver salt and the gelatin, the grating modulation is converted from amplitude to phase.

Materials described in sections 7.2-1 to 7.2-5 have been developed for visible or near IR band performance. They are not suitable for thermal band (3-5 and 8-14 μm) applications however and the number of materials available for such applications is limited.

7.2-6 Chalcogenide glasses

Chalcogenide glasses are currently under investigation because of their excellent IR transmission. They have passbands from 0.5 to 20 μm, depending on composition, and their resolution capability is > 3000 lines/mm. However, their sensitivity is rather low, $\sim 10^{1}$ to 10^{2} J cm^{-2} . Both thin and volume gratings can be made using mask exposure and also by the holographic technique (Kostyshin et al. 1970, Keneman 1971). One of the attractive features of typical chalcogenide glasses, such as those in the As-S system, is the very high modulation in refractive index which is possible using the metal photodissolution effect. Modulations in refractive index as high as 0.5 can be achieved which makes these materials suitable for the fabrication of volume phase gratings.

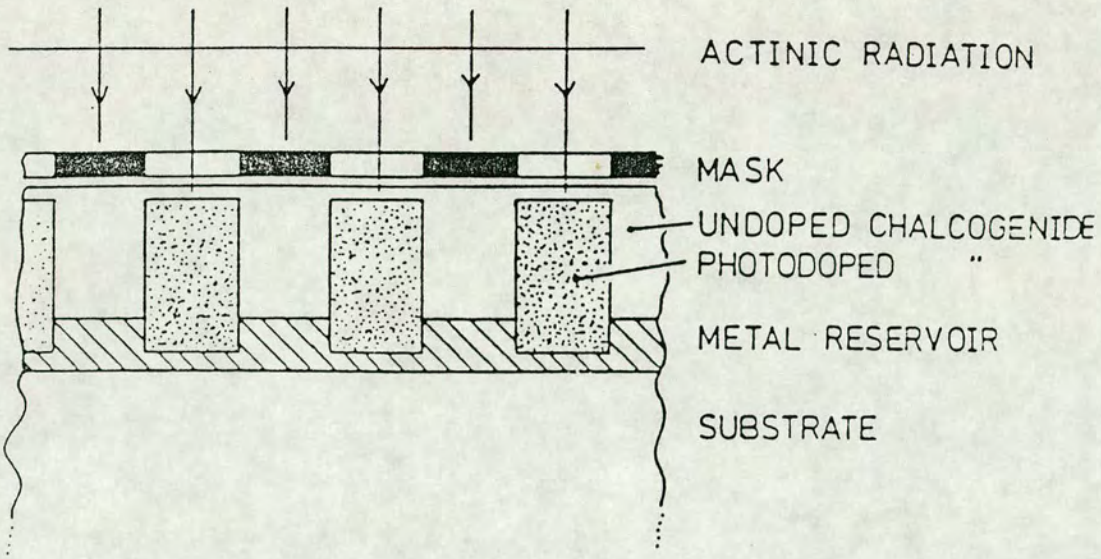

Fig. 7-1 Grating fabrication using mask exposure.

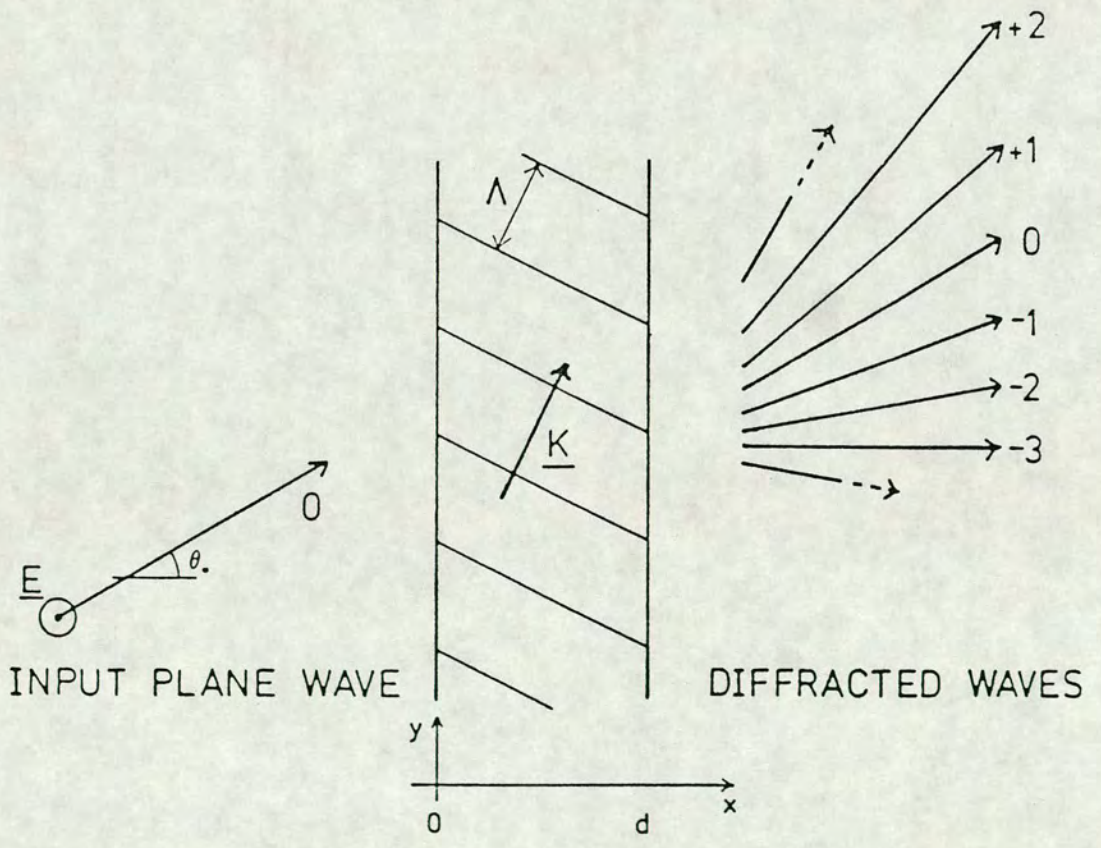

Fig. 7-2(a) Grating system to be analysed.

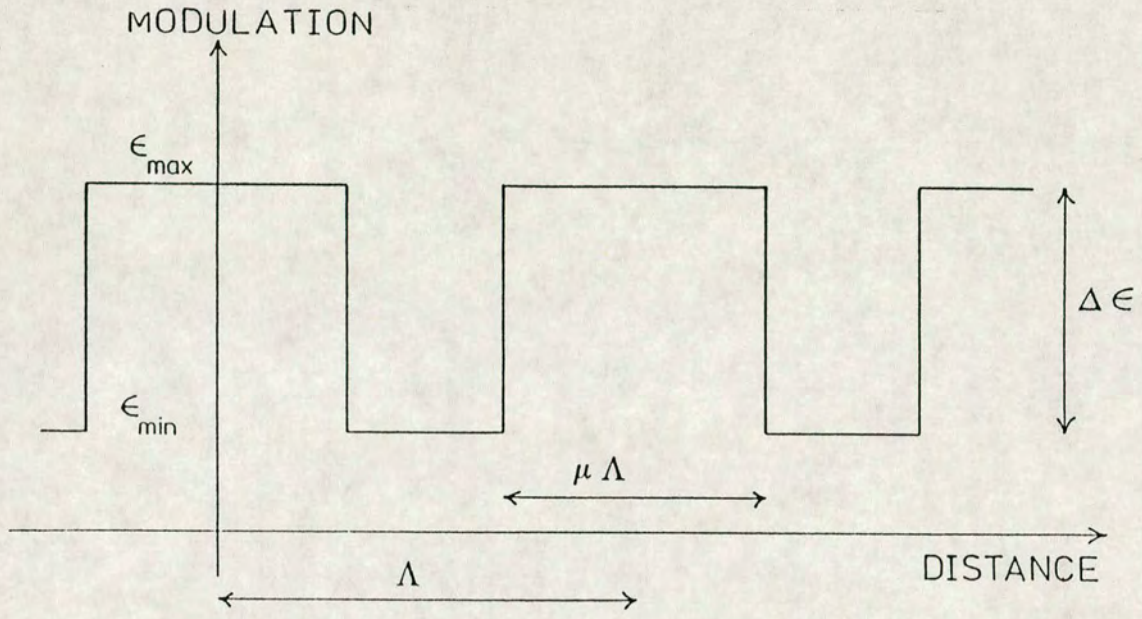

$$\epsilon_o = \epsilon_{min} + \mu \Delta\epsilon$$

$$\epsilon_i = \frac{2\Delta\epsilon}{i\pi} \sin(i\mu\pi)$$

Fig. 7-2(b) The quantity μ determines the mark/space ratio of the rectangular grating. $\mu = 0.5$ corresponds to a square wave grating. If ϵ_{min} is unity, the grating is a surface relief grating. Otherwise, it can be classed as a phase grating.

7.3 Gratings formed by mask exposure

7.3-1 Introduction

The metal photodissolution effect can be used to produce grating patterns either holographically or via exposure through a mask as shown in Fig. 7-1. In the latter case light of a suitable wavelength is passed through a mask to form an intensity pattern on the chalcogenide layer. Since no photodoping occurs in the unilluminated regions there is an abrupt boundary between the undoped and photodoped region and an exact image of the mask pattern is transferred into the chalcogenide film. A bulk (phase) grating is left when the illumination is removed. This structure can be transformed into a surface relief profile if the undoped region is etched away by a simple alkali etchant or reactive ion etching.

7.3-2 Theoretical analysis of grating performance

A theoretical analysis is required to predict the likely performance of gratings and also the grating parameters needed for efficient operation. The analysis used here was developed by Slinger (1988). The grating is considered to be planar and replayed with a plane monochromatic wave, and in general many diffracted orders will be present (see Fig. 7-2(a)). If only one diffracted order beside the zero order (transmitted wave) is present the element is considered to be operating in the volume diffraction regime, whereas if many diffracted orders are significant thin grating behaviour is said to occur. In other words the power in the incident wave is divided between many orders in the case of a thin grating, while it is only divided between the zero and one diffracted order in the case of a volume grating. Hence volume gratings are usually more efficient for practical applications. For the chalcogenide gratings considered in the present study a coupled wave analysis was used to investigate the diffraction characteristics for the case of a rectangular modulation profile.

The grating profile in Fig. 7-2(b) can be written as the Fourier series :

$$\epsilon(r)=\epsilon'_0-j\epsilon''_0+\sum_{i=1}^{\infty}(\epsilon'_i-j\epsilon''_i)cos(iK.r) \quad (1)$$

where the profile is assumed to be an even function. For the rectangular profile we have :

$$\epsilon'_0 = \epsilon_{min} + \Delta\epsilon\ \mu \quad (2)$$

and :

$$\epsilon'_i=(\frac{2}{i\pi})\Delta\epsilon sin(i\mu\pi) \quad (3)$$

where ϵ'_0 is the bulk dielectric constant of the slab; ϵ''_0 is the bulk absorption; ϵ'_i and ϵ''_i are the phase and absorption modulation of the ith harmonic of the grating profile; K is the grating vector (the direction of which is perpendicular to the grating fringes) with $K = 2\pi/\Lambda$, Λ being the grating period; $\Delta\epsilon=\epsilon_{max}-\epsilon_{min}$; and μ is a fill parameter (mark/space ratio). The modulation is taken to be constant throughout the depth of the grating. This assumption is generally valid since results of SIMS measurements (see Chapter 6) showed that composition of the undoped layer is constant with depth and in the photodoped layer the composition changes only slightly with depth. Replay is assumed to be with an infinite monochromatic plane wave at angle θ_0 to the plane of the grating normal. Polarization is assumed to be perpendicular to the grating plane since this ensures maximum coupling (Solymar and Sheppard 1979). The time independent scalar wave equation can be used :

$$\nabla^2E+\beta^2(\frac{\epsilon}{\epsilon'_0})E=0 \quad (4)$$

where $\beta=2\pi\frac{\sqrt{\epsilon'_0}}{\lambda}$ is the propagation constant in the grating, λ being the free space

wavelength of the radiation . It is assumed that the diffracted waves are such that the electric field in the grating is of the form:

$$E = \sum_{i=-\infty}^{\infty} A_m \exp(-jk_m .r) \tag{5}$$

where A_m is the amplitude of the mth diffracted order having wave vector k_m and m = 0 corresponds to the replay wave. A relationship between these vectors is taken to be in the K-vector closure form :

$$k_m = k_0 + mK \tag{6}$$

Substituting Eqn. (5) into (4), with (1) and (6), and equating coefficients of $\exp(-jk_m.r)$, a set of differential equations of the form in Eqn. (7) is obtained.

$$\frac{d^2A_m}{dx^2} - 2jk_{mx}\frac{dA_m}{dx} + [(\beta^2 - k_m^2) - j\beta^2\frac{\epsilon''_0}{\epsilon'_0}]A_m + \frac{\beta^2}{2}\sum_{i=1}^{\infty}[\frac{\epsilon'_i}{\epsilon'_0} - j\frac{\epsilon''_i}{\epsilon'_0}][A_{m+i} + A_{m-i}] = 0 \tag{7}$$

If the amplitudes A_m change relatively slowly with x it can be assumed that the second derivatives in Eqn. (7) are negligible. From (7) it can be seen that this situation will arise if the dephasing parameter $(\beta^2 - k_m^2)$, the ratio $\frac{\epsilon''_0}{\epsilon'_0}$ and the modulation ratios $\frac{\epsilon_i}{\epsilon_0}$ are small. The latter two conditions can be met if :

$$\epsilon''_0,\ \epsilon'_i \text{ and } \epsilon''_i \ll \epsilon'_0.$$

Dropping the second derivatives, Eqn. (7) simplifies to become

$$\frac{k_{mx}}{\beta}\frac{dA_m}{dx} + (\alpha + j\nu_m)A_m + j\sum_{i=1}^{\infty}[\kappa'_i - j\kappa''_i][A_{m+i} + A_{m-i}] = 0 \tag{8}$$

where $\alpha = \beta\frac{\epsilon''_0}{2\epsilon'_0}$, $\nu_m = \frac{(\beta^2 - k_m^2)}{2\beta}$, $\kappa'_i = \frac{\beta\epsilon'_i}{4\epsilon'_0}$, $\kappa''_i = \frac{\beta\epsilon''_i}{4\epsilon'_0}$

The physical interpretation of equations (8) is as follows :

Each diffraction order A_m is coupled to the (m±i) orders (A_{m+i} and A_{m-i}) by the ith coupling coefficients (κ'_i and κ''_i). In contrast to the coupling mechanisms in a sinusoidal grating (i=1 only), the coupling paths in gratings of more complex profile are much more numerous. The central terms include absorption losses (α) and the dephasing term (ν_m), a measure of the mismatch in phase velocities of the diffracted orders. For significant power transfer from one order to another, three conditions must be met (Solymar and Cooke 1981). Firstly, there must be a coupling path between the two orders. Also their phase velocities must be approximately equal. Finally, the length of the interaction region must be correct. Note, however, that indirect coupling can occur via other diffraction orders.

Let the volume parameter Ω and the parameter P be defined as, respectively,

$$\Omega = \frac{K^2}{2\beta\kappa_1} \tag{9}$$

and :

$$P = sin(\theta_0 - \Phi)\frac{2\beta}{K} \tag{10}$$

where $\kappa_1 = \kappa'_1 - j\kappa''_1$ and Φ is the grating slant (angle of the grating vector to the slab face). On substitution into Eqn. (8):

$$\frac{k_{mx}}{\beta}\frac{dA_m}{dx} + \left\{\alpha - jm\kappa_1\Omega(m+P)\right\}A_m + j\sum_{i=1}^{\infty}\kappa_i[A_{m+i} + A_{m-i}] = 0 \tag{11}$$

Absorption losses are now neglected. For the chalcogenides under consideration this is a good approximation over much of their IR transmission band. For example, amorphous $As_{40}S_{60}$ has an absorption coefficient α of around 10^{-2} cm^{-1} in the 1 to 10 μm band (Young 1971). The photodoped regions are only slightly more absorbing (see Chapter 4) in

the above wavelength band. The assumption of no absorption also precludes the existence of absorption modulation. Finally, the grating is assumed to be unslanted, i.e the grating vector is parallel to the input and exit boundaries. Such gratings would result, for example, using a mask with exposure by plane wave, normally incident radiation. Thus the problem becomes one of analyzing a pure phase, lossless, unslanted, transmission grating.

Equations (11) then reduce to the following set of coupled equations, for m= $-\infty$, ..., -1,0,+1,.....,$+\infty$:

$$\frac{dA_m}{d\zeta} - jm\Omega(m+P)A_m + j\sum_{i=1}^{\infty}\frac{\kappa_i}{\kappa_1}[A_{m+i}+A_{m-i}]=0 \qquad (12)$$

where $\zeta=\kappa'_1\frac{x}{\cos\theta_0}$ is the modulation parameter.

These equations obey power conservation. The transmission grating boundary conditions are :

$$A_m(x=0)=0 \quad (m\neq 0) \quad \text{and} \quad A_0(x=0)=1 \qquad (13)$$

Solution of equations (12) subject to these boundary conditions will give the amplitudes of the diffraction orders, A_m , as a function of the modulation ζ, for a given Ω and P .

7.3-3 Diffraction Regimes

In general the solution of the infinite set of equations (12) requires numerical techniques and truncation to a finite number of diffraction orders. However, there are two limiting cases for which analytic solutions are possible. These are at opposite extremes of transmission grating behaviour, and occur when the thickness parameter Ω takes vanishingly small or very large values. The former case is referred to as thin grating

behaviour (often termed Raman-Nath Diffraction after Raman and Nath's thin, sinusoidal grating analysis) (Raman and Nath 1935-6); the latter as volume (or thick) diffraction. In between these is the multiwave regime and these three cases are described in (a), (b) and (c) below.

(a) Thin Grating Regime

As Ω tends to very small values, the dephasing term for each diffraction order becomes very small. Large numbers of orders can have significant power in them and equations (12) reduce to the following, for m= $-\infty$,.....,-1,0,+1,..... $+\infty$:

$$\frac{dA_m}{d\zeta}+j\sum_{i=1}^{\infty}\frac{\kappa_i}{\kappa_1}[A_{m+i}+A_{m-i}]=0 \qquad (14)$$

For the sinusoidal case ($\kappa_i=0$ for $i\neq1$) the solution is well known, and is in terms of Bessel functions :

$$A_m(\zeta)=(-j)^m J_m(2\zeta) \qquad (15)$$

where $J_i(x)$ is a Bessel function of the first kind, of order i. A thin, sinusoidal phase grating is unselective, having a maximum efficiency η_m of 33.9 % , for m = $\pm$ 1 at $\zeta=1.84$, where η_m is defined as the ratio of power in the mth diffraction order to that in the incident, zeroeth order. This low efficiency, combined with the large number of significant orders, generally excludes such gratings from use in many applications (although there are exceptions). For the thin, rectangular grating case, with the modulation as specified by equations (2), then (14) :

$$\eta_0=|A_0(\zeta)|^2=1-4(\mu-\mu^2)\sin^2\left\{\frac{\pi\zeta}{(2\{1-\cos(2\pi\mu)\})^{1/2}}\right\} \qquad (16)$$

and :

$$\eta_m = |A_m(\zeta)|^2 = \frac{2}{(m\pi)^2}(1-\cos(m\,2\pi\mu))\sin^2\left\{\frac{\pi\zeta}{(2\{1-\cos(2\pi\mu)\})^{\frac{1}{2}}}\right\} \qquad (m \neq 0) \qquad (17)$$

Maximum efficiency is 40.5 % for the ± 1 orders. As in the sinusoidal case, such thin, rectangular phase gratings generally have limited use in diffractive elements (computer generated holograms are often of this type, but in their case, efficiency can be increased by copying into a volume medium).

The thin grating regime is found typically for $\Omega \leq 0.01$. As Ω increases much above this value then equations (13) become less accurate as the dephasing terms start to become significant.

(b) Volume Grating Regime

At large values of Ω , Bragg effects become dominant. Diffraction orders, other than the on-Bragg order, have such a large mismatch in phase velocities that very little power is coupled to them. In the limiting case, for replay of the grating in the vicinity of the m = i on-Bragg condition, the infinite set of coupled wave equations (12) reduce to only two in number, provided i is a harmonic of the grating profile:

$$\frac{dA_0}{d\zeta} + j\frac{\kappa_i}{\kappa_1}A_i = 0 \qquad (18)$$

and

$$\frac{dA_i}{d\zeta} - ji\,\Omega(i+P)A_i + j\frac{\kappa_i}{\kappa_1}A_0 = 0 \qquad (19)$$

Analytic solutions are possible when fully on-Bragg, and these reduce to :

$$\eta_0 = \cos^2(\zeta \frac{\kappa_i}{\kappa_1}) \tag{20}$$

$$\eta_i = \sin^2(\zeta \frac{\kappa_i}{\kappa_1}) \tag{21}$$

The solutions in equation (21) agree with Kogelnik's analysis (Kogelnik 1969) when i=1. Thus for large enough Ω (significant volume behaviour is generally taken to occur for $\Omega > 10$), 100 % conversion to the ith order is achievable. This occurs when replay is on-Bragg for the ith harmonic of the grating, at :

$$\zeta = (2n+1)\pi \frac{\kappa_1}{2\kappa_i} \tag{22}$$

where (n= 0,1,2,3,.....)

The high efficiencies of these volume, phase gratings mean that they have many applications. In particular, they find use in diffractive optical elements, for example supermarket scanners and head-up displays. Although most bulk grating volume elements use sinusoidal modulation, since most practical recording media respond in this way, there is no reason why volume rectangular gratings cannot be used to similar effect.

(c) Multiwave Grating Regime

Between the thin and volume regimes there is an intermediate region of grating behaviour. In practice, many gratings may not have large enough values of Ω to guarantee that they will operate in the volume region. Investigation of the multiwave regime is therefore necessary to determine if acceptable grating behaviour is possible. For example, it may be feasible to achieve high enough efficiencies, for a particular application, without wasting unnecessary effort to increase the Ω value of the grating.

In the multiwave regime, the number of significant diffraction orders is generally large but finite. Recourse to numerical solution of a truncated set of equations (12) is therefore necessary. Thus for m = -N, ...,-1,0,+1,.....,N :

$$\frac{dA_m}{d\zeta} - jm\Omega(m+P)A_m + j\sum_{i=1}^{2N}\frac{\kappa_i}{\kappa_1}(A_{m+i}+A_{m-i}) = 0 \qquad (23)$$

where N is the number of the highest diffraction order containing significant power. Generally speaking, if Ω is small, N will be large and as Ω increases, N will decrease accordingly. This reflects the grating's performance as it changes between the two limiting cases of thin and volume behaviour.

Numerical solutions of the coupled wave equations (23) subject to the transmission boundary conditions as given in Eqn. (13) were solved using a Runge Kutta technique (Slinger 1988). These results show that in the bulk case, close to 100 % efficiencies should be possible at least in the volume regime. Fig. 7-3 shows a 3-dimensional plot of calculated diffraction efficiency vs. Ω and ζ. A contour plot of the calculated diffraction efficiency is shown in Fig. 7-4. The contours show first order diffraction efficiency for a rectangular modulated grating as a function of the modulation parameter ζ and the volume parameter Ω . Contour 1 is 10 % efficiency , 2 is 20 % etc. Over 90 % efficiency is possible in the multiwave regime and this operating point (point A) may be useful in some circumstances.

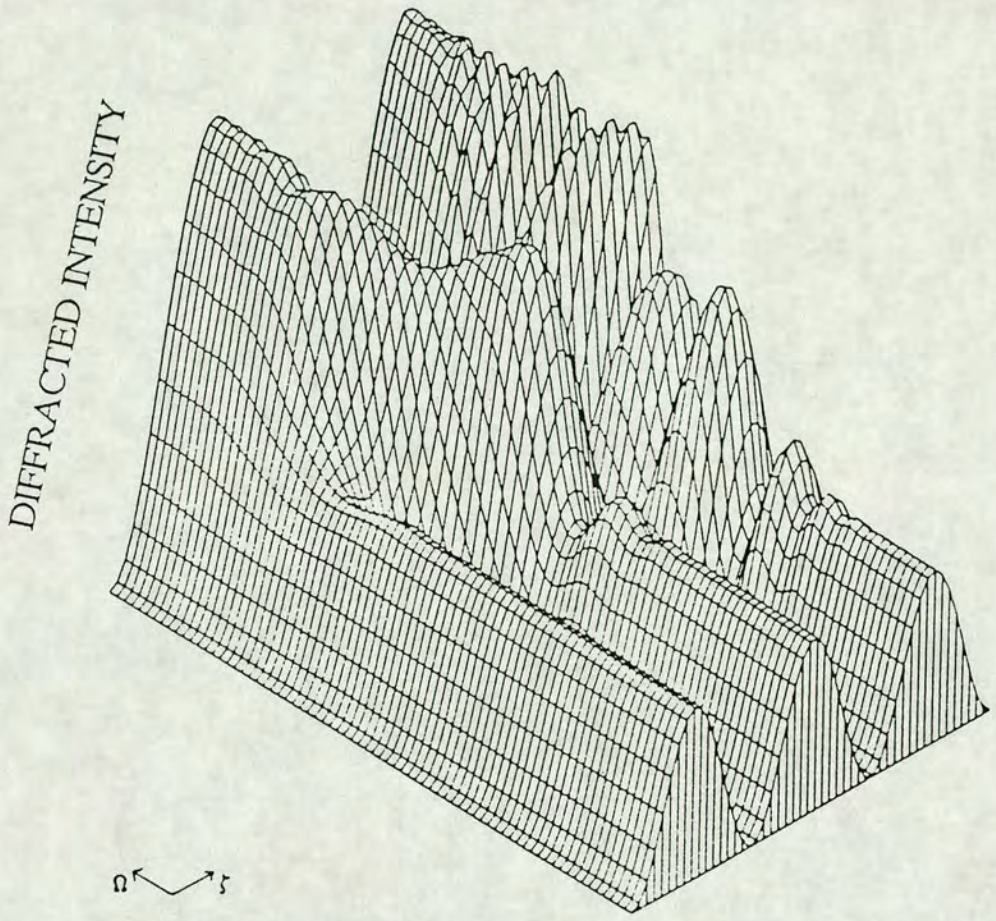

Fig. 7-3 For replay at the first Bragg angle, the amplitudes of the first diffraction order are shown here as a function of Ω (thickness parameter) and ζ (modulation parameter) for a square wave grating. Small values of Ω corresponds to the thin grating regime. It can be seen that in such a case the grating is limited to low values of efficiency. For high values of Ω, the volume regime is encountered and high efficiencies are achievable.

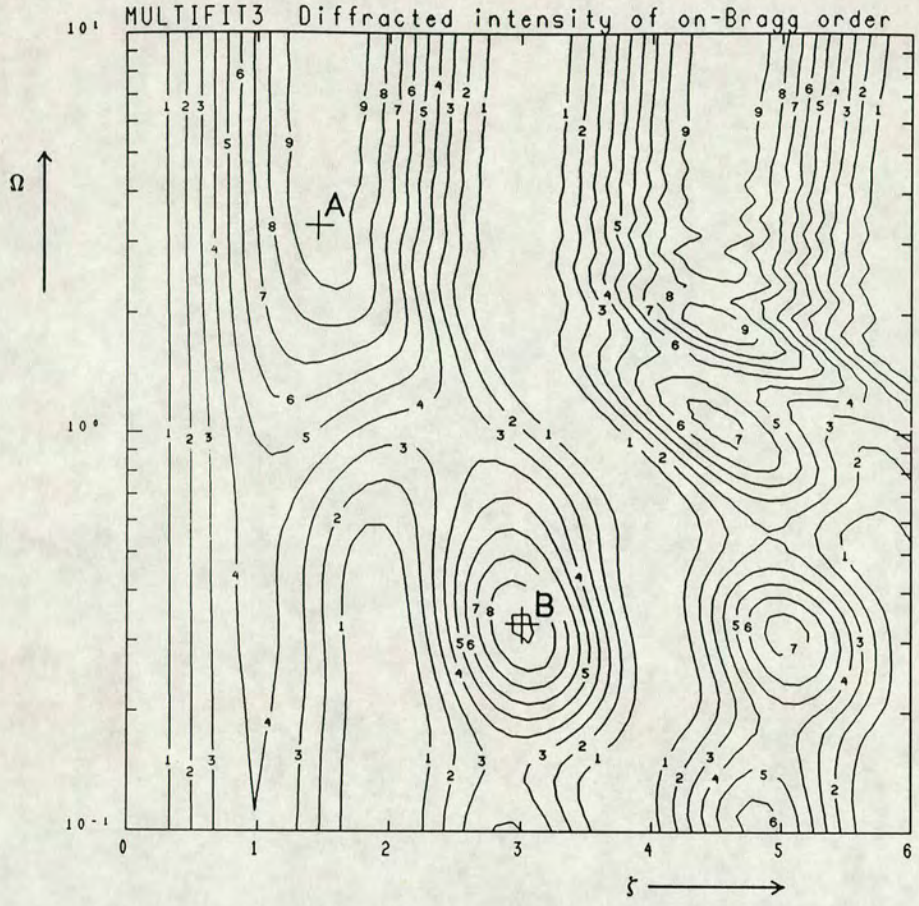

Fig. 7-4 Contour plot for the diffraction efficiency for rectangular grating ($\mu = 0.4$) case. The two potential operating points, A and B, are shown.

Coupled wave theory as discussed above can be used to predict the required thicknesses for different types of grating element at different wavelengths of operation and typical values for photodoped chalcogenide devices are given in Table 7-1. These results are for a square wave profile and assume refractive indices of 2.65 and 2.3 for the doped and undoped materials respectively. For example, thicknesses between approximately 6 and 23 μm are required for 10.6 μm operation. Such large thicknesses set some limits on the applicability of photodissolution, regarding the exposure time. Limitations and possible solutions will be further discussed in some detail in chapter 8.

Element Thicknesses (μm)			
Type of element	Replay wavelength (μm)		
	0.632	4.0	10.6
Bulk grating	1.39	8.77	23.2
Surface relief grating	0.48	3.0	8.06
Blazed zone plate	0.38	2.4	6.42

Table 7-1 The thicknesses of chalcogenide structures required for different types of diffractive element at various wavelengths.

7.4 Fabrication of gratings using mask exposure

The difference between the size of a clean mask feature and the size of its image depends on the mask-to-wafer separation (McGillis and Fehrs 1975). In contact printing the mask and wafer are held about 50 μm apart. A finite gap between mask and wafer leads to a loss of linewidth control due to Fresnel diffraction at the mask edge. The resolution which can be achieved by contact printing is submicron since the limiting factor is diffraction at the edge of the mask feature. The major drawback of contact printing is a steady increase in the defect level from one wafer to the next. Any debris on the surface of a wafer will tend to damage the mask or adhere to the mask surface after mask and wafer

have been brought into contact (Stevenson and Gundlach 1986).

The required period of the mask pattern to provide maximum efficiency of the grating was calculated. It is known that the volume parameter $\Omega = \frac{K^2}{2\beta\kappa_1}$ and the first coupling constant $\kappa_1 = \kappa'_1 - j\kappa''_1$. For a lossless grating $\kappa''_1 = 0$ and hence $\kappa_1 = \kappa'_1$, where $\kappa'_1 = \frac{\beta\epsilon'_1}{4\epsilon'_0}$, ϵ'_1 being the first harmonic of phase modulation and β the propagation constant in the grating:

$$\beta = \frac{2\pi\sqrt{\epsilon'_0}}{\lambda} = \frac{2\pi n}{\lambda}$$

The values of refractive index for undoped $As_{30}S_{70}$ and $As_{30}S_{70}$ photodoped with Ag at 632.8 nm are 2.36 and 2.71 respectively. The values obtained for ϵ'_0 and ϵ'_1 using Eqns (2) and (3) in section 7.4 are 6.28 and 1.07 respectively. From the contour plot of the calculated diffraction efficiency (see Fig. 7-4) for the case $\mu = 0.4$, regions of high efficiency can be found. Point A ($\zeta = 1.46$, $\Omega = 3.30$) shows one of these high efficiency regions. Using this value of Ω a value of 475 nm is obtained for the grating period at 632.8 nm. This value is close to the limit of mask exposure technology. So a holographic technique is more applicable. At 10.6 μm the values of refractive index for undoped $As_{30}S_{70}$ and $As_{30}S_{70}$ photodoped with Ag used to find the optimum grating period were 2.22 and 2.46 respectively. Corresponding values of ϵ'_0 and ϵ'_1 using these values of refractive index are 5.30 and 0.562 respectively. Hence a value of 11.01 μm was obtained for the grating period for efficient operation at 10.6 μm.

A set of masks consisting of four equal-lines-and-spaces patterns of 6,8,10 and 12 μm periods on a 2.5 inch square glass slide were made which were compatible with the mask aligner (Karl Suss MJB-3) used in this work. Masks were made up in emulsion using the pattern generator operated by the Edinburgh Microfabrication Facility and then copied into chrome by an external company (Compugraphics Ltd.). An optical micrograph of the 6 μm grating pattern on the mask is shown in Fig. 7-5. The unevenness of the line edges is about 0.1-0.2 μm and is due to the finite size of the Ag grains in the emulsion used to produce the mask pattern.

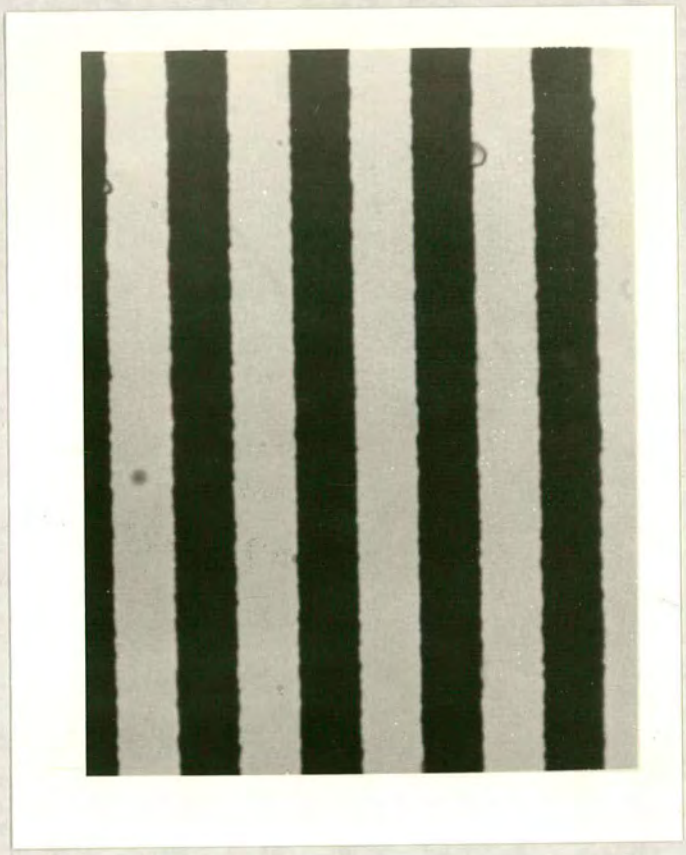

Fig. 7-5 Optical micrograph (× 1500) of part of the 6 μm grating pattern. The small irregularities along the line edges are due to the finite size of the Ag grains in the original emulsion.

In order to produce small scale features the conventional exposure systems used in IC fabrication employ UV illumination (e.g 350-450 nm for the Karl Suss system used in the present study). However, the As-S glasses are highly absorbing in the UV. For very thin films (< 300 nm), such as those used in VLSI microlithography, this high absorption is not a problem but for the thick films required for IR grating fabrication it is a serious limitation because it reduces the amount of light reaching the photodoped/undoped interface and hence slows down the rate at which the photodoped layer grows. Fig. 7-6 is a plot of transmittance (at 632.8 nm and 1.4 μm) vs. exposure time for a $Ag/As_{30}S_{70}$ combination undergoing photodoping using the mask aligner exposure system (the initial film thicknesses being 0.225 and 0.8 μm for the Ag and $As_{30}S_{70}$ films respectively). Clearly, the process does not reach completion until after 200-250 minutes of exposure. The slowness of the process sets an effective limit of ~ 1 μm for the grating thickness that can be made using this system.

7.4-1 Etching Procedure

(a) Chalcogenide Etching

In order to produce surface relief structures it is necessary to remove either the undoped or photodoped regions of the Ag/As-S combination after exposure. Whereas the undoped material is soluble in alkalis, the photodoped material is not: the wet etchant used to remove the undoped As-S in this investigation was a saturated solution of ammonia in methanol having a pH of 9. Dry etching of these materials is also possible and the undoped As-S can be preferentially removed by, for example, a CF_4 plasma. Removal of the photodoped material by wet or dry etching is difficult, although recent results suggest that it can be selectively removed by a sulphur plasma (Belford et al. 1989).

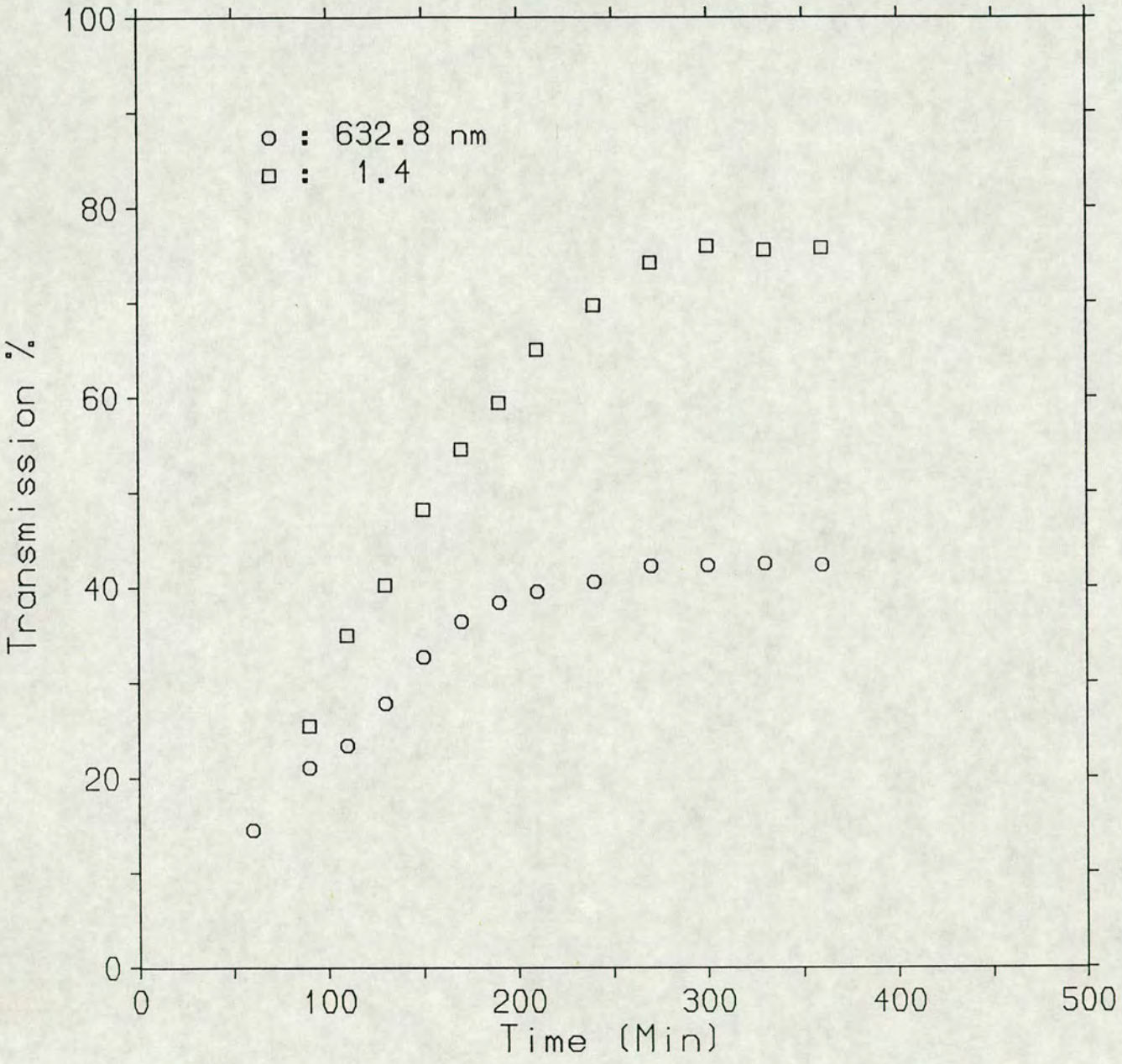

Fig. 7-6 Transmittance (at 632.8 nm and 1.4 μm) vs. exposure time for a $Ag/As_{30}S_{70}$ combination undergoing photo-doping using the mask aligner exposure system (the initial film thicknesses being 0.225 and 0.8 μm for the Ag and $As_{30}S_{70}$ films respectively).

(b) Ag Etching

After the As-S film has been exposed, Ag will remain in any unilluminated regions and, in addition, a residual Ag layer will be left in the illuminated regions if the initial Ag/As-S thickness ratio is > ~ 1/3, or if photodoping is incomplete. As Ag is absorbing in the IR, it must be removed if a transmission grating is being prepared.

Three different etchants were used to dissolve the unreacted silver.

1- A mixture of CH_3OH (methanol), NH_4OH and H_2O_2 in the volume ratio 4:1:1 which yielded a relatively slow etch rate (~ 60 A/sec).

2- $Fe(NO_3)_3$ in CH_3OH prepared in various proportions. Table 7-2 shows the result of the measurements on a 4000 A freshly deposited Ag film. The amount of $Fe(NO_3)_3$ given in Table 7-2 was added to 100 ml CH_3OH. The maximum etch rate is again relatively slow (~ 30 A/sec).

$Fe(NO_3)_3$ (g)	Etch Time (Min)
0.5	11
1.0	4
1.5	3.5
2.0	2.75
2.5	2.15

Table 7-2

3- The most useful etchant was 11 g $Fe(NO_3)_3$ in 9 ml H_2O heated to 44-49 °C . This did not attack the underlying undoped or photodoped layers and gave a fast etch rate (~ 20 μm/min) (Kern and Deckert 1978).

The first two etchants may be used on very thin Ag films but thick films require long immersion times and this leads to peeling of the underlying layers. An attempt to etch Ag with a dry etchant (CF_4 plasma) was not successful.

Fig. 7-7 shows an electron micrograph of a surface relief grating made in a 0.8 μm $As_{30}S_{70}$ film with a 0.14 μm Ag underlayer using the mask aligner (a Si substrate was used in this case to enable the film to be cleaved). A gold coat was deposited on the grating to avoid charging during SEM analysis. The edge definition is comparable with that of the mask. Fig. 7-8 shows the replay of a surface relief grating made in a 0.5 μm $As_{30}S_{70}$ film with 0.1 μm Ag underlayer using the mask aligner. The grating was replayed with a red wavelength (632.8 nm). Many diffracted orders are present which indicates that a thin grating is formed. The measured diffraction efficiency of the first order is ~ 10 % .

7.5 Fabrication of submicron holographic gratings

Submicron holographic gratings can be produced in As-S chalcogenide glasses by the interference of two plane waves. The blue (488 nm) or green (514.5 nm) lines of an Ar-ion laser are the most suitable for producing these holographic gratings. The experimental arrangement used in the present study to produce such submicron (0.5 μm) gratings is shown in Fig. 7-9 . Monochromatic illumination (488 nm) with vertical polarization from an Ar-ion laser is passed through a spatial filter after being attenuated by a set of neutral density filters, and then the expanded beam is directed onto a beam splitter after passing through an iris and a planoconvex lens. Mirrors then reflect the separated beams onto the sample where they interfere to form a set of fringes. It is important to avoid the movement of optical elements during the recording procedure and they were magnetically clamped to an optical table. Fig. 7-10 shows an electron micrograph of a trial submicron holographic grating produced in a Ag-$As_{28}S_{72}$ bilayer sample using the above arrangement. The initial

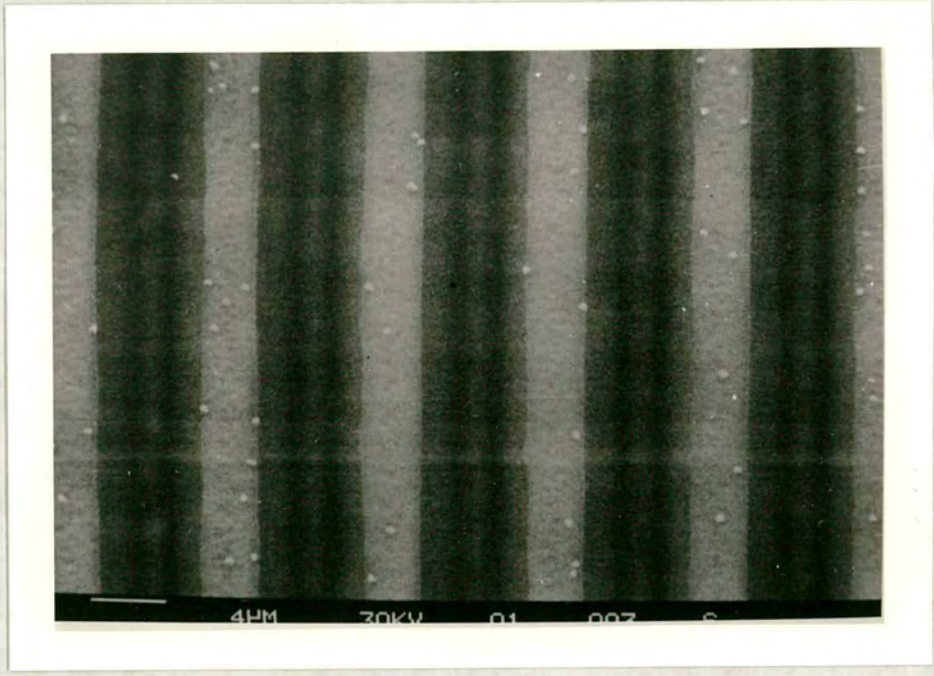

Fig. 7-7 Electronmicrograph of a surface relief grating made in a 0.8 μm $As_{30}S_{70}$ film with a 0.14 μm Ag underlayer, using the mask aligner.

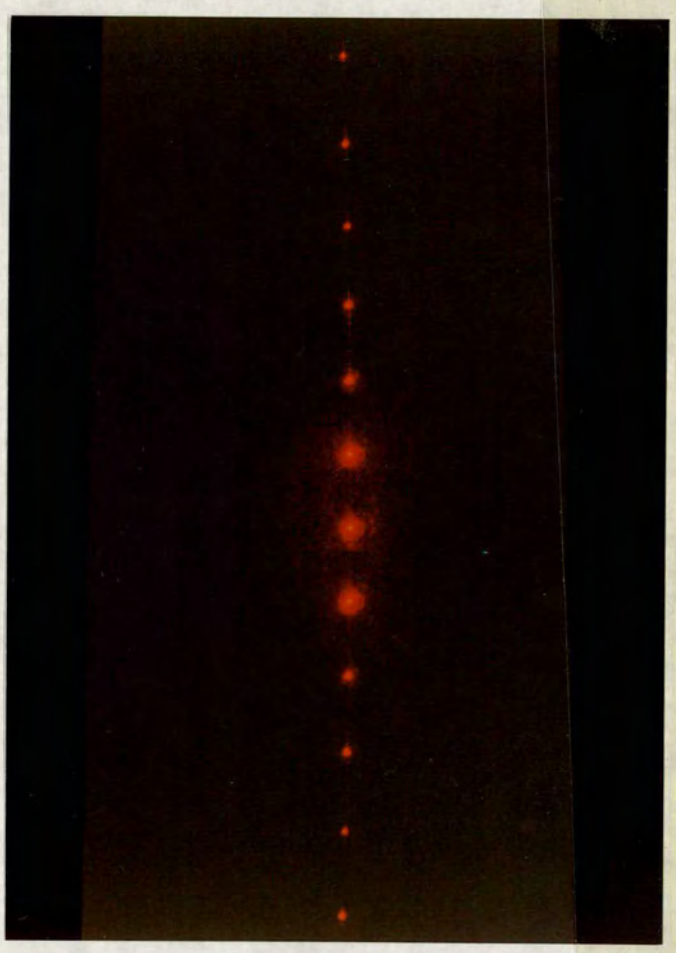

Fig. 7-8 The output of an optically thin grating showing Raman Nath type diffractive behaviour replayed at 632.8 nm. Diffraction efficiencies of up to 10 % at red wavelengths was measured for the first order.

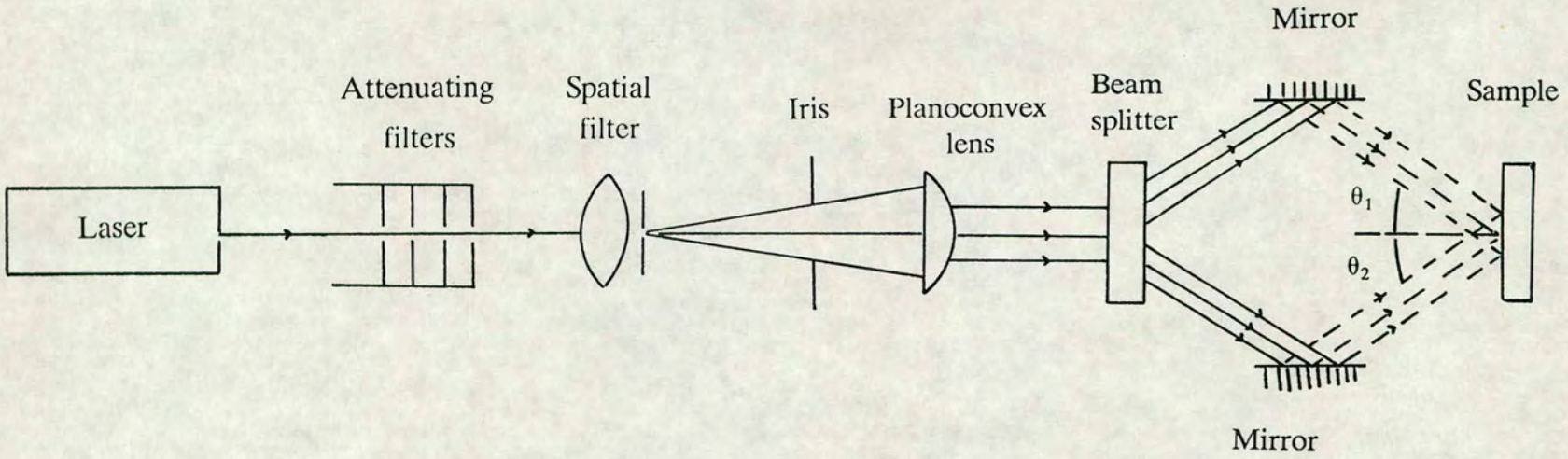

Fig. 7-9 Typical experimental arrangement used for recording of plane holographic gratings.

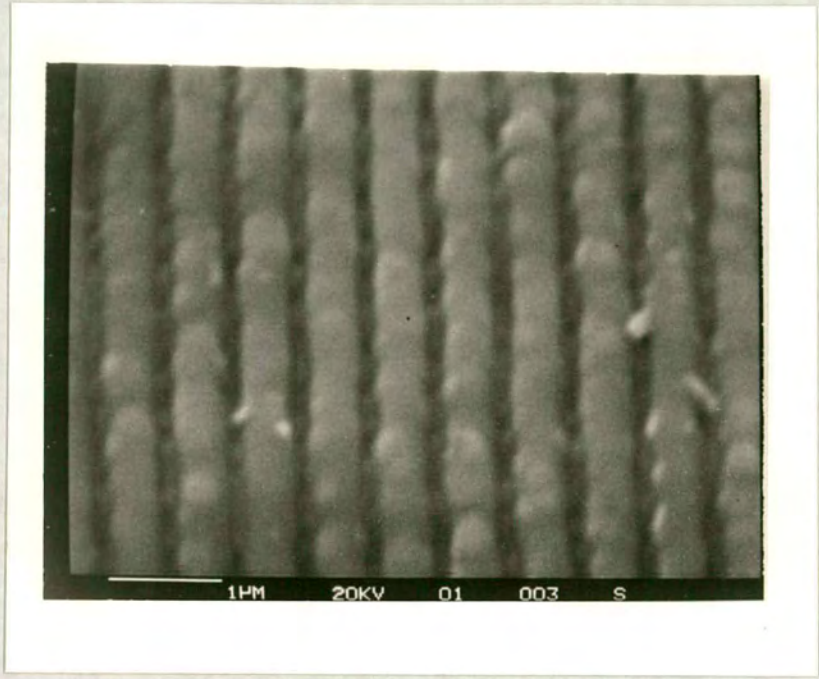

Fig. 7-10 Electronmicrograph of trial holographic grating. The grating spacing is 0.5 μm.

thicknesses of the Ag and $As_{28}S_{72}$ layers were 4600 and 9000 A respectively. The intensity of each beam on the sample was 50 mW/cm^2 and the exposure time was 10 minutes. The recording angles were equal and $\theta_1=\theta_2=23.5°$ which was found from the geometry of the arrangement. There is some unevenness in the line definition of the grating, possibly due to instability in the exposure system. As this micrograph shows, it is possible to fabricate submicron holographic gratings in these materials using this type of arrangement.

7.6 Phase contrast analysis of holographic phase gratings

The purpose of a phase contrast microscope is to make visible specimens which do not change appreciably the intensity of the light passing through them (as stained biological specimens would do, for example), but only change its phase through differences in refractive index from point to point within the specimen (i.e. through differences in optical path length). In other words, ordinary specimens seen by transmitted light are visible because they have intensity-contrast : light passes through certain parts of the specimen with very little absorption and the light waves forming this part of the image have high intensity, while other parts of the specimen through staining or natural absorption, are correspondingly darker. Many specimens do not change the amplitude of the light passing through them but they do change the phase of the light waves relative to the general illumination. Since the eye is not sensitive to phase changes, they do not make the specimen visible. The principle of the phase contrast method is to convert these phase changes into intensity changes which are visible to the eye. Fig. 7-11 shows the phase contrast image of a phase grating produced holographically at the Royal Signals and Radar Establishment (RSRE) in a 1 μm Ag / 3 μm $As_{30}S_{70}$ combination supplied by the author. The grating period is 22 μm . The definition of the grating is reasonable although the small-scale structure that is apparent may be due to some kind of inhomogeneity in the photodoped material, for example phase-separated Ag clusters.

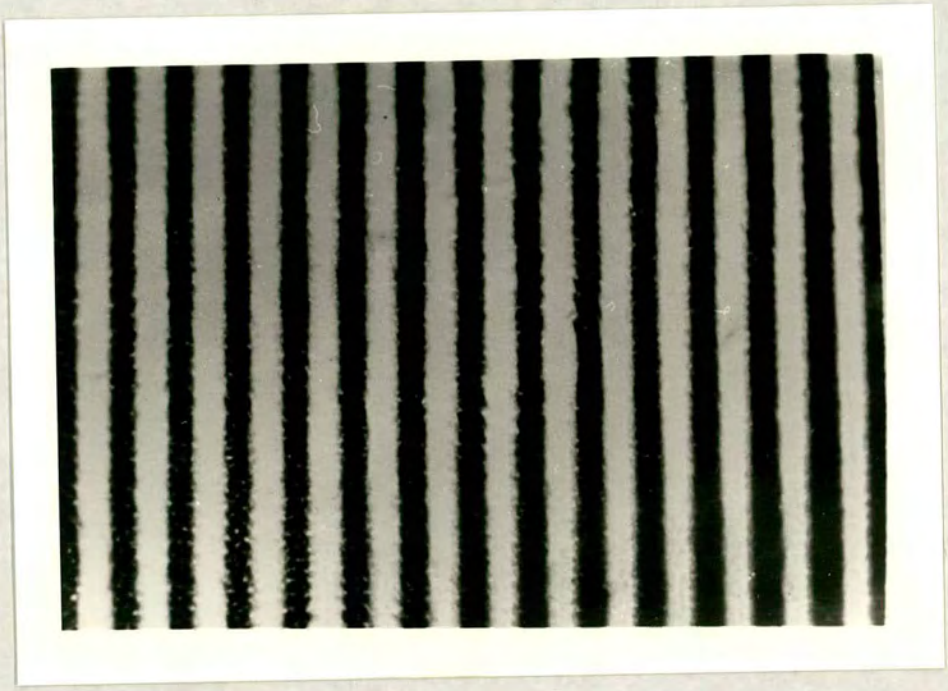

Fig. 7-11 Phase-contrast micrograph of a holographically produced phase grating in a 1 μm Ag/ 3 μm $As_{30}S_{70}$ combination. The grating period is 22 μm.

7.7 Diffraction efficiency measurements

The experimental arrangement used for diffraction efficiency measurements in the present study is schematically shown in Fig. 7-12. The 632.8 nm line (with vertical polarisation) from a He-Ne laser was directed onto the grating after passing through a neutral density filter and a randomly polarized cube beam splitter. The diffracted output of the grating was fed onto a photodiode connected to an I-V convertor and a Keithley 195 digital multimeter (D.M.) was used to measure the output voltage as a function of the angle of incidence. A normalizing photodiode was also used to detect the intensity of the incident beam and, in particular, to correct for the variation of the incident laser light with time. The diffraction efficiency, η, was defined as the ratio of the intensity of each diffracted order to the intensity of the incident beam. Vertical polarization was used to ensure maximum coupling and hence maximum efficiency. The sample used was a 2.5 μm $As_{30}S_{70}$ / 0.49 μm Ag combination (with Ag on the top surface) in which a volume holographic grating had been recorded (at RSRE) using the green line of an Ar ion laser and recording angles of $\pm$ 30°. The illumination intensity used to produce the grating was 150 mW/cm^2 per beam and the exposure time was 120 sec. The unreacted Ag was removed using $Fe(NO_3)_3$/ H_2O etchant at 46° C. The diffraction efficiencies of the 0 and $\pm$ 1 orders were measured using the set up in Fig. 7-12 . It was ensured that the 2nd and higher orders were depleted . Reflection losses were present and the measured reflection loss at 40° was ~ 20 % . It is possible to calculate reflection losses at a given angle and the reflection loss (R) at 40° which is near to the first Bragg angle (38°) was calculated using Eqn. (24) which is given by Heavens (1955):

$$R = (r_{1s})^2 = \left[\frac{n_0\cos\Phi_0 - n_1\cos\Phi_1}{n_0\cos\Phi_0 + n_1\cos\Phi_1}\right]^2 \qquad (24)$$

where Φ_0 is the angle of incidence, Φ_1 the angle of refraction, n_0 the refractive index of air (which is unity) and n_1 is the average value of refractive index in the grating. In the

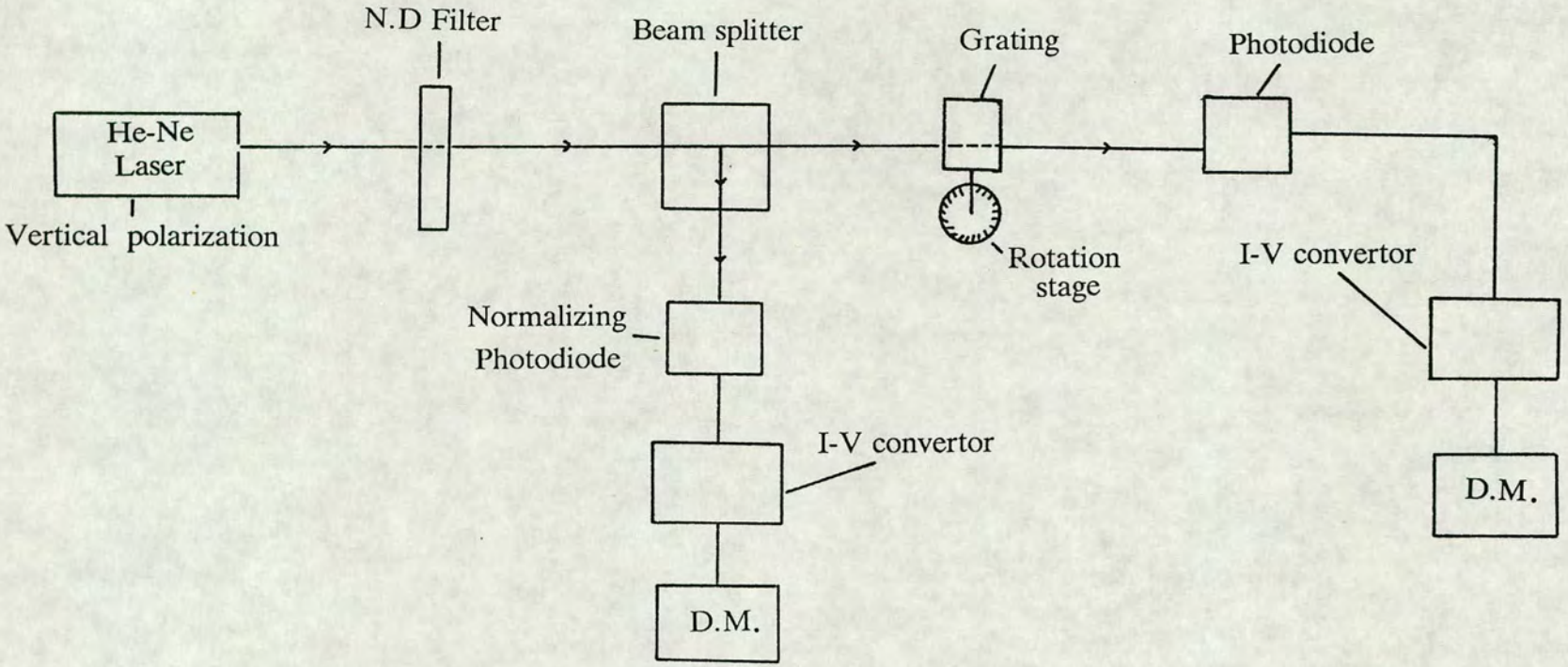

Fig. 7-12 Experimental arrangement for diffraction efficiency measurements.

present case n_1 was taken as the average value of the refractive index in undoped $As_{30}S_{70}$ (2.36) and that of the $As_{30}S_{70}$ photodoped with Ag (2.70) . Hence a value of 2.53 was taken for the refractive index of the grating. The calculated value for R using Eqn. (24) is 0.27 . The difference between the calculated value of R and the measured value is possibly due to the approximate value used for n_1 in Eqn. (24). Also there may be some surface profile associated with the bulk grating, so R as measured may be misleading. Account must also be taken of the contribution of scattering due to inhomogeneities in the photodoped layer (see section 3.4-2). However, it is difficult to calculate or measure the energy loss due to scattering.

Figures 7-13 and 7-14 show the result of the angular response of the diffraction efficiency for the 0 and ± 1 orders respectively. In both cases efficiencies of nearly 20% are achieved. In Fig. 7-14 some difference in the height of the diffraction efficiencies of the ± 1 orders is observed. The same behaviour, although to a lesser extent, has also been seen in the angular response of the diffraction efficiency of gratings produced in silver halide emulsions and was attributed to the presence of an in-phase absorption grating (Syms and Solymar 1983) but the responses are still symmetric about 0. However, the cause of the asymmetry seen in these results is not perfectly clear and may instead be due to noise grating phenomena (Riddy and Solymar 1986), or other interference effects at recording. The other explanation is that the film was not at the exact centre of rotation.

Fig. 7-15 shows the measured angular response for a grating produced in $As_{40}S_{60}$. The measured intensities of the 0 and ±1 diffraction orders are shown as a function of the angle of an incoming probe beam. The grating was recorded at angles of ±25° to the substrate normal, with an exposure time of 120 s and writing intensities of 350 mW/cm^2 per beam. Replay was made in air using light of wavelength 632.8 nm from a helium-neon laser. The figure shows typical Bragg behaviour, the power in the first orders reaching a maximum of 9% near the Bragg angles of 31°. The theoretical fit also shown in the figure is derived from a one-dimensional first order, multiwave coupled theory, allowing for absorption and scatter losses, with phase and amplitude modulation assuming a cosinusoidal paraboloid doped profile (Slinger et al. 1991). A reasonable match is observed between

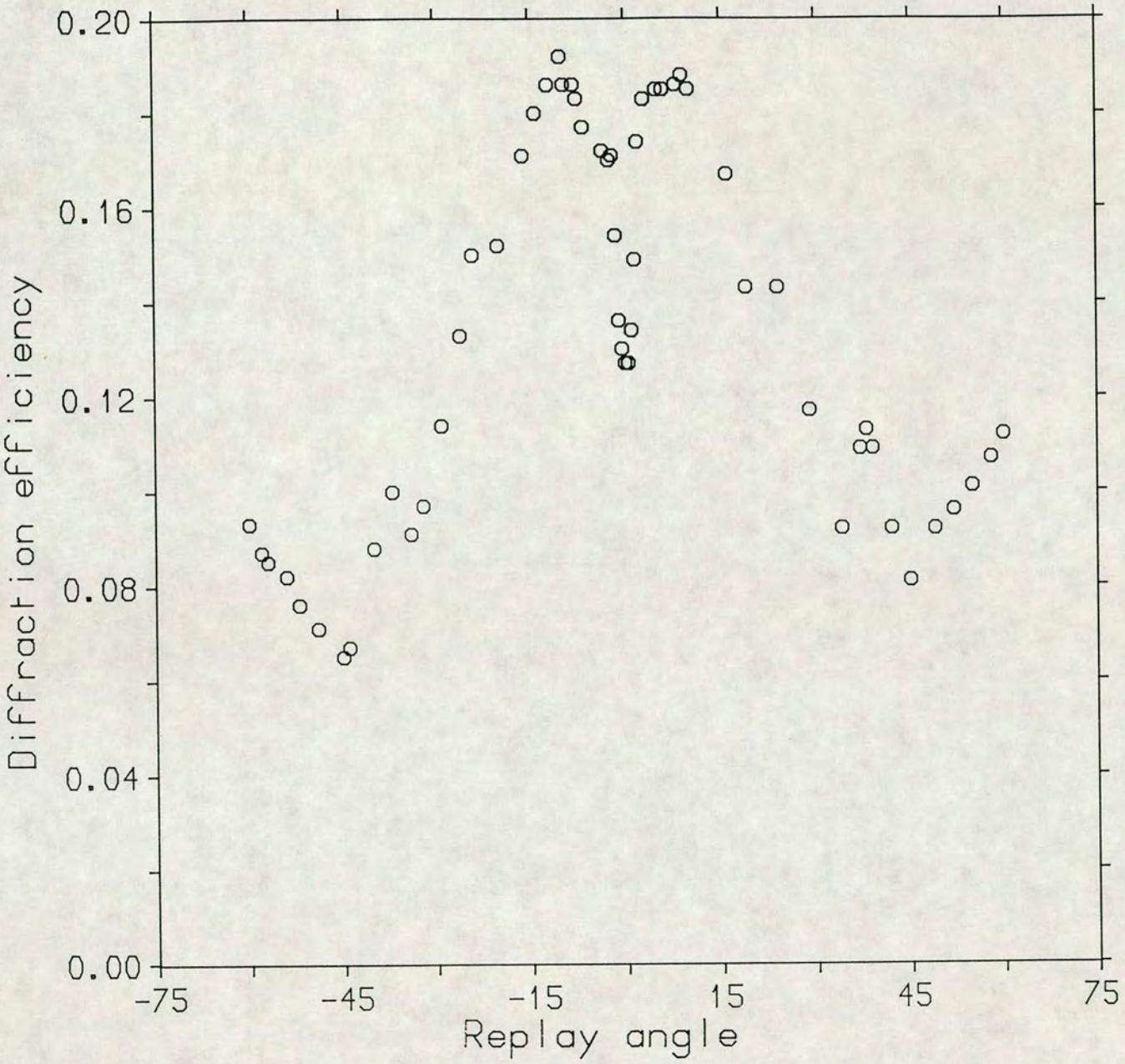

Fig. 7-13 Zero order diffraction efficiency vs. replay angle for a holographic grating produced using the metal photo-dissolution effect. Measured in air at 632.8 nm replay wavelength.

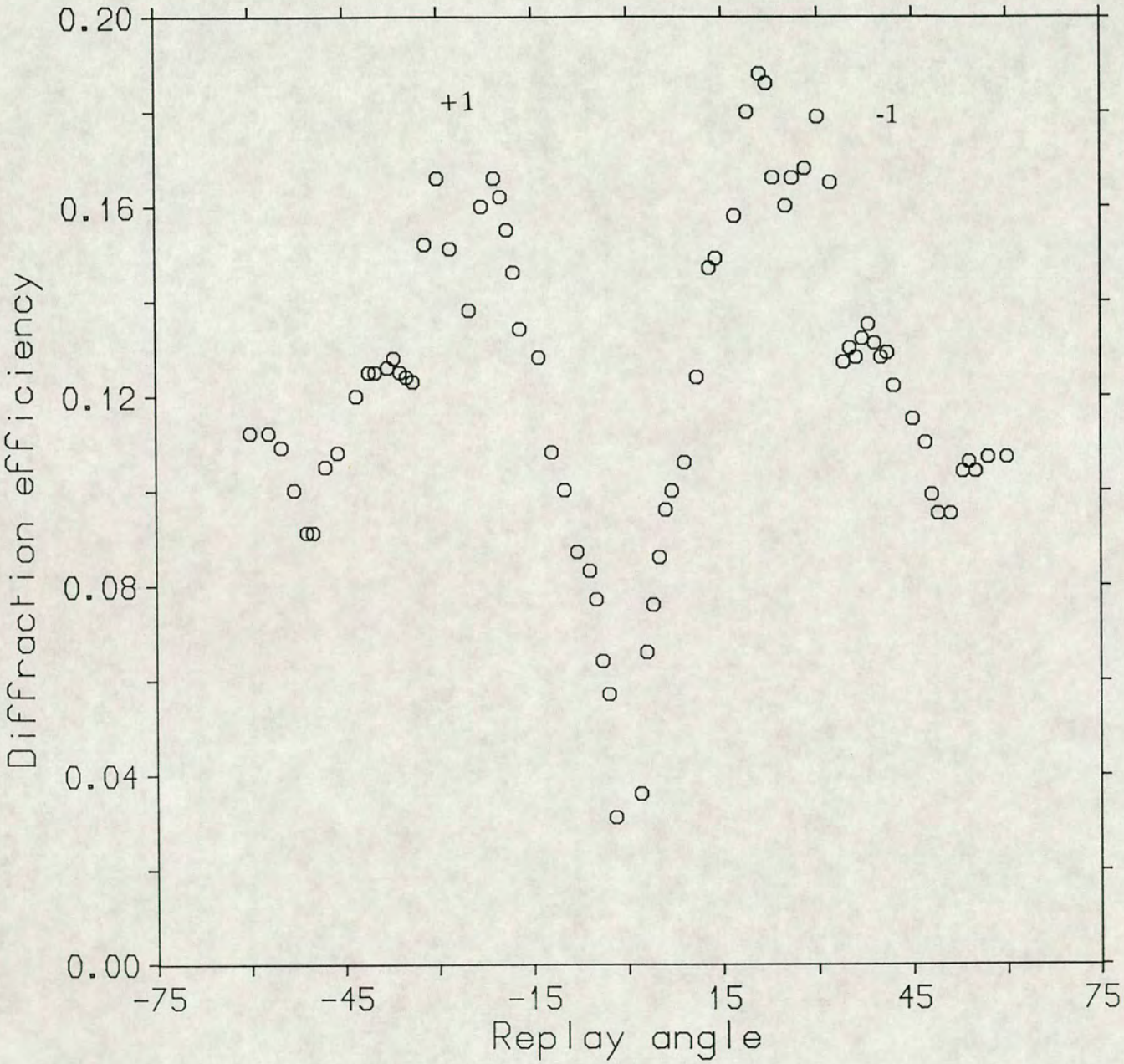

Fig. 7-14 ±1 orders diffraction efficiency vs. replay angle for a holographic grating produced using the metal photo-dissolution effect. Measured in air at 632.8 nm replay wavelength.

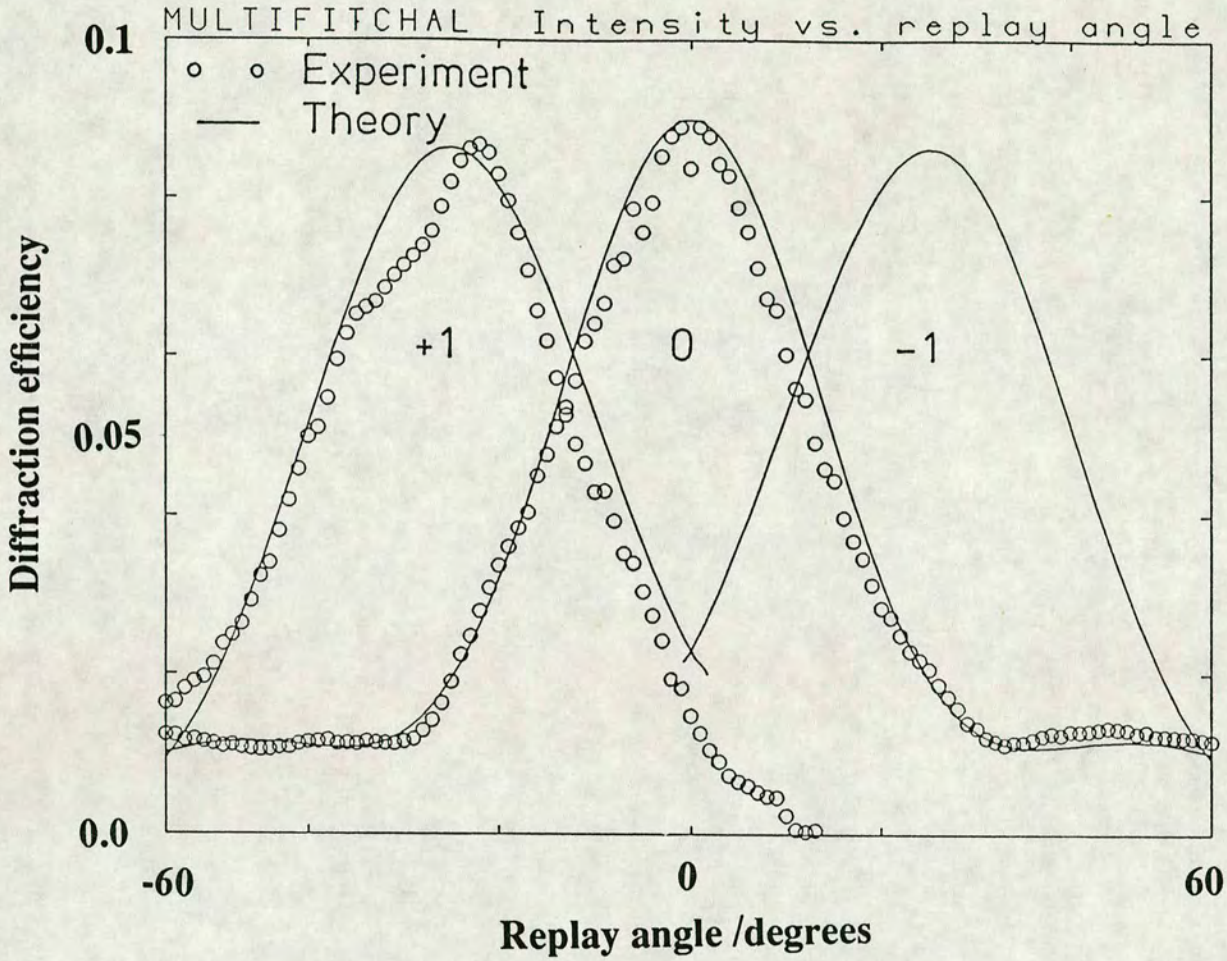

Fig. 7-15 Response of near volume grating recorded by sinusoidal interference pattern. Diffraction order intensity as a function of replay angle, measured in air at 632.8 nm replay wavelength. The theoretical curves were generated from first order coupled wave theory.

theory and experiment. The grating parameters derived from the model are in broad agreement with the bulk material measurements.

Recent measurements of the diffraction efficiency (Ewen et al. 1991) show that for the bulk holographic transmission gratings produced, efficiencies of > 33% were observed for first diffraction orders measured in air at 632.8 nm, the main loss mechanisms being absorption and reflection, with some scatter. Measurements at 1.5 μm have given efficiencies of > 30%, stability requirements during holographic recording currently being the main limitation to higher efficiencies at these and longer wavelengths. The absorption in the IR band is very small and by finding a suitable antireflection coating, it can be concluded that it should be possible to achieve higher efficiencies at IR wavelengths.

7.8 Summary

The recording materials available for grating fabrication have been outlined. Sensitivity, resolution and diffraction efficiency, which are the three most important properties of these media for grating applications, were discussed. The fabrication of submicron holographic gratings in As-S chalcogenide glasses was described and a theoretical analysis of grating formation applicable to gratings formed by a binary mask exposure technique was developed. It is possible to calculate the diffraction efficiency of the grating using the above analysis and the theory shows that diffraction efficiencies of over 90% can be achieved in the multiwave regime. Techniques for the production of both surface relief and phase gratings have been investigated. Different etchants for undoped As-S and Ag layers have been examined and the most useful etchant in each case has been found. An experimental arrangement has been set up and used to measure the diffraction efficiency of the fabricated gratings. In the case of thin gratings, diffraction efficiencies of up to 10% have been measured for the first order. For volume phase gratings diffraction efficiencies of up to 20% have been measured for both 0 and ±1 orders. The difference between the measured diffraction efficiency and the calculated value is attributed to both reflection losses and scattering due to inhomogeneities in the photodoped regions.

7.9 References

Bartolini, R.A., Bloom, A., and Escher, J.S., 1976, Appl. Phys. Lett., 28, pp. 506-507.

Belford, R.E., Hajto, E., and Owen, A.E., 1989, Thin Solid Films, 173, p. 129.

Burke, W.J., Steabler, D.L., Phillips, W., and Alphonse, G.A., 1978, Opt. Eng. 17, pp. 308-16.

Ewen, P.J.S., Slinger, C.W., Zakery, A., Zekak, A., and Owen, A.E., 1991, Proc. of the Int. Congress on Optical Science and Engineering, The Hague, The Netherlands, In press.

Heavens, O.S., 1955, "Optical properties of thin solid films", (London:Butterworth scientific publications).

Keneman, S.A., 1971, Applied Physics Lett., 19(6), pp. 205-207.

Kern, W., and Deckert, C.A., 1978, in "Thin Film Processes", ed. J.L. Vass and W. Kern (Boston : Academic press), p. 473.

Kogelnik, H., 1969, Bell syst. Tech. Journal 48(9), pp. 2909-47.

Kostyshin, M.I., Krasnojonor, E.P., Makev, V.A., and Sobolev, G.A., 1970, Proc. of the international symposium of holography, ed. by J. Vienot, J. Bulabois, J. Pasteur (Univ. Besancon, France), paper 11.7.

Leith, E.N., and Upatnieks, J., 1962, J. Opt. Soc. Amer., 52, pp. 1123-30.

McGillis, D.A., and Fehrs, Delmer L., 1975, IEEE Transaction on electron devices 22(7), p. 471.

Raman. C.V., and Nath, N.S.N., 1935-1936, Proc. Indian Academy Sciences 2(1935)406,413; 3(1936)75,119,459 .

Riddy, G.G.D., and Solymar, L., 1986, Electron. Lett., 22(16), p. 872.

Slinger, C.W., 1988, RSRE Memorandum no. 4121.

Slinger, C.W., Syms, R.R.A., and Solymar, L., 1985, Appl. Phys., B36, pp. 217-24.

Slinger, C.W., Zakery, A., Ewen, P.J.S., and Owen, A.E., 1991, Submitted to Appl. Optics.

Smith, H.M., 1977, "Holographic Recording Materials", (Springer, New York), pp. 22-74.

Solymar, L., and Cooke, D.J., 1981, "Volume holography and volume gratings", Academic Press, Chapter 5.

Solymar, L., and Sheppard, C.J., 1979, J.O.S.A. 69, pp. 491-5.

Syms, R.R.A, and Solymar, L., 1983, Applied Optics 22(10), p. 1479.

Stevenson, J.T.M., Gundlach, A.M., 1986, J.Phys., E : Sci. Instrum., 19, p. 654.

Young, P.A., 1971, J. Phys., C : Solid state Physics 4, pp. 93-106.

8. CONCLUSIONS AND SUGGESTIONS FOR FURTHER WORK

8.1 Introduction

As mentioned in the previous chapter, the grating thicknesses required for efficient operation in the IR are generally large, typical values for bulk gratings being 1.39, 8.77 and 23.2 μm at 0.632, 4.0 and 10.6 μm respectively. The requirement of photodoping such large thicknesses sets some limits on the applicability of the photodissolution effect, for example, very long exposure times are required, which means that it is difficult to ensure stability of the optical components if a holographic technique is employed. In the present chapter different solutions for overcoming these limitations are proposed. Some suggestions regarding further studies of the photodissolution mechanism are also presented.

8.2 Limitations of photodissolution

The physical thickness, d, of the photodoped layer is a function of the intensity of the actinic radiation and (depending upon the amount of silver present) is proportional to the square root of the exposure time. (For samples with thicker chalcogenide layers (Owen et al. 1990) the square root time dependence was always observed irrespective of the silver layer thickness). The intensity dependence of the photodissolution rate is super-linear at low levels but sublinear at higher ones and the rate increases with photon energy, although this is counterbalanced by increasing absorption, particularly for thicker samples. Hence:

$$d \propto f(I) f'(E) \sqrt{t}$$

Where I is the illumination intensity, $E = h\nu$ is the photon energy and t is the exposure time. The above relation shows that doubling the required photodoping thickness requires a

factor of 4 increase in exposure time. Although it is possible to photodope thicknesses of up to 4 μm, as shown in Fig. 8-1, for thicknesses of greater than 3 μm or so, at reasonable power levels, exposures of over an hour or so are required. Thus an important goal is to increase the sensitivity of these materials in order to reduce exposure times and hence improve the ease and cost of device fabrication.

8.3 Possible solutions

In order to enhance the photodissolution sensitivity, various solutions are possible and these are outlined and discussed in sections 8.3-1 to 8.3-4 below.

8.3-1 Application of an electric field

Since the photodissolution phenomenon involves the migration of Ag ions into the chalcogenide layer matrix, it is reasonable to assume that the application of an electric field would speed up the photodissolution rate. Firth (1985) has used a resistance measurement technique to monitor the effect of an electric field on the speed of Ag ion migration in the As-S system . His results show that for a 70 nm Ag/ 250 nm As-S combination, application of 100 mV (with the Ag positive with respect to the As-S) speeds up the photodissolution time by a factor of ~ 2 . This also confirms that photodissolution involves the migration of positive Ag ions into the As-S matrix. Application of an electric field during holographic or mask exposure should be relatively easy to accomplish but would involve the use of a transparent electrode material on the surface of the chalcogenide.

8.3-2 Effect of temperature

The effect of temperature on the photodissolution kinetics has been studied by Rennie (1986) and Plocharsky et al. (1987). Their results show that the photodissolution rate can be increased by a factor of 3-4 as a result of performing the measurements around

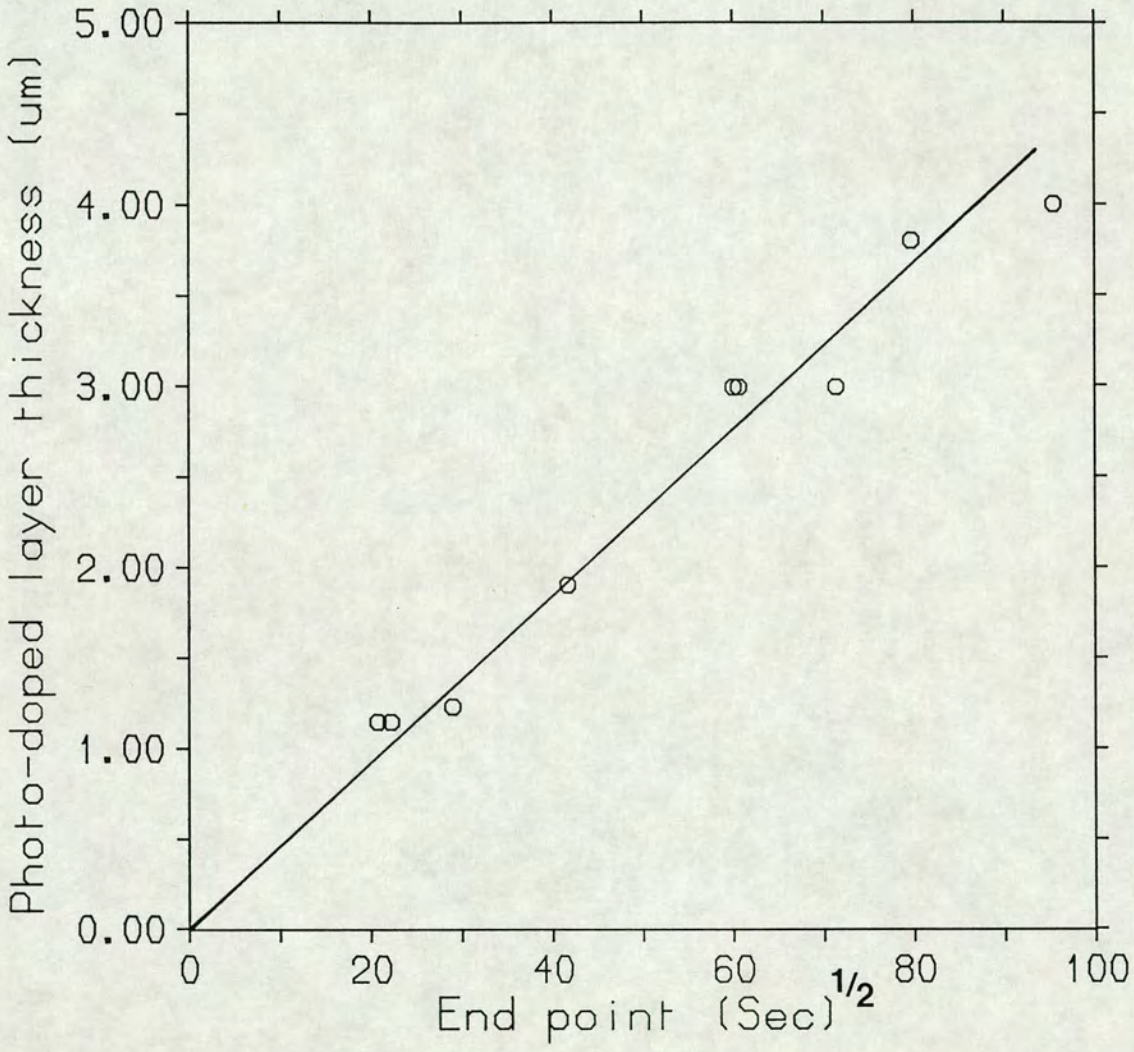

Fig. 8-1 This figure plots, for various Ag/$As_{30}S_{70}$ combinations, the final photo-doped layer thickness against the square-root of the end-point time of the measured reflectance curve. There appears to be, at least approximately, a linear relation between these parameters.

100°C compared with room temperature. However, although the photodissolution rate can be increased appreciably by performing the illumination at elevated temperatures, it should be noted that the thermal diffusion of silver in the As-S system is an isotropic process so this technique might not be suitable for grating fabrication. The extent of this lateral movement needs to be examined experimentally, possibly using a phase contrast technique. It might be that the extent of such thermally-induced lateral migration of Ag ions is small enough to be acceptable for IR gratings, since grating periods of up to ~ 11 μm are required for efficient operation in this waveband. In addition, holographic exposure usually requires a stable temperature environment to avoid air currents, so a more complicated exposure arrangement would be necessary for patterning at elevated temperatures. A mask exposure system might be preferable for this type of technique.

8.3-3 Seeding the chalcogenide with a metal prior to photodoping

It is well known that the addition of a small amount of metal (eg. Ag or Cu) increases the conductivity of these glasses by some 5 orders of magnitude at room temperature (Mott and Davis 1979). In view of this it is plausible to consider that the addition of a small amount of Ag to e.g. As_2S_3 glass prior to photodoping might increase the photodissolution rate significantly. Preliminary experiments were carried out in the present study using samples prepared by coevaporation of a small amount of silver powder (particle size < 100 μm) with As_2S_3. (Silver powder is evaporated at much lower temperatures than the normal melting point of silver because the surface reactivity of silver powder is increased due to the size of the particles). The photodissolution rate in these samples was increased only by ~ 12 % which implies that perhaps ionic transport is the dominant process in the metal photodissolution effect. However, seeding with other additives such as iodine to enhance the ionic transport might increase the photodissolution rate considerably.

4.3-4 Pre-patterning the silver layer using a photolithographic technique

In order to circumvent the problem of sensitivity in the As-S chalcogenide system, a possible solution may be to pattern the silver layer first using a conventional photolithographic technique and then to deposit the chalcogenide layer on top, hence avoiding the stability problem which exists with the holographic technique. To pattern the silver layer a positive resist should be used because in this case, high resolution and less swelling is achieved (Sze 1988). The sensitivity of most standard resists peaks in the 300-400 nm spectral range and hence a UV illumination source can be used. A standard technique proposed by Shipley and a Microposit S1400-31 series (positive resist) could be used in this experiment.

Preliminary experiments on patterning Ag layers were carried out in the present study and showed that this was a relatively straightforward process. The fabrication steps used to pattern the silver layer are shown in Fig. 8-2. First the substrate is dried in an oven at 200 °C for 30 minutes. Then the silver layer of ~ 2000 A thickness is evaporated onto this clean substrate and a layer of photoresist spin-coated on top. Spin times of ~ 30 secs at 4000 rpm yield a uniform film. The sample is then soft baked at 90°C for 30 min and, after cooling to room temperature, it is exposed through a mask for 1 min using a Karl-Suss mask aligner. The sample is then placed in the developer (Shipley Microposit 351) for 60 secs and rinsed in deionized water. After drying the sample with nitrogen gas, it is hard baked at 110°C for 30 min. Once the photoresist has been stripped, the silver can be removed by an etchant (a solution of 11 g $Fe(NO3)_3$ in 9ml H_2O at 44-49 °C –see Chapter 7). It is now possible to deposit a layer of As-S on top of this patterned layer of silver and then illuminate this combination with an expanded green beam from an Ar ion laser. As before, the silver ions from the patterned layer will migrate into the chalcogenide layer and a grating will be formed.

It is expected that one of the techniques described above (8.2-1 to 8.2-4), or a combination of them, will lead to an enhanced sensitivity of photodissolution in the As-S system. However, if the sensitivity still remains a limitation, other chalcogenide systems can

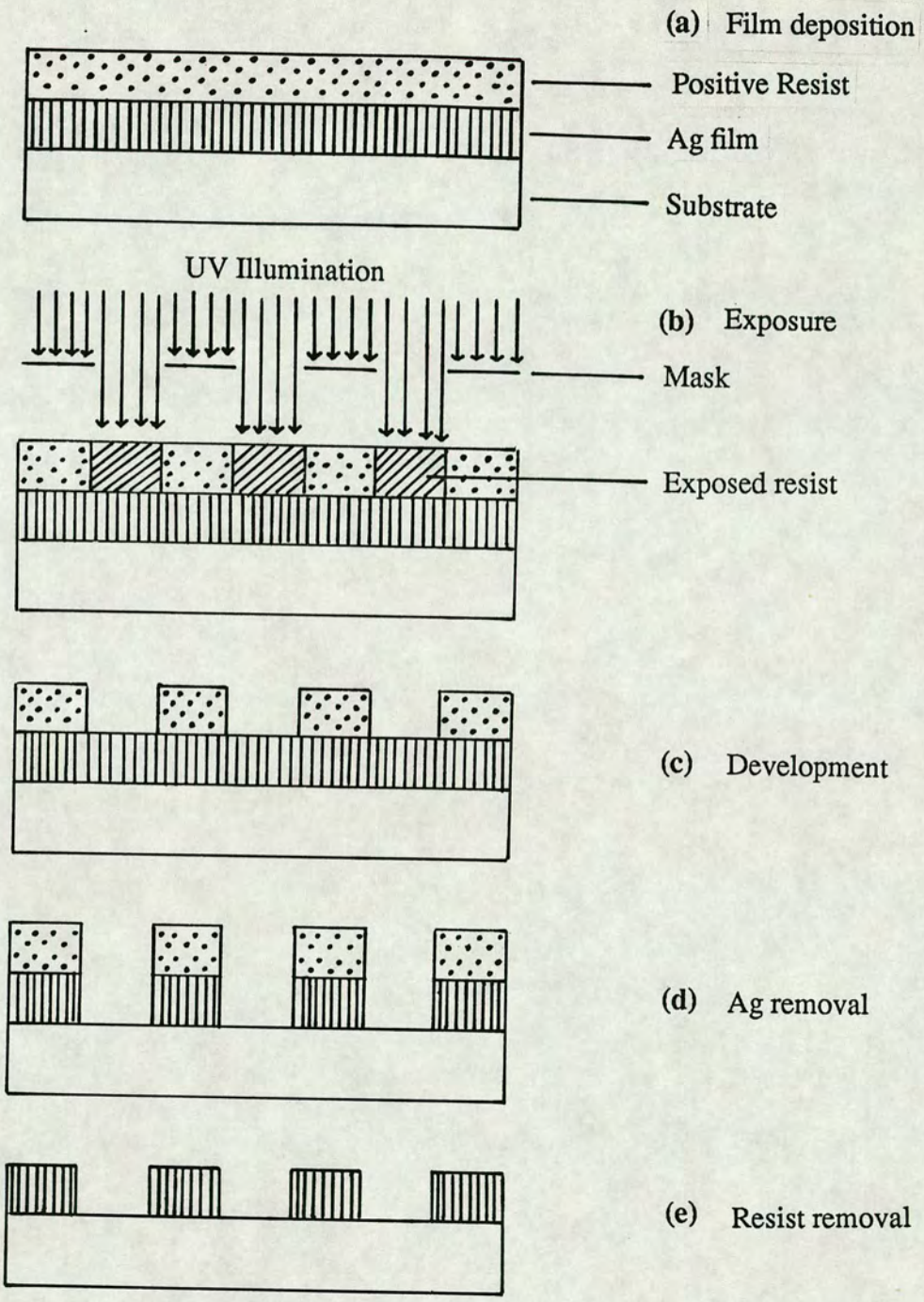

Fig. 8-2 Fabrication procedure to pattern an Ag film.

be examined, although this will require evaluation of their optical properties in the IR as well as their photodissolution kinetics.

8.4 Characterization of the photodoped layer

Regarding the photodissolution mechanism itself, it should be said that any existing model should be confirmed quantitatively. This requires characterization of the photodoped layer, in particular the ionic conductivity, dark d.c electronic conductivity and photoconductivity, and the temperature dependence of these quantities. Determination of the sign of photocarriers is vital in revealing where the effective absorption of radiation is taking place in photodissolution. The sign of thermopower is a reliable indicator of whether the material is *n-type* or *p-type* , in contrast to the Hall effect which is not. So thermopower measurements should be performed along with the conductivity experiments.

As mentioned earlier, for modelling the grating performance it is necessary to know how the optical constants of both the undoped and the Ag-doped As-S films vary with depth. Although a SIMS analysis in the present study has provided some information in this respect, other techniques such as Rutherford backscattering (RBS) should be used to check the results obtained using SIMS. Also, direct measurements of the absorption coefficient of both the undoped and the Ag-doped As-S films in the IR are necessary for a complete modelling of the grating performance in this waveband.

8.5 Conclusions

The main conclusions reached in this work are as follows :

1- For the evaporated films studied, compositions richer in As than $As_{30}S_{70}$ yielded good agreement between the film and source compositions. For sulphur rich compositions however, the films seem to be more As rich than the source.

2- Compositional analysis of the photodoped films show that in $As_{33}S_{67}$ photodoped with Ag, a composition close to smithite ($AgAsS_2$) is obtained. For $As_{40}S_{60}$ photodoped with Ag the composition obtained is richer in Ag than smithite. In addition, photodoped $As_{33}S_{67}$ is more homogeneous than photodoped $As_{40}S_{60}$. The presence of crystals on the surface of photodoped films after long exposure to u.v. illumination may be due to photoinduced crystallization of the Ag doped material or the formation of As_2O_3 crystals.

3- The results of refractive index measurements of undoped As-S films obtained using a method outlined by Swanepoal (1983) are in agreement with results published by other workers (Tanaka et al. 1979) to within 2% at 632.8 nm.

4- Refractive index measurements of photodoped $As_{30}S_{70}$ films containing various amounts of Ag show that for the most heavily doped films a modulation of > 0.5 in refractive index can be achieved in the visible part of the spectral region. The extrapolation of the visible data to IR wavelengths (10.6 μm) shows that the same modulation exists in the IR as well.

5- Direct measurements on $As_{40}S_{60}$ films photodoped with Ag confirm the extrapolation of the visible data at IR wavelengths.

6- Detailed measurements of the absorption coefficient of photodoped $As_{30}S_{70}$ with various amounts of Ag show that although the absorption increases in the visible region as a result of Ag doping, it is small in the near-IR . Transmission measurements on a photodoped $As_{40}S_{60}$ film confirm that there is no significant absorption out to $\sim$ 12 μm.

7- The optical gap deduced from absorption measurements decreases from 2.5 eV for undoped $As_{30}S_{70}$ to 1.8 eV for the most heavily silver-doped sample. The decrease in the optical gap E_g by incorporation of silver is attributed to the smaller binding energy of Ag-S bonds compared with that of As-S bonds .

8- The kinetics of the photodissolution effect in the As-S system can be measured using an automated system for simultaneous monitoring of reflectivity and transmissivity.

9- The results for the time dependence of the photodissolution effect clearly indicate that the kinetics of the photodissolution effect strongly depends on the initial amount of silver available for dissolution. These results show that when the pure Ag source is exhausted a new photodissolution regime is dominant possibly due to the diffusion of Ag from the already photodoped product.

10- Measurements of the compositional dependence of the photodissolution rate using a tungsten source show that it has a peak around a composition $As_{33}S_{67}$ in the As-S system. This peak has been attributed to the morphology of the photodoped product in the As-S-Ag system. The corresponding results using a monochromatic source are more difficult to interpret. The photodissolution rate exhibits a local maximum around $As_{33}S_{67}$ superimposed on a decreasing trend as the sulphur content increases. For the interpretation of the results at compositions richer in As than $As_{30}S_{70}$, other photoinduced effects should also be considered.

11- The spectral dependence of the photodissolution rate shows that it is higher at blue wavelengths than green or red by a factor of 2 and $\sim$ 100 respectively .

12- The photodissolution rate has a superlinear dependence on intensity at low levels while a sublinear dependence on intensity is observed at higher levels. For every 10 photons, approximately one silver ion is dissolved into the As-S film.

13- An increase of up to 0.1 in refractive index as a result of illuminating the As-S film with the green light of an argon laser makes As-S films a promising optical recording media. The extent of photodarkening increases with increasing As content.

14- A technique based on a Gregory-Newton algorithm has been developed to analyze the time dependence of the transmissivity at red wavelengths during photodissolution. The photodissolution rate obtained using this technique was between 0.05 and 3 A/sec for the composition $As_{33}S_{67}$.

15- A model is proposed for photodoping which considers it as an intercalation reaction in an amorphous solid. This model can explain the spectral dependence, intensity dependence and compositional dependence of the photodissolution rate and considers that the actinic radiation is absorbed in the photodoped layer .

16- The result of a secondary ion mass spectroscopy analysis shows that there is very little change in composition with depth for the undoped As-S layer while for the photodoped layer a variation in Ag concentration with depth of up to 20% may occur.

17- Positron ion scattering analysis could not show any difference in the values of S (the line shape parameter) for undoped and photodoped As_2S_3 within the experimental uncertainties.

18- A theoretical model suggests that diffraction efficiencies of over 90% can be achieved in the multiwave regime for the fabricated gratings.

19- Both surface relief and phase gratings have been fabricated in As-S chalcogenide films using the metal photodissolution effect, by mask exposure and also by a holographic technique.

20- The most efficient Ag etchant was found to be a solution of 11 g $Fe(NO_3)_3$ in 9 ml H_2O heated to 44-49 °C.

21- Diffraction efficiencies of up to 10% have been measured at 632.8 nm for the first

order in the case of thin gratings.

22- For volume phase gratings, diffraction efficiencies of up to 20% have been measured at 632.8 nm for both 0 and ±1 orders.

8.6 Summary

It has been confirmed in the present study that it is possible to use Ag photodissolution to fabricate gratings in the As-S system using either mask exposure or the conventional holographic technique. Different grating structures (e.g. surface relief or bulk phase) have been produced. To make these structures, it was necessary to find suitable etchants for removing As-S and Ag layers and these were identified in the present study. The kinetics of the photodissolution effect show that a composition around $As_{30}S_{70}$ is optimum in the As-S system for grating applications because it has maximum sensitivity and also exhibits negligible photodarkening. A theoretical model which has been developed predicts that diffraction efficiencies of up to 90% can be achieved in the multiwave regime at 10.6 μm. Diffraction efficiencies of up to 20% at 632.8 nm have been measured for both the zero and ± 1 orders for volume gratings produced in this work. Diffraction efficiencies measured at visible wavelengths (632.8 nm) are in good agreement with the results of the coupled wave model. The parameters required for efficient operation of different diffractive optical elements in various wavebands have also been predicted by the model. Thicknesses of between 6 and 24 μm are required for efficient operation of these elements at 10.6 μm. Thicknesses of up to 4μm have been photodoped in the present study and there is no indication that thicker films cannot be photodoped. However, the long exposure times (>1 hr) required for films thicker than 3 μm sets a limit on the applicability of the photodissolution effect in producing optical elements thicker than 3 μm. So the main purpose of any further study should be concentrated on finding ways to improve the photodissolution sensitivity.

Recent measurements (Ewen et al. 1991) of the diffraction efficiency at 1.5 μm which showed that efficiencies of > 33% can be achieved for bulk holographic transmission gratings produced by photodissolution, are quite encouraging. Extension of these measurements to longer wavelengths and to thicker optical elements are required to confirm the prediction of the theoretical model for achieving efficient diffractive devices for IR operation.

8.7 References

Ewen, P.J.S., Slinger, C.W., Zakery, A., Zekak, A., and Owen, A.E., 1991, Proc. of the Int. Congress on Optical Science and Engineering, The Hague, The Netherlands, In Press.

Firth, A.P., 1985, PhD Thesis, Edinburgh University.

Mott, N.F., and Davis, E.A., 1979, "Electronic Processes in Non-Cryst. Materials", Clarendon press, Oxford.

Owen, A.E., Ewen, P.J.S., Zakery, A., and Slinger, C.W., 1990, Final technical report, Agreement No. 2087/30/RSRE (unpublished).

Plocharsky, J., Przyluski, J., and Wycislik, H., 1987, J. Non-Cryst. Solids, 93, p. 303.

Rennie, J.H.S., 1986, PhD Thesis, Cambridge University.

Swanepoel, A., 1983, J. Phys., E : Sci. Instrum., 16, p. 214.

Sze, S.M., 1988, "VLSI Technology, 2nd edition".

Tanaka, Ke., and Ohtsuka, Y., 1979, Thin Solid Films, 57, p. 59.

APPENDIX I

SOFTWARE FOR CONTROLLING A CONTINUOUS TIME MEASUREMENT

```
10 REM STORING DATA DEMO2 PROGRAM
20 REM Turn off TV interface and select display mode 3
30*TV 0,1
40 MODE131
50 REM USE CHANNELS 1 AND 2 ON ADC
60*FX 16,2
70 C%=1
75 B%=2
80 REM Initialisation
90 DIM X(1000), Y(1000), M(1000), N(1000)
100PROCconstants
110PROCparams
120 MODE 128
130 PROCaxes
140REM Set graohics and text windows
150VDU24,HM%+4:VM%+4;HM%+AW%;VM%+AH%;
160VDU28,0,31,79,29
170VDU30
180@%=&20209
190REM Main loop for each screenful
200REPEAT 210 j=0
215 l=0
220 REM : Routine for saving data on disc
230 PRINT "Do you want to create a file?"
240 D$=Get$
250 IF D$="N" THEN END
260 INPUT "FILE NAME= ", D$
270 F=OPENOUT(D$)
280PRINT"Type space to acquire data, or return to restart program :";
290X$=INKEY$(0)
300IF ASC(X$)=13 GOTO 30
310IF X$<>" " GOTO 290
320CLG
```

```
330CLS
340T%=O
350PROCsync
360TIME=O
370REM Acquire first point seperately, and move to the appropriate
380 REM position on the vertical axis
390REM Now acquire and display the data
400 REPEAT
405 j=j+1
410 Y%=FNsampl1
415 H%=FNhscale(T%)
420 V%=FNvscale(Y%)
425 X(j)=T%
430 Y(j)=Y%
440 MOVE H%,V%
442 DRAW H%,V%
450 Y1%=FNsampl2
452 H1%=FNhscale(T%)
455 V1%=FNvscale(Y1%)
460 M(j)=T%
465 N(j)=Y1%
467 MOVE H1%,V1%
469 DRAW H1%,V1%
470 UNTIL T%>=W%
480 FOR J=1 TO j
485 PRINT£F,X(J),Y(J)
490 NEXT J
495 FOR J=1 TO j
500 PRINT£F,M(J),N(J)
510 NEXT J
520 UNTIL false
530 PRINT "NO OF POINTS COLLECTED= ", j
540 CLOSE
550 END :REM End of main program
560 REM USES: HM%,VM%,AH%,AW%,RNG%,W%,LOWADC,HIADC
570DEF PROCaxes
580LOCAL N1%,RNGLIM%,NTRVL%,K%,I%
590MOVE HM%,VM%
```

```
600DRAW HM%+AW%,VM%
610MOVE HM%,VM%
620DRAW HM%,VM%+AH%
630VDU5
640REM Vertical scale, with autoscaling
650@%=&000003
660 RNG%=INT(HIADC-LOWADC)
670RNGLIM%=20
680K%=1
690N1%=RNG%
700IF N1%>RNGLIM% THEN N1%=N1%/10:K%=K%*10:GOTO 700
710NTRVL%=K%*AH%/RNG%
720FOR I%=0 TO N1%
730MOVE HM%,VM%+I%*NTRVL%
740PLOT 1,-10,0
750PLOT 0,-50,8
760 PRINT LOWADC+I%*K%
770NEXT I%
780REM Horizontal scale
790@%=2
800 IF W%<=1000 THEN M1%=100 ELSE M1%=10000
810NTRVL%=AW%*M1%/W%
820 FOR I%=0 TO W%/M1%
830 MOVE HM%+I%*NTRVL%,VM%
840PLOT 1,0,-10
850PLOT 0,-16,-8
860 PRINT I%*M1%*10
870NEXT I%
880@%=10
890VDU4
900ENDPROC
910REM Scale the time to fit the axis
920REM Uses: HM%,AW%,W%
930DEF FNhscale(T%)
940=HM%+T%*AW%/W%
950REM Scale the reading vertically
960 REM Uses: VM%,AH%,RNG%,LOWADC
970DEF FNvscale(Y%)
```

```
980LOCAL V1% 990 V1%=VM%+(AH%/RNG%)*Y%
1000IF V1%>VM%+AH% THEN V1%=VM%+AH%
1010IF V1%<VM% THEN V1%=VM%
1020=V1%
1022 DEF FNvscale(Y1%)
1023 LOCAL V2%
1024 IF V2%>VM%+AH% THEN V2%=VM%
1025 IF V2%<VM% THEN V2%=VM%
1027=V2%
1030REM Take a sample
1040 REM USES: C%,B%
1050 DEF FNsampl1
1060PROCwait
1070=ADVAL(C%)
1080 DEF FNsampl2
1082 PROCwait
1085=ADVAL(B%)
1090REM Wait for timer to come up
1100REM Uses: T%,DT%
1120DEF PROCwait
1130T%=T%+DT%
1140IF TIME<T% GOTO 1140
1150ENDPROC
1160REM Wait for an external event
1170DEF PROCsync
1180LOCAL X$
1190PRINT"Press space to go:";
1200X$=INKEY$(0):IF X$<>" " GOTO 1200
1210PRINT 1220REM Start a/d conversion
1230*FX 17,1
1240ENDPROC
1250REM Define various constants
1260DEF PROCconstants
1270AH%=850  :REM Axis height
1280 AW%=1000  :REM Axis width
1290HM%=100   :REM Horizontal margin
1300VM%=150   :REM Vertical margin
1310 LOWADC=0
```

```
1320 HIADC=65520
1330true=1
1340false=0
1350ENDPROC
1360LOWADC=ADVAL(C%)    :REM ADC reading at low end of rrange
1370HIADC=ADVAL(C%)     :REM ADC reading at top end of range
1380REM Read in parameters
1390 REM USES:DT%,W%
1400DEF PROCparams
1410PRINT:PRINT"PARAMETERS":PRINT
1420INPUT "Sample interval in ms (to nearest 10 ms) ",DT%
1430 DT%=DT%/10
1440 INPUT "Horizontal axis length in ms ", W%
1450 W%=W%/10
1460 ENDPROC
```

APPENDIX II

This appendix tabulates the constant parameters A and λ_c in the single oscillator dispersion equation :

$$n = [1 + \frac{A\lambda^2}{\lambda^2 - \lambda_c{}^2}]^{1/2}$$

for various compositions in the As-S system.

As-S SOURCE COMPOSITION	AS-S FILM COMPOSITION	A	λ_c
$As_{16.9}S_{83.1}$	$As_{25.3}S_{74.7}$	3.73	177.00
$As_{19.3}S_{80.7}$	$As_{24.9}S_{75.1}$	3.69	206.74
$As_{24.7}S_{75.3}$	$As_{28.6}S_{71.4}$	3.91	210.54
$As_{28.2}S_{71.8}$	$As_{30.8}S_{69.2}$	3.83	265.91
$As_{29}S_{71}$	$As_{30.6}S_{69.4}$	3.93	236.56
$As_{33.5}S_{66.5}$	$As_{34.4}S_{65.6}$	3.85	265.96
$As_{35.3}S_{64.7}$	$As_{34.6}S_{64.4}$	4.33	239.43
$As_{36.5}S_{63.5}$	$As_{37.8}S_{62.2}$	4.06	255.49
$As_{39.5}S_{60.5}$	$As_{39.5}S_{60.5}$	4.01	267.20

APPENDIX III

LIST OF PUBLISHED WORKS

1- P.J.S. Ewen, A. Zakery, A.P. Firth and A.E. Owen, " Compositional dependence of photodissolution kinetics in amorphous As-S films ", J. Non-Crys. Solids, 97-98(1987)p. 1127.

2- P.J.S. Ewen, A. Zakery, A.P. Firth and A.E. Owen, " Optical monitoring of photodissolution kinetics in amorphous As-S films ", Phil. Mag., B(57) (1988)p. 1.

3- A. Zakery, C.W. Slinger, P.J.S. Ewen, A.P. Firth and A.E. Owen, " Chalcogenide gratings produced by the metal photodissolution effect ", J. Phys. D : Appl. Phys. 21(1988) S78.

4- A.E. Owen, P.J.S. Ewen, A. Zakery, M.N. Kozicki and Y. Khawaja, " Metal-chalcogenide photoresists for high resolution lithography and sub-micron structures ", Proc. of the Int. Symp. on Nanostructure Physics and Fabrication, Academic press, 1989.

5- M.N. Kozicki, Y. Khawaja, A.E. Owen, P.J.S. Ewen and A. Zakery, " As-S / Ag system for Integrated Optics ", Proc. IEEE VLSI Multilevel Interconnection conference, (1989)p. 251.

6- A. Zakery, A. Zekak, P.J.S. Ewen, C.W. Slinger and A.E. Owen, " Optical Constants of Ag-Photodoped As-S Amorphous Films ", J. Non-Cryst. Solids, 114(1989)p. 109.

7- C.W. Slinger, A. Zakery, P.J.S. Ewen and A.E. Owen, " Photodoped chalcogenides as potential infrared holographic media " , Submitted to Appl. Opt., 1991.

8- P.J.S. Ewen, C.W. Slinger, A. Zakery, A. Zekak and A.E. Owen, " The fabrication and properties of chalcogenide IR diffractive elements ", Proc. of the Int. Congress on Optical Science and Engineering, The Hague, The Netherlands, 1991 in press.